Development of a Dual Fermion Approach to the fcc Hubbard Model

Max Howell

Balliol College

University of Oxford

A thesis submitted for the degree of

Doctor of Philosophy

Michaelmas 2019

Contents

Glossary

1Bz . . . . . First Brillouin zone

AFM . . . . . Anti-ferromagnetic

AIM . . . . . Anderson impurity model

CDMFT . . . Cluster dynamical mean field theory

CTAUX . . . . Auxiliary field expansion continuous time quantum Monte Carlo

CTHYB . . . . Hybridisation expansion continuous time quantum Monte Carlo

CTINT . . . . Interaction expansion continuous time quantum Monte Carlo

CTQMC . . . Continuous time quantum Monte Carlo

DCA . . . . . Dynamical cluster approximation

DDMC . . . . Diagrammatic determinant Monte Carlo

DF . . . . . Dual fermion approach

DFT . . . . . Density functional theory

DΓA . . . . . Dynamical vertex approximation

DMFT . . . . Dynamical mean field theory

DOS . . . . . Density of states

ED . . . . . Exact diagonalisation

FCC . . . . . Face-centered cubic

FLEX . . . . . Fluctuation exchange approximation

FM . . . . . Ferromagnetic

GPU . . . . . Graphics processing unit

MaxEnt . . . . Maximum entropy method

NRG . . . . . Numerical renormalization group

Abstract

We develop a codebase for performing dynamical mean field theory (DMFT) and dual fermion (DF) calculations on the Hubbard model, by modifying, extending, and interfacing several pre-existing open-source codes. This is used to examine the Hubbard model on a face-centered cubic (fcc) lattice, to obtain numerically-exact results at the level of DMFT and investigate the effect of non-local electron correlations within the dual fermion approach.

Our code centres around a modified implementation of the CTHYB quantum Monte Carlo technique used as an impurity solver. We discuss the modifications made, and validate our code by comparing its results to known results in the literature. The DF calculations are obtained by using the CTHYB results as inputs to an extension of the OpenDF code, which we likewise validate by comparison of our results to those of previous authors.

We study the magnetic phase diagram, magnetic susceptibilities, and single-particle dynamics of the Hubbard model on the fcc lattice. Within DMFT a large FM region is found above half-filling, the phase boundary of which is located precisely by susceptibility and magnetisation calculations. A large AFM phase is found around and below half-filling with contributions from instabilities towards the X and W points. Single-particle spectra are obtained using the Maximum Entropy method for a wide range of temperatures and fillings demonstrating how the spectra change as the FM phase boundary is crossed.

The non-local correlations taken into account by the DF approach reduce the critical temperatures of both the FM and AFM regions. Corrections in the FM region are small and strongly suggest that DMFT is able to capture the relevant physics in this region of the phase diagram.

The code developed as part of this project opens the door for further investigations of the Hubbard model on the fcc, and other lattices, across wide ranges of parameter space.

1 Introduction

Strongly correlated electron systems are host to some of the most interesting physical phenomena ranging from metal-insulator transitions [1–4] and high-temperature superconductivity [5–7] to itinerant ferromagnetism [8, 9] and the Kondo effect [10]. It is common to study these phenomena in terms of simplified models which have been constructed retaining only the interactions and features that are thought to be relevant to the underlying physics. One such model, and the model studied within this thesis, is the Hubbard model [11]. The Hubbard model is the simplest model of interacting electrons on a lattice, the two main elements of its Hamiltonian are a term describing the kinetic energy of the electrons and an on site Coulomb repulsion representing the energy penalty paid for two electrons of opposing spin to occupy the same site. Despite this simplicity the Hubbard model has all the features relevant in order to study a wide range of strongly correlated electron phenomena and is regularly used to do so. The model has been shown to display metal-insulator transitions [2, 3] and its two dimensional variant is thought to be a good model for the copper oxide planes in high-temperature superconductors [7].

A system is considered to be strongly correlated when its potential and kinetic energy are of the same order. When the potential energy is small we are able to treat these systems using perturbation theories in the Coulomb interaction or using mean field theories such as Hartree-Fock. However when the potential energy

is of the same order as the kinetic energy, these approaches break down and we must use alternative methods. One such method that has seen major success is the dynamical mean field theory (DMFT) [12].

The concept behind DMFT involves mapping the Hubbard model onto a self-consistently determined impurity model, it can be shown that in $d = \infty$ this mapping becomes exact [12]. The above mapping can be thought of as selecting a single site from the lattice and replacing the remaining sites with a non-interacting bath of electrons. The bath and site are then coupled together in a self-consistently determined manner such that the bath best replicates the lattice which it replaced. In this way we are able to retain the local interaction on the site as well as the temporal fluctuations of electrons hopping between the site and bath. However, in replacing the rest of the lattice with the bath of electrons we lose all correlations between the sites. Thus, DMFT is able to capture and fully treat the local correlation on the site however it completely neglects non-local correlations.

While DMFT allows one to reduce the problem of solving a lattice problem, the Hubbard model, to that of solving an impurity problem, the latter is still a complex and fully interacting quantum problem and still presents a challenge. To this end there have been many methods known as impurity solvers designed to tackle this task. These range from exact diagonalisation (ED) approaches [12, 13] and the numerical renormalization group (NRG) [14] to Hirsch-Fye quantum Monte Carlo [15] as well as the approach used in this thesis: continuous-time quantum Monte Carlo (CTQMC) [16, 17]. This collection of numerically exact algorithms works by using a Monte Carlo procedure in order to sample an expansion of the impurity partition function and has recently become a popular choice of impurity solver when studying the Hubbard model within DMFT.

The dynamical mean field theory has found particular success in studying the Mott metal-insulator transition where it is able to describe the localisation of the electrons as the interaction is increased [2, 12]. It is also now regularly used in conjunction with DFT in order to perform electronic structure calculations of correlated materials where a traditional DFT approach would fail [18]. As such

the DFT + DMFT approach has also been adopted by the materials science community [19].

DMFT, however, does have its downfalls. For example it incorrectly predicts a non-zero Néel temperature at half-filling in the 2D Hubbard model [20] where it is known that a transition at finite temperature is forbidden by the Mermin-Wagner theorem and the anti-ferromagnetic state is only obtained at $T = 0$ [21]. It has also been shown to produce a finite critical interaction for the Mott transition in the 2D Hubbard model [2]. However, this has recently been shown to be false using methods taking the non-local correlation missed by DMFT into account. When this is done it is found that a paramagnetic insulating state can be found at low temperature for all non zero values of the interaction [22].

While DMFT is capable of describing the above physics with origins in local correlations, it is clearly by construction not able to properly describe physics with origins in non-local correlations. These include high temperature superconductivity [5, 6] and formation of magnons that are not properly taken into account at the DMFT level [23]. Efforts have been made in order to extend or build upon DMFT in order to take into account the non-local correlations missed when DMFT is applied in finite dimensions. These include cluster extensions of DMFT where one considers a cluster of sites (instead of just a single site) hybridised to self-consistently determined medium [24]. This allows for short range correlation to be taken into account explicitly when treating the cluster. Another method of achieving this involves building diagrammatic perturbation theories around the DMFT result in order to build back in the non-local correlations missed [23]. This is the approach adopted by the method used within this thesis: the dual fermion approach [25, 26].

The dual fermion technique tackles non-local correlation using a perturbative approach, splitting the local and non-local correlation of the model [27, 28]. To achieve this, the original Hubbard model is reformulated as a set of coupled impurity problems. A set of dual fermions are then introduced transforming the coupling between the impurities into a local coupling to the dual fermions. This allows for all the local correlation to be treated in terms of the impurity model, using a

method such as CTQMC. The non-local correlations can then be taken into account through a perturbation theory in terms of the dual fermions. This approach allows for non-local correlation to be taken into account on all length scales.

The dual fermion approach was first applied to the 2D Hubbard model where it was shown to correctly reproduce anti-ferromagnetic pseudogap formation [25, 26]. The approach was also used to investigate the Néel temperature of the same model where DMFT incorrectly predicts a non-zero critical temperature. This was done by Hafermann et. al. who employed a ladder approximation in the perturbation theory for the dual fermions, the study showed that the Néel temperature is reduced from the DMFT value [29]. Subsequently Otsuki et. al. also used the ladder dual fermion approach to show that a critical Néel temperature of 0 is correctly reproduced in accordance with the Mermin-Wagner theorem [5]. The dual fermion approach has also been used to study the Hubbard model on a variety of different lattices such as the triangular lattice [30] and a multiband extension of the method has been used to study the Hubbard model on the honeycomb lattice [31]. It has also been used to study the critical behaviour around the anti-ferromagnetic phase transition of the 3D Hubbard at half-filling [32]. The method has also been used to study models other than the Hubbard model such as the Falicov-Kimball model where it was shown that the dual fermion method is able to correctly capture critical behaviour in the vicinity of phase transitions [33]. There has even been attempts to study high-temperature superconductivity in the 2D Hubbard model using a dual fermion approach [6].

In this work we use a ladder dual fermion approach to the study the ferromagnetic and anti-ferromagnetic phase transitions found in the single band Hubbard model on the face-centered cubic lattice. The magnetic phase diagram of the Hubbard model on the fcc lattice has been studied before using multiple methods. One was a spectral density approach used by Herrmann et. al. where they found a ferromagnetic state arises for all fillings above half-filling and a paramagnetic state otherwise [34]. The model has also been studied using DMFT by Ulmke where he looked at the 3D case as well as an infinite dimensional generalisation where the DMFT result becomes exact [9]. There it was found that there is a substantial

ferromagnetic region in the 3D fcc Hubbard model when next-nearest neighbour hopping is taken into account however, it extends over a smaller range of fillings. Ulmke also reported the existence of an anti-ferromagnetic phase around half-filling. Ulmke's study was carried out using the Hirsch-Fye QMC impurity solver, a method that suffers from time discretisation errors [15]. More recently the magnetic phase diagram of the fcc Hubbard model has been studied using a slave boson approach by Igoshev et. al [35]. This was subsequently built upon by Timirgazin by allowing for the formation of additional magnetic states [36]. In both studies they report a phase diagram for the full range of fillings showing that for large enough values of the Coulomb interaction there exists a ferromagnetic region above half-filling. They also report the existence of an anti-ferromagnetic region at half-filling that extends slightly above and below $n = 1$ and is sandwiched by regions of phase separation.

The ferromagnetic behaviour observed in the above studies and later in this thesis have significance in understanding the magnetic behaviour of the metallic ferromagnets Nickel and Cobalt[37, 38]. Indeed Ulmke notes that the critical temperature obtained in his DMFT study [9] is on the order of $600K$ which compares well with experimental values for Nickel [39]. Lichtenstein et. al. have also performed a DFT + DMFT study of magnetism in Nickel [40]. They were able to achieve reasonable agreement between experiment and calculation for both the magnetisation and susceptibility temperature dependence. Braun et. al. have also been able to interpret the experimental photoemission spectra of ferromagnetic Nickel using a similar DFT + DMFT approach [41], supporting the abilities of DMFT in describing experimentally observed behaviour.

As will be seen in the later chapters of this thesis two anti-ferromagnetic states are found to be prominent within the fcc Hubbard model. These correspond to divergences in the magnetic susceptibility at the X and W points and are otherwise known as type-I and type-III anti-ferromagnet order. These states were also observed in the slave boson studies of Igoshev et. al [35] and Timirgazin et. al. [36] and are referenced in Ulmke's DMFT study [9]. Using neutron diffraction the type-I AFM state has been observed in UO_2 where the crystal structure is such that the

uranium atoms lie in an fcc arrangement [42, 43]. The type-III AFM state has been observed using neutron scattering in the compounds MnS_2 [44] and YbAs [45, 46].

The aim of this work is to study the fcc Hubbard model using DMFT and the dual fermion approach, applying the newer and more accurate CTHYB method as well as newly developed more accurate measurements for the single and two-particle Green's functions [47, 48]. This requires the modification of an existing CTHYB code [49] and the implementation of the more accurate measurements [47, 48] as well as development of a DMFT code. This will allow for a more accurate calculation of the magnetic susceptibility and therefore much better resolution of the DMFT magnetic phase boundaries for this model. Following this we wish to apply the dual fermion method in order to take into account the non-local correlations missed by DMFT. This will allow us to study the effect of non-local correlation on the magnetic phase diagram where it has already been shown that non-local correlations can dramatically change the critical temperature of the anti-ferromagnetic state in the 2D Hubbard model [5, 29]. Applying the dual fermion method will require further code development to modify the existing OpenDF dual fermion software [50] and obtain suitable input measurements from the CTHYB code.

The remaining chapters of this thesis are structured as follows. In chapter 2 we introduce the two models relevant to the work in this thesis. These are the single impurity Anderson model and the Hubbard model. We also take the opportunity here to introduce imaginary time and imaginary frequency Green's functions: these provide a mathematical framework for studying these models and their physical properties at finite-temperature.

In chapter 3 we move on to discuss hybridisation expansion continuous time quantum Monte Carlo, the impurity solver used within this project. We cover the derivation of the method, the Monte Carlo procedure and how measurements of the single and two-particle Green's functions can be performed. We then explain how the code was developed for this project and show that our code accurately reproduces results from the literature. The chapter closes with an introduction

to analytic continuation of imaginary time/frequency Green's functions using the maximum entropy method [51].

The subject of chapter 4 is the dynamical mean field theory. We cover the concepts involved in DMFT, the self-consistency loop and how the calculations are performed in practice. We also present calculations that were performed as a test case for the new DMFT code written for this thesis. These replicate DMFT results from the literature for the 2D Hubbard model showing a metal-insulator transition.

In chapter 5 we present a DMFT study of the magnetic phase diagram of the Hubbard model on the fcc lattice. We cover the ferromagnetic and anti-ferromagnetic regions presenting the magnetic susceptibility and single-particle spectra as well as the determined phase boundaries. For the ferromagnetic region, we also present calculations of the magnetisation as a function of temperature and plots of associated spin resolved spectra.

The topic of chapter 6 is the dual fermion method. We present an overview of the formalism as well as presenting results from calculations performed during testing that were carried out in order to test that accurate results could be obtained. We also present calculations replicating results from the literature for the 2D Hubbard model showing that all of the code produced and modified as part of this thesis is able to perform accurate dual fermion calculations. Following this the results of the dual fermion calculations building upon the DMFT results of the previous chapter are presented, we cover the lattice self-energy as well as the magnetic susceptibility. We also present phase boundaries obtained from the dual fermion results showing how both the ferromagnetic and anti-ferromagnetic regions are affected when non-local correlations are taken into account.

In chapter 7 we finish with a summary and conclusion of the work carried out and results obtained. We also provide some remarks on further work that could be carried out as well as ways the results obtained here could be built upon.

2

Models and Green's Functions

A model at the heart of the work of this project is the Hubbard model, it is the simplest model of interacting electrons on a lattice and is regularly employed in order to study physical phenomena such as metal-insulator transitions [1–3] and, as is the case in this project, magnetism [5, 9, 32]. However, despite its simplicity exact results are often not available and approximate methods have to be employed. One such method is that of the dynamical mean field theory (see chapter 4) within which the Hubbard model is mapped onto an effective self-consistent single impurity Anderson model. Thus, in this chapter we provide an introduction to both the Hubbard model and the single impurity Anderson model, as well as discuss two limits in which exact results are obtainable, namely the atomic limit and non-interacting limit. These results are obtained within the language of imaginary time and imaginary frequency Green's functions. These are at the core of the continuous-time quantum Monte Carlo method employed throughout this work, where they serve as both input and solutions (see chapter 3). Thus, we will provide an introduction to these objects as well as a discussion of some of their properties and their relation to physically relevant quantities such as the single-particle spectrum and magnetic susceptibility. First however we turn our attention back to the models, more specifically to the Hubbard model which is the subject of the following section.

2.1 The Hubbard Model

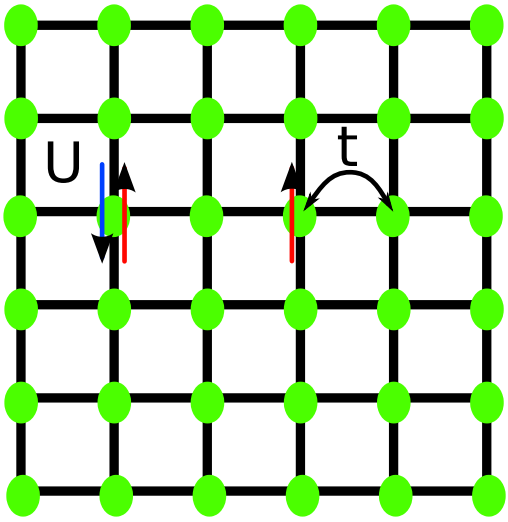

Figure 2.1: A pictorial description of the Hubbard model on the square lattice.

The Hubbard model is central to the work of this thesis as well as the area of strongly correlated electron problems in general. It was originally introduced by Hubbard in order to try and explain itinerant ferromagnetism in transition metals [11]. It is one of the simplest models of interacting electrons on a lattice, with its Hamiltonian consisting of three terms. The first term of the Hamiltonian describes the kinetic energy of the electrons moving around the lattice, the second and third describe the potential energy consisting of a local interaction and the energy cost of having an electron on a given site. As such the Hamiltonian is defined as:

$$H = -t \sum_{\langle ij \rangle, \sigma} c^{\dagger}_{i\sigma} c_{j\sigma} + U \sum_{i} n_{i\uparrow} n_{i\downarrow} - \mu \sum_{i} (n_{i\uparrow} + n_{i\downarrow}) \tag{2.1}$$

where t is the hopping element, U the Hubbard interaction and μ the chemical potential. The operators $c^{\dagger}_{i\sigma}$ and $c_{i\sigma}$ are the usual creation and annihilation operators for an electron on site i with spin σ and $n_{i\sigma}$ is the number operator for σ spin electrons on site i.

The first term is a spin conserving hopping of an electron from site j to site i with an amplitude that is equal for all sites; the angular brackets denote that this sum is restricted to just nearest neighbours. The second term describes the

Coulomb repulsion between two opposing spin electrons when they occupy the same site. The chemical potential sets the electron filling of the lattice and its negative represents the energy of the available orbital on each site. It is also possible to extend this model somewhat to include hopping beyond just nearest neighbour to next-nearest neighbour and beyond. These extensions result in extra hopping terms with additional hopping parameters, for the case of next-nearest neighbours this is usually termed t'. An extension to next-nearest neighbour hopping is used in the study of the magnetic phases of the Hubbard model on the fcc lattice in chapter 5 of this thesis. The Hubbard model can also be studied on many different lattices and in any number of dimensions [52] this just dictates the form of the hopping term.

The above simplified model arises from physically motivated approximations to a much more general lattice model as described by Hubbard [11]. The Hubbard model is restricted to a single band by making the assumption that the physics at low temperature is governed by the behaviour around the fermi-level and there is not enough energy available to make excitations to higher energy bands. Thus, if only one band is present at the fermi-level and it is well separated from the surrounding bands then the physics of the system is going to be governed by the behaviour of this single band. One can then further argue that if the electrons are sufficiently localised to a lattice site, which is the case for magnetic transition metals relevant to this project such as Fe, Ni and Co, then the overlap between orbitals on neighbouring lattice sites is going to be the most relevant with further contributions decaying rapidly. This physically motivates the restriction of the hopping term to just nearest neighbour hopping as well as only taking into account the on-site local interaction and dropping terms arising from interactions between neighbour sites. The above simplifications allow for the model to become simple enough that the problem becomes tractable whilst still retaining the most relevant features in order to describe the physics. These restrictions can however be relaxed somewhat and some interactions between electrons on neighbouring sites can be included through extensions to the Hubbard model, such as multi-orbital extensions [53] and including interactions beyond the just the local Coulomb interaction [54].

Despite the interaction within the Hamiltonian being purely local, non-local correlation arises. For example, due to the interplay between the hopping and Coulomb repulsion it can be energetically unfavourable to hop to a neighbouring site that is already occupied, thus, introducing correlations between all sites on the lattice.

While the Hamiltonian itself is rather simple, the complex interplay between the kinetic and potential energy of the electrons as well as the lattice upon which they reside gives rise to many interesting physical phenomena. The model has been used to study a wealth of interesting physics such as the Mott transition[1, 2], magnetism[5, 6, 9] and high-T_c superconducting behaviour[5, 6]. Despite its relative apparent simplicity, it is very difficult to study in general. Tackling a solution by analytical means is not always possible except in certain limits such as the atomic-limit ($t = 0$) and non-interacting limit ($U = 0$) or in one dimension where analytical methods have much more traction [55]. It is however possible to solve the Hubbard model for a finite-sized system numerically through methods such as exact diagonalisation [56]. However, the exponential growth of the Hilbert space with the number of sites makes this intractable very quickly even for relatively small cases. Thus, approximate methods such as the dynamical mean field theory (see chapter 4), where the Hubbard model is mapped onto an effective impurity model with an accompanying self-consistency condition, are often employed [12]. For this reason, we now turn to the simplest of such impurity models, the Anderson impurity model.

2.2 Single Impurity Anderson Model - AIM

The Anderson impurity model (AIM) was originally introduced by Anderson in order to investigate magnetic impurities embedded within a metallic host[57]. It describes a single impurity atom through an interacting impurity site and the metallic host as a non-interacting bath of conduction electrons. The impurity site and the host are connected through a hybridisation allowing electrons to move from the bath to the impurity site and vice versa. The Hamiltonian for the model reads:

$$H = H_\mu + H_U + H_{bath} + H_{hyb} \tag{2.2}$$

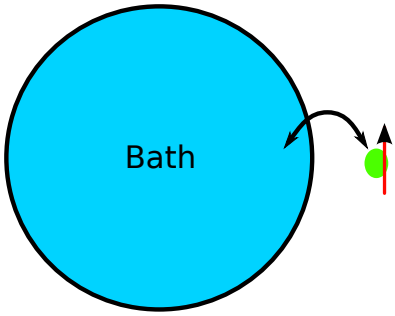

Figure 2.2: A pictorial description of the single impurity Anderson Model.

$$H_\mu = -\mu \left(n_\uparrow + n_\downarrow\right) \tag{2.3}$$

$$H_U = U n_\uparrow n_\downarrow \tag{2.4}$$

$$H_{bath} = \sum_{k\sigma} \epsilon_k a^\dagger_{k\sigma} a_{k\sigma} \tag{2.5}$$

$$H_{hyb} = \sum_{k,\sigma} V_{k,\sigma} c^\dagger_\sigma a_{k,\sigma} + \sum_{k,\sigma} V^*_{k,\sigma} a^\dagger_{k,\sigma} c_\sigma \tag{2.6}$$

where the set of operators $c^\dagger_\sigma$,c_σ act on the impurity and the set $a^\dagger_{k\sigma}$,$a_{k\sigma}$ act on the bath. The two terms $H_\mu + H_U = H_{loc}$ describe the local Hamiltonian on the impurity site with a single orbital of energy $-\mu$ and a Coulomb interaction U between electrons of opposing spin. The H_{bath} term describes the bath states with energies ϵ_k, and H_{hyb} describes the spin preserving coupling between the bath and impurity site parametrised by $V_{k,\sigma}$.

While this is a simpler model than the Hubbard model in principle it is still a fully interacting many-body problem and is not generally exactly solvable or easily studied by numerical means. However, due to the AIM's association with DMFT (see chapter 4) and its relevance to Kondo physics there have been many methods developed in order to solve it and its various extensions. These are known as impurity solvers (see section 3) and generally they provide a solution in the form of a single-particle Green's function. From the single-particle Green's function we are able to calculate physical properties of the system, including the spectral function $A(\omega)$.

2.3 Imaginary time and Imaginary Frequency Green's Functions

In the following sections, we provide a brief introduction to the single-particle and two-particle Green's functions, there are many books available that provide good overviews of the single-particle Green's functions used throughout this thesis such as that of Mahan [58]. We will also introduce the generalised susceptibility, which is an important quantity for the calculation of the magnetic susceptibility within DMFT, and the reducible vertex function that serves as input for the dual fermion approach as well as other extensions to DMFT. For the interested reader there is a very thorough and complete overview of the properties, symmetries and the relationship between the two-particle Green's function and the various vertex functions in a paper by Rohringer[59] as well as his thesis [60]. For an introduction to the single-particle Green's function and the finite temperature / imaginary time formalism in general see Mahan's book [58].

The imaginary time single-particle Green's function is of central importance to the work within this thesis, in order to define it we first introduce the concept of imaginary time. An imaginary time operator is defined by the corresponding Schrödinger operator within the Heisenberg representation.

$$c^{\dagger}_{i\sigma}(t) = e^{itH} c^{\dagger}_{i\sigma} e^{-itH} \tag{2.7}$$

By letting $\tau = it$ we can view this as an imaginary time operator that creates a σ spin electron at site i at imaginary time τ. This may not seem necessary, however, it proves a convenient mathematical trick for working with Green's functions at finite temperature [58].

2.3.1 The Single-Particle Green's Function

The imaginary time single-particle Green's function is defined as:

$$\begin{aligned} G_{i,j|\sigma_1,\sigma_2}(\tau_1,\tau_2) &= -\langle \hat{T}\left[c_{i\sigma_1}(\tau_1)c^{\dagger}_{j\sigma_2}(\tau_2)\right]\rangle \\ &= -\frac{1}{Z}\mathrm{Tr}\left[e^{-\beta H}\hat{T}\left[c_{i\sigma_1}(\tau_1)c^{\dagger}_{j\sigma_2}(\tau_2)\right]\right] \end{aligned} \tag{2.8}$$

where the angular brackets denote the thermal expectation and $Z = \mathrm{Tr}\left[e^{-\beta H}\right]$ is the usual partition function. The operator $\hat{T}$ denotes the Dyson time ordering operator and is defined in (2.9), this orders the operators such that the operator with the most recent imaginary time argument appears on the left whilst also taking care of the sign resulting from permuting fermionic operators.

$$\hat{T}\left[c_{i\sigma_1}(\tau_1)c^{\dagger}_{j\sigma_2}(\tau_2)\right] = \begin{cases} c_{i\sigma_1}(\tau_1)c^{\dagger}_{j\sigma_2}(\tau_2) & : \tau_1 > \tau_2 \\ -c^{\dagger}_{j\sigma_2}(\tau_2)c_{i\sigma_1}(\tau_1) & : \tau_1 \leq \tau_2 \end{cases} \tag{2.9}$$

We are able to derive some important properties of these Green's functions from the definition (2.8). For simplicity and without loss of generality we drop the site index in the following discussion.

Using the cyclic property of the trace, it can be shown that the above Green's function only depends on the time difference $\tau = \tau_1 - \tau_2$. Thus, we can drop one of the imaginary time arguments without any loss of generality. Also since the Hamiltonians that are used within this project do not have any terms involving spin flipping, the Green's function is spin diagonal and is therefore only a function of one spin argument σ. (For the case of a paramagnetic state we also have $G_{\uparrow}(\tau) = G_{\downarrow}(\tau) = G(\tau)$ and the spin indices can be dropped all together).

$$G_{\sigma}(\tau) = -\langle \hat{T}\left[c_{\sigma}(\tau)c^{\dagger}_{\sigma}(0)\right]\rangle \tag{2.10}$$

Again using the cyclic property of the trace it is possible to show the single-particle Green's function obeys the following.

$$G_{\sigma}(\tau - \beta) = -G_{\sigma}(\tau) \quad \text{for} \quad \tau > 0 \tag{2.11}$$

The proof of this is simple and starts from the definition (2.8), we then consider the case of $\tau > 0$ explicitly (the proof for $\tau < 0$ is similar) and proceed as follows:

$$\begin{aligned} G_{\sigma}(\tau) &= -\frac{1}{Z}\mathrm{Tr}\left[e^{-\beta H}e^{\tau H}c_{i\sigma}e^{-\tau H}c^{\dagger}_{j\sigma}\right] \\ &= -\frac{1}{Z}\mathrm{Tr}\left[e^{H(\tau-\beta)}c_{i\sigma}e^{-H(\tau-\beta)}e^{-\beta H}c^{\dagger}_{j\sigma}\right] \\ &= -\frac{1}{Z}\mathrm{Tr}\left[e^{-\beta H}c^{\dagger}_{j\sigma}c_{i\sigma}(\tau-\beta)\right] \\ &= -G_{\sigma}(\tau-\beta) \quad \text{for} \quad \tau > 0 \end{aligned} \tag{2.12}$$

where we have inserted unity $\mathbb{1} = e^{\beta H}e^{-\beta H}$ on line two. Using (2.11) twice we can show that $G_\sigma(\tau)$ is anti-periodic with a period of 2β, thus, we are able to restrict τ to the interval $[0, \beta]$.

This periodicity allows for the above Green's function to be expanded in a Fourier series defining the single-particle imaginary frequency Green's function $G_\sigma(i\nu_n)$.

$$G_\sigma(\tau) = \frac{1}{\beta}\sum_{n\in\mathbb{Z}} G_\sigma(i\nu_n)e^{-i\nu_n\tau} \tag{2.13}$$

$$G_\sigma(i\nu_n) = \int_0^\beta d\tau G_\sigma(\tau)e^{i\nu_n\tau} \tag{2.14}$$

The frequencies $\nu_n = \frac{(2n+1)\pi}{\beta}$ $n \in \mathbb{Z}$ are known as the fermionic Matsubara frequencies so the imaginary frequency Green's functions are often refereed to as Matsubara Green's functions.

While the above imaginary time/frequency Green's functions are important and powerful for studying strongly correlated electron systems at finite temperature they not do have direct physical significance. However, they can be related back to their real time counterparts which do have physical significance and can offer important insight to the single-particle excitations of the system. To this end we introduce the Lehmann representation. Starting from (2.8) and explicitly writing out the trace we have the following.

$$G_\sigma(\tau) = -\frac{1}{Z}\sum_m e^{-\beta E_m}\langle m|\, c_\sigma(\tau)c_\sigma^\dagger(0)\,|m\rangle \tag{2.15}$$

Inserting a complete set of eigenstates between the two operators and rewriting the Heisenberg operators in terms of the Schrödinger operators yields

$$G_\sigma(\tau) = -\frac{1}{Z}\sum_{mm'} e^{-\beta E_m}e^{-\tau(E_{m'}-E_m)}\langle m|\, c_\sigma\,|m'\rangle\langle m'|\, c_\sigma^\dagger\,|m\rangle \tag{2.16}$$

where E_m is the eigenvalue of the state $|m\rangle$ satisfying $H|m\rangle = E_m|m\rangle$. We can now move to the imaginary frequency domain using (2.14) giving us the Lehmann representation of the single-particle Green's function.

$$\begin{aligned} G_\sigma(i\omega_n) &= -\frac{1}{Z}\int_0^\beta e^{i\nu_n\tau}\sum_{mm'} e^{-\beta E_m}e^{-\tau(E_{m'}-E_m)}\langle m|\, c_\sigma\,|m'\rangle\langle m'|\, c_\sigma^\dagger\,|m\rangle \\ &= \frac{1}{Z}\sum_{mm'}\frac{e^{-\beta E_{m'}}+e^{-\beta E_m}}{i\omega_n-(E_m-E_{m'})}\left|\langle m|\, c_\sigma\,|m'\rangle\right|^2 \end{aligned} \tag{2.17}$$

From this expression we are able to extract information about the single-particle excitation energies from the imaginary frequency Green's function. To do this we define the single-particle spectrum as:

$$A_\sigma(\omega) = 2\pi \sum_{mm'} \frac{e^{-\beta E_{m'}} + e^{-\beta E_m}}{Z} \left|\langle m| c_\sigma |m'\rangle\right|^2 \delta(\omega - (E_m - E_{m'})) \tag{2.18}$$

this function clearly only has weight where ω is equal to the excitation energies $E_m - E_{m'}$. We are then able to write the imaginary frequency Green's function in what is known as the spectral representation.

$$G_\sigma(i\nu_n) = \frac{1}{2\pi} \int d\omega \frac{A_\sigma(\omega)}{i\nu_n - \omega} \tag{2.19}$$

From this we would expect to be able to invert (2.19) in order to obtain the single-particle spectrum $A_\sigma(\omega)$ from the Green's function $G_\sigma(i\nu_n)$. However, for the case of CTQMC data, this is an ill-posed problem and requires the use of analytic continuation methods such as the maximum entropy method which is introduced in section 3.2. For analytic results one may continue $G(i\nu_n)$ back onto the real axis by making the substitution $i\nu_n \to \omega + i\eta$ where $\eta \to 0^+$. This gives the finite temperature retarded real frequency Green's function $G^R_\sigma(\omega)$, the imaginary part of which is directly related to the spectral function through the following.

$$A_\sigma(\omega) = -\frac{1}{\pi} \mathrm{Im}\left[G^R_\sigma(\omega)\right] \tag{2.20}$$

The spectral function $A(\omega)$ is experimentally accessible and can be directly measured through photoelectronic spectroscopy, thus, providing a link between theory and experiment.

2.3.2 The Two-Particle Green's Function, Generalised Susceptibility and Vertex Function

In the following section we give a very brief overview of the two-particle Green's function, generalised susceptibility and vertex function, the details of which are complex and technical and we do not go into detail here. A much more in-depth discussion is given in the following article by Rohringer [59] which itself is covered in even more detail in his thesis [60].

The reason for introducing these objects in the case of the two-particle Green's function and generalised susceptibility is they are important ingredients in the calculations of physical quantities such as the magnetic susceptibility [12]. This allows for the DMFT study of magnetism within the Hubbard model on the fcc lattice which is presented in chapter 5. Furthermore, the vertex function is used within the dual fermion approach in order to treat the non-local correlation missed by DMFT (see chapter 6). The generalised susceptibility and the vertex function are themselves derived from the two-particle imaginary time Green's function which is defined as:

$$G^{(2)}_{\sigma_1,\sigma_2,\sigma_3,\sigma_4}(\tau_1,\tau_2,\tau_3,\tau_4) = \langle \hat{T}\left[c_{\sigma_1}(\tau_1)c^{\dagger}_{\sigma_2}(\tau_2)c_{\sigma_3}(\tau_3)c^{\dagger}_{\sigma_4}(\tau_4)\right]\rangle \tag{2.21}$$

this quantity contains all information about the correlated and uncorrelated propagation of a pair of particles through the system. Similarly to the single-particle case making considerations about spin conservation constrains the spin indices to just six non-zero combinations from the possible 16. We can further constrain ourselves to the case of $\sigma = \sigma_1 = \sigma_2$ and $\sigma' = \sigma_3 = \sigma_4$ from which the other possible spin combinations ($\sigma = \sigma_1 = \sigma_4$ and $\sigma' = \sigma_2 = \sigma_3$) can be obtained by means of a crossing symmetry [59].

Using the cyclic property of the trace coupled with time translational symmetry we are able to express $G^{(2)}$ in terms of just three imaginary times. This is achieved in a similar way to the expression of the single-particle Green's function when it is expressed in terms of just one imaginary time. This leads to its Fourier transform, the imaginary frequency two-particle Green's function, being a function of two fermionic frequencies $\nu_n = \frac{(2n+1)\pi}{\beta}$ and an additional bosonic frequency $\omega_m = \frac{2m\pi}{\beta}$. The frequency notation adopted here is known as particle-hole notation and is related back to the Fourier transform of the full four time object by $\nu_1 = \nu_n$, $\nu_2 = \nu_n + \omega_m$, $\nu_3 = \nu_{n'}$ and $\nu_4 = \nu_{n'} + \omega_m$ [60].

$$G^{(2)}_{\sigma,\sigma'}(i\nu_n, i\nu_{n'}, i\omega_m) = \iiint_0^{\beta} d\tau_1 d\tau_2 d\tau_3 G^{(2)}_{\sigma,\sigma'}(\tau_1,\tau_2,\tau_3,0)e^{-i\nu_n\tau_1}e^{i(\nu_n+\omega_m)\tau_2}e^{-i(\nu_{n'}+\omega_m)\tau_3} \tag{2.22}$$

The two-particle Green's function can be analysed using diagrammatic perturbation theory, using this method it can be decomposed into two parts [59].

The connected part $G^{conn}_{\sigma\sigma'}$, describing the correlated propagation of two particles, and the disconnected part G^{diss} describing the uncorrelated propagation of two particles. The disconnected part consists of just two products of single-particle Green's functions. When discussing the disconnected part in the following we drop the spin index on the single-particle Green's function since all two-particle quantities calculated as part of this project are done so for a paramagnetic state.

$$G^{conn}_{\sigma\sigma'}(i\nu_n, i\nu_{n'}, i\omega_m) = G^{(2)}_{\sigma,\sigma'}(i\nu_n, i\nu_{n'}, i\omega_m) - G^{diss}(i\nu_n, i\nu_{n'}, i\omega_m) \tag{2.23}$$

$$G^{diss}(i\nu_n, i\nu_{n'}, i\omega_m) = G(i\nu_n + i\omega_m)G(i\nu_{n'})\delta_{\omega_m,0} - G(i\nu_n + i\omega_m)G(i\nu_{n'})\delta_{\nu_n\nu_{n'}}\delta_{\sigma\sigma'} \tag{2.24}$$

Furthermore, using diagrammatic perturbation theory, the connected part of the two-particle Green's function is related to the so called two-particle vertex function $\gamma_{\sigma,\sigma'}(i\nu_n, i\nu_{n'}, i\omega_m)$. This is an important part of the dual fermion method where it describes the interactions between the dual fermions as will be seen later in chapter 6 [25]. The vertex function is obtained from the connected part of the two-particle Green's function by dividing through with a product of four one particle Green's functions.

$$\gamma_{\sigma,\sigma'}(i\nu_n, i\nu_{n'}, i\omega_m) = \frac{G^{conn}_{\sigma\sigma'}(i\nu_n, i\nu_{n'}, i\omega_m)}{G(i\nu_n)G(i\nu_n + i\omega_m)G(i\nu_{n'} + i\omega_m)G(i\nu_{n'})} \tag{2.25}$$

Diagrammatically this corresponds to amputation of the 'legs' from the connected part of the two-particle Green's function.

Another important quantity derived from the two-particle Green's function is the generalised susceptibility $\chi_{\sigma,\sigma'}(i\nu_n, i\nu_{n'}, i\omega_m)$ which is related to the physical magnetic susceptibility. This is obtained from the full two-particle Green's function through:

$$\chi_{\sigma,\sigma'}(i\nu_n, i\nu_{n'}, i\omega_m) = G^{(2)}_{\sigma,\sigma'}(i\nu_n, i\nu_{n'}, i\omega_m) - G(i\nu_n + i\omega_m)G(i\nu_{n'})\delta_{\omega_m,0} \tag{2.26}$$

where we can see that this is subtracting just one of the terms in the disconnected part. In order to calculate the magnetic susceptibility within DMFT, we use the generalised susceptibility within the magnetic channel defined by the following equation.

$$\chi^m(i\nu_n, i\nu_{n'}, i\omega_m) = \chi_{\uparrow\uparrow}(i\nu_n, i\nu_{n'}, i\omega_m) - \chi_{\uparrow\downarrow}(i\nu_n, i\nu_{n'}, i\omega_m) \tag{2.27}$$

A discussion of how the magnetic susceptibility is calculated from this quantity is given within section 4.3 and is also covered in [12, 47].

2.4 Green's Functions For The Atomic and Non-interacting Limits

To illustrate the above formalism in the following section we derive the single-particle Green's function in two limits where it is possible to do so, the atomic limit and the non-interacting limit. This produces some useful results and insight that will be useful for the later chapters of this thesis as well as provide some exact results that were useful for testing the code written as part of this project.

2.4.1 The Non-interacting ($U = 0$) Green's Functions

The Hamiltonian for the case of the non-interacting Anderson impurity model is given by the following equation.

$$H = H_\mu + H_{bath} + H_{hyb} \tag{2.28}$$

Using an equations-of-motion method the non-interacting impurity Green's function $G^0(i\nu_n)$ can be obtained in imaginary frequency in terms of a frequency dependent hybridisation function $\Delta(i\nu_n)$ [10].

$$G^0(i\nu_n) = \frac{1}{i\nu_n + \mu - \Delta(i\nu_n)} \tag{2.29}$$

$$\Delta(i\nu_n) = \sum_k \frac{V_k^2}{i\nu_n - \epsilon_k} \tag{2.30}$$

The hybridisation function contains all information about the bath states themselves (ϵ_k) as well as the coupling between the impurity and bath states (V). It is a central object to dynamical mean field theory (see section 4) where it plays the role of the frequency dependent mean field. It is also an important part of hybridisation expansion continuous-time quantum Monte Carlo, the impurity solver used within this work (see section 3), where it serves as an input in order to obtain the interacting impurity Green's function.

From equation (2.29) we are able to define the interacting impurity Green's function $G(i\nu_n)$ by introducing the self-energy $\Sigma(i\nu_n)$ which takes into account the effects of the on-site interactions:

$$\Sigma(i\nu_n) = \left[G^0(i\nu_n)\right]^{-1} - \left[G(i\nu_n)\right]^{-1} \tag{2.31}$$

$$G(i\nu_n) = \frac{1}{i\nu_n + \mu - \Delta(i\omega_n) - \Sigma(i\nu_n)} \tag{2.32}$$

Calculation of the self-energy from the the non-interacting Green's function requires the use of an impurity solver and presents a complex many-body problem that is not easily solvable. We describe the CTHYB method in chapter 3 as well as an improved-estimator method that provides greater accuracy over direct calculation of (2.31) [48].

2.4.2 The Atomic Limit ($t = 0$, $V_k = 0$) Green's Functions

For the Hubbard model the atomic limit corresponds to turning off the hopping between sites ($t = 0$), while for the AIM it corresponds to turning off the hybridisation between the bath and impurity site ($V_k = 0$). In both cases the problem now reduces to that of a single site with Coulomb interaction U. The resulting Hamiltonian is:

$$H = -\mu\left(n_\uparrow + n_\downarrow\right) + U n_\uparrow n_\downarrow \tag{2.33}$$

and is diagonal in the occupation number basis. For simplicity consider the case of half-filling ($\mu = \frac{U}{2}$): the four relevant eigenstates are unoccupied, a singly occupied site with an up/down spin electron and the doubly occupied site. The corresponding eigenvalues for these states are 0, $-\frac{U}{2}$, $-\frac{U}{2}$ and 0 respectively. From these values we are able to obtain the partition function simply by evaluating the trace in the equation $Z = \mathrm{Tr}\left[e^{-\beta H}\right]$, the result is the following.

$$Z = 2(1 + e^{\beta\frac{U}{2}}) \tag{2.34}$$

In this case we are also able to explicitly evaluate the trace in the definition of the imaginary time Green's function (2.8). Here we choose to demonstrate the calculation for the case of $\sigma = \uparrow$, although the result is the same for the down

spin case due to (2.33) being symmetric with respect to exchanging the spins. The up state and doubly occupied state do not contribute to the trace due to the creation operator in the definition of the Green's function, thus, the trace consists of the following two terms:

$$\mathrm{Tr}\left[e^{H(\tau-\beta)}c_{\uparrow}e^{-\tau H}c_{\uparrow}^{\dagger}\right] = e^{\tau\frac{U}{2}} + e^{-\frac{U}{2}(\tau-\beta)} \tag{2.35}$$

and yields the atomic limit imaginary time Green's function:

$$G(\tau) = -\frac{e^{\tau\frac{U}{2}} + e^{-\frac{U}{2}(\tau-\beta)}}{2(1+e^{\beta\frac{U}{2}})} \tag{2.36}$$

We are also able to obtain its imaginary frequency counterpart using the Fourier transform defined in (2.14)

$$G(i\nu_n) = -\int_0^{\beta} d\tau \frac{e^{i\nu_n\tau}(e^{\tau\frac{U}{2}} + e^{-\frac{U}{2}(\tau-\beta)})}{2(1+e^{\beta\frac{U}{2}})} \tag{2.37}$$

which leads to

$$G(i\nu_n) = \frac{1}{2}\left[\frac{1}{i\nu_n + \frac{U}{2}} + \frac{1}{i\nu_n - \frac{U}{2}}\right] \tag{2.38}$$

This provides an easily computable test case for checking the implementation of the CTHYB solver in chapter 3.

We are also able to glean some insight to the spectrum in the atomic limit by performing the substitution $i\nu_n \to \omega + i\eta$ where $\eta \to 0^+$ and using equation 2.20 the spectra is found to be:

$$A(\omega) = \frac{1}{2\pi}\left[\delta(\omega + \frac{U}{2}) + \delta(\omega - \frac{U}{2})\right] \tag{2.39}$$

and consists of two peaks centred at $\pm\frac{U}{2}$, these peaks are known as the upper and lower Hubbard bands. As will be seen later (section 4.4) when the hopping of the electrons is turned back on these peaks remain centred on these locations however, they become broadened.

3

Continuous-Time Quantum Monte Carlo

Impurity solvers have become an important part of research into strongly correlated electron problems. This is in part due to their use within DMFT, a popular method for studying lattice-based systems. Within DMFT an interacting lattice problem is mapped onto an effective impurity model with an accompanying self-consistency condition. This allows an approximate solution of an interacting lattice problem to be found from solutions of impurity models.

Multiple different numerical methods of solving impurity problems have been developed and applied to DMFT problems. One such method is exact diagonalization (ED) where the bath states are discretised and the resulting Hamiltonian matrix is then diagonalised [12, 13]. While this method does provide exact results for a given Hamiltonian matrix, it is limited to treating a small number of bath states. This is due to the exponential growth of the associated Hilbert space making the diagonalization prohibitively expensive. Also due to this computational limit it is not generally possible to include enough states in the discretisation of the bath such that physical properties can be calculated in the thermodynamic limit.

Another popular method is the numerical renormalization group (NRG). Similarly to ED the bath states are discretised, however in the case of NRG this is performed on a logarithmic scale [14]. This allows the method to treat problems where multiple different energy scales are at play. The discretised problem is

subsequently mapped onto a semi-infinite chain and iteratively diagonalised whilst only retaining the most relevant low-energy states. This method has been used widely in the study of Kondo problems and is a very good method of choice for low temperature problems [14].

Another widely used method is Hirsch-Fye quantum Monte Carlo [15]. This method is built around a time discretisation of a functional integral for the partition function. A Hubbard-Stratonovich transformation is then used in order to decouple the quartic terms resulting from the interactions of the Hamiltonian. This however results in the introduction of new sets of Ising variables on each time slice. While the interactions are removed from the problem this comes at the expense of a coupling to a time dependent magnetic field. However, this problem can be solved and the partition function can be calculated through a Monte Carlo procedure sampling configurations of the Ising variables. As one would expect the method suffers from time discretisation errors through its construction: these can be somewhat alleviated by extrapolating $\Delta\tau \to 0$ but this is costly and requires multiple simulations. In order to try and avoid the problems associated with discretisation of the bath states and/or the imaginary time axis in the methods above, a collection of continuous-time methods have been developed and are now amongst some of the most widely used impurity solvers.

3.1 Hybridisation Expansion Continuous-time Quantum Monte Carlo

Continuous-time quantum Monte Carlo (CTQMC) methods work by sampling a diagrammatic expansion of the partition function through a Monte Carlo procedure. The methods are numerically exact and only suffer from statistical errors arising from the sampling procedure. They also provide access to the two-particle Green's functions that are essential for calculations of susceptibilities as well the vertices that serve as input for extensions to DMFT that will be discussed later. The different CTQMC algorithms result from which part of the Hamiltonian is used to form the diagrammatic expansion. The partition function can be expanded in terms of the

hybridisation (CTHYB [16]), interaction (CTINT [61]) or an auxiliary field (CTAUX [62]). A performance analysis comparing the accuracy with which single-particle Green's functions, as well as other physical quantities, can be measured for a fixed CPU time using the CTINT, CTHYB and the older Hirsch-Fye QMC methods has been performed by Gull et. al. [63]. Here we will focus on the CTHYB variant used for this project. For the interested reader a review and thesis covering all of the above CTQMC methods in detail can be found here [17, 64].

The CTHYB variant was reported by Werner et. al. in 2006 for the single site Anderson Impurity Model [16]. This algorithm is also sometimes referred to as the strong coupling formulation due to how well it performs in cases of strong interaction. This is due to the average perturbation order decreasing with increasing U as the electrons become more localised and higher order terms contribute less and less to the expansion. This allows lower temperature calculations to become more tractable than when using the other algorithms in cases of strong coupling. Its segment formulation is known to be the method of choice for studying single-site impurity models with density-density interactions such as those found within the Hubbard model. This is due to the calculation of the impurity trace being particularity computationally efficient for problems of this type [17, 65].

3.1.1 The Partition Function Expansion

Here we provide an overview of the derivation of the partition function expansion for the case of the single impurity Anderson model. This is covered in more detail in the following papers and thesis [16, 17, 64] as well as in Werner's lecture notes [65] which we will be following.

All of the above mentioned CTQMC methods start from an expansion of the partition function in terms of the interaction representation of quantum mechanics. The interaction picture defines the Hamiltonian as having two parts $H = H_0 + H_1$, with H_0 usually being viewed as a 'non-interacting' Hamiltonian and H_1 providing some 'interaction'. However, this does not have to be the case and the choice of

H_0 and H_1 is ours to make. This allows one to define time-dependent operators for a general operator $\hat{O}$ in the following manner.

$$\hat{O}(\tau) = e^{\tau H_0} \hat{O} e^{-\tau H_0} \tag{3.1}$$

It is also helpful to make the definition $U(\beta) = e^{\beta H_0} e^{-\beta H}$ which can be expressed in terms of an time-ordered exponential

$$U(\beta) = \hat{T}\left[e^{-\int_0^\beta d\tau H_1(\tau)}\right] \tag{3.2}$$

where $\hat{T}$ is the Dyson time ordering operator. These definitions allow one to write the partition function $Z = \mathrm{Tr}\left[e^{-\beta H}\right]$ as

$$Z = \mathrm{Tr}\left[e^{-\beta H_0}\hat{T}\left[e^{-\int_0^\beta d\tau H_1(\tau)}\right]\right] \tag{3.3}$$

which can then be expanded in terms of a given H_1 yielding an expansion for the partition function.

$$Z = \sum_{k=0}^{\infty} \frac{(-1)^k}{k!} \int_0^\beta d\tau_1 \cdots \int_0^\beta d\tau_k \mathrm{Tr}\left[\hat{T}\left[e^{-\beta H_0} H_1(\tau_k)\cdots H_1(\tau_1)\right]\right] \tag{3.4}$$

In CTHYB one choose to split the Hamiltonian as $H_0 = H_{loc} + H_{bath}$ and $H_1 = H_{hyb}$ where the Hamiltonian of the Anderson impurity model is defined by equation (2.2). The hybridisation term describes the coupling of the impurity site to the bath by means of a hopping process.

$$H_{hyb} = \sum_{k,\sigma} V_{k,\sigma} c_\sigma^\dagger a_{k,\sigma} + \sum_{k',\sigma'} V_{k',\sigma'}^* a_{k',\sigma'}^\dagger c_{\sigma'} = H_1^\dagger + H_1 \tag{3.5}$$

If the expansion of operators within (3.4) is to yield a non-zero trace then every electron that jumps onto the impurity needs to jump back and vice versa. This is equivalent to every $c_\sigma^\dagger$ being matched by a corresponding c_σ and forming an alternating sequence. This can be realised by pairing each $H_1^\dagger$ term with a H_1 term, thus, we are able to write the partition function expansion in the following way.

$$Z = \sum_{n=0}^{\infty} \frac{1}{n!} \int_0^\beta d\tau_1 \cdots \int_0^\beta d\tau_n \int_0^\beta d\tau_1' \cdots \int_0^\beta d\tau_n' \mathrm{Tr}\left[\hat{T}\left[e^{-\beta H_0} H_1(\tau_n) H_1^\dagger(\tau_n') \cdots H_1(\tau_1) H_1^\dagger(\tau_1')\right]\right] \tag{3.6}$$

We are also able to split the full trace into bath and impurity contributions since the bath and impurity operators commute. We can further split the bath and impurity contributions by spin as there is no coupling between different spin types within H_1. Taking this into consideration leads to the following expansion [65]

$$\begin{aligned} Z = \sum_{n_\sigma=0}^{\infty} \frac{1}{n_\sigma!} \prod_\sigma \int_0^\beta d\tau_1^\sigma \cdots \int_0^\beta d\tau_{n_\sigma}^\sigma \int_0^\beta d\tau_1^{'\sigma} \cdots \int_0^\beta d\tau_{n_\sigma}^{'\sigma} \\ \times \mathrm{Tr}_c \left[e^{-\beta H_{loc}} \hat{T} \left[\prod_\sigma c_\sigma(\tau_{n_\sigma}^\sigma) c_\sigma^\dagger(\tau_{n_\sigma}^{'\sigma}) \cdots c_\sigma(\tau_1^\sigma) c_\sigma^\dagger(\tau_1^{'\sigma}) \right] \right] \\ \times \mathrm{Tr}_a \left[e^{-\beta H_{bath}} \hat{T} \left[\prod_\sigma \sum_{k_1 \cdots k_{n_\sigma}} \sum_{k_1' \cdots k_{n_\sigma}'} V_{k_1\sigma} V_{k_1'\sigma}^* \cdots V_{k_{n_\sigma}\sigma} V_{k_{n_\sigma}'\sigma}^* \right. \right. \\ \left. \left. a_{\sigma k_{n_\sigma}}^\dagger(\tau_{n_\sigma}^\sigma) a_{\sigma k_{n_\sigma}'}(\tau_{n_\sigma}^{'\sigma}) \cdots a_{\sigma k_1}^\dagger(\tau_1^\sigma) a_{\sigma k_1'}(\tau_1^{'\sigma}) \right] \right] \end{aligned} \quad (3.7)$$

where n_σ is the expansion order in the spin σ and $\mathrm{Tr}_a/\mathrm{Tr}_c$ represent the trace over the bath/impurity operators. Since the bath is non-interacting we are able to integrate out its contribution which can be shown [64, 65] to take the form of a determinant of the hybridisation function. Given by:

$$\begin{aligned} \frac{1}{Z_{bath}} \times \mathrm{Tr}_a \left[e^{-\beta H_{bath}} \hat{T} \left[\prod_\sigma \sum_{k_1 \cdots k_{n_\sigma}} \sum_{k_1' \cdots k_{n_\sigma}'} V_{k_1\sigma} V_{k_1'\sigma}^* \cdots V_{k_{n_\sigma}\sigma} V_{k_{n_\sigma}'\sigma}^* \right. \right. \\ \left. \left. a_{\sigma k_{n_\sigma}}^\dagger(\tau_{n_\sigma}^\sigma) a_{\sigma k_{n_\sigma}'}(\tau_{n_\sigma}^{'\sigma}) \cdots a_{\sigma k_1}^\dagger(\tau_1^\sigma) a_{\sigma k_1'}(\tau_1^{'\sigma}) \right] \right] \\ = \prod_\sigma \det \Delta_\sigma \end{aligned} \quad (3.8)$$

where $Z_{bath} = \prod_\sigma \prod_k (1 + e^{-\beta\epsilon_k})$ and the hybridisation matrix is defined by the following.

$$(\Delta_\sigma)_{i,j} = \Delta_\sigma(\tau_i^\sigma - \tau_j^{'\sigma}) \quad (3.9)$$

$$\Delta_\sigma(\tau) = \sum_k \frac{|V_k^\sigma|^2}{1 + e^{-\beta\epsilon_k}} \begin{cases} e^{-\epsilon_k(\beta-\tau)} & \tau > 0 \\ e^{-\epsilon_k(-\tau)} & \tau < 0 \end{cases} \quad (3.10)$$

The determinant of the hybridisation function takes into account all the different electron paths through the bath that could lead to the impurity having its current configuration. The contribution from the impurity itself is taken into account by the trace over the impurity operators and can be computed as will be shown later.

Taking equation (3.8) and substituting it into equation (3.7) we obtain the following.

$$\begin{aligned} Z = Z_{bath} \sum_{n_\sigma=0}^{\infty} \frac{1}{n_\sigma!} \prod_\sigma \int_0^\beta d\tau_1^\sigma \cdots \int_0^\beta d\tau_{n_\sigma}^\sigma \int_0^\beta d\tau_1^{'\sigma} \cdots \int_0^\beta d\tau_{n_\sigma}^{'\sigma} \\ \times \mathrm{Tr}_c \left[e^{-\beta H_{loc}} \hat{T} \left[\prod_\sigma c_\sigma(\tau_{n_\sigma}^\sigma) c_\sigma^\dagger(\tau_{n_\sigma}^{'\sigma}) \cdots c_\sigma(\tau_1^\sigma) c_\sigma^\dagger(\tau_1^{'\sigma}) \right] \right] \\ \times \prod_\sigma \det \Delta_\sigma \end{aligned} \tag{3.11}$$

We are then able to define the weight of a given configuration as the following.

$$w_Z = \mathrm{Tr}_c \left[e^{-\beta H_{loc}} \hat{T} \left[\prod_\sigma c_\sigma(\tau_{n_\sigma}^\sigma) c_\sigma^\dagger(\tau_{n_\sigma}^{'\sigma}) \cdots c_\sigma(\tau_1^\sigma) c_\sigma^\dagger(\tau_1^{'\sigma}) \right] \right] \times \prod_\sigma \det \Delta_\sigma \tag{3.12}$$

3.1.2 Monte Carlo procedure

Equation (3.11) takes the form a sum of high dimensional integrals. In CTQMC this expansion is sampled through a Monte Carlo procedure. An efficient method for doing so is employing the Metropolis−Hastings algorithm where we are able to generate configurations according to the weight with which they contribute to the integral [66, 67]. The weight of a configuration in (3.11) is given by the impurity trace and the hybridisation matrix determinant as defined in equation (3.12). The sampling is achieved by implementing a random walk through phase space in such a way that in the limit of infinite samples the configurations will have been drawn according to their weight. Using a method such as this allows for the accurate sampling of all orders of (3.11) at the same time due to the higher orders of the expansion being suppressed by the factors $\frac{1}{n_\sigma!}$.

In order to define the Metropolis procedure used within CTHYB we must first define how a configuration is represented. For the case of the single impurity Anderson model the individual configurations are best viewed within the segment picture [17]. This is due to the partition function expansion being written in such a way that it consists of strings of alternating creation and annihilation operators for each spin type. Thus, we are able to represent this operator string by a collection of segments defining when each of the spin orbitals of the impurity is occupied. An example configuration is pictorially represented in Figure 3.1. A segment can be thought of as a creation-annihilation operator pair, and is represented in the figure

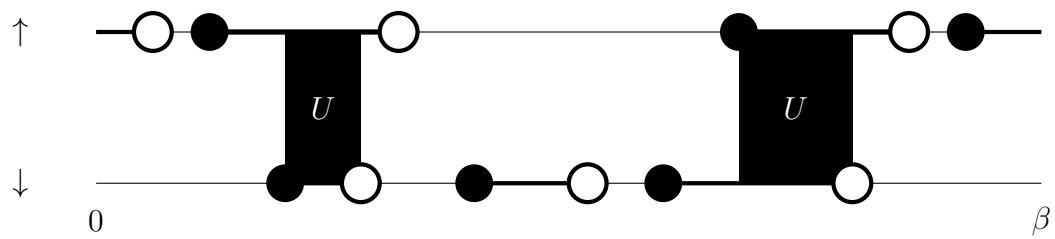

Figure 3.1: A pictorial representation of a configuration consisting of 3 ↑-spin segments and 3 ↓-spin segments within the segment picture. The upper line is the ↑-spin track, the lower line is the-↓ spin track. Impurity creation operators are represented by filled circles, annihilation operators by non-filled circles. The σ spin track is occupied by an electron between a creation annihilation operator pair as depicted by a thick black line representing a segment. When the impurity is doubly occupied there is an additional contribution to the impurity trace from the Coulomb interaction, indicated here by the filled black boxes.

by a thick line connecting a filled circle (creation) and non-filled circle (annihilation). Within this picture the impurity trace (3.13) can be evaluated efficiently using the occupation number basis. This is done by considering the total length of time each spin track is occupied l_σ, as well as the length of time both spin tracks are occupied O (filled black squares). The contribution to the impurity trace from the chemical potential is then easily obtained from the individual track occupations l_σ and the contribution from the Hubbard interaction by the overlap O.

$$Tr_{imp} = \mathrm{Tr}_c \left[e^{-\beta H_{loc}} \hat{T} \left[\prod_\sigma c_\sigma(\tau^\sigma_{n_\sigma}) c^\dagger_\sigma(\tau'^\sigma_{n_\sigma}) \cdots c_\sigma(\tau^\sigma_1) c^\dagger_\sigma(\tau'^\sigma_1) \right] \right] \tag{3.13}$$

$$Tr_{imp} = e^{\mu \sum_\sigma l_\sigma} \times e^{-UO} \tag{3.14}$$

The segment picture also allows easy access to accurate measurements of the site occupancy $\langle n_\sigma \rangle$ and double occupancy $D = \langle n_\uparrow n_\downarrow \rangle$ [17]. The occupancies of the individual spin tracks are calculated by summing the length of all the segments in the track and dividing by the length of the track $n_\sigma = \langle \frac{L}{\beta} \rangle$. An estimate of the double occupancy is similarly obtained through $D = \langle \frac{O}{\beta} \rangle$ where O is the total length of imaginary time where segments overlap.

The algorithm transitions between configurations by means of a Markov process. In order to ensure that this process samples configurations according to their weight, it has to satisfy ergodicity and detailed balance conditions. Detailed balance

ensures that the probability of moving out of state x and into state y is the same as the probability of the reverse.

$$p_x p(x \to y) = p_y p(y \to x) \tag{3.15}$$

The Metropolis−Hastings algorithm satisfies the above condition by splitting the transition probabilities $p(x \to y)$ into two parts $p_{prop}(x \to y)$ and $p_{acc}(x \to y)$ [17, 64]. These are the probability of proposing a move from x to y and the probability of accepting that move. This allows us to choose the acceptance probability such that it satisfies equation (3.15), the common choice is

$$\frac{p_{acc}(x \to y)}{p_{acc}(y \to x)} = \frac{P_x p_{prop}(x \to y)}{P_y p_{prop}(y \to x)} \tag{3.16}$$

$$p_{acc}(x \to y) = \left(1, \frac{P_x p_{prop}(x \to y)}{P_y p_{prop}(y \to x)}\right) \tag{3.17}$$

Ergodicity says that it must be possible to get from any one configuration to any other in a finite number of moves. Ergodicity is easily satisfied by including moves that randomly insert or remove a segment [17, 64]. This makes it possible to get from any one configuration to any other by removing all the segments in the first and inserting the segments forming the second. Although the above two moves are enough to satisfy ergodicity, there are other moves that are commonly used to improve sampling efficiency. These include the addition and removal of anti-segments (annihilation-creation operator pairs) and the shifting of whole segments or their individual start and end points [17, 64].

In certain cases it can also be important to include global moves [17]: these involve switching a set of orbital indices on two segment tracks. For the case of the single impurity Anderson model this would involve switching the segments for up and down spins. These types of moves are very computationally expensive compared to the moves above. This is due to the fact they require the hybridisation matrices and determinants to be fully recalculated every time a move of this type is performed. Moves of this type can be useful when studying systems with broken spin-symmetry such as an anti-ferromagnetic or ferromagnetic phase where the sampling procedure could be susceptible to getting trapped in certain configurations [17]. However, for

the case of a paramagnetic phase, using these moves is equivalent to spin averaging of the measured quantities post calculation, thus, they do not need to be included [17].

3.1.3 Measurements

We now turn our attention to measurements of the single-particle and two-particle Green's functions within the CTHYB algorithm. The measurements themselves can be carried out directly in terms of imaginary time or imaginary frequency however Boehnke et. al. have shown that it can be preferable to make measurements in an alternative basis of Legendre polynomials [47]. There are also improved estimator methods available that allow one to make much more accurate measurements of both single and two-particle Green's functions by measuring higher order correlation functions [48]. How these measurements are made and the advantages of doing so are the topic of the next two sections, we start with the measurements of single-particle quantities.

Single-Particle Measurements

$$G_{\sigma_G}(\tau, \tau') = -\langle \hat{T} \left[c_{\sigma_G}(\tau) c^{\dagger}_{\sigma_G}(\tau') \right] \rangle \tag{3.18}$$

Measurements of the Green's function in CTHYB are performed through creating configurations contributing to the Green's function from the current configuration for the partition function [17, 64]. This is achieved by choosing a creation and annihilation operator pair to be the Green's function operators and removing the hybridisation process connecting them. That is, one views the current configuration for the partition function as an order $n-1$ Green's function configuration with an additional hybridisation process. At a given order n there are n creation and n annihilation operators: we could choose any pair for the Green's function operators, thus, we are able to generate n^2 Green's function configurations from each current

partition function configuration [17].

$$\begin{aligned} G_{\sigma_G}(\tau,\tau') = -Z_{bath} \sum_{n_\sigma=0}^{\infty} \frac{1}{n_\sigma!} \prod_\sigma \int_0^\beta d\tau_1^\sigma \cdots \int_0^\beta d\tau_{n_\sigma}^\sigma \int_0^\beta d\tau_1^{'\sigma} \cdots \int_0^\beta d\tau_{n_\sigma}^{'\sigma} \\ \times \mathrm{Tr}_c \left[e^{-\beta H_{loc}} \hat{T} \left[c_{\sigma_G}(\tau) c_{\sigma_G}^\dagger(\tau') \prod_\sigma c_\sigma(\tau_{n_\sigma}^\sigma) c_\sigma^\dagger(\tau_{n_\sigma}^{'\sigma}) \cdots c_\sigma(\tau_1^\sigma) c_\sigma^\dagger(\tau_1^{'\sigma}) \right] \right] \\ \times \prod_\sigma \det \Delta_\sigma \end{aligned} \tag{3.19}$$

We are able to calculate the weight of the generated Green's function configuration from the current partition function weight (3.12). Since we have chosen the Green's function operators from the current partition function configuration the contribution from the impurity (3.13) remains unchanged. However, the removal of the additional hybridisation process corresponds to removing a row and column from the hybridisation matrix [17]. We are then able to sample the Green's function through importance sampling in order to take into account that the configurations are generated according to the distribution of the partition function not the Green's function itself. Thus, we accumulate:

$$\frac{W_G(x)}{W_Z(x)} = \frac{\det \Delta_\sigma^{\tau,\tau'}}{\det \Delta_\sigma} = M_{\tau',\tau}^\sigma \tag{3.20}$$

where $\Delta^{\tau,\tau'}$ is the hybridisation matrix with the removed row and column. The computation of these determinants is very costly and it is best to use a fast-update procedure [17] where (3.20) can easily be computed from $M = \Delta^{-1}$. The measurement of $G_\sigma(\tau)$ is then given by:

$$G_\sigma(\tau) = \frac{1}{\beta} \left\langle \sum_{i,j} M_{j,i}^\sigma \tilde{\delta}(\tau, \tau_i - \tau_j') \right\rangle \tag{3.21}$$

$$\tilde{\delta}(\tau,\tau') = \begin{cases} \delta(\tau-\tau') & \tau' > 0 \\ -\delta(\tau-\tau'-\beta) & \tau' < 0 \end{cases} \tag{3.22}$$

where $\tilde{\delta}(\tau,\tau')$ takes into account time-translational invariance.

Equation (3.21) allows us to make measurements directly in imaginary time. However, it is possible to perform measurements in imaginary frequency [48], or alternative representations such as an expansion of Legendre polynomials which we now turn our attention to [47].

Boehnke et al. showed that is was possible and advantageous to measure the impurity Green's function through its expansion coefficients in terms of Legendre polynomials [47]. This allows for a compact representation of the Green's function and can provide essentially noise-free measurements by truncating the expansion at some value l_{max}. The expansion coefficients G_l are defined by

$$G_l = \sqrt{2l+1}\int_0^\beta d\tau P_l[x(\tau)]G(\tau) \tag{3.23}$$

and are related back to the imaginary time Green's function $G(\tau)$ through the following:

$$G(\tau) = \sum_{l\geq 0}\frac{\sqrt{2l+1}}{\beta}P_l[x(\tau)]G_l \tag{3.24}$$

where $x(\tau) = \frac{2\tau}{\beta} - 1$ and the Legendre polynomials $P_l(x)$ are defined on the interval $x \in [-1, 1]$. The representation is compact since the coefficients are shown to decay faster than any power of $\frac{1}{l}$ meaning that all information about the Green's function is heavily localised at lower values of l. Thus, one would hope to be able to truncate the series at some value $l = l_{max}$ and retain an accurate representation of the Green's function. The authors show by studying the convergence of the imaginary time Green's function with respect to l_{max}, that there exists a plateau where the Green's function is accurately represented [47]. If l_{max} is increased further the statistical errors in the high l coefficients get transferred back into $G(\tau)$ degrading the results. By choosing l_{max} to be in this plateau one is able to obtain accurate, essentially noise-free, measurements of the Green's function.

It is often convenient to work with the impurity Green's function in terms of imaginary frequency. One is able to obtain an expression for the imaginary frequency Green's function in terms of the Legendre representation by Fourier transforming (3.24) obtaining the following.

$$G(i\nu_n) = \sum_{l\geq 0} G_l \frac{\sqrt{2l+1}}{\beta}\int_0^\beta d\tau e^{i\nu_n\tau}P_l[x(\tau)] \tag{3.25}$$

We can then identify that the above equation takes the form:

$$G(i\nu_n) = \sum_{l\geq 0} T_{nl}G_l \tag{3.26}$$

and the transformation coefficients are readily identified as the following.

$$T_{nl} = \frac{\sqrt{2l+1}}{\beta} \int_0^\beta d\tau e^{i\nu_n \tau} P_l[x(\tau)] \tag{3.27}$$

These coefficients can be written in the following more convenient form:

$$T_{nl} = (-1)^n i^{l+1} \sqrt{2l+1} j_l \left(\frac{(2n+1)\pi}{2} \right) \tag{3.28}$$

where n denotes the Matsubara frequency index, l the Legendre polynomial and $j_l(z)$ are the spherical Bessel functions [47]. The Legendre coefficients are able to be measured directly as part of the calculation using the following accumulation formula

$$G_{l,\sigma} = \frac{-\sqrt{2l+1}}{\beta} \left\langle \sum_{i,j} M^\sigma_{j,i} \tilde{P}_l(\tau'_j - \tau_i) \right\rangle \tag{3.29}$$

where $\tilde{P}_l(\tau)$ is defined as

$$\tilde{P}_l(\tau) = \begin{cases} P_l[x(\tau)] & \tau' > 0 \\ -P_l[x(\tau+\beta)] & \tau' < 0 \end{cases} \tag{3.30}$$

and the corresponding Green's function in imaginary time (equation (3.24)) or imaginary frequency (equation (3.26)) can be reconstructed after the calculation.

When using the Green's function accumulated directly in imaginary time or imaginary frequency one often encounters problems with noise in the high-frequency region of the self-energy when it is computed using Dyson's equation.

$$\Sigma_\sigma(i\nu_n) = \left[G^0_\sigma(i\nu_n) \right]^{-1} - \left[G_\sigma(i\nu_n) \right]^{-1} \tag{3.31}$$

This is due to Dyson's equation involving the inverse of the measured Green's function, thus, at high-frequency when the Green's function takes small values any statistical noise present from the sampling procedure is amplified. A method of avoiding this problem has been proposed by Hafermann et. al. where they provide an improved estimator for the self-energy [48]. The improved estimator allows the self-energy to be expressed as a ratio of the impurity Green's function and an additional higher order correlation function.

$$\Sigma_\sigma(i\nu_n) = U \frac{F^{\bar{\sigma}}_\sigma(i\nu_n)}{G_\sigma(i\nu_n)} \tag{3.32}$$

For the case of the single impurity Anderson model the higher order correlation function takes the same form as the impurity Green's function with an additional number operator $n_{\bar{\sigma}}(\tau')$ for the opposing spin.

$$F_{\sigma}^{\bar{\sigma}}(\tau - \tau') = -\langle \hat{T} \left[c_{\sigma}(\tau) c_{\sigma}^{\dagger}(\tau') n_{\bar{\sigma}}(\tau') \right] \rangle \tag{3.33}$$

This means we are able to accumulate $F_{\sigma}^{\bar{\sigma}}(\tau - \tau')$ at the same time as the impurity Green's function for essentially no additional computational cost, just by checking if there is a segment present in the opposing spin track at τ'. The expression for the self-energy as the ratio of these two correlation functions had already been reported and used for the single impurity Anderson model within the context of NRG calculations by Bulla [68]. This expression avoids using Dyson's equation altogether and eliminates much of the problem with noise at high-frequency. However, the method still requires accurate measurement of the impurity Green's function and the higher order correlation function. For this the authors of the paper suggest combining the improved estimator approach with the noise filtering capabilities of the Legendre representation detailed above [47, 48]. The accumulation formula for the additional correlation function in the Legendre representation is given by:

$$F_{l\sigma}^{\bar{\sigma}} = \frac{-\sqrt{2l+1}}{\beta} \left\langle \sum_{i,j} M_{j,i}^{\sigma} \tilde{P}_l(\tau_j^{'} - \tau_i) n_{\bar{\sigma}}(\tau_i) \right\rangle \tag{3.34}$$

where $\tilde{P}_l$ is defined as in (3.30) and $n_{\bar{\sigma}}(\tau_i)$ is the additional factor checking if the opposing spin tack is occupied. Using this method allows for fast and highly accurate measurements of the correlation functions required for the improved estimator method, further improving the calculation of the self-energy. The DMFT calculations contained within this work were all performed using using the improved estimator method for the self-energy where the associated correlation functions were measured in their Legendre representation.

Two-Particle Measurements

Similarly to the single-particle Green's function it is also possible to represent the two-particle Green's function in terms of its expansion in Legendre polynomials [47].

This allows for a particularly compact representation of the two-particle Green's functions when compared with the equivalent representation in terms of imaginary time or imaginary frequency where memory/storage requirements are very large. The above is achieved through defining the two-particle Green's function as

$$G^{(2)}_{\sigma\sigma'}(\tau_{12},\tau_{34},\tau_{14}) = -\langle \hat{T}\left[c_\sigma(\tau_1)c^\dagger_\sigma(\tau_2)c_{\sigma'}(\tau_3)c^\dagger_{\sigma'}(\tau_4)\right]\rangle \tag{3.35}$$

where $\tau_{ij} = \tau_i - \tau_j$ and the imaginary time arguments have been chosen such that τ_{12}, τ_{34} are β-anti-periodic and τ_{14} is β-periodic. The first two imaginary time arguments can then be expanded in terms of Legendre polynomials while the final argument is Fourier transformed to an associated bosonic imaginary frequency.

$$\begin{aligned} G^{(2)}_{\sigma,\sigma'}(l,l',i\omega_m) = \iiint_0^\beta d\tau_{12}d\tau_{34}d\tau_{14}\sqrt{2l+1}\sqrt{2l'+1}(-1)^{l'+1} \\ \times P_l[x(\tau_{12})]P_{l'}[x(\tau_{34})]e^{-i\omega_m\tau_{14}}G^{(2)}_{\sigma\sigma'}(\tau_{12},\tau_{34},\tau_{14}) \end{aligned} \tag{3.36}$$

The final argument is not expanded into Legendre polynomials due to the calculation of the susceptibility being diagonal in this bosonic frequency. This mixed Fourier-Legendre representation allows for the equations defining the susceptibility to be written simply in terms of the first two Legendre indices as will be seen later when the calculation of the magnetic susceptibility is discussed in section 4.3.

The corresponding full Fourier representation can be obtained using the same transformation coefficients defined in (3.28) through

$$G^{(2)}_{\sigma,\sigma'}(i\nu_n,i\nu_{n'},i\omega_m) = \sum_{l,l'\geq 0} T_{nl}G^{(2)}_{l,l'}(i\omega_m)T^*_{n'l'} \tag{3.37}$$

and can be reconstructed after the calculation. The accumulation formula for $G^{(2)}_{l,l'}(i\omega_m)$ within the CTHYB algorithm is given by:

$$\begin{aligned} G^{(2)}_{\sigma,\sigma'}(l,l',i\omega_m) = \frac{\sqrt{2l+1}\sqrt{2l'+1}}{\beta}(-1)^{l'+1} \\ \times \langle \sum_{ijkl}(M^\sigma_{ji}M^{\sigma'}_{lk} - M^\sigma_{li}M^{\sigma'}_{jk}\delta_{\sigma\sigma'})\tilde{P}_l(\tau'_j-\tau_i)\tilde{P}_l(\tau'_l-\tau_k)e^{i\omega_m(\tau'_j-\tau_k)}\rangle \end{aligned} \tag{3.38}$$

where $\tilde{P}_l$ is defined as before in (3.30) [47].

In the same paper where the improved estimator for the self-energy was provided the authors also provide an improved estimator for the connected part of the two-particle Green's function [48].

$$\chi^{conn}_{\sigma,\sigma'}(i\nu_n, i\nu_{n'}, i\omega_m) = -U \Big[F^{\bar{\sigma}}_{\sigma}(i\nu_n + i\omega_m) G^{(2)}_{\sigma,\sigma'}(i\nu_n, i\nu_{n'}, i\omega_m) \\ - G_{\sigma}(i\nu_n + i\omega_m) H^{\bar{\sigma}}_{\sigma,\sigma'}(i\nu_n, i\nu_{n'}, i\omega_m) \Big] \tag{3.39}$$

This is achieved by introducing a further correlation function $H^{\bar{\sigma}}_{\sigma,\sigma'}(\tau_1, \tau_2, \tau_3, \tau_4)$ analogous to that introduced for the self-energy.

$$H^{\bar{\sigma}}_{\sigma,\sigma'}(\tau_1, \tau_2, \tau_3, \tau_4) = -\langle \hat{T} \Big[n_{\bar{\sigma}}(\tau_1) c_{\sigma}(\tau_1) c^{\dagger}_{\sigma}(\tau_2) c_{\sigma'}(\tau_3) c^{\dagger}_{\sigma'}(\tau_4) \Big] \rangle \tag{3.40}$$

This allows one to remove some of the problems with noise at high-frequency when calculating the vertex functions and the authors found the method to improve the stability of dual fermion calculation when the input vertices were calculated in this fashion [48]. The vertex functions are highly susceptible to noise in the connected part of the two-particle Green's function. This is due to division of the connected part of the two-particle Green's function by four single-particle Green's functions, as can be seen in the definition of the vertex functions.

$$\gamma_{\sigma,\sigma'}(i\nu_n, i\nu_{n'}, i\omega_m) = \frac{\chi^{conn}_{\sigma,\sigma'}(i\nu_n, i\nu_{n'}, i\omega_m)}{G_{\sigma}(i\nu_n) G_{\sigma}(i\nu_n + i\omega_m) G_{\sigma'}(i\nu_{n'} + i\omega_m) G_{\sigma'}(i\nu_{n'})} \tag{3.41}$$

Thus, when the single-particle Green's functions get small they highly amplify the errors in the connected part of the two-particle Green's function as well as introduce the statistical errors associated with their own measurement [48].

Similarly to $F^{\bar{\sigma}}_{\sigma}$, accumulation of $H^{\bar{\sigma}}_{\sigma,\sigma'}$ can be done alongside the two-particle Green's function by performing the additional step of checking the opposing σ spin track to see if it is occupied. The only sizeable additional computational overhead is storing another large two-particle correlation function. The accumulation formula's for $G^{(2)}_{\sigma,\sigma'}(i\nu_n, i\nu_{n'}, i\omega_m)$ and $H^{\bar{\sigma}}_{\sigma,\sigma'}(i\nu_n, i\nu_{n'}, i\omega_m)$ are given below and $\chi^{conn}_{\sigma,\sigma'}$ is reconstructed after the calculation through (3.39).

$$G^{(2)}_{\sigma,\sigma'}(i\nu_n, i\nu_{n'}, i\omega_m) = \frac{1}{\beta} \Big\langle \sum_{ijkl} (M^{\sigma}_{ji} M^{\sigma'}_{lk} - M^{\sigma}_{li} M^{\sigma'}_{jk} \delta_{\sigma\sigma'}) \\ e^{i\nu_n(\tau'_j - \tau_i)} e^{i\nu_{n'}(\tau'_l - \tau_k)} e^{i\omega_m(\tau'_j - \tau_k)} \Big\rangle \tag{3.42}$$

$$H^{\bar{\sigma}}_{\sigma,\sigma'}(i\nu_n, i\nu_{n'}, i\omega_m) = \frac{1}{\beta}\Big\langle \sum_{ijkl}(M^{\sigma}_{ji}M^{\sigma'}_{lk} - M^{\sigma}_{li}M^{\sigma'}_{jk}\delta_{\sigma\sigma'}) \\ e^{i\nu_n(\tau'_j-\tau_i)}e^{i\nu_{n'}(\tau'_l-\tau_k)}e^{i\omega_m(\tau'_j-\tau_k)}n_{\bar{\sigma}}(\tau'_j)\Big\rangle \tag{3.43}$$

In order to optimise the measurements (3.42) and (3.43) as much as possible we implemented them using low-level BLAS routines. The measurements were also further optimised as per Appendix C of Boehnke et. al. [47] where the authors state that the second product of M matrices can be generated from the first by means of a crossing-symmetry. Thus, we only directly measure the first product of M matrices which is able to be factorised, this gives the up-down quantities. The crossing-symmetry is then used in order to obtain the up-up quantities, further speeding up the calculation. Once $\chi^{conn}_{\sigma,\sigma'}$ has been obtained the corresponding vertex functions are calculated and output ready to be used with the dual fermion code.

It is possible to use this improved estimator method for the connected part of the two-particle Green's function in conjunction with the noise filtering capabilities of the mixed-Fourier Legendre representation. However, this has been shown to lead to systematic errors in the obtained vertex functions at higher Bosonic frequencies [48]. Thus, the vertices used as input for the dual fermion calculations performed in this thesis are calculated from two-particle Green's functions measured in terms of imaginary frequency as per the improved estimator method just described.

3.1.4 Implementation and Testing

An existing CTHYB [49] application based upon the TRIQS project [69] was modified by Martin Galpin in order to adopt the segment picture. Myself and Martin implemented and extensively tested the measurements of the single and two-particle Green's functions discussed above as well as the calculation of the susceptibility and vertex functions. Following this the code has been used for all calculations within the later chapters of this thesis.

As a test case for the adapted segment picture code and the implementation of the measurements detailed above, we have reproduced figures 9 and 10 from the improved estimator paper [48]. These calculations were performed on a simple

two-site model consisting of the impurity connected to a single non-interacting bath site. The corresponding input non-interacting Green's function is given by:

$$G^0(i\nu_n) = \left[i\nu_n + \mu - \frac{1}{i\nu_n} \right]^{-1} \tag{3.44}$$

where μ is the usual chemical potential. The model parameters were set to $t = 1$ and $U/t = 4$ and the calculations were performed at half-filling such that the chemical potential was fixed as $\mu = \frac{U}{2}$. The self-energy calculation was performed at an inverse temperature of $\beta t = 50$, while the two-particle quantities were calculated at $\beta t = 10$.

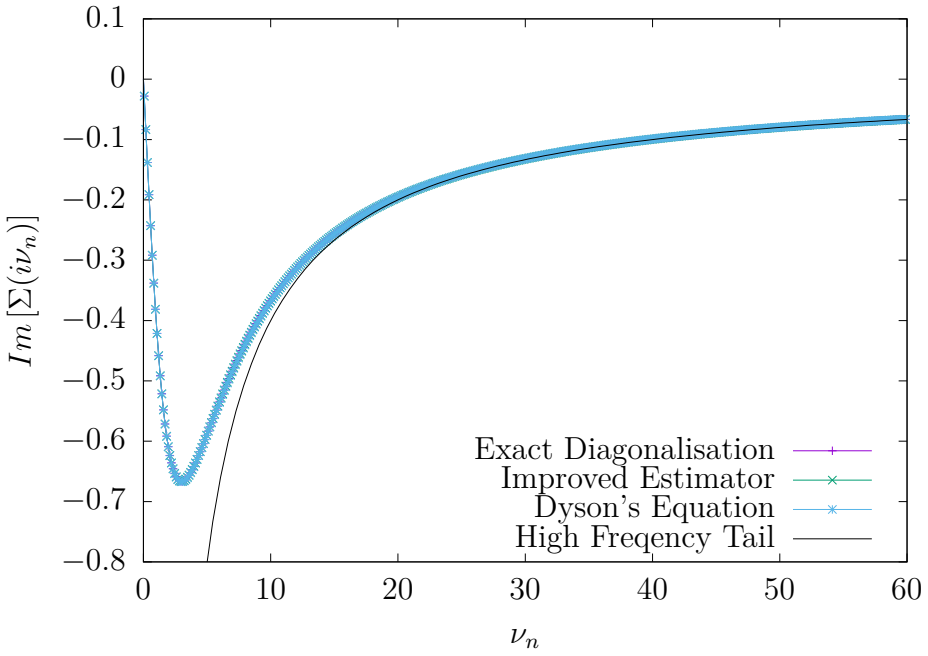

Figure 3.2: Imaginary part of $\Sigma(i\nu_n)$ for the two-site model test case, reproducing figure 7 from the improved estimators paper [48].

Figure 3.2 shows the self-energy calculated using Dyson's equation (3.31) and the improved estimator (3.32). Also shown is the high-frequency tail of the self-energy and the self-energy result obtained from exact diagonalisation. The exact diagonalisation results were obtained from calculations performed using the Pomerol code [70], and the high-frequency tail of the self-energy is calculated from the following

$$\lim_{\omega_n \to \infty} \Sigma(i\nu_n) = U\langle n \rangle + \frac{U^2 \langle n \rangle (1 - \langle n \rangle)}{i\nu_n} \tag{3.45}$$

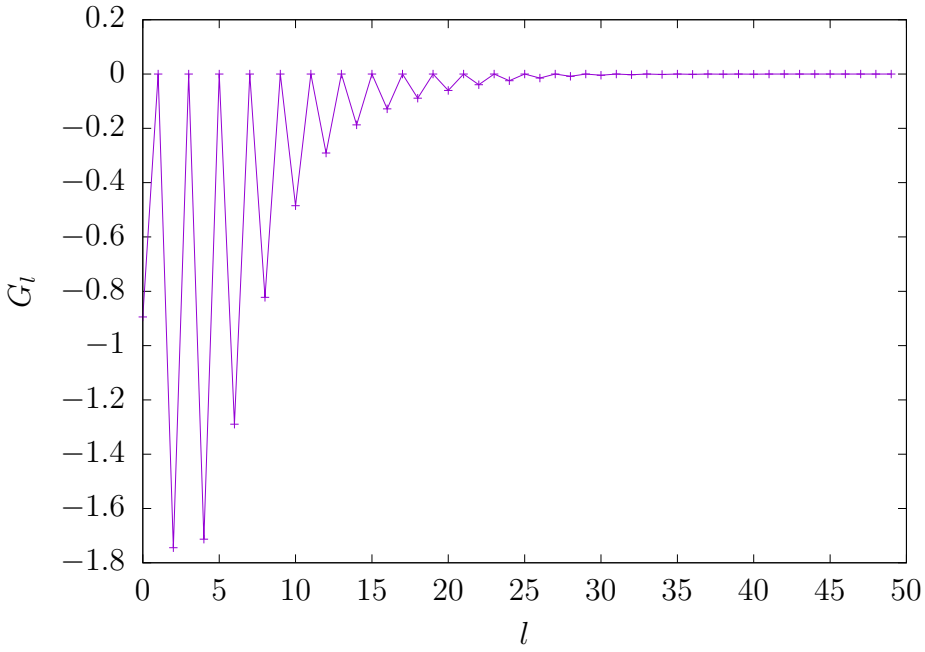

Figure 3.3: Plot of G_l for the two-site model test case with a Legendre cut-off $n_l = 50$

as per the following paper by Wang et. al. [71].

We can see that both the improved estimator and Dyson self-energies yield the expected high-frequency behaviour and reproduce the exact diagonalisation self-energy to a very good level of accuracy. The Dyson equation result and improved estimator result also agree remarkably well. This is largely due to the effective noise filtering capabilities of the Legendre representation used to measure the impurity Green's function removing much of the noise from $G_\sigma(i\nu_n)$, thereby stabilising the Dyson's equation result.

Figure 3.3 shows the Legendre representation of the impurity Green's function for the calculation of the self-energy. The rapid decay of the coefficients is clear and after $l = 40$ they carry essentially no weight. We would expect Legendre cut-offs selected in this region to all produce results of a high level of accuracy. This also clearly demonstrates how efficient the Legendre representation is for representing imaginary frequency Green's functions. Here the self-energy and impurity Green's function has been reproduced to a very high level of accuracy across a vast number of frequencies from measuring just fifty Legendre coefficients.

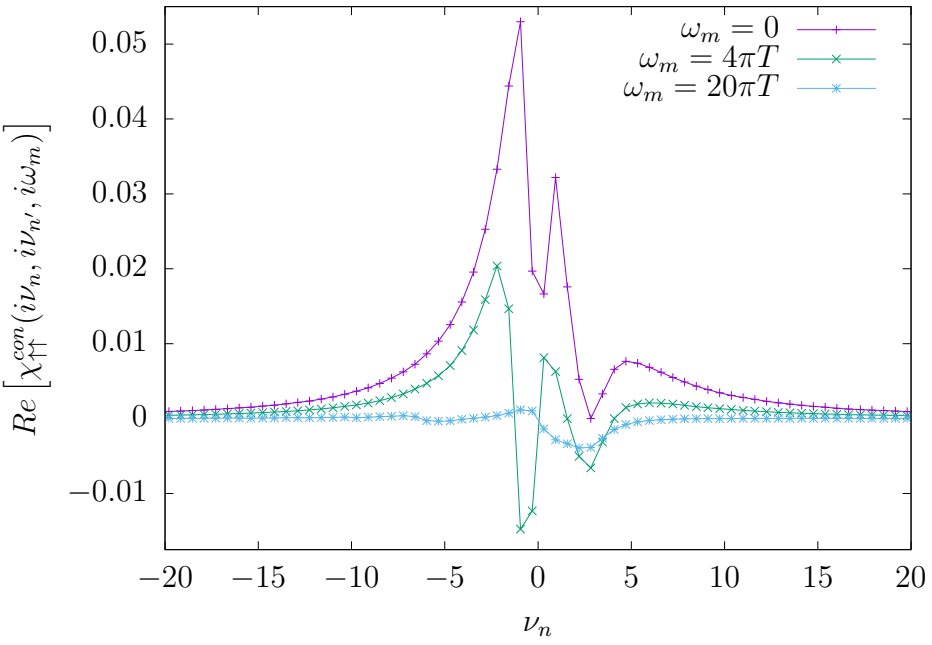

Figure 3.4: Real part of $\chi^{con}_{\uparrow\uparrow}(i\nu_n, i\nu_{n'}, i\omega_m)$ with fixed $\omega_{n'} = 9\pi T$ for the two-site model test case, reproducing figure 9 from the improved estimators paper [48].

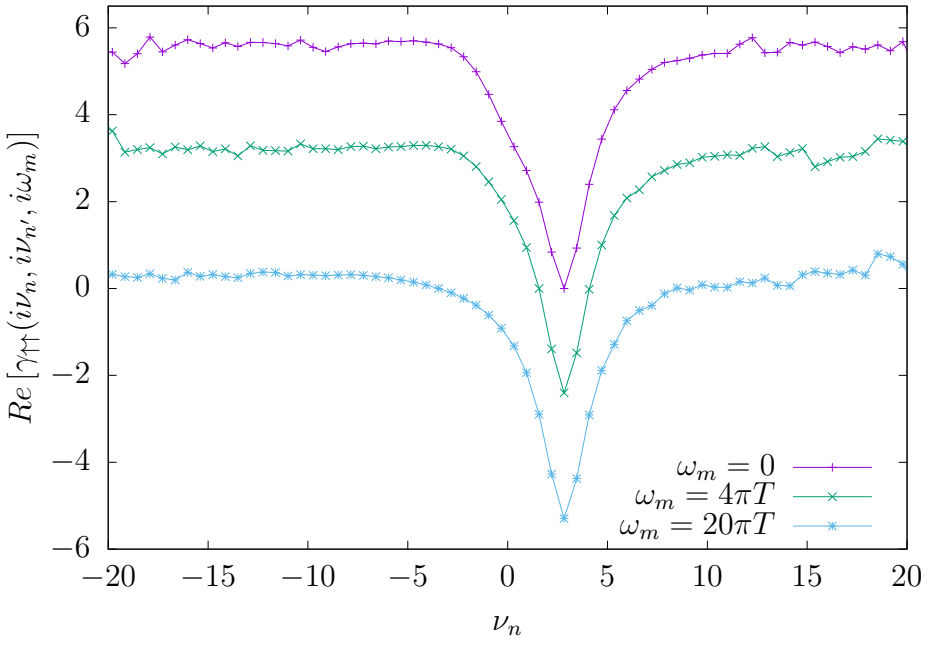

Figure 3.5: Real part of $\gamma_{\uparrow\uparrow}(i\nu_n, i\nu_{n'}, i\omega_m)$ with fixed $\omega_{n'} = 9\pi T$ for the two-site model test case, reproducing figure 10 from the improved estimators paper [48].

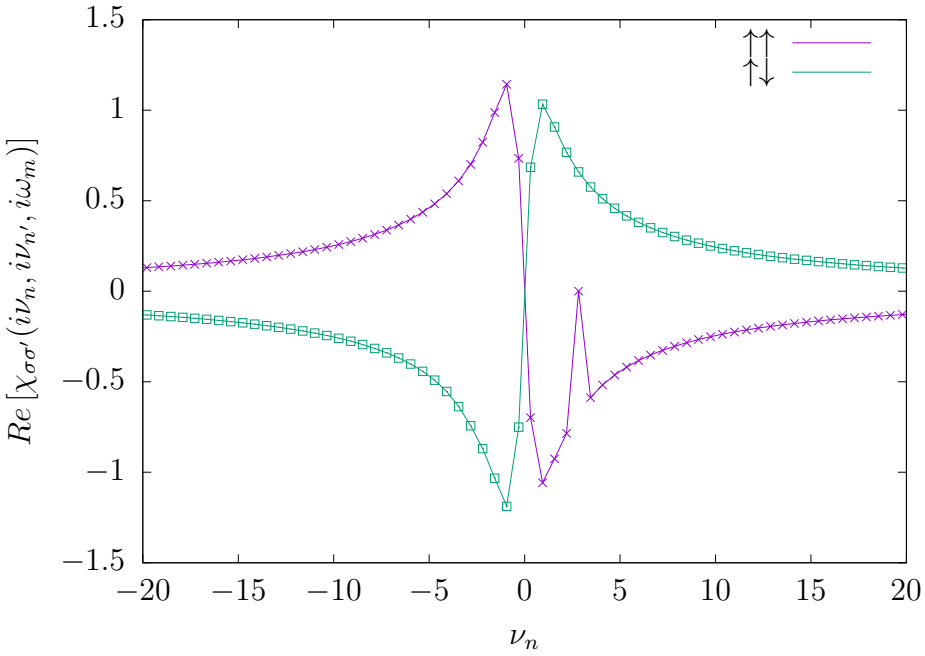

Figure 3.6: Real part of $G^{(2)}_{\sigma\sigma'}(i\nu_n, i\nu_{n'}, 0)$ with fixed $\omega_{n'} = 9\pi T$ ($\uparrow\uparrow$) and $\omega_{n'} = -9\pi T$ ($\uparrow\downarrow$) for the two-site model test case. Symbols are from improved estimator measurements, lines are from Legendre measurements.

Figure 3.4 shows the connected part of the up-up component of the two-particle Green's function ($\chi^{con}_{\uparrow\uparrow}(i\nu_n, i\nu_{n'}, i\omega_m)$), and figure 3.5 shows the associated vertex ($\gamma_{\uparrow\uparrow}(i\nu_n, i\nu_{n'}, i\omega_m)$), reproducing figure 9 and figure 10 from the Hafermann paper [48]. In order to obtain the level of accuracy shown in the figures above 3.2×10^8 measurements were required, split across 16 cores, resulting in a run time of 4-5 days. These are therefore very expensive calculations in order to obtain this level of accuracy.

Figure 3.6 shows the two-particle Green's function ($G^{(2)}_{\sigma\sigma'}(i\nu_n, i\nu_{n'}, i\omega_m)$) at the lowest bosonic frequency ($i\omega_0 = 0$) for both up-up and up-down components. Shown is the two-particle Green's function calculated using the improved estimators method (symbols) and direct accumulation in the Legendre representation (lines). We can see that we get very good agreement between the two methods and the results are essentially indistinguishable at this level. Showing that both the improved estimators method and measurements performed directly in terms of Legendre polynomials are able to produce accurate results for both spin components of the two-particle Green's

functions. The above tests and replication of results from the literature show that both the modified CTHYB code and the newly implemented measurements of the single and two-particle Green's functions are capable of producing accurate results.

3.2 Analytic Continuation

Once the fully interacting Green's functions of the impurity model have been obtained using the CTQMC method described above, we wish to extract the single-particle spectrum. Since the Green's functions are imaginary time/frequency objects this has to be done through analytic continuation. For exact results, such as the case of the atomic limit described in section 2.4.2, this can be done simply though making the substitution $i\nu_n \to \omega + i\eta$ where $\eta \to 0^+$ is some small positive infinitesimal. For cases where statistical noise is not present in the result or the data is very accurate one may also use Padé approximants which amounts to fitting a rational function to the Matsubara data [72]. However, this is a very delicate and sensitive procedure and, where there is some noise present in the data, often the results are poor or even unphysical [51, 73]. Also when the temperature is relatively high the spacing between the Matsubara frequencies is large, therefore, fitting the rational function accurately becomes problematic.

In CTQMC data statistical noise is present and a different method must be used. The two main methods are the maximum entropy method, and the stochastic optimisation method. While the stochastic optimisation method is best for when no prior information is known about the spectra, it takes on the order of hours to compute a single spectrum compared to the maximum entropy method which takes on the order of minutes. Also with new developments in the maximum entropy method, many of the problems found when performing maximum entropy calculations can be minimised or at least controlled [74]. For this reason the maximum entropy method is used in this project through Bergeron's implementation in the ΩMaxEnt code [75]. However, before we introduce the maximum entropy method as well as the implementation within Bergeron's code, we will briefly discuss the problem of analytic continuation in general. More information about analytic

continuation and the maximum entropy method can be found in Jarrell's review of the topic [51] as well this book chapter [73]. It is also covered in the following book chapter and paper on the stochastic optimisation method by Mishchenko [76, 77].

The purpose of analytic continuation is to solve the following integral equation

$$G(i\nu_n) = \int_{-\infty}^{\infty} d\omega K(i\nu_n, \omega) A(\omega) \tag{3.46}$$

$$K(i\nu_n, \omega) = \frac{1}{i\nu_n - \omega} \tag{3.47}$$

where $K(i\nu_n, \omega)$ is some known kernel and $A(\omega)$ is the spectra to be determined. This turns out to be quite a formidable task because solving this equation is an example of what is known as an ill-posed problem, i.e. a problem to which there is no unique solution when $G(i\nu_n)$ is subject to noise. This becomes more clear if we transform the above equation into matrix form by discretising it in the following manner.

$$A(\omega) = \sum_{m=1}^{M} A(\omega_m)\delta(\omega - \omega_m) \tag{3.48}$$

$$G(i\nu_n) = \sum_{m=1}^{M} K(i\nu_n, \omega_m) A(\omega_m) \tag{3.49}$$

$$\bar{G} = \bar{\bar{K}}\bar{A} \tag{3.50}$$

Here $\bar{G}$ is the n component vector of the Green's function, $\bar{\bar{K}}$ is a $N \times M$ matrix of the kernel (3.47) and $\bar{A}$ is a M component vector of the spectrum to be found. This equation is only satisfied when the true Green's function is known. However, when there is any noise present in $G(i\nu_n)$ there are many possible spectra that give results close to the Green's function, however, none that satisfy equation (3.49) exactly. Thus, when solving problems of this type it is often useful to use any available information about the form of the solution in order to inform what sort of solution is expected. This is exactly what the maximum entropy method does, by framing the above problem in terms of Bayes' theorem.

$$P[A|G] = \frac{P[G|A]P[A]}{P[G]} \tag{3.51}$$

Here $P[A|G]$ is known as the posterior probability and it tells us what is the probability we obtain the spectrum A given the data for the Green's function G.

$P[G|A]$ is known as the likelihood and tells us the probability of obtaining the data G given the spectrum A. $P[A]$ is known as the prior and allows us to take into account any information we have about the form of the spectrum. The original ill-posed problem can now be tackled by finding the most probable A given G through maximising $P[A|G]$. This can be achieved by maximising the probability of obtaining G given a spectrum A ($P[G|A]$) and taking into account any knowledge we have of A in the form of $P[A]$: the value of $P[G]$ can be ignored here since we only have one set of data for G, thus, it is a constant.

The way the maximum entropy method achieves the above is by generating some initial spectrum $\tilde{A}$ while taking into account the information we have on the spectrum in the form of a default model encoded in $P[A]$. It then tries to maximise the probability $P[G|A]$. This involves obtaining the back-continued Green's function for a given guess of the spectrum through (3.46) and comparing it to the input data using some fitting metric as will be seen later. We now make choices for the likelihood and prior probabilities above. Within the maximum entropy method, the likelihood probability is modelled as being proportional to

$$P[G|A] \propto e^{-\frac{\chi^2}{2}} \tag{3.52}$$

where χ^2 is the usual metric of 'goodness of fit' and is in this case given by:

$$\chi^2 = \sum_i \frac{\left(G_i - \tilde{G}_i\right)^2}{\sigma_i^2} \tag{3.53}$$

where $\tilde{G} = KA$ is the back-continued estimate of G for the spectrum A, and σ_i^2 is the variance on the input data point G_i. The prior probability is written in terms of an entropy $S[A]$ defined in reference to a function known as the default model $D(\omega)$. It is given by:

$$P[A] \propto e^{\alpha S[A]} \tag{3.54}$$

where the entropy is defined as

$$S[A] = -\int d\omega A(\omega) \ln\left[\frac{A(\omega)}{D(\omega)}\right] \tag{3.55}$$

and α is introduced as an undermined Lagrange multiplier allowing control over how much weight it put into the prior information [74, 78]. The default model is used in order to enforce things we know about the spectrum, such as it is positive, normalised and possess higher order moments that can be extracted from the Green's function. Combining the above forms for the prior and likelihood probabilities we know that the posterior probability $P[A|G]$ can be maximised by obtaining the maximum entropy solution relative to the constraint that the G coming from A is close to the input data, hence the name maximum entropy method.

$$P[A|G] \propto P[G|A]P[A] \propto e^{\alpha S[A] - \frac{\chi^2}{2}} \tag{3.56}$$

In practice however, this is achieved through minimising $Q = \frac{\chi^2}{2} - \alpha S[A]$. The problem is then tackled by computing the spectrum for a range of fixed α, then selecting the spectrum from the optimal value of α. The value of α determines how much weight is put into the entropy and therefore the prior information: when it is very small we put very little weight in the prior information and we end up just fitting the data. When it is very large Q will be minimised by a solution very similar to the default model. The optimal α will lie somewhere between these two extremes. The minimisation presented by Q however, is not easily solvable due to Q being non-linear in $A(\omega)$ by means of the entropy term. A process for overcoming this as well as finding the optimal α is presented by Bergeron in [74] and is implemented in the maximum entropy code used for this project [75].

It starts by choosing a very large value of α where the solution is very close to the default model and is therefore easily obtainable. Then the value of α is decreased in small increments such that the new solution is relatively close to the current solution; in this case the new solution can be found by means of Newton's method. This process is then iterated until the spectrum has been obtained for a range of α.

The optimal value of α, and therefore the optimal spectrum, is then chosen by looking at the curvature of $\log_{10}(\alpha)$ vs $\log_{10}(\chi^2)$. This allows one to gauge how the value of α affects how well the back-continued spectra fits the input data. Bergeron

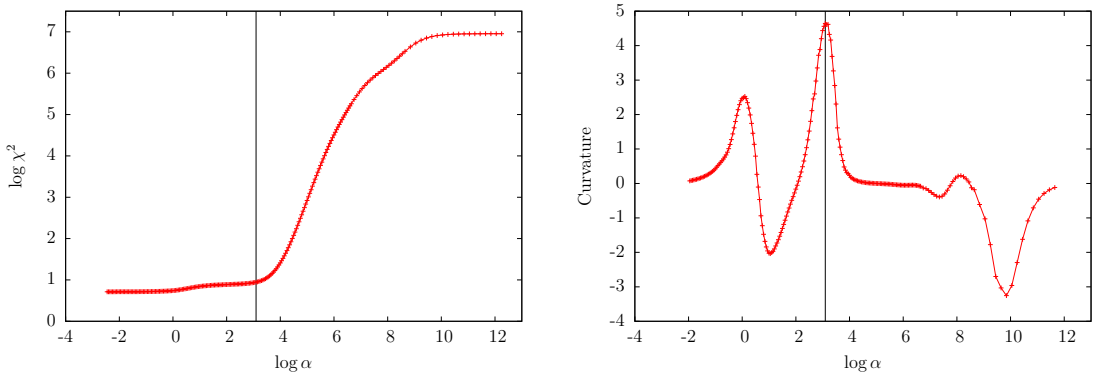

(a) (b)

Figure 3.7: Plots displaying the typical form of the $\log \chi^2$ Vs. $\log \alpha$ plot (**a**) along with a plot of the corresponding curvature. Note: the vertical black line corresponds to the optimal value of α.

argues that this log-log plot contains three regions. An example plot from a real calculation is shown in figure 3.7 along with a plot of the curvature of the log-log plot.

The first region is that of large α where the minimisation of Q has so much weight in favour of the entropy term that it completely dominates and the penalty for deviating from the default mode is so large that the obtained spectrum is essentially the same as the default model. This region is indicated by a flat section with a large value of χ^2 at high α. At the other extreme of very small α the minimisation is almost completely dominated by χ^2, this is where we run the risk of fitting noise in the data, thus, Bergeron terms this the noise-fitting region. This noise fitting region can be somewhat explained by the entropy term having a small enough weight that the penalty for deviating far from the default model has become very small. This allows the spectrum to make very large deviations away from the default model and characteristics enforced by the entropy term in order to fit the noise in the data. This region takes the form of a relatively flat plateau at low χ^2. For values of α between these two extremes there is a region formed by a downward slope; this is where the value of α is small enough that the entropy is becoming less dominant, thus, the spectrum is allowed to deviate enough from the default model to fit the data. This is the region of α where information is being extracted from the input data, Bergeron terms this the information-fitting region. From the descriptions

above it is clear that the optimal value of α lies on the boundary between the information-fitting and noise-fitting regions. Bergeron claims that we are able to identify this point as the maximum in the curvature of the log-log plot.

The only problem remaining is how to choose the default model such that it contains the prior information that we know about the spectrum. Using older variations of the maximum entropy method, it was found that the output spectrum can rely heavily on the form of the default model and therefore it needs to be chosen carefully [51]. This dependence is due to an approximation used in order to find the value of α only being valid when the output spectrum and default model are close. When this is not the case the approximation leads to very small values of α resulting in over-fitting the data as too much weight is put into the chi-squared term [74]. Thus, with the old methods one runs the risk of imposing features on the spectrum that are not informed by the data by biasing the spectrum through the default model. However, the approach described above for finding the optimal value of α does not require that the default model be close to spectrum. This allows us to use relatively featureless default models only containing information we know to be true. This means that any features that do appear in the spectrum are most likely as a result of the input data.

The ΩMaxEnt code [75] used for the maximum entropy calculations performed within this thesis defines the default model as a featureless Gaussian with the same first two moments as those of the high-frequency tail of the input Green's function. It also enforces these moments on the spectrum through the chi-squared term by splitting the frequency grid into low and high-frequency parts. The low-frequency part is fit normally through least-squares but the high-frequency part, which is described by the moments, is replaced by two terms enforcing the moments. It also has other optimisations in order to adapt the grid that the output spectral function is calculated on such that is has a higher density around the main spectral range and where any features are expected to appear [74]. This approach, along with the optimisations of the real frequency grid, allows for relatively robust maximum entropy calculations. While one may not always be able to achieve quantitative

accuracy it is possible to achieve good qualitative results and study the behaviour of spectra with respect to changes in the filling or temperature, for example.

3.2.1 Example Calculation

The paper detailing the above method that accompanies the code used in this project details how to use the code and how to perform robust maximum entropy calculations [74]. However, here we will present the general method using results obtained from the CTHYB and DMFT code written as part of this project. The result used below is for a dynamical mean field theory calculation of the Hubbard model on the square lattice. A more detailed presentation of these DMFT results is given in the following chapter; here we take the result as given and present only the maximum entropy calculation. The input data used below was obtained from a calculation performed at $\beta = 20$ ($T \sim 0.05$) and $U = 6$, the chemical potential was $\mu = -\frac{U}{2}$ so as to obtain half-filling.

Figure 3.8a shows the low-frequency part of the input Green's function. We can see that over this range the Green's function has decayed sufficiently in order to allow us to accurately extract the moments from the data. The fitted moments are used in order to define the default model and are also enforced during the calculation. The low-frequency behaviour of the input Green's function is also examined by the code in order to extract information about the form of the spectrum around the Fermi-level: this along with the moments allows the code to make an informed decision on how to define the frequency grid upon which the spectrum is calculated [74].

Figure 3.8b and 3.8c show the grid density selected for this data as well as the default model. In this case there is a peak expected at the Fermi-level, so the code chooses a high density of grid points around the Fermi-level. We also know that the model is particle-hole symmetric, therefore at half-filling the spectrum should be centred at the Fermi-level and symmetric; this is reflected in both the grid density and the default model. In this case, since the exact error is not known, we have chosen to set a constant error for the Green's function of $\sigma = 1 \times 10^{-4}$:

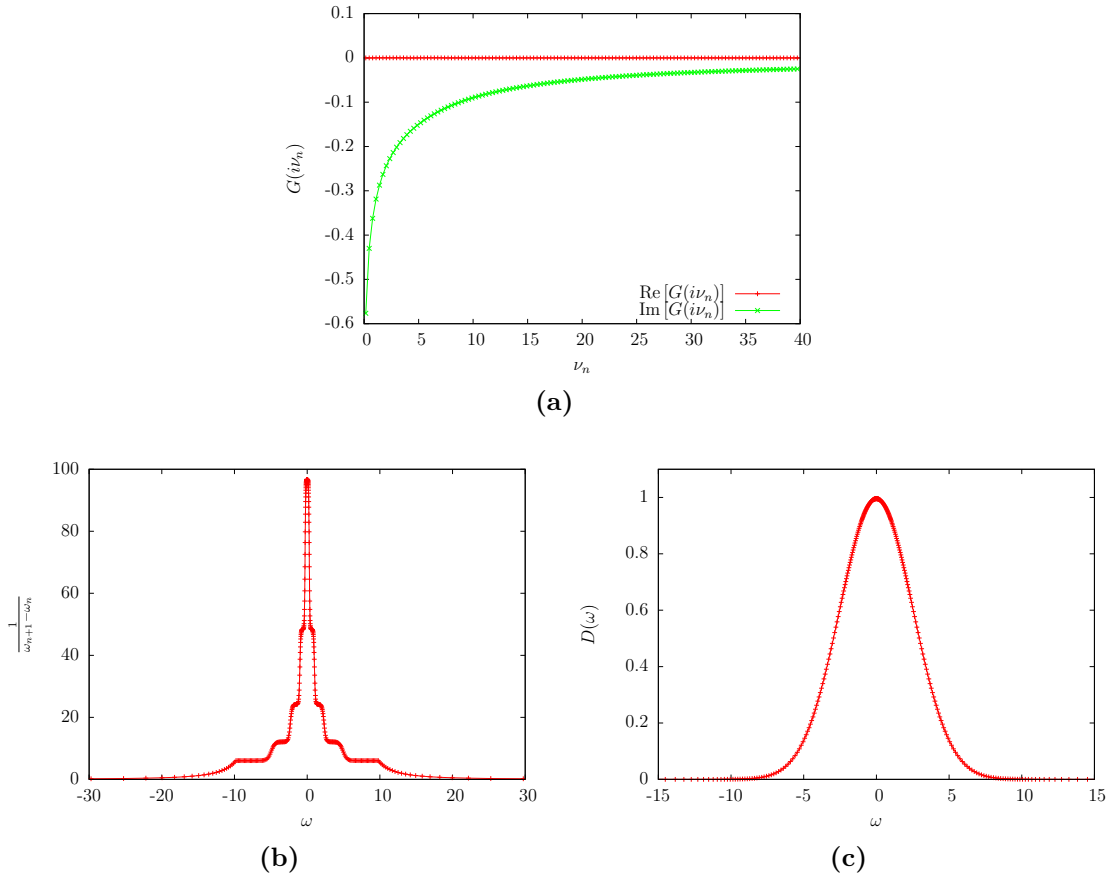

Figure 3.8: Plots showing the relevant data preprocessing figures for a maximum entropy calculation. **a)** plot of the input data, **b)** plot of the density of the output real-frequency grid and **c)** plot of the default model used for the calculation.

this is in line with Monte Carlo errors scaling as $\sim \frac{1}{\sqrt{N}}$ where N is the number of measurements which here was on the order of 1×10^8.

We then perform the calculation, figure 3.9a shows the log-log plot of χ^2 vs α where we can see the three regimes described above: the vertical line depicts the optimal value of α which is found to lie just before the plateau in the plot signalling the start of the noise fitting region. This is much more clear from figure 3.9b showing the curvature of the log-log plot. The peak in the plot of the curvature is clear and is used by the code to select the optimal value of α. Figure 3.9c shows how the spectrum changes with respect to α at some selected sample frequencies. The sample frequencies were chosen to be symmetric about the Fermi-level providing some insight into the symmetry of the spectrum for each value of α. At high α the spectrum will essentially be the default model which is symmetric, this is

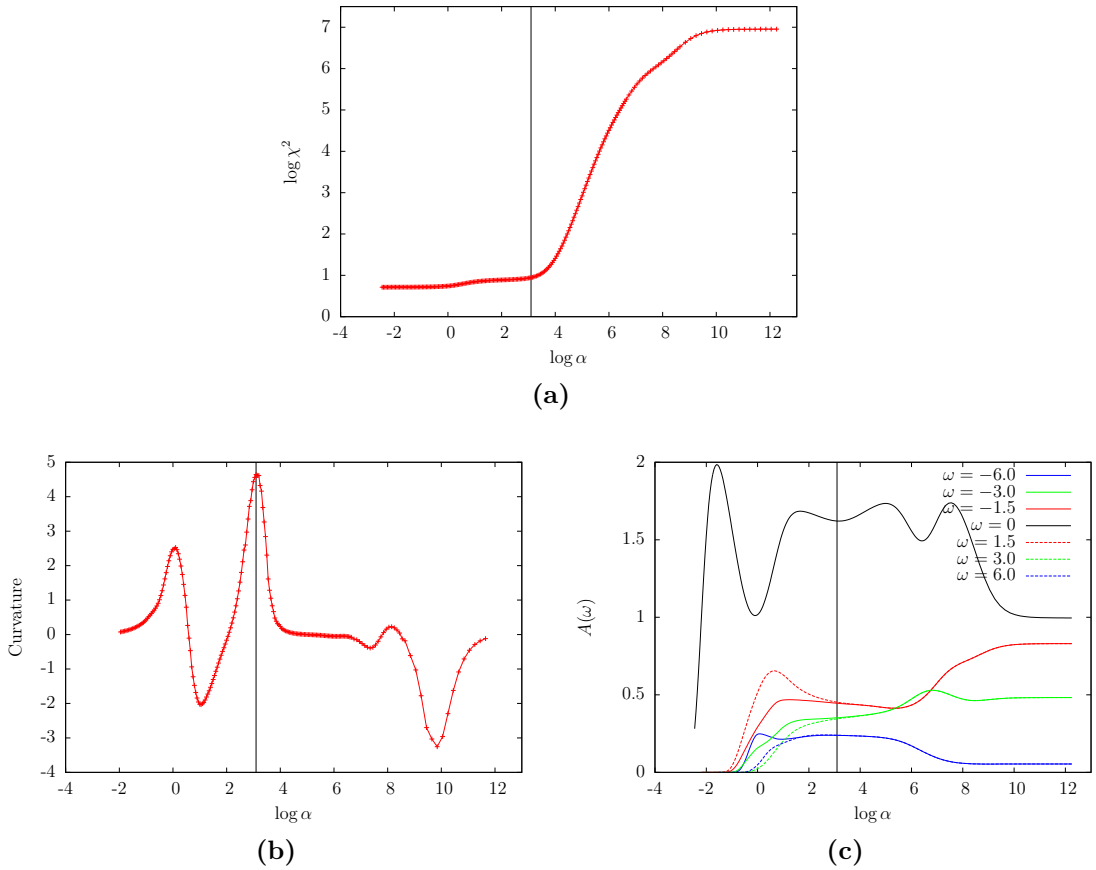

Figure 3.9: Plots showing some post-processing figures from a maximum entropy calculation. **a)** plot of $\log \chi^2$ Vs. $\log \alpha$, **b)** plot of the curvature of the log-log plot of χ^2 Vs. α and **c)** plot of the value of the spectrum for some sample frequencies.

shown here by the corresponding lines of $\pm\omega$ laying on top of each other. As α is decreased the value changes however each of the pairs track together. We then reach the optimal value of α below which we see particle-hole symmetry is not respected due to the noise in the data starting to be fitted. We can also deduce that the spectrum has converged with respect to α by the plateaus in each of the curves around the optimal value of α.

Figure 3.10a shows the optimal spectrum as well as spectra for two values of α slightly above and below the optimal α. We find the features of the spectrum are stable with respect to changes in α around the optimal value, indicating that the spectrum has converged and further supporting the conclusions from figure 3.9c. We can also see that even though the default model contained none of the sharp pronounced features seen in the spectrum, they are present in the spectrum and

have therefore arisen out of fitting the information contained within the data. This provides confidence that the features that do appear in the spectrum are as a result of information from the data and have not been biased by including them in the default model, one of the main selling points of this method.

All of the single-particle spectra shown within this thesis were obtained using the ΩMaxEnt code [75] and the method detailed above.

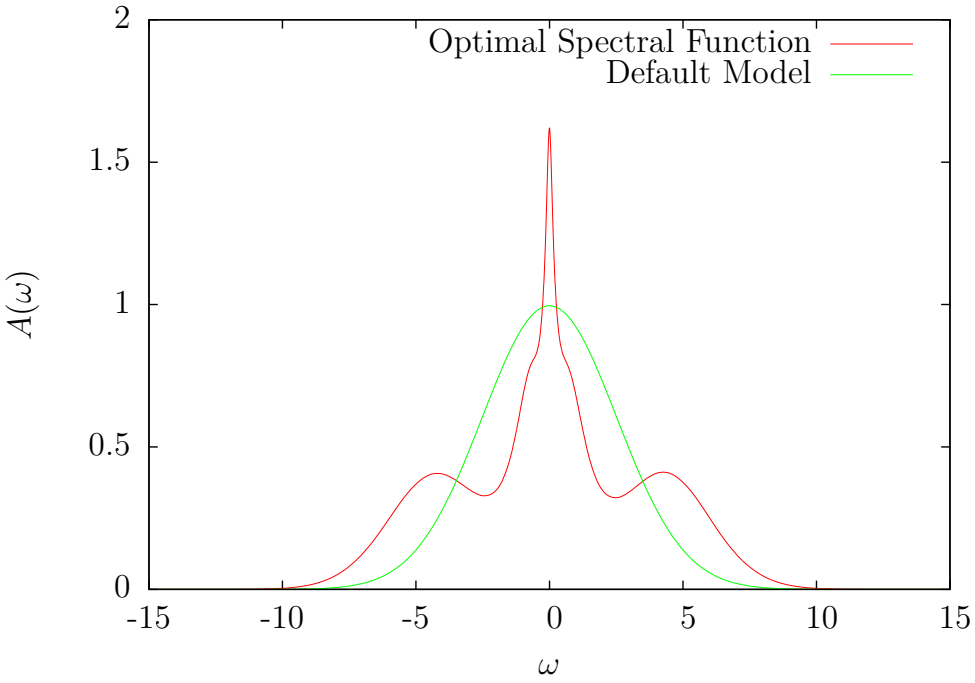

(a)

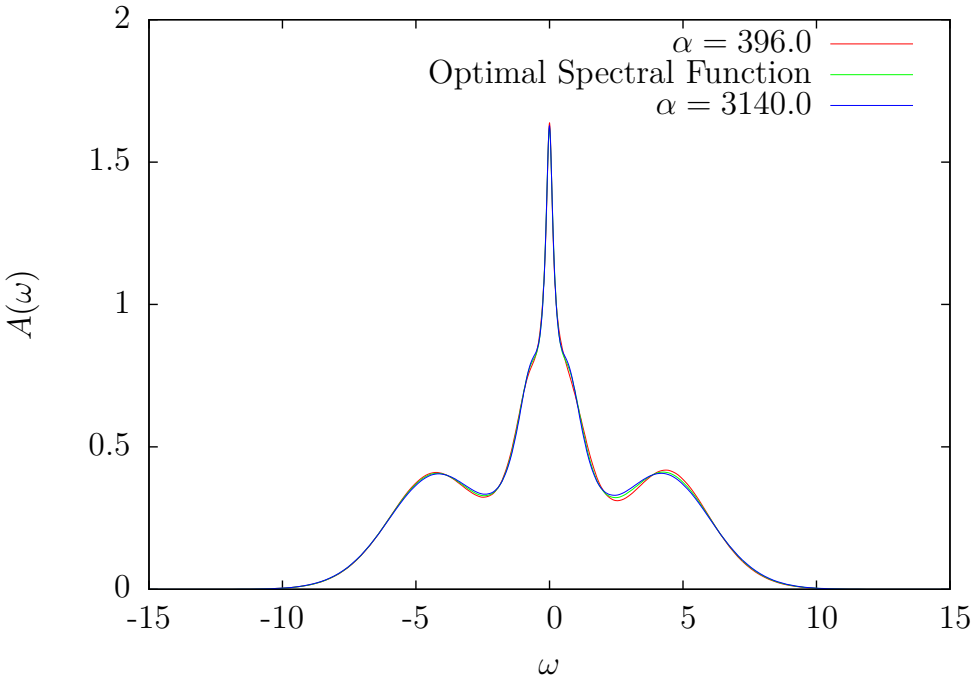

(b)

Figure 3.10: Plots showing the output spectrum from the above maximum entropy calculations. **a)** Plot of the optimal spectral function and the default model, **b)** plot of the spectrum for the optimal value of $\alpha = 1252.02$ along with two values of α around the optimal value.

4

Dynamical Mean Field Theory

The dynamical mean field theory (DMFT) is used widely for the study of correlated lattice problems such as the Hubbard model. Its development followed from two important findings: one that the calculation of non-local quantities greatly simplifies in the limit of infinite dimensions $d \to \infty$ (or equivalently lattice coordination z) [79, 80], and two, that the Hubbard model can be *exactly* mapped onto a self-consistent impurity problem within this limit[52]. For a full review of the DMFT method, including a derivation of the DMFT equations, see [12]. For the interested reader there is also a very informative book chapter by Vollhardt [81]. Here we will provide an overview of the concepts behind the DMFT method as well as discuss the DMFT equations, self-consistency loop and how calculations are performed in practice.

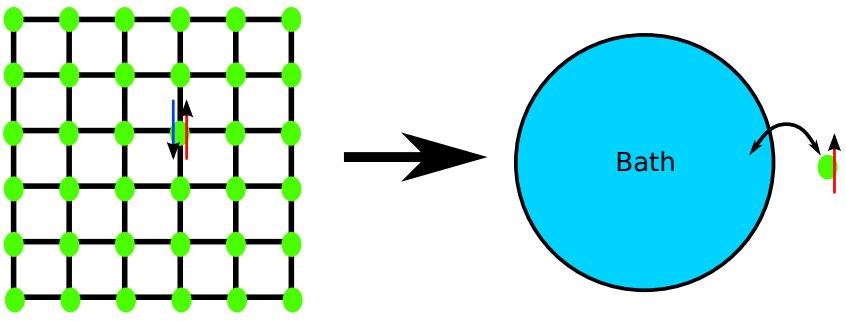

Figure 4.1: A pictorial description of the dynamical mean field theory.

4.1 The DMFT Equations

The general idea behind the dynamical mean field theory is rather similar to that of classical mean field theory. Consider the mean field treatment of the Ising model where the effect of the many different interactions between neighbouring spins are replaced by a single interaction with an effective mean field formed by the other spins [82]. Within DMFT, one selects a single site from the lattice and replaces all remaining sites with a non-interacting bath of electrons. The single site is then coupled to the bath via a hybridisation function $\Delta(i\nu_n)$, allowing electrons to jump between the site and bath (see figure 4.1). The hybridisation is then self-consistently determined such that it best represents a bath of electrons that recreate the rest of the lattice it replaced. In this way $\Delta(i\nu_n)$, or equivalently the corresponding non-interacting impurity Green's function $G^0(i\omega_n)$, can be seen as the analogue of the effective field within the mean field treatment of the Ising model. The main difference is that $G^0(i\nu_n)$ (or $\Delta(i\nu_n)$) retains a frequency dependence, i.e. it is not just a static mean field as with classical mean field theory, hence the name dynamical mean field theory. This allows for temporal fluctuations to occur on the impurity site retaining and fully treating the local dynamics of the lattice problem.

When $d = \infty$ the exact mapping between the Hubbard model and a self-consistent impurity model is a result of the self-energy of the lattice model $\Sigma(i\nu_n, \mathbf{k})$ becoming purely local [79, 80]. This corresponds to the freezing of all spatial correlations and the self-energy becoming independent of momentum.

$$\Sigma(i\nu_n, \mathbf{k}) \overset{d=\infty}{=} \Sigma(i\nu_n) \tag{4.1}$$

The proof of why this is the case is one that is made using diagrammatic perturbation theory and power counting in terms of $\frac{1}{d}$, it is discussed in [81, 83]. Within the diagrammatic perturbation theory the self-energy is constructed in terms of skeleton diagrams, the building blocks of which are interacting Green's functions. It is shown that the Green's functions depend on the dimension of the lattice in the following way

$$G_{i,j} = \mathcal{O}(d^{-\frac{1}{2}||\mathbf{R}_i - \mathbf{R}_j||}) \tag{4.2}$$

where i, j denote lattice sites and $||\mathbf{R}_i - \mathbf{R}_j||$ is the Manhattan distance between the two sites (i.e. the smallest number of hops between lattice sites). What this tells us is that the Green's functions depend strongly on the distance between the lattice sites and decay more rapidly for higher dimensions. From this it can be shown that the skeleton diagrams for $i \neq j$ decay according to $\mathcal{O}(d^{-\frac{1}{2}||\mathbf{R}_i - \mathbf{R}_j||})$ at a minimum, while from above it is clear that when $i = j$ the Green's functions decay as $\mathcal{O}(d^0)$. Thus, in the limit of $d \to \infty$ only the local $i = j$ diagrams survive and the self-energy is a purely local quantity.

Using the above result we are able to make an argument for the DMFT equations. In order to do this we have to introduce the lattice Green's functions. We will start with the non-interacting lattice Green's function which is given by:

$$G^0_{latt}(i\nu_n, \mathbf{k}) = \frac{1}{i\nu_n + \mu - \epsilon_{\mathbf{k}}} \tag{4.3}$$

where μ is the chemical potential and $\epsilon_{\mathbf{k}}$ is the dispersion of the lattice which defines the non-interacting density of states.

$$A^0(\omega) = \frac{1}{N} \sum_{\mathbf{k}} \delta(\omega - \epsilon_{\mathbf{k}}) \tag{4.4}$$

The non-interacting and interacting lattice Green's functions are related to each other through the lattice Dyson's equation involving the momentum dependent lattice self-energy.

$$[G_{latt}(i\nu_n, \mathbf{k})]^{-1} = \left[G^0_{latt}(i\nu_n, \mathbf{k})\right]^{-1} - \Sigma(i\nu_n, \mathbf{k}) \tag{4.5}$$

$$G_{latt}(i\nu_n, \mathbf{k}) = \frac{1}{i\nu_n + \mu - \epsilon_{\mathbf{k}} - \Sigma(i\nu_n, \mathbf{k})} \tag{4.6}$$

This is analogous to the Dyson's equation for the impurity Green's functions (2.31) introduced previously. From the lattice Green's functions we are also able to define their local counterparts by taking the lattice Fourier transform.

$$G^0_{loc}(i\nu_n) = \frac{1}{N} \sum_{\mathbf{k}} \left[i\nu_n + \mu - \epsilon_{\mathbf{k}}\right]^{-1} \tag{4.7}$$

$$G_{loc}(i\nu_n) = \frac{1}{N} \sum_{\mathbf{k}} \left[i\nu_n + \mu - \epsilon_{\mathbf{k}} - \Sigma(i\nu_n, \mathbf{k})\right]^{-1} \tag{4.8}$$

For the case of the non-interacting lattice Green's function we can then rewrite this expression in terms of an integral over the non-interacting density of states using the sampling property of the delta function.

$$G^0_{loc}(i\nu_n) = \int_{-\infty}^{\infty} d\epsilon \frac{A^0(\epsilon)}{i\nu_n + \mu - \epsilon} \tag{4.9}$$

While this integral is over all ϵ, in practice we only have to integrate over the finite bandwidth of the non-interacting density of states.

Having now laid the groundwork of the lattice Green's functions we turn our attention back to equation (4.1). While this is only true in the limit of $d = \infty$ it is the basis of the approximation that DMFT makes in finite dimensions and here we will take it as true. The implications of this result are that the interacting local lattice Green's function now only depends on momentum through the dispersion of the lattice. This is also true of the non-interacting local lattice Green's function. As such the interacting lattice Green's function now takes the same form as the non-interacting local lattice Green's function but with a frequency dependent shift of the chemical potential $\mu \to \mu - \Sigma(i\nu_n)$. We are therefore able to use equation (4.9) to obtain an expression for the fully interacting local lattice Green's function as an integral over the non-interacting density of states.

$$G_{loc}(i\nu_n) = \int_{-\infty}^{\infty} d\epsilon \frac{A^0(\epsilon)}{i\nu_n + \mu - \Sigma(i\nu_n) - \epsilon} \tag{4.10}$$

Also given that in $d = \infty$ the mapping between the Hubbard model and the self-consistently determined impurity model is exact we would expect that the local lattice Green's function coincides with the impurity Green's function. Thus, this equation coupled with the impurity Dyson's equation (2.31) for $G^0(i\omega_n)$, the mean field, allow one to solve for the self-energy and therefore the local lattice Green's function in a self-consistent manor.

$$\left[G^0(i\nu_n)\right]^{-1} = [G(i\nu_n)]^{-1} + \Sigma(i\nu_n) \tag{4.11}$$

The equation (4.10) can be thought of as ensuring that the mean field $G^0(i\omega_n)$ is the one that corresponds to the Hubbard model on the lattice with the non-interacting density of states $A^0(\epsilon)$.

The reason these equations have to be solved self consistently is clear when you consider that equation (4.11) allows us to determine the mean field that corresponds to the exact mapping from knowledge of $G_{loc}(i\omega_n)$ and $\Sigma(i\nu_n)$. However, the mean field determines the $G(i\omega_n)$ and thereby $\Sigma(i\nu_n)$ by means of an impurity solver and therefore themselves depend on the mean field. Thus, there is a situation where the local Green's function depends on the mean field but the mean field depends on the local Green's function and we have to solve self-consistently. This process is known as the DMFT self-consistency loop which is discussed in the section below.

4.2 The DMFT Self-Consistency Loop

The process for solving the DMFT equations is shown in figure 4.2, one starts with an initial guess for the mean field $G^0(i\nu_n)$. The impurity problem that this describes is then solved with an impurity solver yielding $G(i\nu_n)$. The self-energy is then extracted from $G(i\nu_n)$ by Dyson's equation (2.31) this is then used to obtain the corresponding local lattice Green's function $G_{loc}(i\nu_n)$ (4.10). We then check for self consistency $G^{loc}(i\nu_n) = G(i\nu_n)$ and if required update $G^0(i\nu_n)$ using $G_{loc}(i\nu_n)$ through equation (4.11) and so on, until self-consistency is reached. Note that for simplicity the above discussion only considers the case of paramagnetic solutions $G_\downarrow(i\nu_n) = G_\uparrow(i\nu_n) = G(i\nu_n)$. However, the above generalises to the case of broken spin symmetry simply by treating the two independent spin components separately.

Within the above procedure the most time consuming and non-trivial part is solving the impurity model, however, evaluating the integral over the density of states accurately can also prove problematic. There are cases where the non-interacting density of states takes a particularly simple form and the integral can be evaluated explicitly, such as the case of the Bethe lattice [12]. However, for more realistic lattices, such as the fcc lattice considered in the later chapters of this thesis, a closed form of the non-interacting density of states is not known. Thus the integral has to be evaluated numerically and is a rather delicate process.

The DMFT solutions usually converge relatively quickly with most converging in 10 - 20 DMFT loops. However, there are occasions where many loops are required

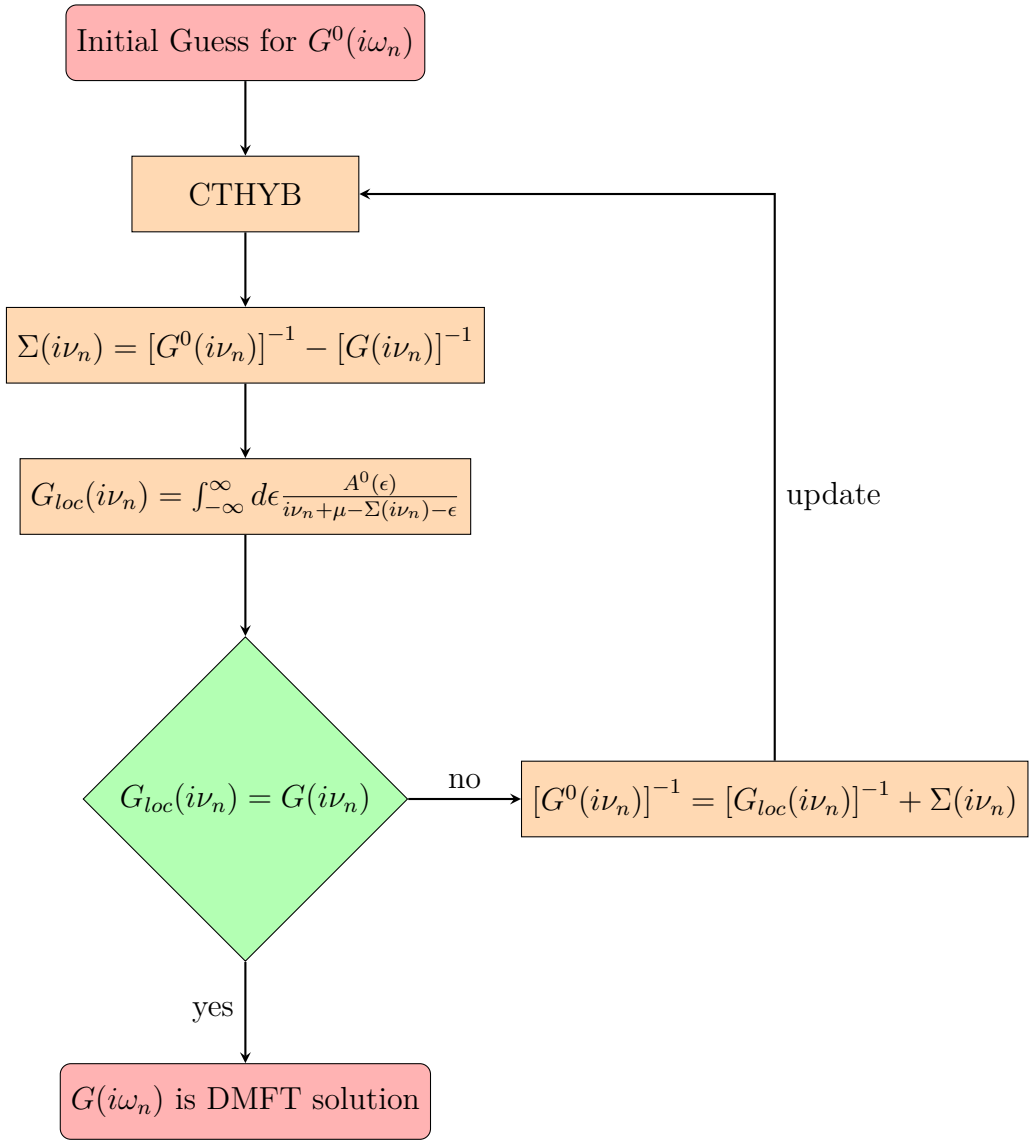

Figure 4.2: Flowchart of the DMFT self-consistency loop.

to reach convergence. Such as the case of converging solutions with broken spin symmetry near the phase boundary where well over 100 DMFT loops could be required. This problem could in principle be helped by the inclusion of global moves (see 3.1.2), however, due to the computational expense of these moves it is often faster to not include them and perform more DMFT loops. This was found to be the case for the magnetisation calculations performed as part of this project.

The mapping between the Hubbard model and a self-consistent impurity model described above is exact in $d = \infty$. However, when used in $d < \infty$ it becomes an approximation. The approximation that the self-energy is purely a local quantity

corresponds to neglecting all non-local correlation. Attempts have been made in order to improve upon DMFT results by including non-local correlation through extensions to DMFT. This can be achieved using cluster methods such as cluster DMFT (CDMFT) or the dynamical cluster approximation (DCA) [84]. These methods consider a cluster of sites coupled to a non-interacting bath and are therefore able to treat non-local correlation on small length scales. Diagrammatic methods have also been developed such as the dynamical vertex approximation (DΓA) [85] and the dual fermion approach that is used within this project (See Chapter 6) [25].

While DMFT is an approximation it is used regularly in dimensions as low as $d = 2$ [2]. It is also regularly used in conjunction with density functional theory in order to perform electronic structure calculations on real world materials [12, 18]. DMFT has also seen particular success in studying the Mott transition [1], a metal-insulator transition driven by the interaction localising the electrons [12, 86]. It is also believed to produce a good approximation in relatively low dimensions such as $d = 3$, where it has been used in conjunction with LDA in order to study the Mott transition in V_2O_3 [4]. This produced a very good agreement between theoretical and experimental photoemission spectra. However, it has recently been shown that DMFT fails qualitatively for $d = 2$ where a Mott transition has been previously been found [2, 87], but through comparisons to calculations performed above the DMFT level, this is now believed to be an artefact of DMFT and in fact, an insulating state can be found at low enough temperatures for all $U > 0$ [22]. Nonetheless the Mott transition in the 2D Hubbard model does provide a good and interesting test case for reproducing results from the literature using a newly implemented code and is used as such in section 4.4. However, before we present the results of these calculations we wish to take the opportunity to discuss the calculation of the magnetic susceptibility within DMFT.

4.3 The Magnetic Susceptibility within DMFT

The studies of magnetic phase boundaries within the later chapters of this thesis require calculations of the magnetic susceptibility $\chi^m(i\omega_m, \mathbf{q})$. Formally the magnetic

susceptibility can be calculated by building a diagrammatic perturbation theory [88]: this results in a Bethe-Salpeter equation involving the full momentum dependent vertex of the lattice problem [12, 88]. It is generally not possible to calculate the full momentum dependent vertex; however, for the case of $d = \infty$, it has been shown that we are able to replace it by its local but still fully frequency-dependent counterpart [12, 88, 89]. This argument is made using the same power counting arguments used to argue the locality of the self-energy in $d = \infty$ and therefore when used in finite dimensions does represent an approximation. When the vertex is replaced by its local counterpart we obtain the following equation for the lattice susceptibility

$$\begin{aligned}\tilde{\chi}_{latt}(i\nu_n, i\nu_{n'}, i\omega_m, \mathbf{q}) =& \tilde{\chi}^0_{latt}(i\nu_n, i\nu_{n'}, i\omega_m, \mathbf{q}) + \\ & \tilde{\chi}^0_{latt}(i\nu_n, i\nu_{n'}, i\omega_m, \mathbf{q}) \frac{1}{\beta} \sum_{\nu_{n''}} \Gamma(i\nu_n, i\nu_{n''}, i\omega_m) \tilde{\chi}_{latt}(i\nu_n, i\nu_{n'}, i\omega_m, \mathbf{q})\end{aligned} \tag{4.12}$$

where $\tilde{\chi}^0_{latt}(i\nu_n, i\nu_{n'}, i\omega_m, \mathbf{q})$ is the bare lattice susceptibility defined by

$$\tilde{\chi}^0_{latt}(i\nu_n, i\nu_{n'}, i\omega_m, \mathbf{q}) = -\sum_{\mathbf{k}} G^{latt}_{\mathbf{k}+\mathbf{q}}(i\nu_n + i\omega_m) G^{latt}_{\mathbf{k}}(i\nu_n) \delta_{n,n'} \tag{4.13}$$

$$G^{latt}_{\mathbf{k}}(i\nu_n) = \frac{1}{i\nu_n + \mu - \epsilon_{\mathbf{k}} - \Sigma(i\nu_n)} \tag{4.14}$$

and the tilde on $\tilde{\chi}_{latt}(i\nu_n, i\nu_{n'}, i\omega_m, \mathbf{q})$ denotes that we obtain the dynamical susceptibility from summing over both the fermionic frequencies as will be seen later. The local vertex $\Gamma(i\nu_n, i\nu_{n''}, i\omega_m)$ is still not known, however, in $d = \infty$ it can be obtained through the following equation [12, 88]

$$[\Gamma](i\omega_m) = \left[\chi^0_{loc}\right]^{-1}(i\omega_m) - [\chi_{loc}]^{-1}(i\omega_m) \tag{4.15}$$

where the inverses are matrix inverses performed in terms of the two fermionic frequencies, χ_{loc} is the generalised susceptibility as defined in equation (2.26) and χ^0_{loc} is the bare local susceptibility.

$$\chi^0_{loc}(i\nu_n, i\nu_{n'}, i\omega_m) = -G(i\nu_n + i\omega_m) G(i\nu_n) \delta_{n,n'} \tag{4.16}$$

Thus, this allows one to obtain the local vertex in terms of quantities of the self-consistent DMFT impurity model only [12]. We can then use equation (4.15)

within equation (4.12) obtaining the following matrix equation for the susceptibility within DMFT [12, 90].

$$[\chi_{latt}]^{-1}(i\omega_m, \mathbf{q}) = [\chi_{loc}]^{-1}(i\omega_m) - \left[\chi^0_{loc}\right]^{-1}(i\omega_m) + \left[\chi^0_{latt}\right]^{-1}(i\omega_m, \mathbf{q}) \tag{4.17}$$

One then obtains the magnetic susceptibility by using the generalised magnetic susceptibility $\chi^m_{loc}(i\omega_m) = \chi_{\uparrow\uparrow}(i\nu_n, i\nu_{n'}, i\omega_m) - \chi_{\uparrow\downarrow}(i\nu_n, i\nu_{n'}, i\omega_m)$ in place of χ_{loc} in equation (4.17) [47]. Thus, this equation allows for the calculation of the magnetic susceptibility from the purely local quantities of the DMFT impurity model [12].

The matrix equation (4.17) can be treated either in terms of the Matsubara indices n, n' or the corresponding Legendre indices l, l'. The magnetic susceptibility for a specific field vector $\mathbf{q}$ is then obtained by performing the sum over all fermionic frequencies or Legendre polynomials.

$$\begin{aligned}\chi^m(i\omega_m, \mathbf{q}) &= \frac{1}{\beta^2}\sum_{n,n'}\chi^m_{latt}(i\nu_n, i\nu_{n'}, i\omega_m, \mathbf{q}) \\ &= \frac{1}{\beta^2}\sum_{l,l'\geq 0}(-1)^{l+l'}\sqrt{2l+1}\sqrt{2l'+1}\chi^m_{latt}(l, l', i\omega_m, \mathbf{q})\end{aligned} \tag{4.18}$$

This sum can be performed in two parts, the sum over the bubble part χ^m_{bubble} formed from the lattice and local bare susceptibilities (equations (4.13) and (4.16)), and the sum over the vertex part χ^m_{vert} treating each part either in terms of frequency or Legendre polynomials. It has been shown that the Legendre representation of the vertex part of χ^m is largely localised around the lower order coefficients and has no directions of slow decay [47]. This allows for rapid convergence of the value of the vertex part of the susceptibility when it is summed in the Legendre representation [47]. However, the Legendre representation of the bubble part of the susceptibility is largely localised around the main $l = l'$ diagonal and decays rather slowly, thus, it is better to treat this part of the sum in the Matsubara representation. This method was shown to achieve rapid convergence of susceptibility values with respect to the cut-off of the Legendre representation used allowing for efficient calculations of accurate magnetic susceptibility values [47]. Thus, when performing calculations of the magnetic susceptibility for the work contained within this thesis the two-particle Green's functions are measured in terms of the mixed Legendre-Fourier

representation and the susceptibility calculation performed using the procedure described above. The systematic deviations away from the exact result that are found at higher bosonic frequencies [48] are not a problem for the calculation of the susceptibility used here. This is because we are only concerned with the static magnetic susceptibility and therefore only the first bosonic frequency.

4.4 Implementation and Testing

The above DMFT procedure was implemented using the TRIQS library [69] and made use of the modified CTHYB impurity solver developed in chapter 3) [69]. This has then been tested extensively and used in all subsequent DMFT calculations for this project.

As one of these tests we have reproduced some DMFT results studying the Mott transition in the 2D Hubbard model on the square lattice from Park et.al. [2]. Within this paper the authors study the Mott transition at half-filling using both single-site and cluster DMFT. For single-site DMFT they present a phase diagram in the (U, T) plane consisting of two temperature dependent critical lines, $U_{c1}(T)$ and $U_{c2}(T)$. For $U > U_{c1}(T)$ they are able to find a Mott insulating solution, while for $U < U_{c2}(T)$ they are able to find a metallic solution. These two lines of critical values of U meet at a critical endpoint (U_{mit}, T_{mit}) above which there is a crossover region between bad metal and bad insulator phases, U_{mit} is found to be $9.35t$ and $T_{mit} = 0.09t$. For interactions between $U_{c1}(T)$ and $U_{c2}(T)$ and $T < T_{mit}$ there is a coexistence region where both metallic and insulating solutions can be found. We chose to perform calculations at $\beta t = 20$, from the phase diagram within the paper we are able to predict that U_{c1}, above which we expect to find insulating solutions, is expected to occur for $\frac{U}{t} \sim 9.475$ at this temperature.

The transition to the Mott insulating state can be detected in two ways. The first is directly observing the gap opening in the single-particle spectra which can be obtained from the DMFT solution through analytic continuation using the maximum entropy method (see 3.2). The second is by looking at the low-frequency behaviour of the self-energy. This is due to it's relation to the quasi-particle weight

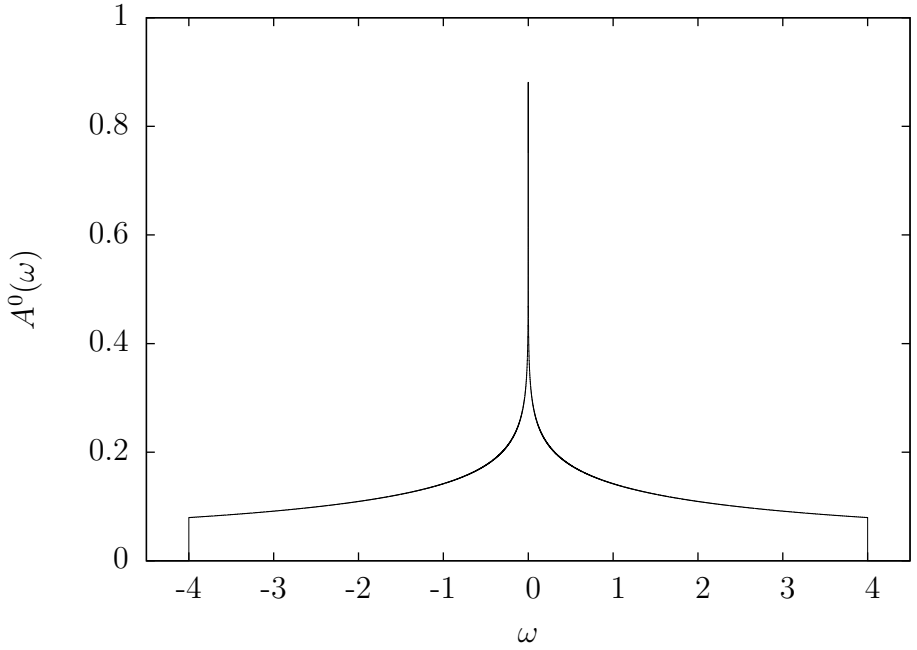

Figure 4.3: Plot of the non-interacting density of states $A^0(\omega)$ of the square lattice with $t = 1$.

z which tells us about the weight of the quasi-particle peak at the Fermi-level and therefore if a solution has a finite density of states at the Fermi-level [10].

$$z = \left[1 - \left.\frac{\partial Re[\Sigma^R(\omega)]}{\partial\omega}\right|_{\omega\to 0}\right]^{-1} \tag{4.19}$$

However, the quasi-particle weight is defined in terms of the retarded self-energy $\Sigma^R(\omega)$, which is a real frequency quantity and could be obtained by analytically continuing the imaginary frequency self-energy back onto the real axis. Arsenault et. al. however, show that it is possible to approximate z by using the value of the imaginary frequency self-energy at the smallest positive imaginary frequency $\omega_{n=0}$ through the following [91].

$$\left.\frac{\partial Re[\Sigma^R(\omega)]}{\partial\omega}\right|_{\omega\to 0} = \left.\frac{Im[\Sigma(i\omega)]}{i\omega}\right|_{\omega_n\to 0} \tag{4.20}$$

This equation coupled with equation (4.19) allows us to determine that when the low-frequency part of the imaginary frequency self-energy extrapolates towards 0 we have a metallic state with a finite quasi-particle weight, while if it extrapolates towards a large finite value we have an insulating state.

Before we are able to perform these calculations the non-interacting density of states of the square lattice has to be calculated. It is possible to obtain a closed form of the non-interacting density of states for the square lattice in terms of the complete elliptic integral of the first kind $\mathbf{K}(k)$ [92]. This is achieved through using the following expression for the non-interacting Green's function on the square lattice [93]

$$G(\omega) = \frac{2}{\pi\omega}\mathbf{K}\left(\frac{B}{\omega}\right) \quad : \quad |\omega| < B \tag{4.21}$$

where $B = 4t$ is the bandwidth. The non-interacting density of states is then obtained through equation (2.20) resulting in the expression.

$$A^0(\omega) = \frac{2}{B\pi^2}\mathbf{K}\left(\sqrt{1-\left(\frac{\omega}{B}\right)^2}\right)\theta(B-|\omega|) \tag{4.22}$$

This can then be evaluated on a grid and used in the integral (4.10) during the DMFT calculation. The value of t was chosen to be unity, thereby fixing the bandwidth as $B = 4$, the resulting density of states is plotted in Figure 4.3.

Figure 4.4a shows the imaginary part of the self-energy for a range of U covering where we would expect to observe the transition. We can see there are two distinct low-frequency behaviours corresponding to the cases of metallic and insulating solutions described above. From the data in figure 4.4a we would expect the Mott transition to occur for $U \in [9.45, 9.5]$ in good agreement with the results of Park et. al. This is further confirmed by examining the local spectral function $A(\omega)$, shown in figure 4.4b, where we observe the opening of a gap at the Fermi-level as the Coulomb interaction is increased from $U = 9.45$ to 9.5.

Each of the spectra obtained from the DMFT solutions above shows the familiar Hubbard bands located at $\pm\frac{U}{2}$. At $\frac{U}{t} = 6$ we have a finite density of states at the Fermi-level and therefore a metallic state in agreement with the deduction from the corresponding self-energy. As the interaction strength is increased we can see that the peak at $\omega = 0$ reduces in height and weight until between $\frac{U}{t} = 9.45$ and 9.5 where there is a transition between a metallic and insulating state with the quasi-particle peak disappearing and the formation of a gap at the Fermi-level. As the value of $\frac{U}{t}$ is increased further the size of the gap grows as we go further into the insulating phase.

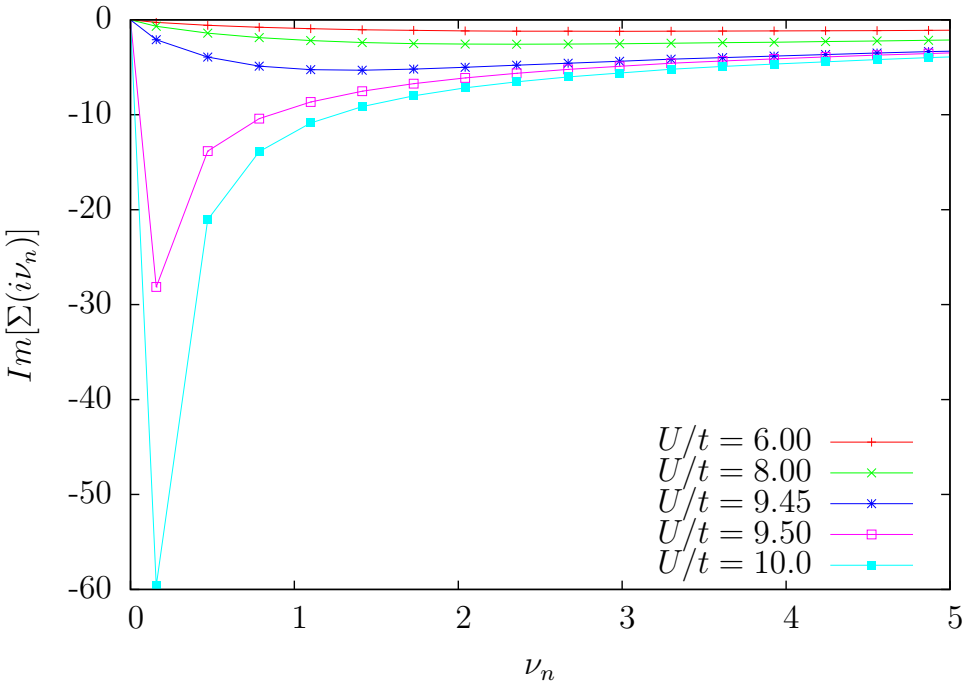

(a) Self-energy

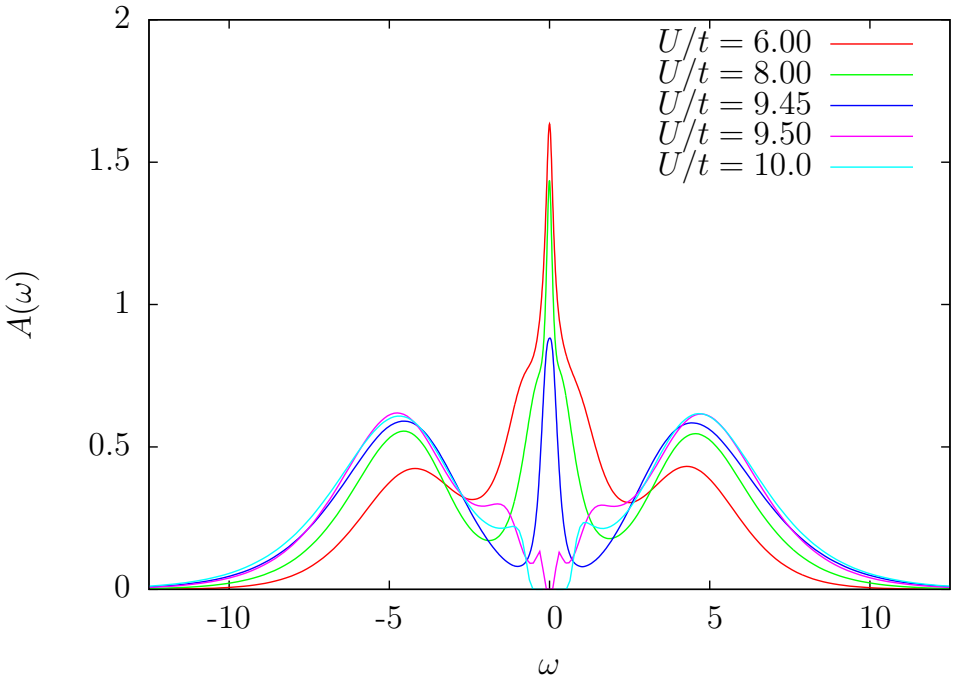

(b) $A(\omega)$

Figure 4.4: Plots of the low-frequency region of the imaginary part of the self-energy and the local spectral function $A(\omega)$ from the DMFT solutions obtained over a range of U covering U_{c1}.

5

DMFT Study of The Hubbard Model on The fcc Lattice

In the following chapter we present DMFT results for the Hubbard model on the fcc lattice obtained using the CTHYB solver of chapter 3 and the DMFT code of chapter 4. This includes calculations of the magnetic susceptibility throughout the first Brillouin zone, calculations of the critical temperatures and the associated magnetic phase diagram, also results for the single-particle spectra. Before this, however, we will cover the topic of magnetism in the Hubbard model, focusing mostly on metallic ferromagnetism and introducing some previous work that has been performed. Following this we will present an overview of the fcc lattice along with the calculation of the non-interacting density of states with the relevant hopping parameters. This is not analytically available and therefore presents a problem in its own right. We then present DMFT results for the ferromagnetic region of the model, showing example solution Green's functions and self-energies, the susceptibility for fillings throughout the region, magnetisation data and single-particle spectra. We then present similar results for the anti-ferromagnetic region found around half-filling.

5.1 Magnetism In The Hubbard Model

The Hubbard model itself was originally devised in order to understand the origin of metallic ferromagnetism in the transition metals such as Fe, Ni and Co [11]. However anti-ferromagnetism and ferromagnetism are constantly competing within the model and usually anti-ferromagnetism is more energetically favourable. This is because the anti-ferromagnetic alignment of spins allows electrons to hop to neighbouring sites of opposing spin, leading to a favourable gain in kinetic energy. From the above simple argument it is clear that ferromagnetism arises out of a delicate balance between the interaction and kinetic energy. This raises the question of how one might be able to create favourable conditions for ferromagnetism. This subject has been discussed in several papers by Vollhardt et. al. [94–96], and we will repeat the main points below.

The lattice structure is thought to play a very important role in the stabilisation of metallic ferromagnetism. This is partially due to the lattice structure being able to frustrate the competing anti-ferromagnetic state. A non-bipartite lattice frustrates the anti-ferromagnetic state by removing the ability of the spins to favourably satisfy all anti-ferromagnetic interactions at once. The inclusion of next-nearest neighbour hopping in the model can further frustrate the competing anti-ferromagnetism by removing the Fermi-surface nesting, as shown by Hofstetter et. al. [97]. These two factors combined are able to remove some of the favourable kinetic energy advantages of anti-ferromagnetism, making the case for ferromagnetism stronger.

The lattice structure is also thought to play a further role in the stabilisation of metallic ferromagnetism in the Hubbard model for the following reason. The Hubbard interaction is site diagonal: it is therefore independent of the dimension and structure of the underlying lattice. The kinetic energy, however, is directly affected by the lattice structure. Thus, the existence of ferromagnetism in the Hubbard model is expected to depend heavily on the underlying lattice as this can have a large influence on the balance of kinetic and interaction energy [95, 96]. This has been investigated by Hanisch et. al. who studied the stability of the Nagaoka state on various lattices [98]; this has been further investigated by Wahle

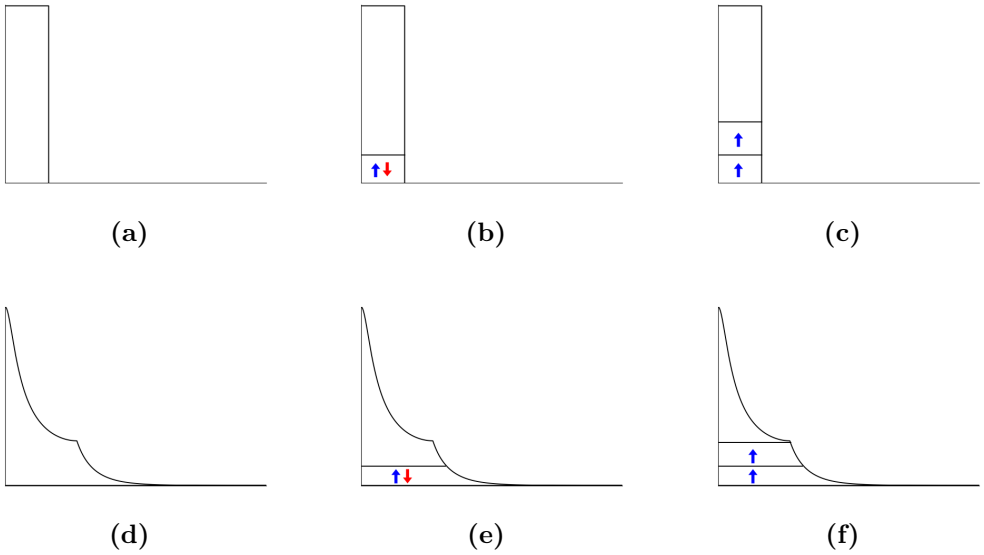

Figure 5.1: Plots demonstrating the argument for why a divergence at the band edge is thought to be favourable for ferromagnetism. Top: the case of a flat band. Bottom: face-centered cubic density of states.

et. al. where they found extended regions of fillings for which ferromagnetism is stable for a range of U [54]. In both cases they found that a strong divergence at the edge of the density of states is an important feature for the stability of metallic ferromagnetism. This feature is present in the non-interacting density of states of non-bipartite lattices and can be further enhanced by including hopping beyond just nearest neighbour [9, 94].

One can get an idea of why a divergence near the band edge is thought to be important by considering two cases: that of a flat band, and a band with a divergence near the band edge. These examples are shown in figure 5.1. We can consider a (naive) paramagnetic state by occupying the lowest energy states of each of the σ spin bands with spin paired electrons up to the Fermi-level: this is shown in figures 5.1b and 5.1e. We can then obtain the fully-polarised ferromagnetic state from the paramagnetic state by taking all the down spin electrons, flipping them and placing them in the lowest energy available states in the up spin band. The resulting Fermi-level of the ferromagnetic state is twice that of paramagnetic state in the case of a flat band, see figure 5.1c. However, if the band has a divergence at the band edge, there is a higher availability of lower energy states to put the

flipped electrons in, thus, the resulting energy penalty for adopting a ferromagnetic state is less, see figure 5.1f [95, 96]. This argument has of course been made for the non-interacting case: the presence of electron interactions makes the physics more complex, yet one could expect some remnant of this argument to hold.

One model possessing the above characteristics thought to be favourable for ferromagnetism is the Hubbard model on the face-centered cubic lattice with nearest and next-nearest neighbour hopping. This is the model studied within this work. To this end we turn our attention to the fcc lattice in the following section.

5.2 The Face-Centered Cubic Lattice

The face-centered cubic (fcc) lattice is a cubic Bravais lattice and is a common crystal structure. Some metals adopting this crystal structure are copper, aluminium and palladium, as well as the metallic ferromagnet nickel [99]. The unit cell of the face-centered cubic lattice has atoms situated on each of the corners of a cubic unit cell, along with an atom centred in each of the cube's faces. The three basis vectors generating this structure are $\mathbf{a_1} = \frac{a}{2}(0,1,1)$, $\mathbf{a_1} = \frac{a}{2}(1,0,1)$ and $\mathbf{a_1} = \frac{a}{2}(1,1,0)$, where a is the lattice constant and is set to unity throughout this work [100]. Using these we are able to plot the unit cell of the fcc lattice by taking integer combinations of the above basis vectors forming lattice vectors $\mathbf{R}$. The unit cell is shown in figure 5.2.

The coordination of the fcc lattice is relatively high, with each lattice site having 12 nearest-neighbours at distances of $\frac{a}{\sqrt{2}}$. The locations of these nearest neighbours are most easily visualised by considering the lattice site at the center of the bottom square face. We find the first four nearest neighbours located at the corners of the bottom square face, another four are found at the centres of the faces of each side of the unit cell. The remaining four can be visualised by taking our reference lattice site and visualising that is the located at the center of the top face of the cell below. The last four nearest neighbours are then located at

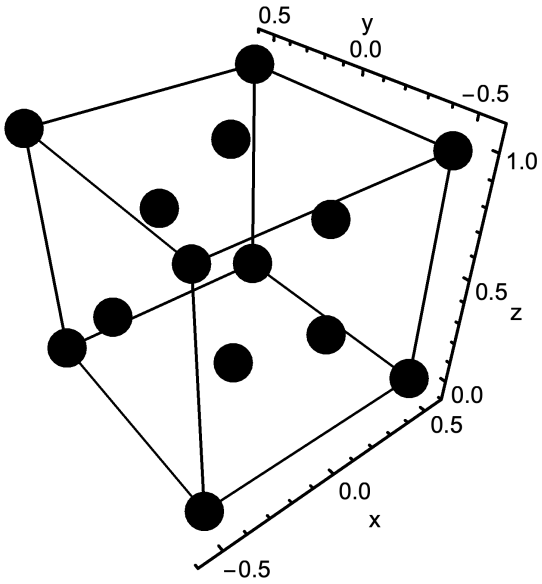

Figure 5.2: Plot showing the unit cell of the face-centered cubic lattice.

the center of the faces of the unit cell below. The lattice vectors corresponding to the nearest neighbours are given by the following.

$$\frac{a}{2}(\pm 1, \pm 1, 0) \quad \frac{a}{2}(\pm 1, 0, \pm 1) \quad \frac{a}{2}(0, \pm 1, \pm 1) \tag{5.1}$$

The six next-nearest neighbours are found a distance of a away. Their location can be visualised from the same reference site as that of the nearest neighbours. They are found a distance of a along each of the axis directions at the center of the opposing face. The lattice vectors for the next-nearest neighbours are given by the following.

$$a(\pm 1, 0, 0) \quad a(0, \pm 1, 0) \quad a(0, 0, \pm 1) \tag{5.2}$$

These, along with those of the nearest neighbours, will become useful when calculating the tight-binding dispersion for the fcc lattice in order to calculate the non-interacting density of states.

The dynamical mean field theory is exact in $d = \infty$ but is an approximation when used in finite dimensions. However, power counting arguments (see chapter 4) suggest that the approximation is good when d (or Z - coordination number of the lattice) is large. From the above discussion we find that the coordination number of the fcc lattice is $Z = 12$, this suggests that the DMFT approximation should perform relatively well for calculations performed on the fcc lattice.

5.2.1 The First Brillouin Zone - 1Bz

When working with problems that have lattice symmetry, such as the Hubbard model on the fcc lattice, it is useful to look at the first Brillouin zone (1Bz). This is the set of unique points in reciprocal space that describe the periodicity of the lattice. Any points laying outside of the 1Bz can be mapped back into the 1Bz by shifting it by a reciprocal lattice vector [100]. Thus, by studying properties, such as the magnetic susceptibility, within the 1Bz we are able to know about the behaviour across the full lattice. In order to construct the 1Bz we have to introduce the reciprocal lattice, this has the associated basis vectors $\mathbf{b_1}$, $\mathbf{b_2}$ and $\mathbf{b_3}$ which are formed from the lattice vectors.

$$[\mathbf{b_1}\mathbf{b_2}\mathbf{b_3}]^{\mathrm{T}} = 2\pi\,[\mathbf{a_1}\mathbf{a_2}\mathbf{a_3}]^{-1} \tag{5.3}$$

The basis vectors of the reciprocal lattice for the fcc lattice are found to be $\mathbf{b_1} = \frac{2\pi}{a}(-1,1,1)$, $\mathbf{b_2} = \frac{2\pi}{a}(1,-1,1)$ and $\mathbf{b_3} = \frac{2\pi}{a}(1,1,-1)$ [100]. The reciprocal lattice is then formed in the same way as the corresponding real lattice, by taking integer combinations of the basis vectors to form reciprocal lattice vectors. The reciprocal lattice of the fcc lattice takes the form of a body-centered cubic lattice and is shown in figure 5.3.

We are now in a position to construct the first Brillouin zone. This is achieved by forming perpendicularly bisecting planes between the origin of the reciprocal lattice, known as the Γ point, and each of the reciprocal lattice points in the unit cell. The first Brillouin zone is then the set of points in k-space that one can reach from the lattice origin without crossing one of these planes. In order to help visualise the first Brillouin zone, a notebook was produced using Wolframs Mathematica implementing the above procedure and plotting the result. The 1Bz of the fcc lattice is plotted in figure 5.4a, and takes the form of a truncated octahedron [100]. On the edge of the first Brillouin zone there are a set of high symmetry points, which under symmetry operations are mapped back onto their self, these are labelled in figure 5.4a and are summarised in table 5.1. Waves corresponding

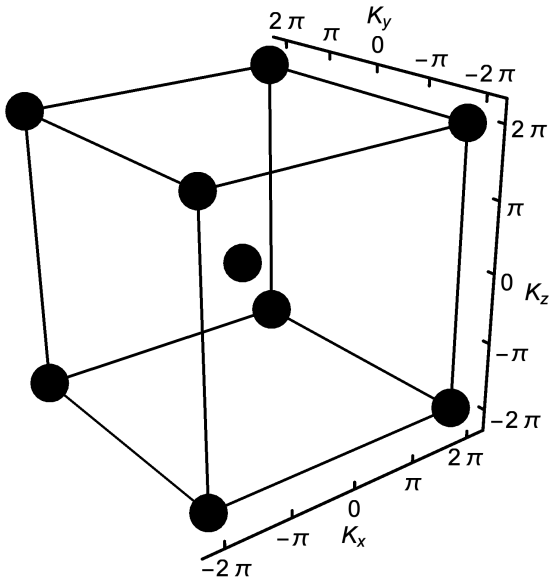

Figure 5.3: Plot of the body-centered cubic reciprocal lattice of face-centered cubic lattice.

	Location	Coordinates
Γ	Brillouin zone center	$(0, 0, 0)$
X	Center of truncated square face	$(0, 2\pi, 0)$
W	Corner of truncated square face	$(\pi, 2\pi, 0)$
K	Middle of edge between two hexagonal faces	$\left(\frac{3\pi}{2}, \frac{3\pi}{2}, 0\right)$
U	Middle of edge between square and hexagonal faces	$\left(\frac{\pi}{2}, 2\pi, \frac{\pi}{2}\right)$
L	Center of hexagonal face	(π, π, π)

Table 5.1: Table of the high symmetry points of the first Brillouin zone of the face-centered cubic lattice.

to these wave vectors form standing waves within the lattice since they lie on the boundary of the first Brillouin zone [99].

When studying quantities such as the magnetic susceptibility in three dimensions one has to sample these functions throughout the first Brillouin zone. This is usually achieved by choosing a path through the 1Bz covering the main high symmetry points. Due to symmetry relations between the points in the Brillouin zone it is only necessary to sample points in a reduced section of the 1Bz. For example we are able to restrict ourself to the eighth of the 1Bz confined by $k_x, k_y, k_z \in [0, 2\pi]$. We then sample this region along a path starting from the center of the 1Bz at the Γ point and

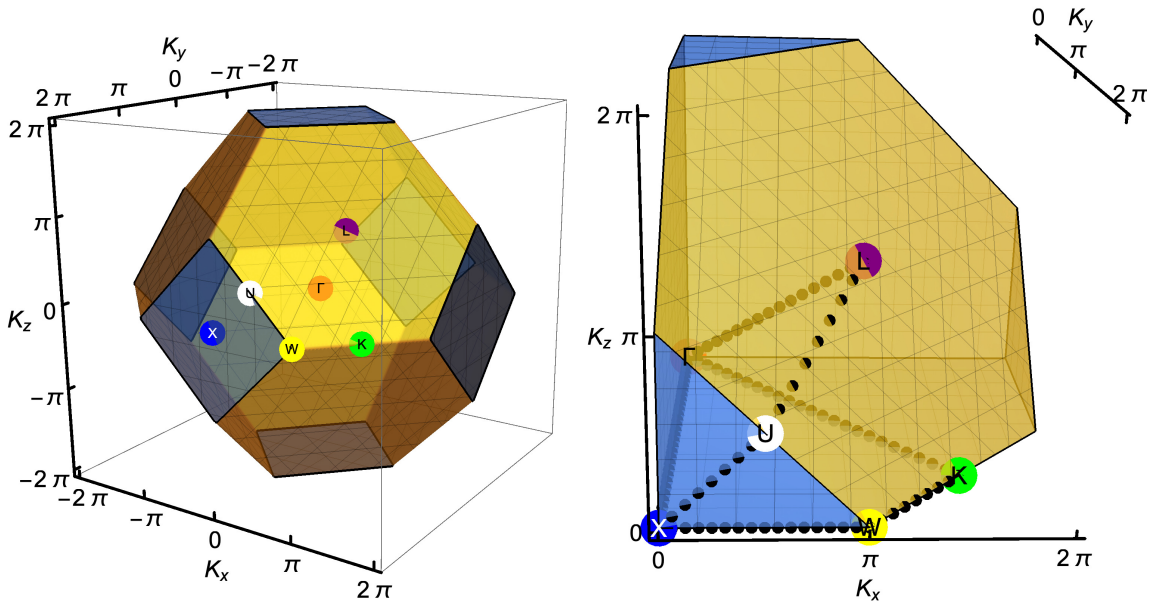

Figure 5.4: **(a)** Plot of the first Brillouin zone of the face-centered cubic lattice, **(b)** zoomed plot of the path sampled through the first Brillouin. Note: coloured points represent high symmetry points.

covering the high symmetry points. In this work the path used was the following:

$$\Gamma \to \mathrm{X} \to \mathrm{W} \to \mathrm{K} \to \Gamma \to \mathrm{X} \to \mathrm{U} \to \mathrm{L} \to \Gamma$$

and can be thought of as consisting of two loops originating from Γ. One taking in X, W and K followed by another involving U and L, the full path is plotted in figure 5.4b. When plotting quantities along this path we treat these two loops separately and plot them against their normalised distance along the loop.

5.2.2 The Non-Interacting Density of States

In order to perform the DMFT calculations we require the non-interacting density of states ($A^0(\epsilon)$) of the lattice for use in equation (4.10). The density of states is given by:

$$A^0(\epsilon) = \sum_{\mathbf{k}\in 1\mathrm{Bz}} \delta(\epsilon - \epsilon_{\mathbf{k}}) \tag{5.4}$$

where $\epsilon_{\mathbf{k}}$ is the tight binding dispersion relation. We can therefore obtain $A^0(\epsilon)$ numerically by binning the dispersion relation according to the energy of a given

$\mathbf{k}$ within the first Brillouin zone. The dispersion relation, is calculated from the tight binding Hamiltonian and takes the form

$$\epsilon_{\mathbf{k}} = -t \sum_{\mathbf{a}\in \mathrm{nn}} \cos\left(\mathbf{k}\cdot\mathbf{a}\right) - t' \sum_{\mathbf{a}\in \mathrm{nnn}} \cos\left(\mathbf{k}\cdot\mathbf{a}\right) \tag{5.5}$$

where $\mathbf{k} = (k_x, k_y, k_z)$ and t, t' are the nearest and next-nearest neighbour hopping parameters. The sum's run over the nearest and next-nearest neighbour lattice vectors. Taking the definitions of the nearest and next-nearest neighbour lattice vectors given in equations (5.1) and (5.2), respectively, the dispersion relation is given by:

$$\begin{aligned}\epsilon_{\mathbf{k}} = &-4t\left(\cos\left(\frac{k_x}{2}\right)\cos\left(\frac{k_y}{2}\right) + \cos\left(\frac{k_x}{2}\right)\cos\left(\frac{k_z}{2}\right) + \cos\left(\frac{k_y}{2}\right)\cos\left(\frac{k_z}{2}\right)\right) \\ &- 2t'(\cos(k_x) + \cos(k_y) + \cos(k_z))\end{aligned} \tag{5.6}$$

as also obtained by Timirgazin et. al. (where the same model was studied using a slave-boson approach with the exception of an opposing sign for the nnn hopping parameter) [36]. From this expression it can be shown that for $0 < t' < \frac{t}{2}$ the band width is $W = 16t + 4t'$ with the lower-edge of the band situated at $\epsilon_l = -12t - 6t'$ and upper-edge of the band at $\epsilon_u = 4t - 2t'$ [9].

We now turn our attention to evaluating equation (5.4) numerically by viewing this equation as a histogram of the values of the dispersion (5.6). In practice this was achieved using a Monte Carlo method where we discretise the bandwidth into N equally spaced "bins", where $\Delta\epsilon$ is the width of the bins [91]. This can be thought of as approximating the delta function by a rectangle of width $\Delta\epsilon$ and a height of one. We then uniformly generate random k-points $\mathbf{k} = \{k_x, k_y, k_z\}$ in the range $k_x, k_y, k_z \in [0, 2\pi]$, evaluate the dispersion, and add one to the tally of the relevant energy bin. Since the full range $[0, 2\pi]$ of the reciprocal lattice unit cell is sampled this procedure samples two times the first Brillouin zone. (This is because the 1Bz shown in Figure 5.4a is fully sampled, along with one eighth of each of the eight neighbouring 1Bz's at the corners of the reciprocal lattice unit cell.) The choice of sampling this way was made in order to maintain the efficiency of the sampling procedure. Once the Monte Carlo simulation is complete we take the histogram generated and divide through by the number of samples taken, the width of the

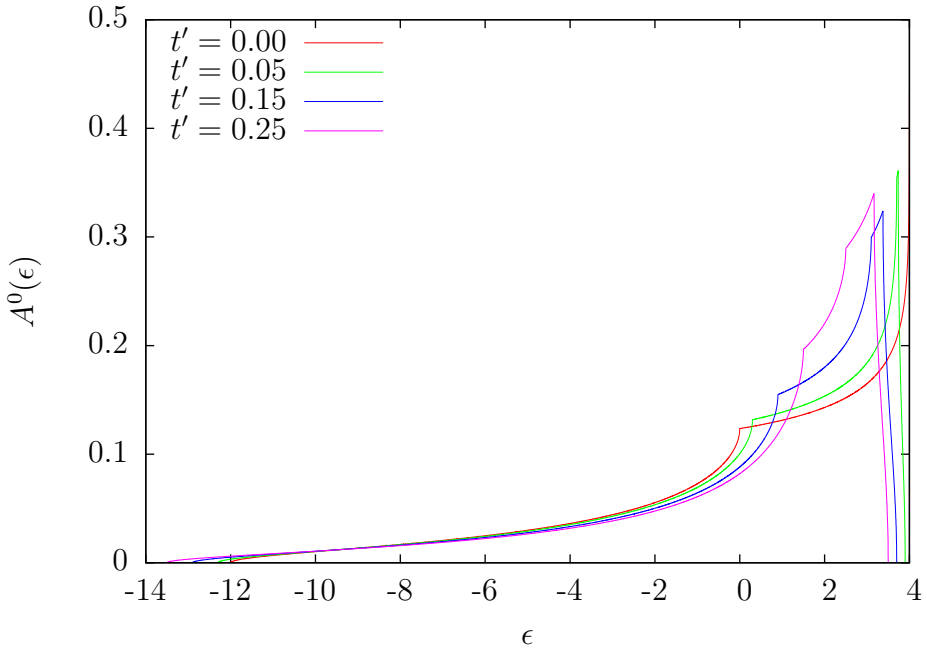

Figure 5.5: Plot of the non-interacting density of states $A^0(\epsilon)$ for the fcc lattice with $t = 1.0$ and various values of t'.

energy bins and divide by two (accounting for the sampling procedure), yielding an estimate of the non-interacting density of states.

The above method was implemented using NVIDIA's CUDA programming language in order to be able to run on GPU's [101]. This choice was made due to the efficiency of GPU's when performing massively parallel tasks such as the Monte Carlo method described above. High-quality random numbers were generated using an implementation of the GPU compatible Mersenne Twister algorithm (MTGP) from NVIDIA's cuRAND library [102, 103].

An equivalent CPU based implementation was also written making use of the BOOST libraries and MPI for parallelism [104]. It was found that the GPU implementation achieves over an order of magnitude speed up over the CPU based implementation running on 16 cores. The GPU code running on a single GTX 970Ti GPU was able to achieve $\sim 1.5 \times 10^{13}$ samples in approximately 12 hours. This is a dramatic speed up over the CPU implementation and allows for much more accurate results to be obtained in the same computation time. It is also worth noting that the GPU algorithm could easily achieve further parallelism by

adding more GPU's with little modifications to the code. However, this was not pursued as we did not have access to the hardware and the current implementation is more than sufficient as we will see.

To demonstrate the effect of the nearest neighbour hopping parameter t' on the density of states, we fixed $t = 1$ and calculated the density of states for various values of t' from 0 to $\frac{t}{4}$. The resulting densities of states are shown in figure 5.5. For $t' = 0$ we obtain the density of states with only nearest-neighbour hopping; this is also shown in a paper by Arsenault et. al. and agrees well with the DOS obtained using the method above [91]. The $t' = 0$ DOS features a strong divergence at the upper band edge, however, this is over a rather narrow range and does not carry much weight. As we increase the value of t' we find more and more weight is shifted towards the upper edge of the band, this is favourable for stabilising ferromagnetism. We find that the divergence is no longer situated directly at the upper band edge but is found just before: this is in line with what was found by Vollhardt et. al. (for an opposingly signed hopping) [94, 96]. From the above we are able to see that we can push spectral weight towards the band edge by increasing the next-nearest-neighbour hopping relative to the nearest-neighbour hopping.

In the next section we will present the results of the DMFT calculations, however, before this we will discuss an important point about how the density of states effects the DMFT results. It was found that the density of states had to be calculated very accurately in order to get the correct decay behaviour in the Legendre Green's functions for calculations performed at high chemical potentials. This is largely due to the numerical calculation of the Hilbert transform (4.10) during the DMFT calculation being rather numerically sensitive. If it is not performed accurately enough then non-analytic behaviour can be introduced into the Green's functions. We found that if the number of bins used in the DOS calculation is too small then all of the features are not well represented and the large l behaviour of G_l does not decay but oscillates around zero. However, if too many bins are used then the statistics for each bin suffers and the error becomes larger for each point leading again to bad high l behaviour in the Legendre Green's function. Thus, there has to

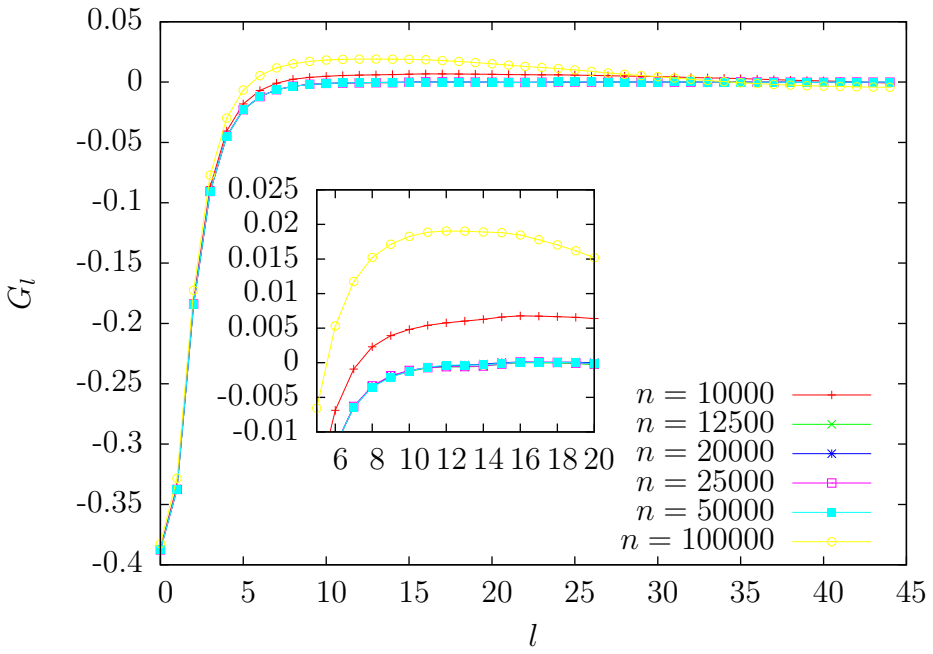

Figure 5.6: A plot of the Legendre Green's function G_l for DMFT calculations performed at high chemical potential using the non-interacting density of states calculated on differing grids. Note: insert is zoomed in around zero to better display decay behaviour.

be a balance between obtaining good statistics for each bin and having a sufficiently fine enough grid in order to represent all features of the density of states well.

This is demonstrated in Figure 5.6, where the Legendre Green's functions are shown for DMFT calculations that have been performed with $t = 1$, $t' = \frac{t}{2}$, $U = 21$ and $\mu = 25$ leading to a large filling of $n \sim 1.9$. For $n = 10000$ we find that the coefficients of the Legendre Green's function do not decay towards zero as should be the case (see section 3.1.4). We also note that the error on the coefficients can be seen to be much smaller than the distance to zero and therefore this is a structural deviation away from the correct decay behaviour. We believe this is due to the grid not being accurate enough to well represent the sharp features present in the density of states. If we increase the number of bins further we find G_l obtains the correct decay behaviour and the coefficients decay to zero for large l. We also find a wide range of bin numbers leading to essentially the same results within the statistical error of the measurements. However, increasing the number of bins further to $n = 100000$ leads to the same bad decay behaviour that was observed for

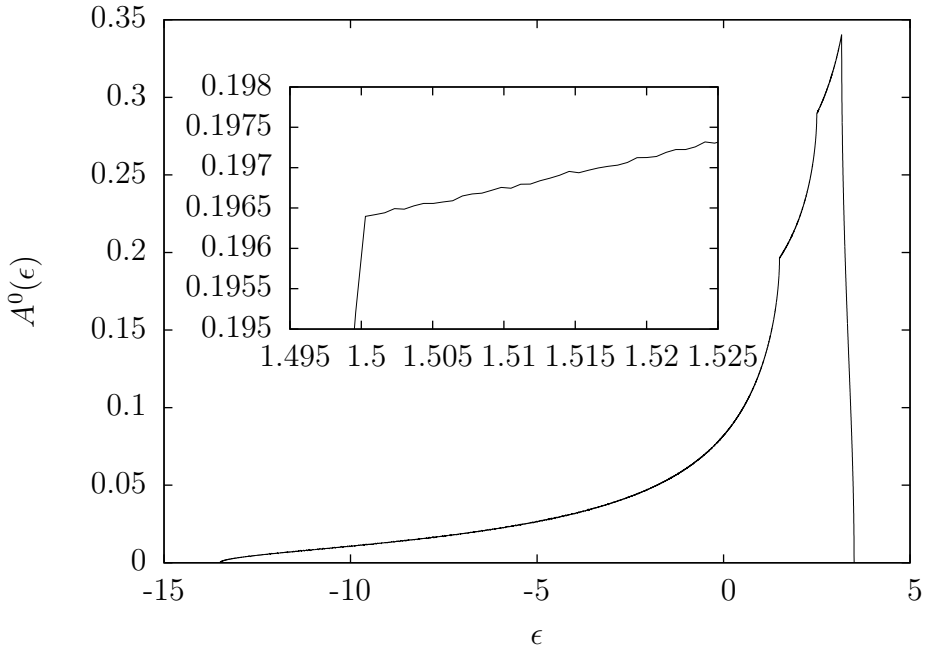

Figure 5.7: Plot of the non-interacting density of states $A^0(\epsilon)$ for the fcc lattice with $t = 1.0$ and $t' = 0.25$. Insert: zoomed in plot around the kink at $\epsilon = 1.5$.

lower bin numbers due to bad statistics in the sampling procedure.

For the calculations in the latter half of this thesis it was chosen to use the density of states with $n = 25000$ as this is situated in the middle of the range of bins that display the correct decay behaviour at a high chemical potential.

A plot of the density of states used is shown in figure 5.7 along with a zoomed inset of the kink at $\epsilon = 1.5$. This shows how accurately, the density of states has to be determined, in order to obtain accurate results with the correct decay behaviour of the Legendre Green's functions, and hence the importance of the GPU implementation of the sampling procedure.

5.3 Magnetism In The Hubbard Model On The fcc Lattice

Studying metallic ferromagnetism has proven to be a formidable task. This is because ferromagnetism arises at intermediate to strong interaction strengths, thus requiring the use of non-perturbative methods [95]. This means there are very few exact results, and those that are known are usually obtained in various limits or

low dimensions where the theoretical framework at our disposal is much stronger. One notable result is that of Nagaoka [105] which proves (on various lattices) that ferromagnetism is stable in the Hubbard model for some range of the hopping parameter t. However, all of these results are obtained at $U = \infty$ and very specific fillings, thus, providing a somewhat idealised and restricted case. For example, it was shown that for one electron more than half-filling the ground state of the Hubbard model on the fcc lattice is the fully polarised ferromagnetic state. While for the simple cubic and body-centered cubic lattices the ferromagnetic state is shown to be stable for one electron fewer than half-filling.

The dynamical mean field theory (see chapter 4) has been used by Ulmke to show that ferromagnetism is stable in the Hubbard model with next-nearest neighbour hopping on the fcc lattice in the realistic case of $d = 3$ as well as the lattices generalisation to $d = \infty$ (where the DMFT approach used is exact) [9, 106]. Herrmann and Nolting have also reported extended regions of ferromagnetism on the fcc lattice in $d = 3$ while investigating the effect of the lattice structure on the stability of a ferromagnetic state by means of a spectral density approach [34]. They find a ferromagnetic state arises for all fillings in the range $1 \leq n \leq 2$ and a paramagnetic state for all other fillings.

Igoshev et. al. have also studied the ground state magnetic phase diagram of the fcc Hubbard model, as well as other lattices, using both the Hartree-Fock approximation and a slave boson approach [35]. This allowed them to study these models for a wide range of U and different values of nearest and next-nearest neighbour hopping parameters. They were also able to take into account non-commensurate magnetic states, such as spiral magnetic states. They report a magnetic phase diagram of the fcc Hubbard model for the full range of fillings showing large regions of ferromagnetism at fillings above one for $t' = 0.3t$ and reporting the structure of the AFM region found around and below half-filling. For the AFM region they report the W point AFM state to be the ground state for fillings slightly below and at half-filling, with regions of phase separation between the paramagnetic state and a non-commensurate state either side of this. A visualisation

of the W point AFM state will be presented later in this work along with other relevant magnetic states. The work of Igoshev et. al. has subsequently been built upon by Timirgazin et. al. who use a slave boson approach but allow for further non-collinear AFM states as well as investigating the Mott transition at half-filling [36].

We wish to study the model and determine the magnetic phase diagram at fixed filling, however, as seen in chapter 4, DMFT calculations are performed at a fixed chemical potential. Thus, the required chemical potential in order to fix the filling to a specific value is a priori not known. In order to perform the calculation at fixed filling the DMFT code has been wrapped within another code written to find the chemical potential required to fix the filling to the desired value. This is achieved using a bisection algorithm where the desired filling is treated as the 'root' of the following function.

$$f(\mu) = n_{DMFT}(\mu) - n_{fix} \tag{5.7}$$

A range for the chemical potential $\mu \in [a, b]$ and the desired filling n_{fix} are supplied to the code, a DMFT calculation is performed at each of the endpoints to check that n_{fix} does indeed lie in the interval. The chemical potential is then adjusted, a new DMFT calculation is performed and the process is iterated until the filling has been fixed to the chosen value within some tolerance. In order to speed up the convergence of the DMFT calculation at each iteration, the converged results of the previous iteration was used as a starting point for the input non-interacting Green's function. This helps the DMFT calculations to converge faster as the initial guess should not be far from the final solution provided the change in chemical potential is not too large.

The hopping parameters were chosen to be $t = 1$, $t' = \frac{t}{4}$, meaning we make use of the non-interacting density of state shown in figure 5.7. The Coulomb interaction was set to $U = 21$. This choice of parameters allows for a close comparison to the previous study of Ulmke where similar values of the parameters were used [9].

In the following sections we cover the different regions and phases that were found within the model described above. We start by covering the ferromagnetic region that is found for fillings $n > 1$ (see section 5.4), then the anti-ferromagnetic

region for fillings $n \sim 1$ and below (see section 5.5). For each of these phases we discuss the divergences seen in susceptibility, their behaviour as the filling and temperature is changed and finally the fitting of a linear function in order to extract the critical temperatures. We go on to discuss the resulting phase diagrams, their comparison to previous results, and show single-particle spectra obtained through analytic continuation using the maximum entropy method.

5.4 Ferromagnetic Instability

In order to investigate the ferromagnetic instability of we model we wish to determine the phase diagram in terms of n and T. This is achieved through calculating the magnetic susceptibility at the Γ point for various temperatures over a range of fillings. Using this data we can then study Curie-plots of $\frac{1}{\chi}$ vs. T and fit linear functions to the data in order to extract an estimate of the critical temperatures for a range of fillings.

To this end we first perform bisection calculations in order to fix the fillings such that we obtain DMFT solutions for fixed n and T across the region where we expect ferromagnetism. These calculations were performed for fillings in the range $n \in [1.1, 1.9]$ and over inverse temperatures of $\beta \in [1, 10]$ ($T \in [0.1, 1]$). Once the DMFT calculations were converged and the fillings were fixed, a second calculation was performed in order to obtain the two-particle Green's functions, from this we are able to calculate the magnetic susceptibility. The two-particle Green's functions are only calculated once the DMFT calculations have converged and the filling has been fixed due to their calculation being a very computationally expensive procedure.

Like Ulmke, we find that the susceptibility diverges at the Γ point over a range of fillings $n \in [1.1, 1.9]$ indicating the presence of a ferromagnetic region [9]. However, before we turn our attention to the magnetic susceptibility we first examine some DMFT results for a filling in the middle of this region where the ferromagnetic instability is later shown to be strongest (see section 5.4.2).

5.4.1 DMFT Results

Figure 5.8 shows some of the DMFT results for a filling of $n = 1.3$ at various temperatures above the transition. The Legendre Green's function is shown in figure 5.8a, we find that G_l has completely decayed by a Legendre polynomial order of 25. We also find that as the temperature is lowered most of the change between the results is largely confined to the Legendre polynomials of low order. This shows that all of the coefficients with large weight have been captured within the chosen cut-off. The cut-off also proves to be relatively independent of temperature over this range of temperatures studied here. Thus, we are able to accurately represent the single-particle Green's function in imaginary frequency when transformed from the Legendre representation (eq. (3.26)), as shown in figures 5.8d and 5.8e. As the temperature varies we find that most of the change in the single-particle Green's function is largely confined to low-frequency with the high-frequency tail remaining relatively independent of temperature. Indeed it looks as if when the temperature is change one is sampling the same function at the Matsubara frequencies relevant for that temperature.

Figures 5.8b and 5.8c show the real and imaginary parts of the self-energies for the same four calculations. We find that at high-frequency they have again all converged to very similar results. This is what we would expect given the form of the high-frequency tail in equation (3.45) where the behaviour is set by the values of U and $\langle n \rangle$ which here are fixed. By looking at the low-frequency behaviour of the self-energy we are also able to determine if these solutions are metallic or insulating in character. This is due to the relationship between the low-frequency behaviour of the self-energy and the quasiparticle weight (see section 4.4). We find that at all temperatures shown here the low-frequency part of the imaginary part of the self-energy tends towards zero. This indicates a metallic solution as is confirmed later through maximum entropy calculations (see section 5.4.3).

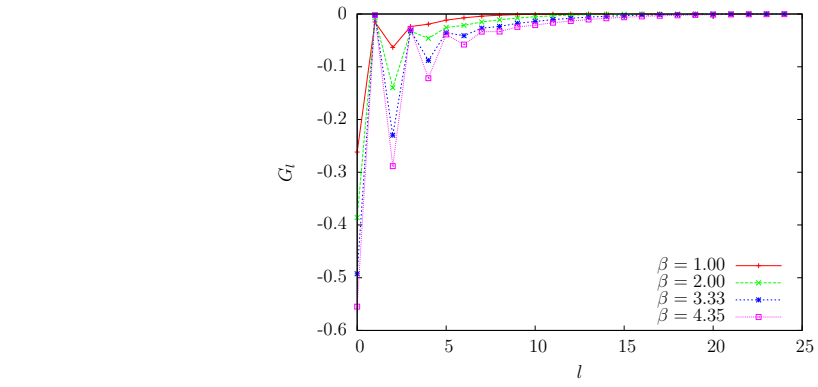

(a) Legendre

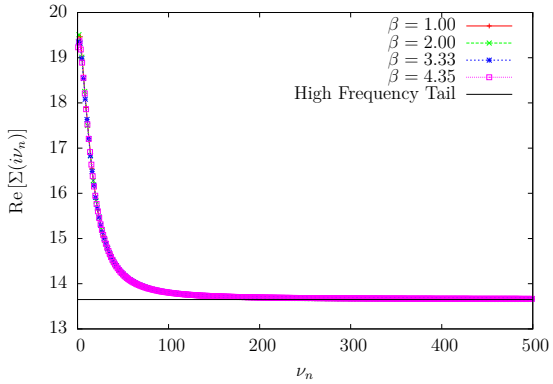

(b) Real

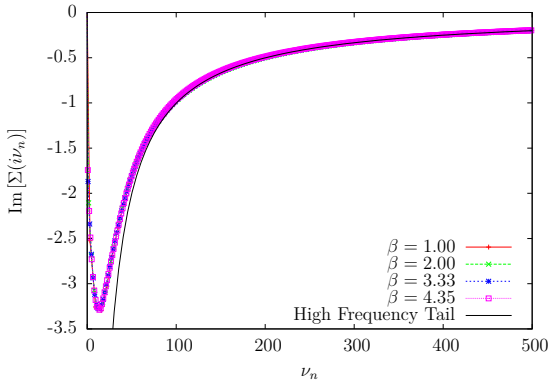

(c) Imaginary

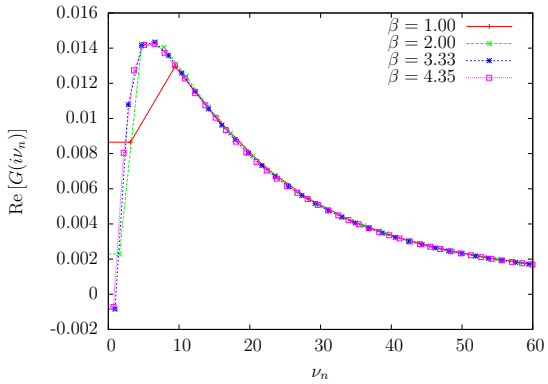

(d) Real

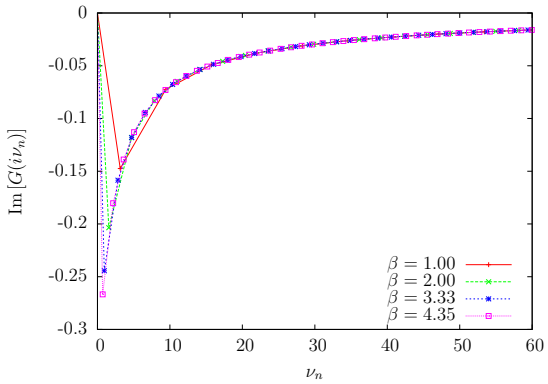

(e) Imaginary

Figure 5.8: Plots of G_l (top), the real and imaginary parts of the self-energy (middle) and imaginary frequency Green's function (bottom) at various temperatures above the ferromagnetic transition for a filling of $n = 1.3$.

5.4.2 Magnetic Susceptibility and Phase Diagram

We now turn our attention to the magnetic susceptibility $\chi^m(\mathbf{q}, i\omega_n)$. We are only interested in the static susceptibility ($\omega_m = 0$) this means we are able to plot the

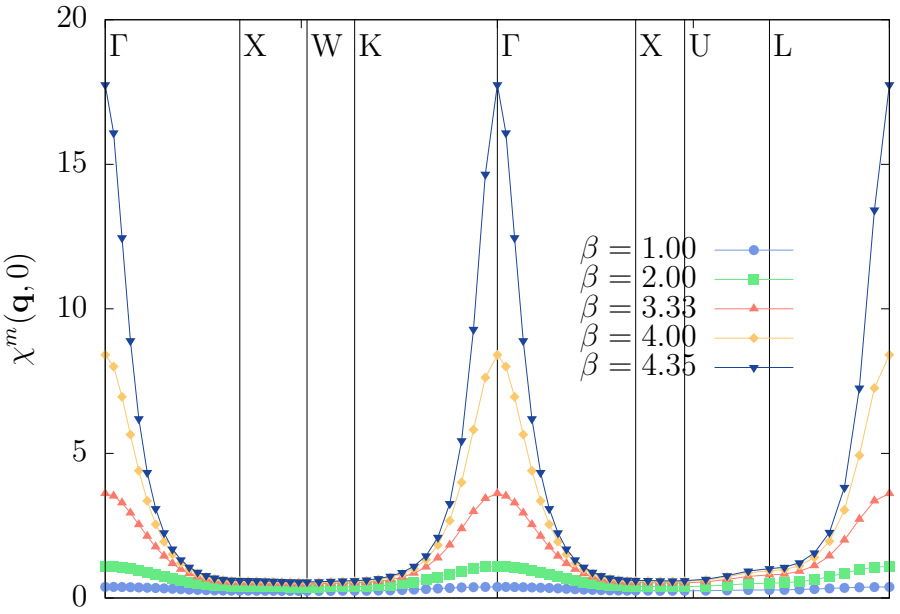

Figure 5.9: A plot of the magnetic susceptibility $\chi^m(\mathbf{q}, 0)$ along the high symmetry path of the 1Bz for a fixed filling of $n = 1.3$ across a temperature range leading up to the transition.

susceptibility as only a function of the field vector. However, this is still a three dimensional object and we cannot directly plot the whole susceptibility. Thus, we plot the susceptibility along a path covering the high symmetry points of the first Brillouin zone (see section 5.2). We plot this path against the normalised distance along each of the two loops the full path consists of. As discussed previously, for a ferromagnetic state we would expect the susceptibility to diverge at the Γ point which corresponds to a uniform field with field vector $\mathbf{q} = \{0, 0, 0\}$.

Figure 5.9 shows the susceptibility along this path for a filling of $n = 1.3$ at various temperatures. We can see that there is a peak in the susceptibility at the Γ point for all temperatures. When the temperature is lowered the peak grows strongly indicating an instability towards a ferromagnetic phase. There are no signs of instabilities due to fields of other field vectors.

This ferromagnetic instability arises over a range of fillings. Figure 5.10 shows the susceptibility at a fixed temperature of $\beta = 3.33$ ($T \sim 0.3$) for fillings between $n = 1.1$ and 1.8. From figure 5.10b we see that the divergence is strongest around

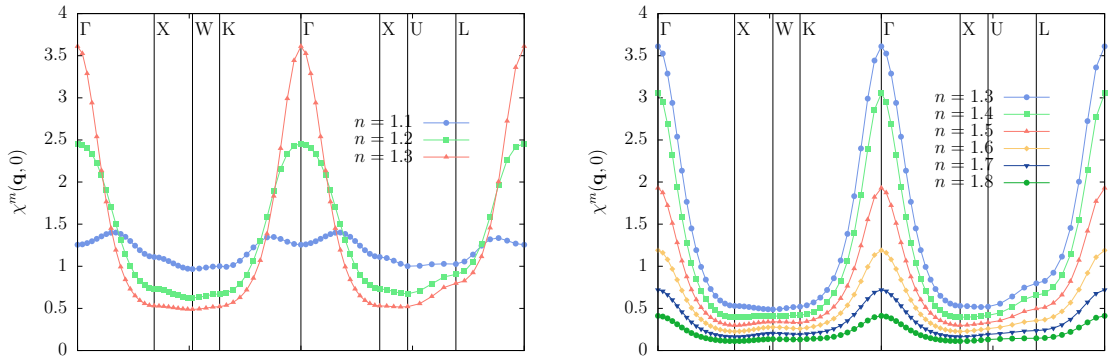

(a) $n \leq 1.3$ **(b)** $n \geq 1.3$

Figure 5.10: Plots of the magnetic susceptibility $\chi^m(\mathbf{q}, 0)$ along the high symmetry path of the 1Bz at a fixed temperature of $\beta = 3.33$ ($T = 0.3$) for a range of fillings.

$n = 1.3$ and then slowly loses strength as the filling is increase towards 2. This falls in line with the results of Bei der Kellen et. al. who studied the fcc lattice using an effective medium approach and found the Curie temperature to peak between $n = 1.3$ and 1.4 for large values of U [107]. The divergence drops off much more rapidly as the filling is lowered towards half-filling and it essentially disappears by a filling of $n = 1.1$. This is to be expected as around half-filling we would expect anti-ferromagnetism (see section 5.5): this is somewhat preempted here by increased susceptibility values around the X, W and K points relative to the Γ point showing an increased susceptibility towards anti-ferromagnetic field vectors. From the above results we would expect the ferromagnetic phase boundary to be peaked around a filling $n \sim 1.3$, to slowly drop towards higher fillings and to drop off rapidly as half-filling is approached.

In order to extract a value of the critical temperature from the susceptibility data we plot $\frac{1}{\chi^m(\Gamma,0)}$ vs. T, forming the familiar Curie-Weiss plot. From this we are able to calculate the critical temperature T_c as the x-intercept. This is achieved by fitting a power law to the data closest to the transition. This takes the form

$$\frac{1}{\chi^m(\Gamma, 0)} \sim \left(\frac{T - T_c}{T_c}\right)^{\gamma} \tag{5.8}$$

where T_c is the critical temperature and γ is the critical exponent describing how the susceptibility diverges as the transition is approached from above [82]. At high

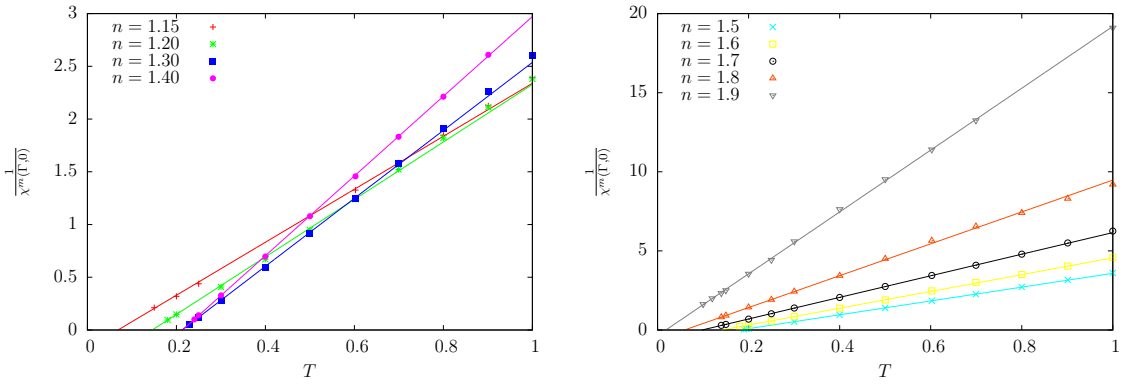

(a) $n \leq 1.4$ **(b)** $n > 1.4$

Figure 5.11: Plots of $\frac{1}{\chi^m(\Gamma,0)}$ Vs. T for a range of fillings along with linear fits to the data.

temperatures away from the transition we would expect the susceptibility to diverge linearly, however, closer to the transition this can vary. This was investigated and susceptibility data points were obtained close to the transition as can be seen in figure 5.11. We find that there is no evidence to suggest that the approach to the transition is anything but linear. Thus, we set $\gamma = 1$ and fit linear models to the data, these are shown in figure 5.11.

We find that all the datasets fit the linear form very well: the table 5.2 summarises the critical temperatures obtained as well as estimates of the errors. The linear trend displayed here for the susceptibility data corresponds to the model having a critical exponent $\gamma = 1$, indicating mean field critical exponents as one would expect from the DMFT approach used here [82].

In order to get a handle on the errors of the critical temperatures we produced a 95% confidence interval for each of the fits. We then found the point at which the upper and lower bands of this interval intercept the x-axis producing estimates of the errors in the critical temperatures. The estimates of the errors found are shown in table 5.2 alongside the critical temperatures. We find that all of the errors are relatively small and on the order of $\sim 10^{-3}$ at most shrinking to $\sim 10^{-4}$ for larger critical temperatures where data is more readily available close to the transition.

Taking the critical temperatures and plotting them as a function of the filling we are able to plot the phase boundary for the ferromagnetic region. This is shown in

n	T_c	Upper Bound	Lower Bound
1.15	0.06875	0.00507	0.00514
1.20	0.14565	0.00178	0.00162
1.30	0.21261	0.00084	0.00056
1.40	0.21352	0.00072	0.00048
1.50	0.17973	0.00030	0.00010
1.60	0.14040	0.00102	0.00098
1.70	0.09766	0.00116	0.00084
1.80	0.05903	0.00278	0.00262
1.90	0.01826	0.00295	0.00286

Table 5.2: Table of critical temperatures predicted from linear fits to the susceptibility data along with errors in T_c predicted from the 95% confidence interval of the fit.

figure 5.12 alongside data which has been reproduced from the study by Ulmke [9].

We find the phase boundary is strongly peaked between $n = 1.3$ and 1.4 which was also found to be the case in the DMFT study of Ulmke [9]. This result also agrees with the findings of Herrmann et. al. where they found the Curie temperature takes a maximal value around a filling of $n = 1.4$ [34]. We also find that there is both an upper and lower critical density between which we observe ferromagnetism. Note however, that the solid line in figure 5.12 is a spline fit to the data points and is just a guide to the eye. The phase boundary determined as part of this work is in good agreement with the previous study by Ulmke [9]. This study was performed on the same model (with a slightly higher coulomb interaction, ($U \sim 21.1$)) using DMFT and the older, less accurate, Hirsch-Fey quantum Monte Carlo impurity solver. They were also not able to make use of the new Legendre representation for more accurate measurements of the Green's functions and magnetic susceptibility used within this work [47]. (Note that, in the Ulmke study, they have used the opposing sign for the hopping t, which results in a switching of electrons and holes. Thus, the fillings in the paper n are related to the fillings here n' through $n' = 2 - n$.)

The errors determined from the linear fits to the data are shown on the phase diagram, however, in most cases they are smaller or of the same size as the markers used. The main source of the larger errors on phase boundary reproduced from the Ulmke paper is the extrapolation of the results to take into account time

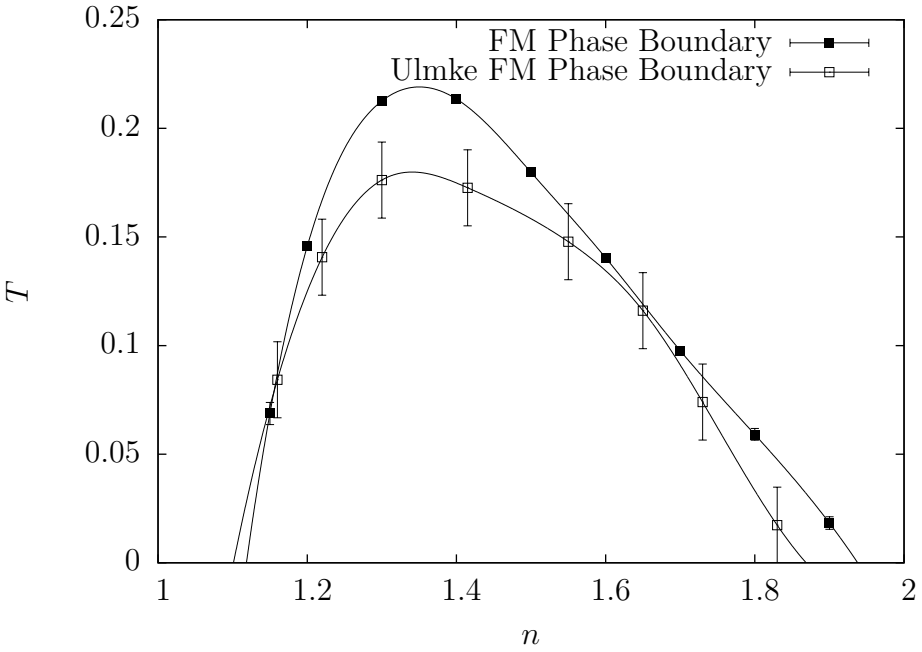

Figure 5.12: A plot of the phase boundary of the ferromagnetic region formed from T_c values obtained in the fits show in figure 5.11. Also shown are data for a similar model studied by Ulmke reproduced from [9]. Note: error bars are plotted however most are the same size as the marker or smaller, also solid lines are spline fits to the data and are shown as guides to the eye.

discretisation errors present in the Hirsch-Fey impurity solver [106]. This is not something that is present in the continuous-time QMC method used in this work allowing for a much more accurate determination of the phase boundary.

Ulmke found a finite critical lower density below which there is no ferromagnetism: this would correspond to a finite upper critical density in this work, which is indeed what appears to be the case in our results. However, from the current work it can not be ruled out that the ferromagnetic phase does not persist to full occupancy. This is because, for calculations at very high occupancy, the Monte Carlo move acceptance rates are very low leading to bad statistics. This makes it hard to obtain accurate results in this region of the phase diagram where we would need to be able to determine very small critical temperatures. Note that a study by Igoshev et. al. of the ground state phase diagram of the fcc Hubbard model using both Hartree-Fock and slave boson methods also found a finite upper critical density [35].

The magnetisation below the phase boundary was also calculated for two fillings,

$n = 1.3$ and 1.5. The data are shown in figure 5.13. Figure 5.13a, shows the magnetisation alongside the corresponding susceptibility for these fillings. The solid lines through the susceptibility are the linear fits from above (eq (5.8)) while the solid line through the magnetisation data is a power law fit to the magnetisation closest to the transition. As can be seen we find very good agreement between the magnetisation and susceptibility data, supporting the accuracy of the phase boundary and confirming the transition temperature from below. The critical temperatures from each fit are in good agreement with each other. The critical exponent of the fits to the magnetisation takes a value of $\sim \frac{1}{2}$. This, along with the linear behaviour of the susceptibility are consistent with the critical exponents of the mean field universality class [82].

Figure 5.13b shows the same power law fits close to the transition along with a fit of a Brillouin function to the magnetisation at low temperature. The data fit the function well showing that the low temperature magnetisation data are consistent with a fully saturated ferromagnetic state at $T = 0$. This was also found to be the case for the $d = \infty$ generalisation of the fcc lattice studied by Ulmke [9]. However, in this study magnetisation data was not calculated close to the transition and only a Brillouin function was fitted.

5.4.3 Analytic Continuation

In order to determine if the ferromagnetic states found in the above section are indeed metallic and therefore examples of metallic/band ferromagnetism, we have calculated the single-particle spectrum using the maximum entropy method (see section 3.2). However, before we examine the results below the transition it makes sense to examine some paramagnetic solutions from above the transition. Figure 5.14a shows how the spectra vary as the temperature is lowered for a fixed filling of $n = 1.3$. All the spectra here correspond to a paramagnetic metallic state, clearly indicated by the finite density of states at the Fermi-level. We can also identify the upper and lower Hubbard bands centred on $-\mu$ and $-\mu + U$. These remain relatively fixed as we lower the temperature due to only small changes in

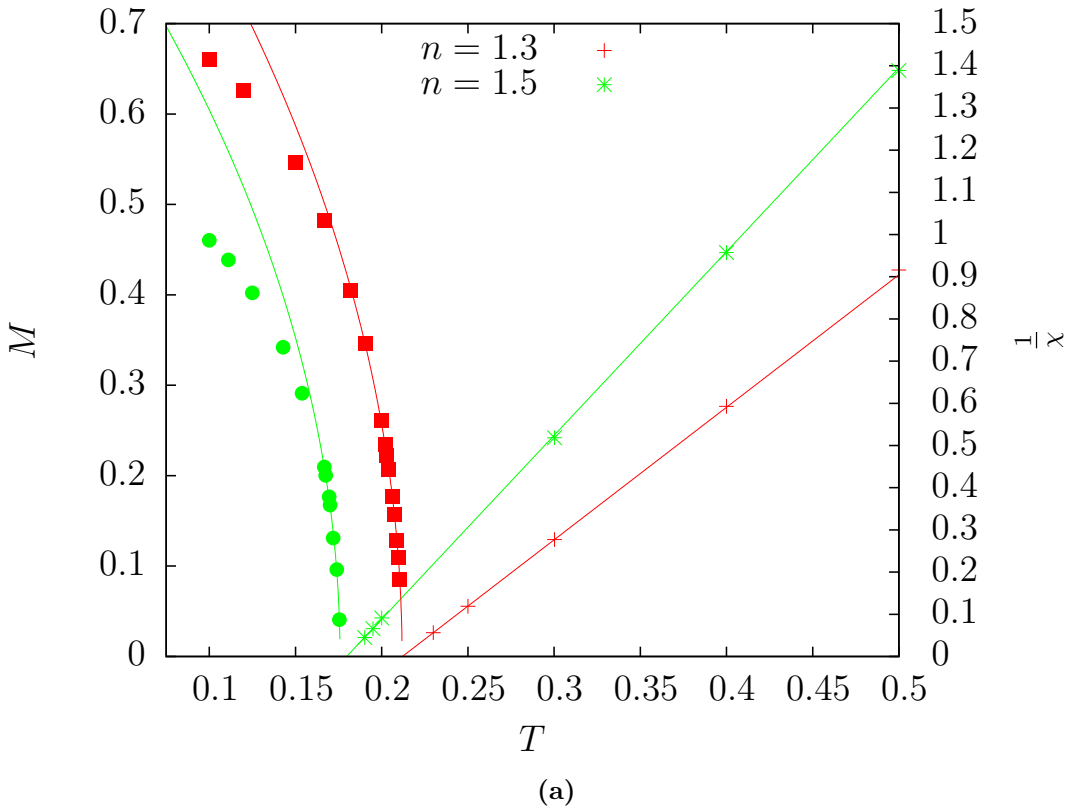

(a)

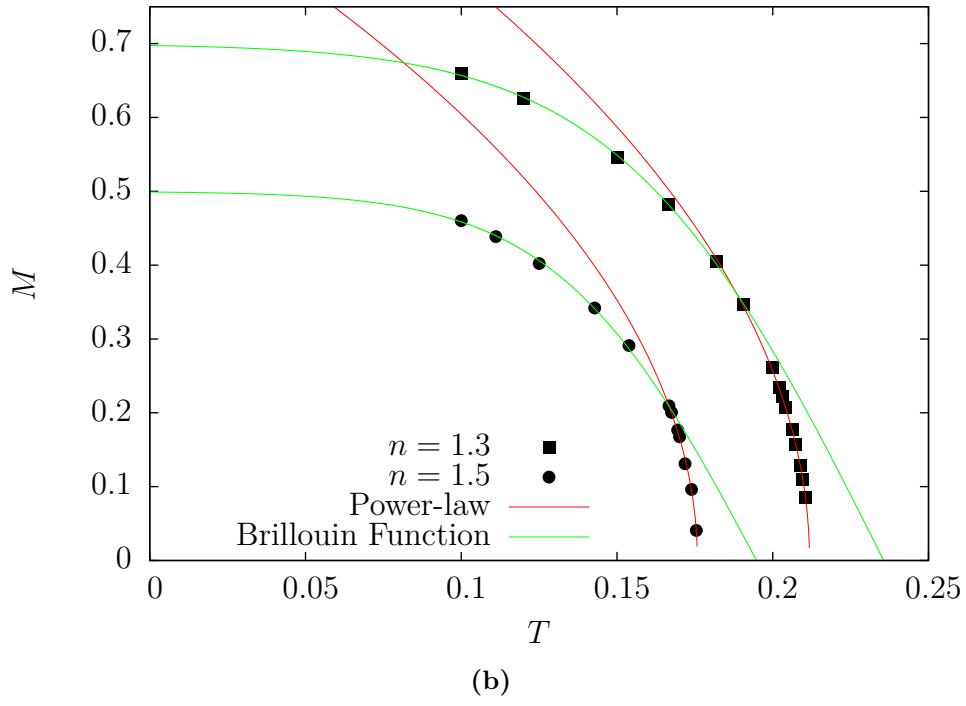

(b)

Figure 5.13: Plots of the magnetisation and magnetic susceptibility. Top: plot of $\frac{1}{\chi}$ Vs. T and M Vs. T (notice separate y-axes), solid lines are power-law fits to the magnetisation and a linear fit to the susceptibility. Bottom: plot of M Vs. T for fixed filling, solid lines are power-law fit to data close to the transition (red) and Brillouin function fit to low T data (green).

the chemical potential being required to fix the filling. However, as the temperature is lowered the features of the spectrum become more defined as they feel less of the effects of temperature broadening. This is particularly strong around the Fermi-level at which we see a quasiparticle peak at the lower temperatures that is washed out at higher temperatures [10, 91, 108].

It is also interesting to also consider the effects of changing the filling at fixed temperature: this is shown in figure 5.14b for $T \sim 0.6$ ($\beta = 1.66$). As the chemical potential is increased and the fillings are raised we see the Hubbard bands shifting to lower energies while maintaining their spacing at U. We also find the lower Hubbard band becomes broadened and the upper Hubbard band becomes more defined. The thinning of the upper Hubbard band can be understood in simple terms by noting that there are fewer available singly occupied sites for an electron to hop to. While the lower Hubbard band is broadened due to the higher availability of doubly occupied sites for a hole to hop to. We also find that as the filling approaches full double occupancy the spectrum starts to approach a shifted version of the non-interacting density of states. This happens because at very high fillings there is very little availability of unoccupied states, while there is a high availability of singly occupied states. Thus, almost all of the states available involve an added electron having to pay the energy cost of the Coulomb interaction. This situation however is the same as that of a non-interacting model with a shifted energy level, resulting in the spectrum tending towards that of the non-interacting density of states.

We now turn our attention to how the spectra change as we cross the transition. Since the spin symmetry is broken and we have a ferromagnetic state, we now have to consider the spin-resolved single-particle spectra. Plots of the majority and minority spin spectra are shown in figure 5.15 for solutions obtained at a filling of $n = 1.3$.

The first thing of note is that all of the spectra have a finite density of states at the Fermi-level and therefore are metallic, confirming that the ferromagnetism here is itinerant as found in the previous study by Ulmke [9]. We also observe that rather than a shifting of the bands according to Um with no redistribution of spectral weight, as predicted by the naive Stoner treatment of the Hubbard

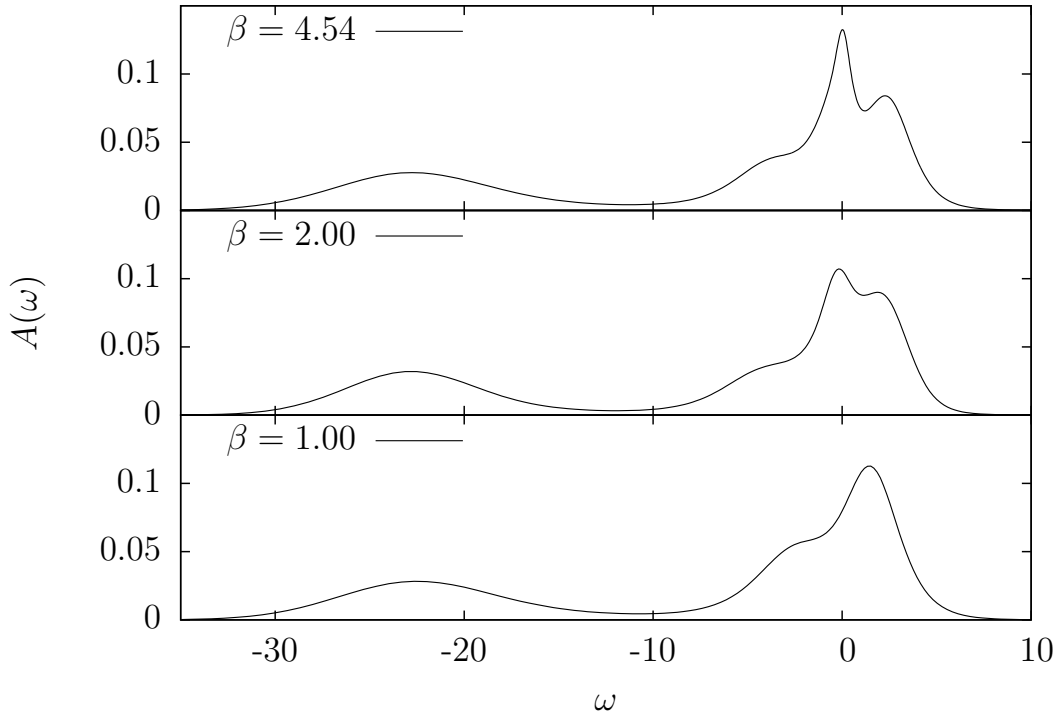

(a) Fixed filling

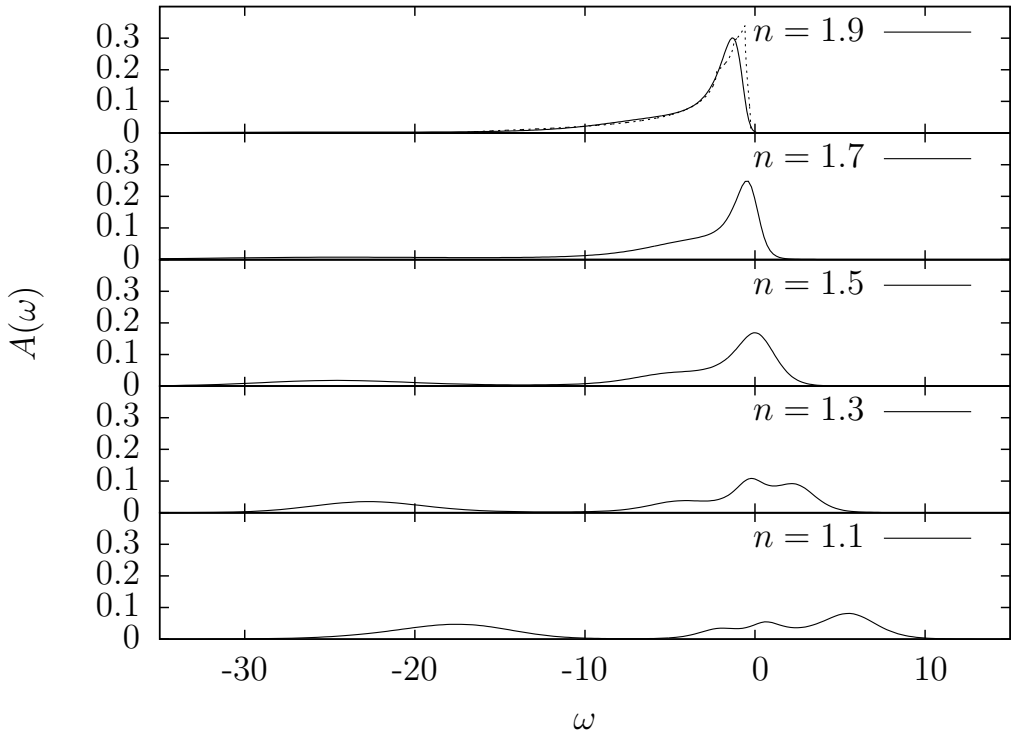

(b) Fixed temperature

Figure 5.14: Plots showing how the single-particle spectra $A(\omega)$ for paramagnetic solutions varies with filling and temperature: **(a)** fixed $n = 1.3$ varying temperature down towards the transition, **(b)** fixed $T \sim 0.6$ ($\beta = 1.66$) varying n. Note dashed line in $n = 1.9$ plot is the shifted non-interacting density of states.

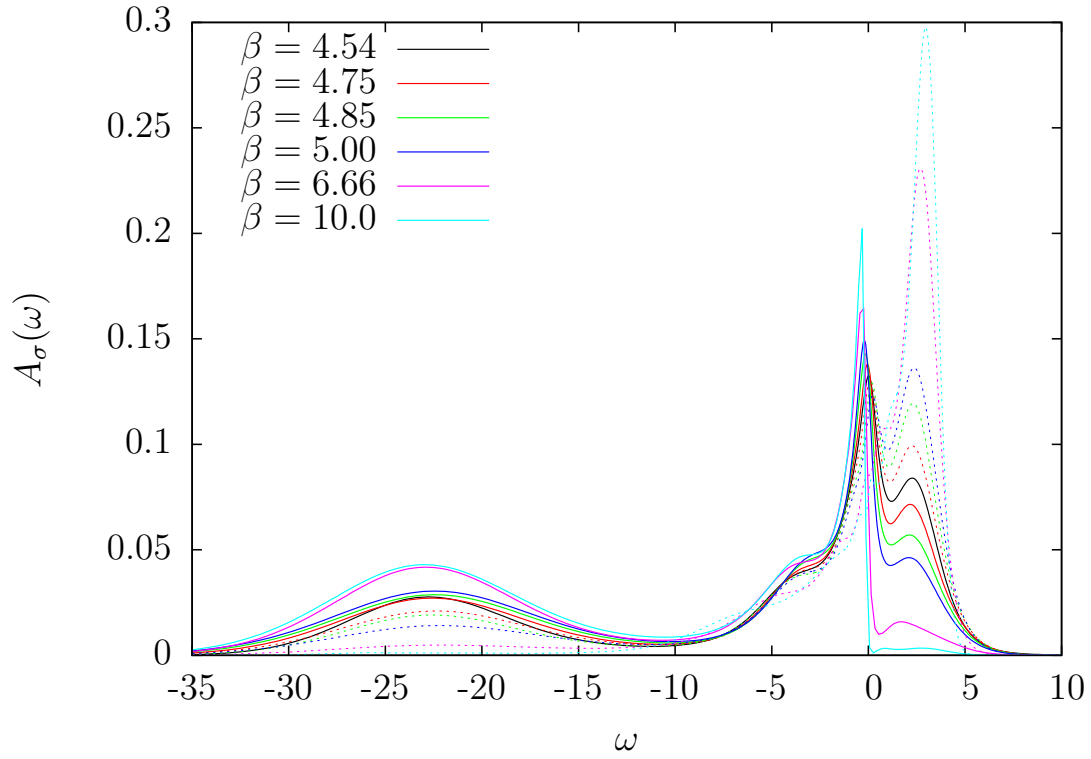

(a) Both Spins

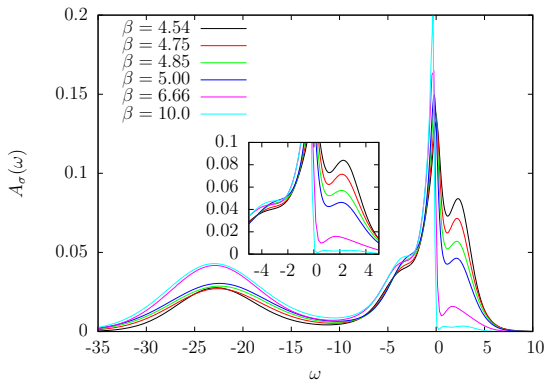

(b) Majority Spin

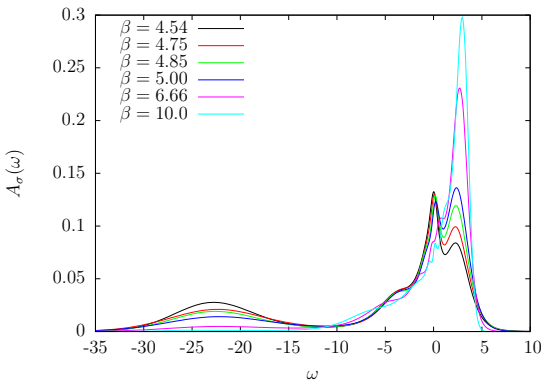

(c) Minority Spin

Figure 5.15: Plot of $A(\omega)$ Vs. ω for magnetic solutions at $n = 1.3$. Note: black solid line in all plots is the paramagnetic spectra at $\beta = 4.54$ just above the transition and is shown as a reference. Note different scale in **(b)**. Inset shows the region around the Fermi-level.

model [8]. We find only a small shift in the bands with a large redistribution of spectral weight which grows as the magnetisation increases. This was also found in the previous study by Nolting et. al. using a spectral density approach [8] and is also in line with the findings of Ulmke where he presented spectra for the $d = \infty$ generalisation of the fcc Hubbard model [9]. We find that the majority spin spectra have a redistribution of spectral weight from above the Fermi-level to below, and the converse for the minority spin. This redistribution in the case of the majority spin is due to the lower availability of unoccupied majority spin states as the magnetisation grows. While for the minority spin case, weight is transferred above the Fermi-level due to the higher availability of unoccupied states.

Once we reach an almost fully-saturated state the majority spin spectra holds essentially all its weight below the Fermi-level, while the minority spin spectra hold most of its weight above the Fermi-level. The minority spin spectra, at low temperature where the state is almost fully-saturated, resembles the non-interacting density of states of the model. This is due to the filling being above one and the magnetisation being rather large, thus, essentially all sites on the lattice are occupied by a majority spin. This means that all of the minority spin electrons will reside on a site already occupied by a majority spin electron, thus, paying the energy penalty of double occupancy U. This is the same situation as an unoccupied lattice with a shifted site energy and no interaction, thus, the minority spin spectra tend towards the non-interacting density of states.

We do observe a small shifting of the peaks within the spectra when compared to the paramagnetic result. The majority spin spectra are shifted to lower energies while the minority spin spectra are shifted to higher energies, this splitting appears to grow with the magnetisation.

5.5 Anti-Ferromagnetic Instability

We now turn our attention to the anti-ferromagnetic region of the model which occurs around half-filling and below. Before the results obtained as part of this

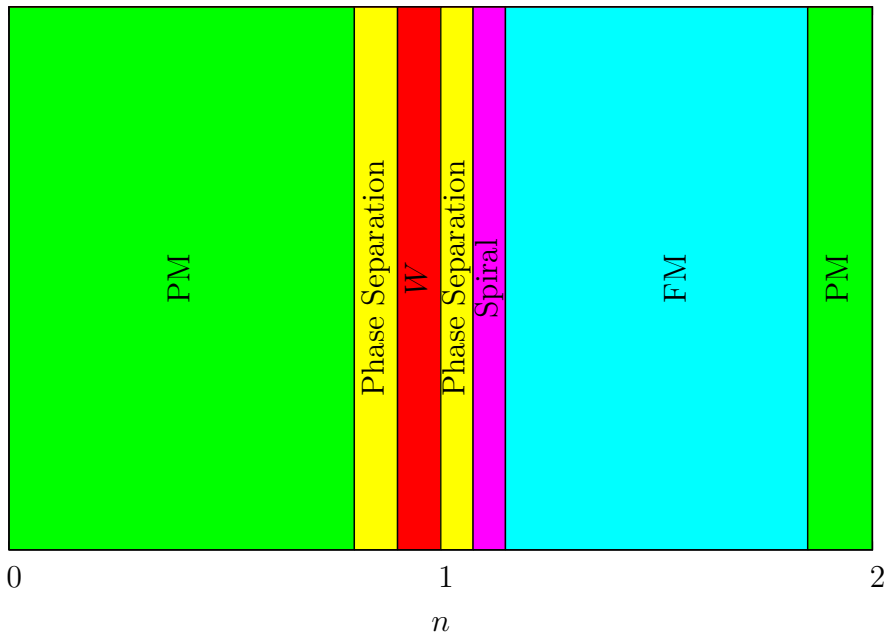

Figure 5.16: Schematic representation of the magnetic phase diagram of the fcc Hubbard model determined using a slave boson approach by Igoshev et. al. [35]. The parameters of the model are $U = 21$ and $t' = 0.3t$ which is slightly larger than the work of this thesis.

thesis are presented, we will give a brief overview of previous results obtained for similar models, as well as discussing the relevant AFM states found in the model.

An anti-ferromagnetic region has been previously reported in this model by Ulmke; however, only results for fillings above one were presented [9]. Ulmke found a small region of anti-ferromagnetism at half-filling extending up to $n \sim 1.1$ with the highest T_c value occurring at half-filling. The instabilities found in the susceptibility were at the X and W points, with the W point being dominant at half-filling. In addition, it was reported that there are additional low temperature instabilities for $n = 1$ at the $L = \{\pi, \pi, \pi\}$ point, and $\{\pi, \pi, 0\}$ which does not coincide with any of the high symmetry points of the 1Bz of the fcc lattice. Thus, this could indicate an instability towards a magnetic phase with order not commensurate with the lattice.

For less than half-filling the ground state phase diagram has been studied using both the Hartree-Fock and slave boson approaches by Igoshev et. al. [35]. A schematic version of this phase diagram displaying how it relates to this work is shown in figure 5.16. Starting at low fillings the ground state is found to be

paramagnetic across a wide range of fillings. As the filling approaches half-filling a region of phase separation between the paramagnetic state and a spiral magnetic state is found. Increasing the filling further a region is found with a ground state corresponding to the W point, this terminates at half-filling where a further region of phase separation is found. A ferromagnetic region is reported over a wide range of fillings above one, this region and the anti-ferromagnetic region are separated by a spiral magnetic phase of wave vector $(0, 0, \mathbf{Q})$. The large region of ferromagnetism is found to terminate before full occupancy, indicating an upper critical density in line with the findings of Ulmke and this work (see section 5.4) [9].

Before we move onto the results for the susceptibility across the AFM region, we will discuss and show visualisations of the real-space behaviour of the magnetisation for the states found in the above previous work. We are able to visualise this using the following equation

$$F(\mathbf{k}, \mathbf{r}) = \frac{1}{2}\left(e^{i\mathbf{k}\cdot\mathbf{r}} + e^{-i\mathbf{k}\cdot\mathbf{r}}\right) = \cos\left(\mathbf{k}\cdot\mathbf{r}\right) \tag{5.9}$$

where $\mathbf{r}$ is some position vector and $\mathbf{k}$ the wave-vector of the field we wish to study. We are then able to plot the density within the unit cell for a given $\mathbf{k}$. The high symmetry points we will look at are the $\Gamma = \{0, 0, 0\}$ point, corresponding to a uniform field and therefore the ferromagnetic state also the $X = \{0, 2\pi, 0\}$ and $W = \{\pi, 2\pi, 0\}$ points which are two different anti-ferromagnetic states. The plots are shown in figure 5.17.

The Γ point (figure 5.17a), as expected, yields a uniform field throughout the unit cell and therefore the fully aligned ferromagnetic state. The behaviour of the two anti-ferromagnetic points however, is more complex. We find the X point (figure 5.17b) has alternating planes of ferromagnetically ordered up and down spins, this is analogous to the fully AFM ordered state on a bipartite lattice. While the W point (figure 5.17c) is more complex and is better visualised by looking at an enlarged cell formed by plotting an additional unit cell in $\pm$ each of the axis directions. When this is done we find that the W point has alternating planes of ferromagnetically ordered up and down spins orientated diagonally across the unit

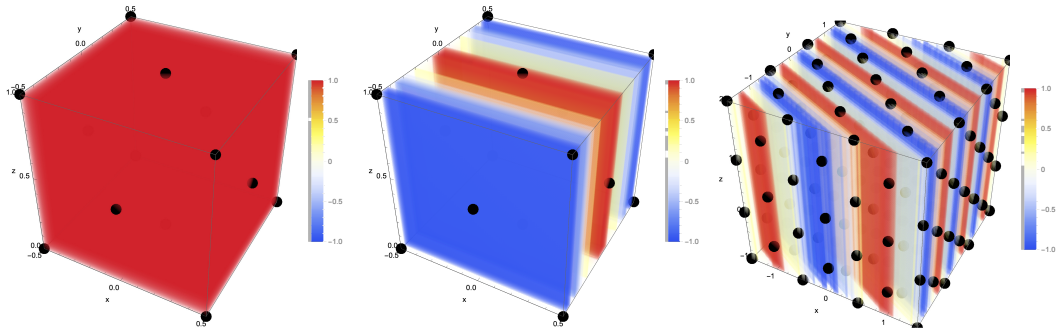

(a) $\Gamma = \{0, 0, 0\}$ **(b)** $X = \{0, 2\pi, 0\}$ **(c)** $W = \{\pi, 2\pi, 0\}$

Figure 5.17: Plots of the real-space behaviour of the magnetisation within the unit cell of fcc lattice for field vectors corresponding to certain high symmetry points. Note the W point is plotted in an extended unit cell for better visualisation.

cell and separated by planes of sites where there is no density. These are the fields towards which instabilities have been found in the previous work above, we also find instabilities towards these fields in this work. We now turn our attention to the susceptibility results for the fillings across the AFM region.

5.5.1 Magnetic Susceptibility and Phase Diagram

Figure 5.18 shows the magnetic susceptibility plotted along the high symmetry path of the 1Bz for fillings above and below half-filling at various temperatures. For all fillings shown here we observe strong divergences around the AFM symmetry points, particularly at the X and W points. Around and just below half-filling the W point takes larger values than that of the X point at low-temperature. This indicates a stronger instability towards the W point field. All fillings also show evidence of instability around the K point, however, this is never as strong as that of the X or W point and is strongly suppressed away from half-filling. There is also evidence of a very weak instability at the L point but this is rapidly suppressed as the filling deviates away from one. The instabilities observed here are in line with those observed in the study by Ulmke where the W point was found to be dominant at $n = 1$ then suppressed with respect to the X point when the filling is increased [9]. The divergences observed here also fit qualitatively well with the reports of the ground state phase diagram studied using the slave boson method

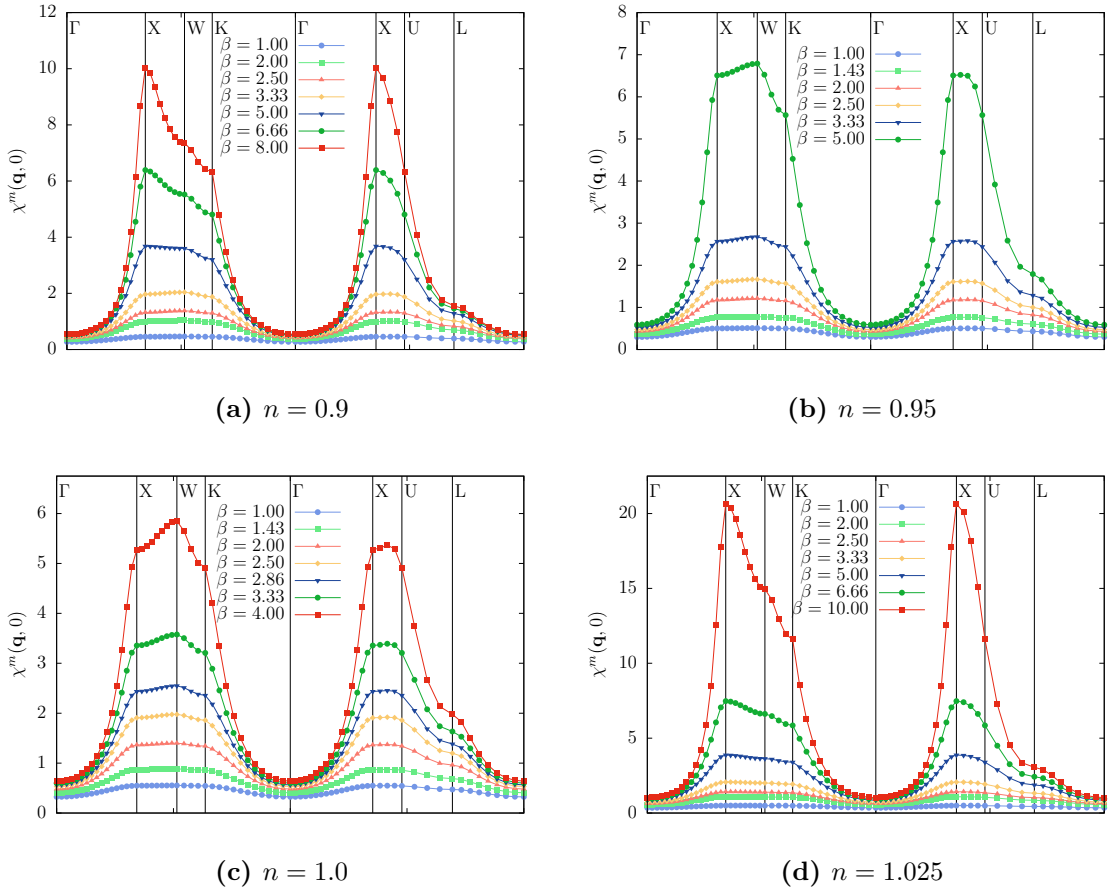

(a) $n = 0.9$ **(b)** $n = 0.95$

(c) $n = 1.0$ **(d)** $n = 1.025$

Figure 5.18: Plots of the magnetic susceptibility $\chi^m(\mathbf{q}, 0)$ along the high symmetry path of the 1Bz for a range of fillings across the anti-ferromagnetic region.

[35]. There the authors found the W phase was found to be dominant around half-filling with regions of phase separation to either side.

We can perform the same analysis of the susceptibility that was done for the ferromagnetic region in the previous section where a linear fit to the data was used in order to extract estimates of the critical temperature. Figures 5.19 and 5.20 show plots of $\frac{1}{\chi}$ Vs. T for the X and W points respectively along with the linear fits to the data. We find that the susceptibility displays a strong linear relationship for both the X and W points in line with the expected mean field behaviour at higher temperatures. It is interesting that in the anti-ferromagnetic region changing the filling is found to have the effect of just shifting the critical temperature with the slope remaining relatively constant, as observed across the range of fillings studied here. We find that the highest critical temperature is obtained at half-filling in

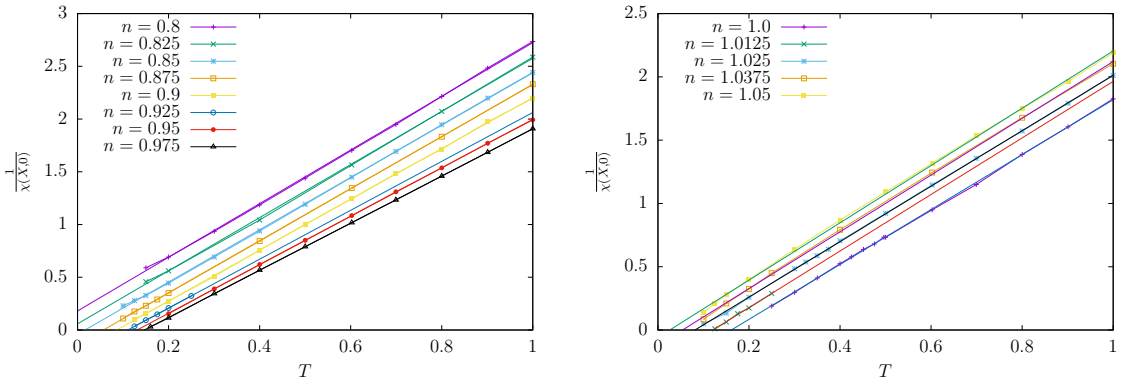

(a) $n \leq 1$ **(b)** $n > 1$

Figure 5.19: Plots of $\frac{1}{\chi(X,0)}$ Vs. T for a range of fillings along with linear fits to the data.

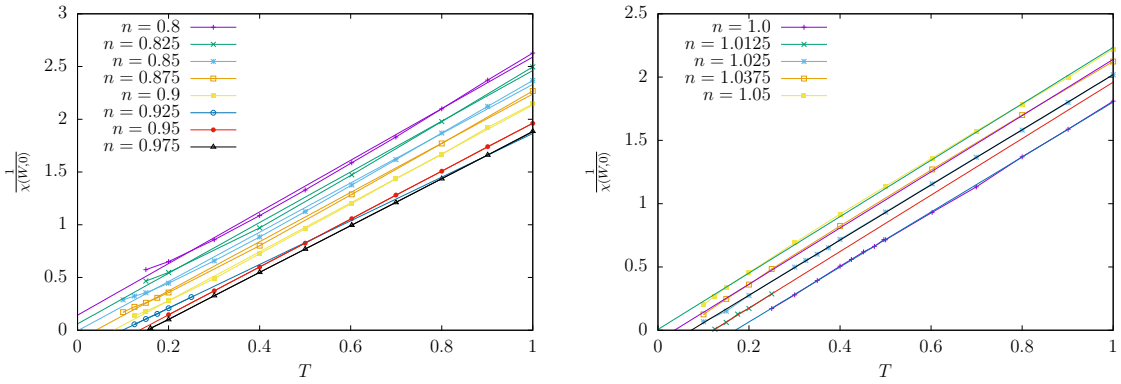

(a) $n < 1$ **(b)** $n \geq 1$

Figure 5.20: Plots of $\frac{1}{\chi(W,0)}$ Vs. T for a range of fillings along with linear fits.

line with the findings of Ulmke [9]. For both the X and W points at fillings less than 0.85 the extrapolated critical temperatures are negative. This indicates that the termination of the anti-ferromagnetic region lies around this filling. The upper boundary of the region is found to be $n \sim 1.05$ for the W point while a finite critical temperature persists for the X point. There is the possibility that the AFM region terminates at the same point that the FM region begins, however, this can not be determined through the data obtained as part of this project.

Taking the above estimates of the critical temperatures for the X and W points and plotting them in the (n, T) plane we can obtain their respective phase boundaries (see figure 5.21a). Estimates of the errors in the fits were obtained using

n	T_c	Lower Bound	Upper Bound
0.8500	0.01643	0.00458	0.00442
0.8750	0.05658	0.00163	0.00137
0.9000	0.08565	0.00297	0.00283
0.9250	0.11045	0.00097	0.00083
0.9500	0.13584	0.00119	0.00101
0.9750	0.15327	0.00157	0.00123
1.0000	0.16987	0.00357	0.00343
1.0125	0.12130	0.00333	0.00327
1.0250	0.08138	0.00284	0.00276
1.0375	0.05397	0.00724	0.00716
1.0500	0.02591	0.00809	0.00791

Table 5.3: Table of critical temperatures predicted from linear fits to the susceptibility data along with errors in T_c predicted from a 95% confidence interval of the fit.

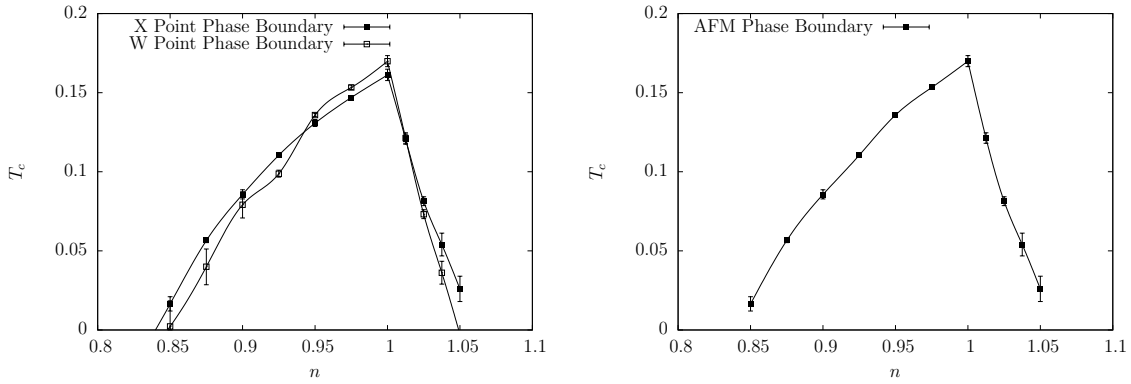

(a) **(b)**

Figure 5.21: Left: plot of the extrapolated critical temperatures from the X and W point susceptibility data plotted in the n, T plane. Right: combined phase boundary formed by taking the largest critical temperature from fits to the susceptibility data. Note: solid line is a spline fit to the data and serves as a guide to the eye.

the same method that was used for the ferromagnetic region (see 5.4.2) where the x-intercepts of the upper and lower bands of the 95% confidence interval of the fit is used to gain a handle on the error in T_c. The estimates of the errors in the critical temperatures are found to be on the order of $\sim 10^{-3}$ at most. We combine the two phase boundaries into an AFM phase boundary by taking the highest of the critical temperatures for the X and W point, below this we would expect to see an AFM state. A summary of the critical temperatures obtained for the AFM phase boundary is given in table 5.3 along with estimates of the errors. Note that

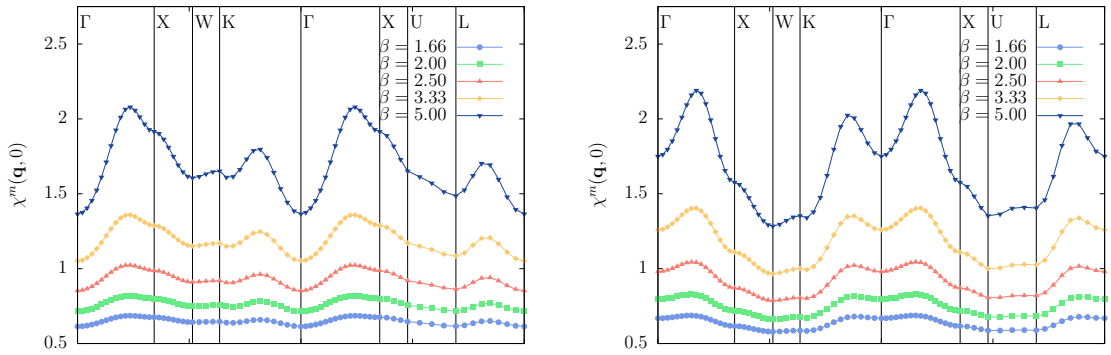

(a) $n = 1.075$ **(b)** $n = 1.1$

Figure 5.22: Plots of the magnetic susceptibility $\chi(\mathbf{q}, 0)$ along the high symmetry path of the 1Bz for two fillings lying between the anti-ferromagnetic and ferromagnetic regions.

estimates of the errors are plotted for both the X and W point phase boundaries in figure 5.21a. In most cases we find the critical temperatures for each point lies outside of the error bounds of one another. We find that both phase boundaries are relatively smooth and we can observe the crossover between the dominance of the W point around half-filling to that of the X point for fillings away from one: these crossovers happen for fillings $n \sim 0.94$ and $n \sim 1.02$.

We now turn our attention to what happens for fillings between the AFM region shown above and the FM region shown in the previous section. It is possible that the AFM region terminates where the FM region begins. This is somewhat supported by Nolting et. al. who studied magnetism on a bipartite lattice structure using a spectral density approach [8]. They observed that at $T = 0$, for relatively large values of U, such as the one used in this work, there exists a transition directly between an FM and AFM state without an intermediate paramagnetic phase. However, this study was performed on a bipartite lattice using a method that does not take into account local correlation. It remains to be seen if this persists when local correlation is taken into account and the AFM state is frustrated through both next-nearest neighbour hopping and a non-bipartite lattice. It is also possible that there exists a region of paramagnetism between the two regions, another possibility is a different magnetic state. Igoshev et. al. using a slave boson approach to a model with slightly larger next-nearest neighbour hopping predicted that the two regions are

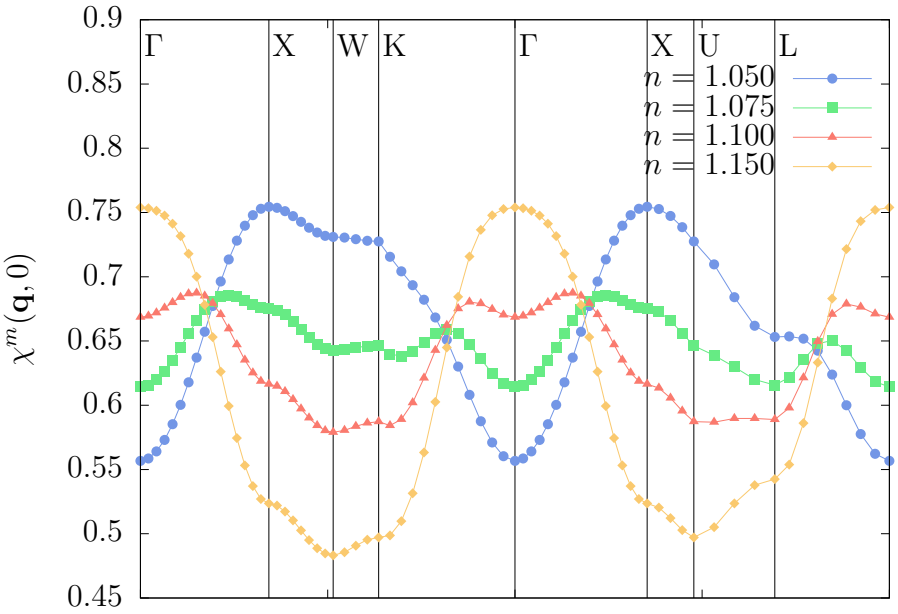

Figure 5.23: A plot of the magnetic susceptibility $\chi^m(\mathbf{q},0)$ along the high symmetry path of the 1Bz for fillings starting in the AFM region and increasing into the FM region. The temperature is fixed as $\beta = 1.66$ ($T \sim 0.6$).

separated by a spiral phase of wave vector $(0,0,\mathbf{Q})$ (see figure 5.16). Calculations were performed for fillings between the two regions in order to see if the susceptibility predicts a paramagnetic state or if there is evidence of the spiral magnetic state.

Figure 5.22 shows the magnetic susceptibility along the high symmetry path of the 1Bz for two fillings ($n = 1.075$ and $n = 1.1$) between the two magnetic regions. From this figure we can see that neither of these two fillings has the maximum in their susceptibility at either the Γ or X points. The maximum is not found at any of the high symmetry points, this indicates that these fillings are most susceptible to magnetic states not commensurate with the lattice. We do however, find that the maximum in the susceptibility lies on the straight line traced between the $\Gamma = (0,0,0)$ and $X = (0,2\pi,0)$ points. This coincides with the wave vectors reported for the spiral state by Igoshev et. al. therefore supporting the possibility of a spiral magnetic state between the anti-ferromagnetic and ferromagnetic regions.

We can also compare the profiles of the susceptibility for fillings between the AFM and FM regions at a fixed temperature ($\beta = 1.66$). This is shown in figure

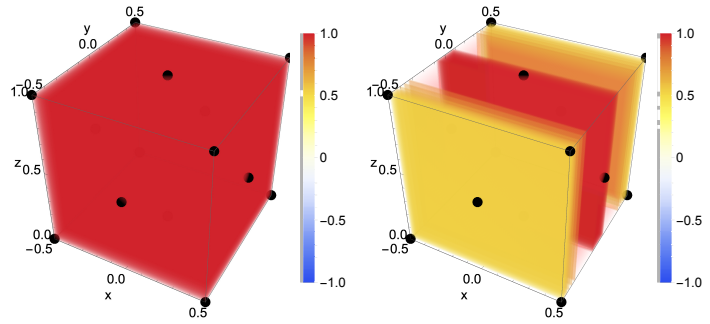

(a) Γ **(b)** $Q = (\frac{2\pi}{3}, 0, 0)$

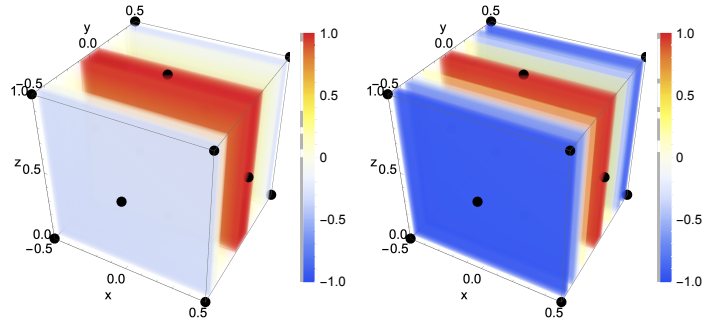

(c) $Q = (\frac{4\pi}{3}, 0, 0)$ **(d)** X

Figure 5.24: Plots of the real-space behaviour of the magnetisation resulting from the wave vectors laying on the path between the Γ and X points.

5.23 starting at a filling of $n = 1.05$, belonging to the AFM region with a divergence at the X point, and increasing to $n = 1.15$ belonging to the FM region with a divergence at the Γ point. The first thing of note is that the susceptibility has less of a dependence on $\mathbf{q}$ for the fillings between the AFM and FM regions than at the two fillings belonging to the magnetic regions. Focusing around the AFM symmetry points we find that as we increase the fillings the values in this region fall, indicating less instability towards the AFM states. We also see that the converse is true around the Γ point, with the value at the Γ point increasing with the filling. If we look at the real-space behaviour of the magnetisation for the wave vectors along the straight line between the X and Γ point. We find that this corresponds to taking all of the down spins in the X state and flipping them forming the ferromagnetic state, this is shown in figure 5.24.

It would be interesting to be able to study the AFM phase from below the phase boundary and look at the magnetisation and solutions with broken spin

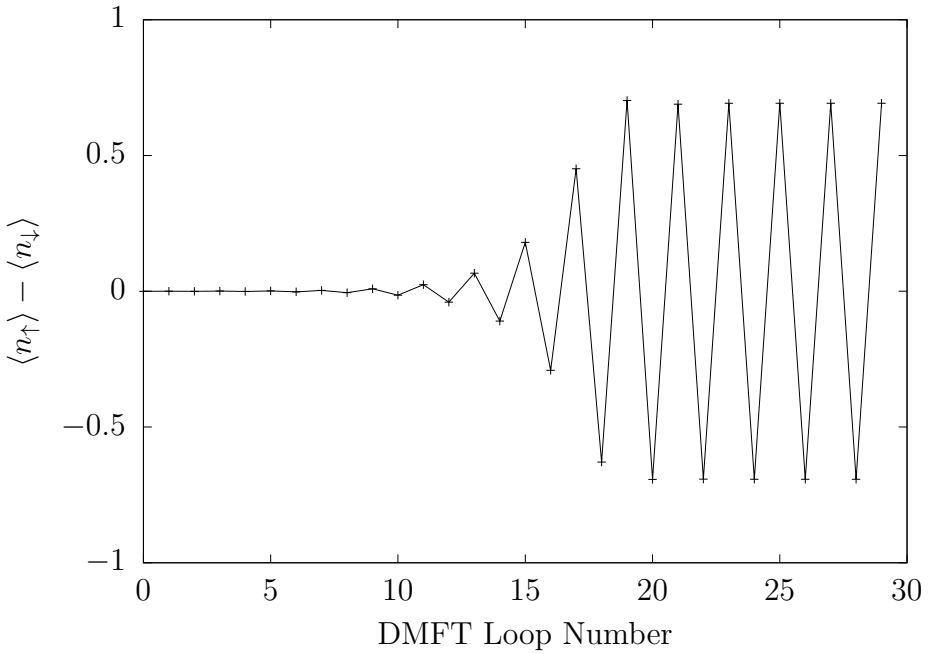

Figure 5.25: A plot of $\langle n_\uparrow \rangle - \langle n_\downarrow \rangle$ Vs. DMFT loop number for $n = 1.0$ at an inverse temperature of $\beta = 3.33$ ($T \sim 0.3$).

symmetry. This would in principle require a sublattice decomposition into the distinct different types of sites found in the AFM state. For the case of the usual Néel state on a bipartite lattice this can be achieved by making the usual bipartite lattice decomposition into sites of types A and B where all the neighbours of A sites reside on the B lattice and vice versa. However, since the fcc lattice is not bipartite it is not possible to make the relevant sublattice decomposition and we are not able to study this transition from below using this method.

We finish with one further observation. When the model is unstable towards a state with an order that has not been allowed for it is well-known that oscillations can arise in the DMFT solution from one loop to the next. This behaviour has been reported previously in studies of the Hubbard model at half-filling on the Bethe lattice. In these studies they found the anti-ferromagnetic states become unstable towards a possible magnetic state incommensurate with the lattice and oscillatory behaviour is found [109, 110].

Such oscillations have also been observed here when performing the calculations for this thesis, an example of such behaviour is shown in figure 5.25 for a filling

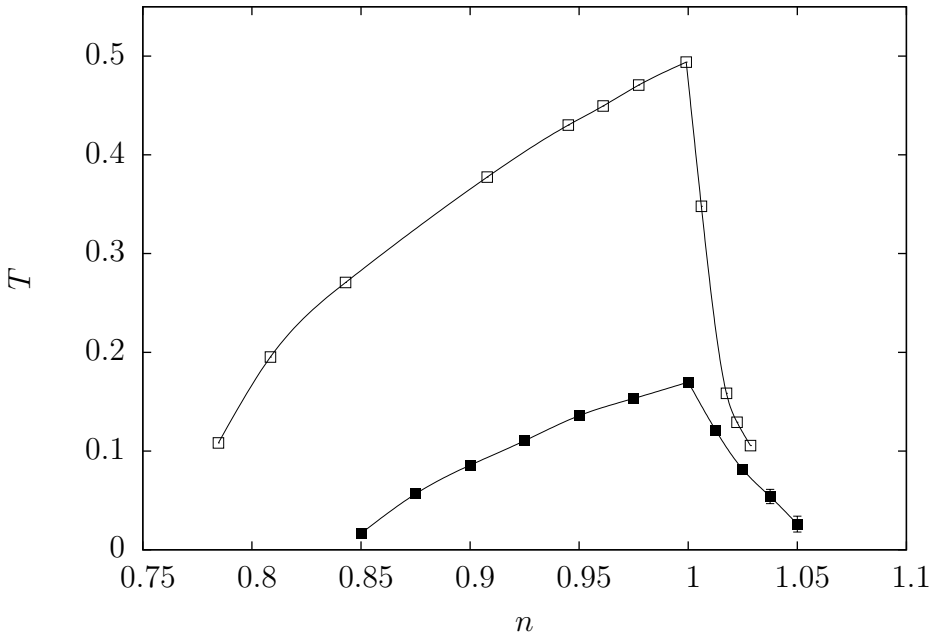

Figure 5.26: Plot showing the point where anti-ferromagnetic fluctuations become large enough to break the paramagnetic spin symmetry (blank squares) alongside the susceptibility phase boundary (filled squares). Note: solid lines are a spline fit to the data and are shown as guides to the eye.

of $n = 1.0$ at an inverse temperature of $\beta = 3.33$ ($T \sim 0.3$), which is above the critical temperature predicted by the susceptibility $T_c \sim 0.175$. If the spin symmetry is not enforced we find that the calculation remains paramagnetic for the first 10 loops, but then the spin symmetry is broken and a large magnetisation is built. The magnetisation flips with each DMFT loop, indicating anti-ferromagnetic fluctuations, i.e. that the anti-ferromagnetic order has not been allowed for within the calculation. After 20 DMFT loops the magnetisation appears to stabilise to a constant absolute value with the sign of the magnetisation switching each loop. It is interesting that the oscillations arise so far above the critical temperature predicted from the susceptibility calculations.

This behaviour is observed throughout the AFM region: the point at which we start to observe this behaviour is plotted in figure 5.26. We find that this behaviour is observed even for fillings below the lower critical filling for the AFM region where the susceptibility calculations predicted negative critical temperatures. Showing again that the fluctuations start to build well above the critical temperature. We can also

see that this boundary takes on roughly the same shape as that of the susceptibility phase boundary indicating that what is being observed here is correlated with the phase transition predicted through the susceptibility calculations.

5.5.2 Analytic Continuation

We now present some results showing how the single-particle spectrum varies throughout the AFM region found above. A metal-insulator transition occurring at half-filling has been found in the same model using a slave boson approach by Timirgazin et. al. [36], therefore it would be interesting to examine the character of the single-particle spectrum around half-filling. For the parameters at which the calculations within this thesis were performed the phase diagram from the paper predicts an insulating state with an order corresponding to the W point at half-filling and $T = 0$. It would therefore be interesting to see if this insulating state persists at finite temperature, also if an insulating state is adopted does this occur at the same time as the AFM state is adopted. The slave boson approach used also predicts that the insulating states are only possible at half-filling and any deviation away will result in a metallic solution. Thus, it would also be interesting to see if and how far away from half-filling the insulating phase persists. For other models the region of doping where an insulating state can be found has been reported to be very small [111, 112].

Figure 5.27 shows the spectra obtained from paramagnetic solutions at $T = 0.5$ ($\beta = 2.0$) for a range of fillings covering the region of anti-ferromagnetism found above. The first thing of note is that all the solutions are metallic with the exception of half-filling where there is a large gap at the Fermi-level. This along with the divergence at the W point in the susceptibility agrees well with the findings of Timirgazin et. al. [36]. This also shows that the insulating state persists even to relatively large finite temperatures and the gap is not filled by temperature. We also find that the insulating state appears to be very localised around half-filling. Hole doping the model by as little as 0.025 away from half-filling we find that the gap is filled and we obtain a metallic solution. For electron doping, while the spectra

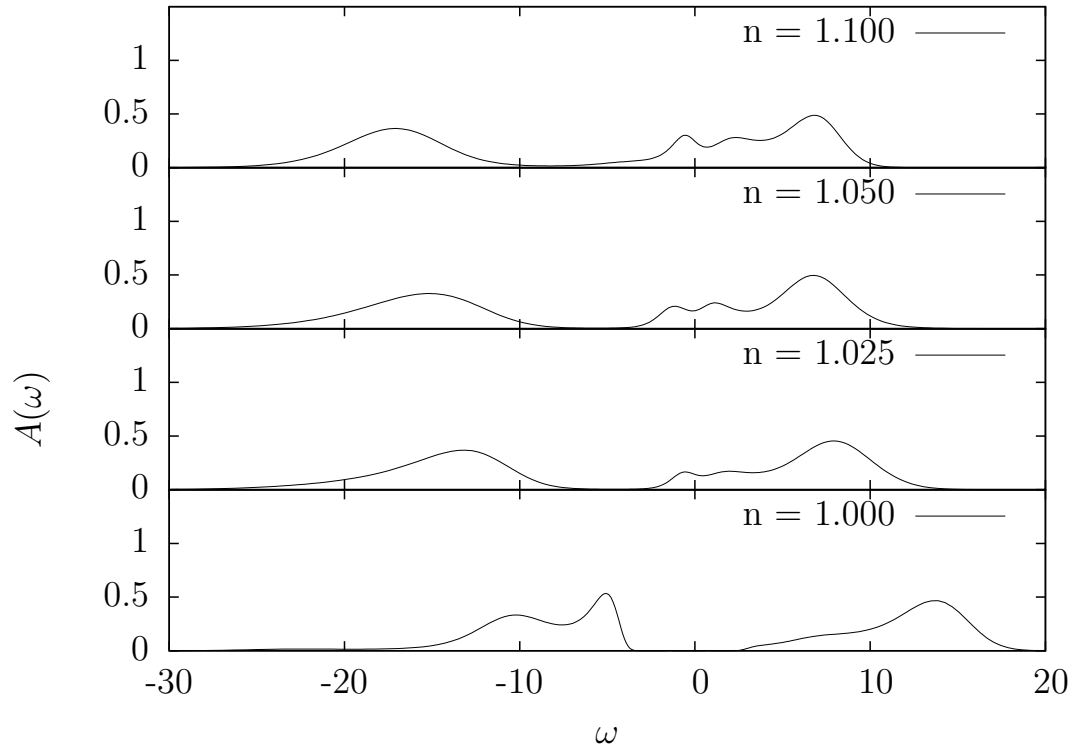

(a) $n \geq 1$

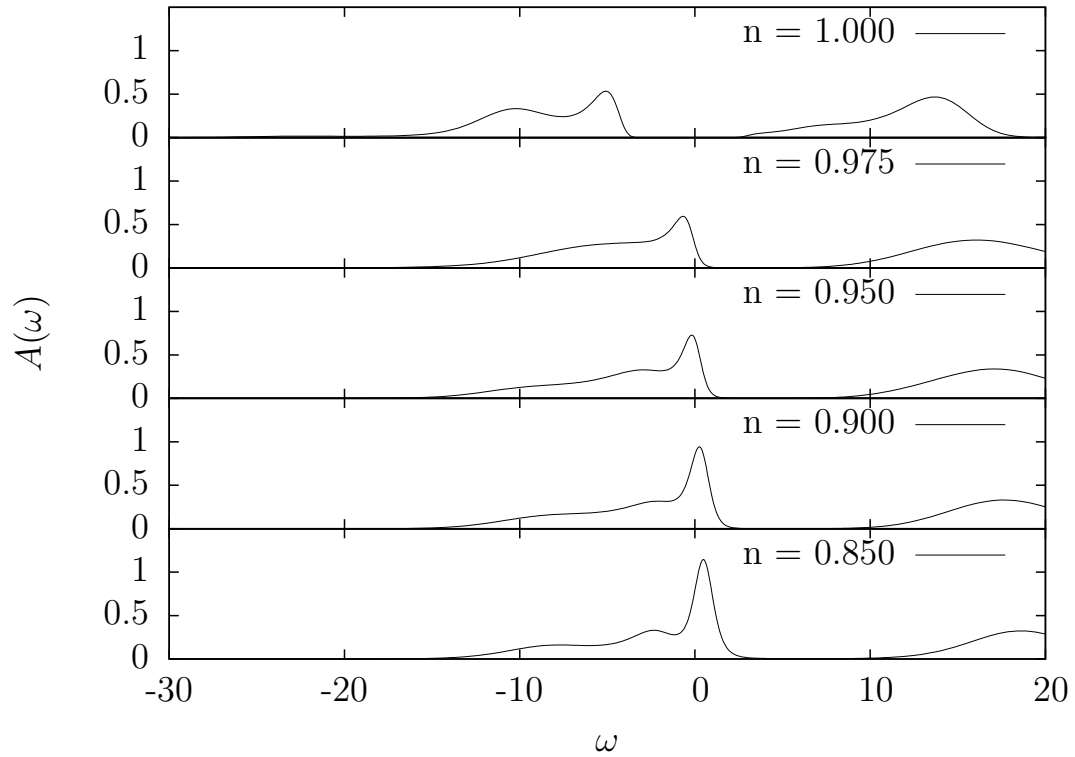

(b) $n \leq 1$

Figure 5.27: Plots of single-particle spectra for $T = 0.5$ ($\beta = 2.0$) for a range of fillings across the AFM region. Note: $n = 1$ spectrum is plotted in both plots for reference.

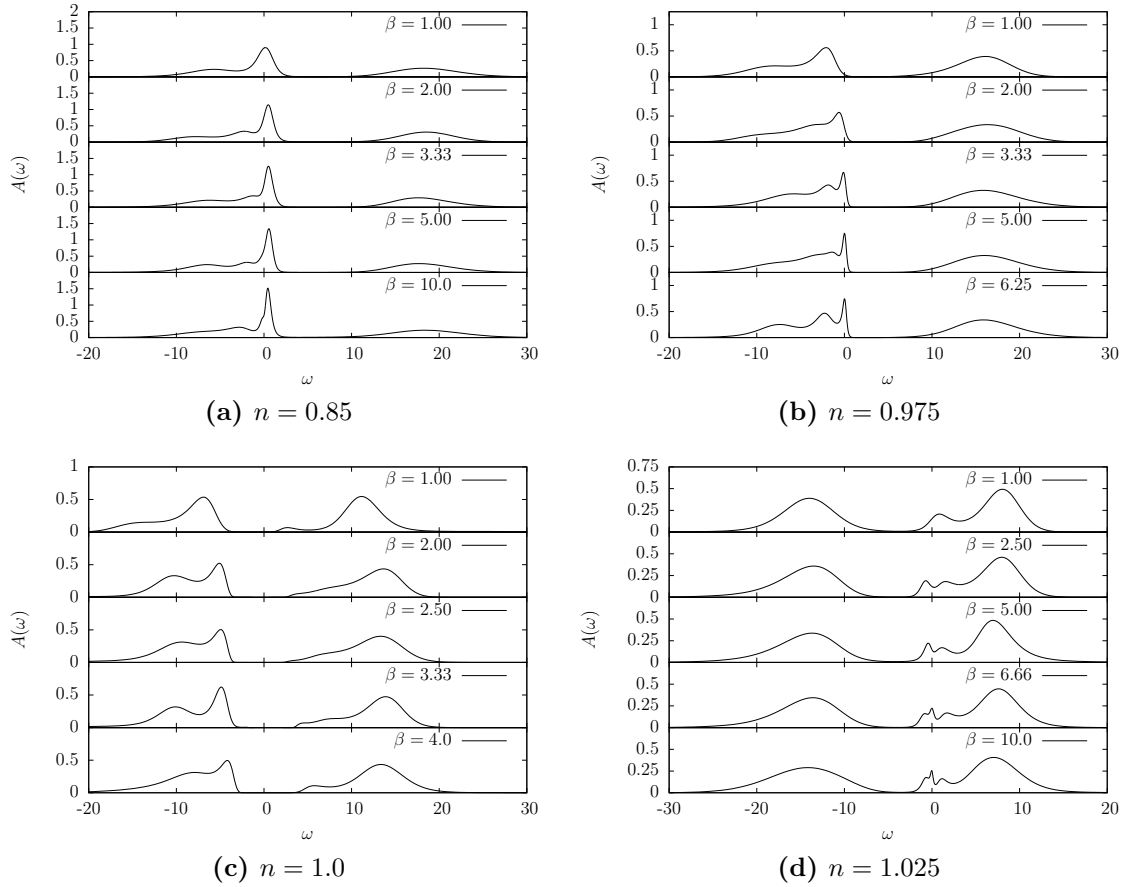

(a) $n = 0.85$ **(b)** $n = 0.975$

(c) $n = 1.0$ **(d)** $n = 1.025$

Figure 5.28: Plots of single-particle spectra for fillings throughout the AFM region plotted for a range of temperatures down to the paramagnetic to AFM phase transition.

do take a finite value at the Fermi-level, they do have some pseudogap character, displaying a small local minimum at the Fermi-level. This is not observed on the hole doped side where we find a strong peak developing below the Fermi-level on the upper edge of the lower Hubbard band. As the filling falls further away from one this peak increases in size forming a large peak around the Fermi-level. Given that as we lower the temperature this develops into a peak at the Fermi-level, as will be shown below, this can be considered as the remanence of the quasi-particle peak that has been washed out by temperature.

Figure 5.28 shows spectra for four different fillings at various temperatures down to the paramagnetic to AFM phase transition. All of the solutions that are metallic at higher temperatures retain their metallic character down to the transition. This indicates that the transition is to a metallic anti-ferromagnetic state. In all the

metallic cases we find that as the temperature is lowered the quasi-particle peak at the Fermi-level becomes more prominent and thins, while the Hubbard bands remain relatively unchanged with only small shifts according to the changing chemical potential required to fix the filling. For fillings below one, we find that a secondary peak appears at the upper edge of the lower Hubbard band at lower temperatures. While for fillings above one this secondary peak appears above the Fermi-level at the lower edge of the upper Hubbard band. At half-filling however, there appears to be evidence of these secondary peaks in both the upper and lower Hubbard bands, with the peak in the lower Hubbard being stronger.

5.6 Summary

In summary of the above chapter the work performed as part of this thesis provides a DMFT level study of magnetism in the fcc Hubbard model. The results were obtained using the modern CTHYB impurity solver along with accurate measurements of the single and two-particle Green's functions making use of the Legendre representation as well as the improved estimator formalism. The results were obtained using the extensively modified CTHYB code and the DMFT code developed in chapters 3 and 4 which are able to obtain very good agreement with previous results from the literature.

A large region of ferromagnetism is found in agreement with the study of Ulmke [9]. However, the use of the more accurate and modern methods, that were not available at the time, significantly improve the accuracy to which the DMFT phase boundary is determined. The results also obtain good qualitative agreement with slave boson studies where spiral and non-commensurate phases are taken into account [35, 36]. We also provide a more extensive study of the transition from below achieving remarkable agreement between susceptibility and magnetisation calculations. Both the susceptibility and magnetisation are found to possess mean field critical exponents near the transition, indicating that the transition, when studied at the DMFT level, belongs to the mean field universality class.

Further to the above, single-particle spectra were obtained using the maximum entropy method in both the paramagnetic and ferromagnetic phases. This allowed for a detailed study of the single-particle spectra as the transition is crossed and clearly displayed the splitting of the spin resolved single-particle spectra as well as the redistribution of spectral weight as the magnetisation builds.

Plots of the susceptibility along the high symmetry path of the 1Bz are also shown for a range of fillings and temperatures. This showed that the model is only unstable towards a divergence at the Γ point for the parameters studied here. We also provide susceptibility results for fillings between the ferromagnetic and anti-ferromagnetic region found around half-filling and below. This provides evidence of a possible spiral magnetic state laying between the AFM and FM phases, supporting the findings of slave Boson studies by Igoshev et. al. [35] and Timirgazin et. al. [36].

An AFM region around half-filling has also been determined where previously results at the DMFT level have only been presented for above half-filling by Ulmke [9]. We find an extensive AFM region consisting of a W point divergence at and around half-filling, agreeing well the slave Boson studies [35, 36]. We also find X point divergences either side of the W phase. We also found a large region of instability of the DMFT solution around the AFM region. Here the solution becomes unstable towards anti-ferromagnetic fluctuations, breaking the spin symmetry well above the phase boundary and stopping the DMFT solution from converging. This indicates that the ground state of the model could be that of a magnetic state not allowed for in the calculations performed here.

Single-particle spectra for paramagnetic solutions above the AFM region are also presented for a range of fillings and temperatures. These spectra prove to be metallic all the way down to the transition, with the exception of half-filling where the Fermi-level lies within a large gap and an insulating solution is obtained for all temperatures studied here.

In the following chapter we build upon the DMFT results obtained here, taking into account some of the non-local correlation missed by the DMFT approximation. This is achieved through the dual fermion approach, a diagrammatic extension to

DMFT. We provide an overview of the dual fermion method and present results for both the FM and AMF regions covered in this chapter.

6

Dual Fermion Study of Magnetism in the fcc Hubbard Model

In this chapter we move on to treating the model using an extension of the dynamical mean field theory that takes into account some of the non-local correlations missed by the DMFT approximation. We achieve this using the dual fermion approach, which is a diagrammatic extension built upon the DMFT solution [25]. We will discuss some other methods of tackling this problem as well as some results of dual fermion studies of the Hubbard model on other lattices. The dual fermion formalism is then presented, and we discuss some factors relevant to being able to perform accurate dual fermion calculations. Following this we will present calculations replicating results from the literature for the Hubbard model on the square lattice. These calculations were performed to test and validate the code we have written. We move onto presenting the results obtained for the ferromagnetic and anti-ferromagnetic regions described in the previous chapter.

Within DMFT the self-energy is momentum independent and therefore a purely local quantity: this has the effect of completely neglecting all non-local correlation and is an approximation, except when $d = \infty$. Efforts have been made in order to treat the missed non-local correlation through two main branches of approach. The

first is treating clusters of sites instead of a single-site, while the second involves diagrammatic extensions built around DMFT.

The cluster extensions follow quite straightforwardly from single-site DMFT, where we have a single-site coupled to a dynamical mean field, by instead coupling a cluster of sites to a dynamical mean field. This allows for non-local correlation to be explicitly taken into account within the cluster and neglects non-local correlations, using the same approximation as single-site DMFT, for anything beyond the cluster. These cluster approaches include the dynamical cluster approximation [113] and cluster dynamical mean field theory [24]. A review of quantum cluster theories has been given by Maier et. al. [84], and the above two approaches are also covered in the following conference proceedings by Potthoff [114]. These methods however, are limited by the size of the clusters they are able to treat, with the problem rapidly becoming intractable and calculations involving only relatively small clusters are achievable. The formulation of these theories also results in breaking translational symmetry leading to discontinuities in the momentum dependence of the self-energy. The results of the calculations are also found to be rather dependent on the size of the cluster treated. There is the possibility of performing finite-size scaling on the results in order to obtain results in the thermodynamic limit, however, this not usually able to be performed reliably [114]. Due to the small cluster sizes these methods, by construction, are only capable of treating short range correlations on the order of the cluster size and neglect longer range correlation. Diagrammatic approaches, however, are able to treat correlations on all length scales.

The diagrammatic extensions work through building perturbation theories around the DMFT result in order to include some spatial non-locality. The methods vary in which local vertex is used to build the perturbation theory, as well which diagrams are included and summed. A comprehensive review of diagrammatic extensions to DMFT has recently been given by Rohringer et. al. [23]. The dynamical vertex approximation, dual fermion approach and the one-particle irreducible approach are also covered in detail in his thesis [60]. The first developed of these theories was the dynamical vertex approximation [115], an overview of

which can be found here [116]. This somewhat directly extends the idea of DMFT where the self-energy, also known as the one particle irreducible vertex, is assumed to be local and extends this concept to the two-particle level [23, 115]. The dual fermion approach was developed by Rubtsov et. al. in 2008 and has the ability to treat both short and long range correlations [25, 26].

The derivations of these theories involve the coherent state path integral description of quantum mechanics, as well as diagrammatic perturbation theory and as such are complex and involved. Thus, in the following section we will only provide a brief overview of the derivation and will focus more on the resulting equations and calculation procedure. For an in depth treatment of the derivation, as well as the construction of the perturbation theory, see the original papers by Rubtsov [25, 26] or this book chapter by Lichtenstein [117] as well as this introduction to diagrammatic perturbation theories by Hafermann [28] which the following section follows. The review of diagrammatic approaches to non-local correlation by Rohringer et. al. also provides a derivation [23]. All of the results obtained as part of this thesis were done so for a paramagnetic phase as such in the following discussion spin indices have been dropped where applicable.

6.1 The Dual Fermion Method

The general idea behind the dual fermion method, as with any perturbation theory, is to split the model into an 'easily' solvable part plus some perturbation. In the context of the dual fermion method we wish to split the problem into local and non-local parts with the non-local parts being treated as the perturbation. We start from the action for the Hubbard model given by:

$$S\left[\bar{c},c\right] = -\sum_{n,k,\sigma}\left(i\nu_n + \mu - \epsilon_k\right)\bar{c}_{n,k,\sigma}c_{n,k,\sigma} + U\sum_i \int_0^\beta d\tau \bar{c}_{i,\uparrow}(\tau)c_{i,\uparrow}(\tau)\bar{c}_{i,\downarrow}(\tau)c_{i,\downarrow}(\tau) \tag{6.1}$$

where $\bar{c}$ and c are Grassmann variables of the corresponding fermionic creation and annihilation operators. In order to achieve the separation of local and non-local parts a hybridisation function is introduced at each site. This allows the original lattice

problem to be rewritten exactly in terms of a set of impurities that are coupled in some way encoding the non-local correlations. In principle this hybridisation function can take any form, however, we are able to make an informed choice as will be discussed later. The action with the hybridisation introduced is given by:

$$S\left[\bar{c},c\right]=\sum_{i}S_{imp}\left[\bar{c}_{i},c_{i}\right]-\sum_{n,k,\sigma}\left(\Delta(i\nu_{n})-\epsilon_{k}\right)\bar{c}_{n,k,\sigma}c_{n,k,\sigma} \tag{6.2}$$

$$S_{imp}\left[\bar{c}_{i},c_{i}\right]=\sum_{n,\sigma}\left(\Delta(i\nu_{n})-\mu-i\nu_{n}\right)\bar{c}_{i,n,\sigma}c_{i,n,\sigma}+U\int_{0}^{\beta}d\tau\bar{c}_{i,\uparrow}(\tau)c_{i,\uparrow}(\tau)\bar{c}_{i,\downarrow}(\tau)c_{i,\downarrow}(\tau) \tag{6.3}$$

where we have introduced the impurity action describing the impurity model at each site. While the impurity problem is able to be solved using the CTHYB method described in chapter 3 or some other impurity solver, the coupling between them (second term of equation (6.2)) is non-local and presents a problem. In order to tackle this a set of dual fermions are introduced to the problem by means of a Hubbard-Stratonovich transformation. This allows the non-local coupling between the impurities to be expressed as a local coupling between the physical fermions and the dual fermions. It can be shown that the transformation results in the following action which can be split into local and non-local parts [25, 26].

$$S\left[\bar{c},c,\bar{f},f\right]=\sum_{i}S_{site}\left[\bar{c}_{i},c_{i},\bar{f}_{i},f_{i}\right]+\sum_{n,k,\sigma}G^{-2}(i\nu_{n})\left[\Delta(i\nu_{n})-\epsilon_{k}\right]^{-1}\bar{f}_{n,k,\sigma}f_{n,k,\sigma} \tag{6.4}$$

Here $G(i\nu_n)$ is the impurity Green's function, $\bar{f}$ and f are Grassmann variables describing the dual fermions and the site action is given by the following.

$$S_{site}\left[\bar{c}_{i},c_{i},\bar{f}_{i},f_{i}\right]=S_{imp}\left[\bar{c}_{i},c_{i}\right]+\sum_{n,\sigma}G^{-1}(i\nu_{n})\left(\bar{f}_{n,i,\sigma}c_{n,i,\sigma}+\bar{c}_{n,i,\sigma}f_{n,i,\sigma}\right) \tag{6.5}$$

Note that now the full action of the problem only depends on the original physical fermions through the site action. It is now possible to integrate out the original physical fermions from the site action leaving the original problem written exclusively in terms of the dual fermions.

$$S\left[\bar{f}_{i},f_{i}\right]=\sum_{n,k,\sigma}G^{-2}(i\nu_{n})\left[\left(\Delta(i\nu_{n})-\epsilon_{k}\right)+G(i\nu_{n})\right]^{-1}\bar{f}_{n,k,\sigma}f_{n,k,\sigma}+\sum_{i}V\left[\bar{f}_{i},f_{i}\right] \tag{6.6}$$

The integration of the original set of fermions results in the introduction of the dual potential ($V\left[\bar{f}_i, f_i\right]$) describing a local interaction between dual fermions. Formally it can be shown that the dual potential is constructed from the n-point vertex functions of the impurity problem at all orders [25, 28]. In practice however, it is usually truncated to just contain the two-particle vertex function which was introduced in chapter 2. This is one of the approximations made in the dual fermion approach; here we will take it as given, however, this approximation will be touched on later. We can also deduce the non-interacting dual Green's function from the first term of equation (6.6) as

$$\begin{aligned}\tilde{G}^0(\mathbf{k}, i\nu_n) &= -G^{-2}(i\nu_n)\left[(\Delta(i\nu_n) - \epsilon_k)^{-1} + G(i\nu_n)\right]^{-1} \\ &= \left[G^{-1}(i\nu_n) + \Delta(i\nu_n) - \epsilon_k\right]^{-1} - G(i\nu_n)\end{aligned} \tag{6.7}$$

which describes the dual fermions in the absence of the dual potential. Note that in the following all dual quantities will be denoted by the presence of a tilde.

The transformation from the original action to the dual action is exact when all orders in the expansion of the dual potential are taken into account. This allows us to derive exact relationships between the Green's functions of the physical and dual fermions. For example the Green's function of the original lattice problem ($G^{latt}(i\nu_n, \mathbf{k})$) can be obtained in terms of the dual Green's function ($\tilde{G}(i\nu_n, \mathbf{k})$) and quantities of the impurity model [25, 26].

$$G^{latt}(i\nu_n, \mathbf{k}) = G^{-2}(i\nu_n)\left[\Delta(i\nu_n) - \epsilon_k\right]^{-2}\tilde{G}(i\nu_n, \mathbf{k}) + \left[\Delta(i\nu_n) - \epsilon_k\right]^{-1} \tag{6.8}$$

Introducing a dual self-energy, describing the effect of the dual potential, the above equation can be written in the following form expressing the lattice self-energy in terms of the impurity and dual self-energies [50, 117].

$$\Sigma^{latt}(i\nu_n, \mathbf{k}) = \Sigma^{imp}(i\nu_n) + \frac{\tilde{\Sigma}(i\nu_n, \mathbf{k})}{1 - G(i\nu_n)\tilde{\Sigma}(i\nu_n, \mathbf{k})} \tag{6.9}$$

Here $\Sigma^{imp}(i\nu_n)$ is the self-energy of the underlying impurity problem and $\tilde{\Sigma}(i\nu_n, \mathbf{k})$ denotes the dual self-energy.

It is now useful to examine some of the above equations in the limit that $U = 0$ and $V = 0$ as well as just $U = 0$. We will start with the former. In this case the

impurity Green's function $G(i\nu_n)$ takes the form of the non-interacting impurity Green's function seen previously (equation (2.29)) and, since $V = 0$, the dual Green's function takes its non-interacting form too. Substituting the impurity Green's function into equation (6.7) we obtain the following.

$$\tilde{G}^{U=0,V=0}(i\nu_n, \mathbf{k}) = -\left[G^0(i\nu_n)\right]^{-2}\left[(\Delta(i\nu_n) - \epsilon_k)^{-1} + G^0(i\nu_n)\right]^{-1} \tag{6.10}$$

Then, substituting this into the equation (6.8) for the lattice Green's function and simplifying we obtain

$$G^{U=0,V=0}(i\nu_n, \mathbf{k}) = \frac{1}{(G^0(i\nu_n))^{-1} + \Delta(i\nu_n) - \epsilon_k} \tag{6.11}$$

which is the same as the non-interacting Green's function of the Hubbard model as previously seen (equation (4.3)). Thus, we find that the non-interacting dual theory along with the non-interacting impurity model correctly reproduces the non-interacting result for the Hubbard model.

If we now turn on the interactions of the impurity model while still maintaining the non-interacting dual theory, such that the interactions of the Hubbard model are somewhat taken into account through the interacting impurity Green's function. We obtain equation (6.11) but now with the interacting impurity Green's function (equation (2.32)).

$$G^{V=0}(i\nu_n, \mathbf{k}) = \frac{1}{G^{-1}(i\nu_n) + \Delta(i\nu_n) - \epsilon_k} \tag{6.12}$$

Substituting in equation (2.32) for the interacting impurity Green's function we find the following.

$$G^{V=0}(i\nu_n, \mathbf{k}) = \frac{1}{i\nu_n + \mu - \epsilon_k - \Sigma^{imp}(i\nu_n)} \tag{6.13}$$

Thus, to zeroth order in the dual interaction the Hubbard model Green's function can be found by solving the interacting impurity model and using the corresponding momentum independent impurity self-energy as an approximation for the Hubbard models lattice self-energy. This sounds rather similar to the approach of DMFT. However, within DMFT the hybridisation is chosen such that it satisfies the DMFT

self-consistency condition. Here the hybridisation function has not yet been specified, therefore it does not necessarily satisfy the DMFT self-consistency condition. However, it has been shown that choosing such a hybridisation function provides an optimal starting point for the dual perturbation theory [26]. We are able to enforce this by means of asserting that the local part of the dual Green's function is zero.

$$\tilde{G}_{loc}(i\nu_n) = \frac{1}{N}\sum_k \tilde{G}(i\nu_n, \mathbf{k}) = 0 \tag{6.14}$$

This is self-consistently enforced by updating the hybridisation function through the following condition.

$$\Delta^{new}(i\nu_n) = \Delta^{old}(i\nu_n) + \frac{\tilde{G}_{loc}(i\nu_n)}{G(i\nu_n)G^{latt}_{loc}(i\nu_n)} \tag{6.15}$$

With this choice of hybridisation we find that the non-interacting theory in the dual fermions results in the DMFT result. To see this we can evaluate equation (6.14) with the dual non-interacting Green's function (6.7).

$$\frac{1}{N}\sum_k \left[G^{-1}(i\nu_n) + \Delta(i\nu_n) - \epsilon_k\right]^{-1} - G(i\nu_n) = 0 \tag{6.16}$$

Moving the impurity Green's function to the R.H.S and substituting equation (2.32) in for the inverse impurity Green's function we obtain the following.

$$\frac{1}{N}\sum_k \frac{1}{i\nu_n + \mu - \epsilon_k - \Sigma^{imp}(i\nu_n)} = G(i\nu_n) \tag{6.17}$$

We find the L.H.S is the local Green's function of the Hubbard model under the DMFT approximation that the self-energy is local.

$$G^{DMFT}_{loc}(i\nu_n) = \frac{1}{N}\sum_k G^{DMFT}(i\nu_n, \mathbf{k}) = G(i\nu_n) \tag{6.18}$$

Thus, we find that enforcing equation (6.14) enforces that the local part of the DMFT lattice Green's function is the same as the impurity Green's function, which is the DMFT self-consistency condition.

Now that we have fixed the previously unspecified hybridisation function, what remains is the question of how to calculate the dual self-energy $\tilde{\Sigma}(i\nu_n, \mathbf{k})$. This is done by constructing a diagrammatic perturbation theory in terms of the dual

interaction (impurity vertex function) and the dual Green's function. This is involved and we shall not go into detail here: it is covered in the following two book chapters [27, 28]. The two commonly used methods are the second-order approximation [26] and the ladder approximation [29]. While the second-order approximation to the dual self-energy has been shown to provide improvements over DMFT when studying the AFM state of the 2D Hubbard model [6, 26], the ladder approximation provides further improvement by summing collections of diagrams that are more physically relevant around magnetic phase transitions [5, 29]. As such, in this work we make use of the ladder approximation.

The ladder approximation to the dual self-energy involves two steps. The first involves using a Bethe-Salpeter equation in order to obtain an estimate of the full dual vertex. This is subsequently used in the Schwinger-Dyson equation which relates the full vertex to the self-energy. The Bethe-Salpeter equation that is solved is given by [28]:

$$\begin{aligned}\Gamma^{\alpha}(i\nu_n, i\nu_{n'}, i\omega_m, \mathbf{k}) =& \gamma^{\alpha}(i\nu_n, i\nu_{n'}, i\omega_m) + \\ & \sum_{i\omega_{n''}} \gamma^{\alpha}(i\nu_n, i\nu_{n''}, i\omega_m)\tilde{\chi}(i\nu_{n''}, i\omega_m, \mathbf{k})\Gamma^{\alpha}(i\nu_{n''}, i\nu_{n'}, i\omega_m, \mathbf{k})\end{aligned} \tag{6.19}$$

where α denotes either the density or magnetic vertex function defined by

$$\gamma^{d}(i\nu_n, i\nu_{n'}, i\omega_m) = \gamma_{\uparrow,\uparrow}(i\nu_n, i\nu_{n'}, i\omega_m) + \gamma_{\uparrow,\downarrow}(i\nu_n, i\nu_{n'}, i\omega_m) \tag{6.20}$$

$$\gamma^{m}(i\nu_n, i\nu_{n'}, i\omega_m) = \gamma_{\uparrow,\uparrow}(i\nu_n, i\nu_{n'}, i\omega_m) - \gamma_{\uparrow,\downarrow}(i\nu_n, i\nu_{n'}, i\omega_m) \tag{6.21}$$

and $\tilde{\chi}(i\nu_n, i\omega_m, \mathbf{q})$ is known as the dual two-particle bubble given by the following.

$$\tilde{\chi}(i\nu_n, i\omega_m, \mathbf{q}) = -\frac{T}{N}\sum_{k} \tilde{G}(\mathbf{k}, i\nu_n)\tilde{G}(\mathbf{k}+\mathbf{q}, i\nu_n + i\omega_m) \tag{6.22}$$

The equation (6.19) can be solved for each fixed $\mathbf{k}$ and $i\omega_m$ through matrix inversion [28, 50]. The resulting estimates of dual magnetic and density vertices are then used in the Schwinger-Dyson equation yielding the dual self-energy as given by:

$$\begin{aligned}\tilde{\Sigma}(i\nu_n, \mathbf{k}) =& \frac{T}{2N}\sum_{i\omega_m, \mathbf{q}} \Bigg(3\left[\Gamma^{m}_{i\nu_n, i\nu_n, i\omega_m, \mathbf{q}} - \frac{1}{2}\Gamma^{(2)m}_{i\nu_n, i\nu_n, i\omega_m, \mathbf{q}}\right] \\ & + \Gamma^{d}_{i\nu_n, i\nu_n, i\omega_m, \mathbf{q}} - \frac{1}{2}\Gamma^{(2)d}_{i\nu_n, i\nu_n, i\omega_m, \mathbf{q}}\Bigg)\tilde{G}_{\mathbf{k}+\mathbf{q}, i\nu_n + i\omega_m}\end{aligned} \tag{6.23}$$

where $\Gamma^{(2)\alpha}$ is known as the second-order correction and is subtracted in order to avoid double counting of diagrams [28]. The second-order correction for the density or magnetic vertex is given by the following.

$$\Gamma^{(2)\alpha}(i\nu_n, i\nu_n, i\omega_m, \mathbf{k}) = \sum_{i\nu_{n''}} \gamma^{\alpha}(i\nu_n, i\nu_{n''}, i\omega_m)\tilde{\chi}(i\nu_{n''}, i\omega_m, \mathbf{k})\gamma^{\alpha}(i\nu_{n''}, i\nu_{n'}, i\omega_m) \tag{6.24}$$

Once the dual self-energy has been obtained the dual Green's function can be found by using the usual Dyson equation (2.31) with the corresponding non-interacting dual Green's function.

We are now in a position to solve the above equations self-consistently. This involves two self-consistency loops: an inner self-consistency loop to determine the dual Green's function given the input from the impurity model, and an outer self-consistency loop taking into account updates to the hybridisation (equation (6.15)). This process is summarised in figure 6.1.

The dual fermion calculation starts with a DMFT calculation. The resulting hybridisation, interacting Green's function and vertex functions are used as input for the inner loop of the dual fermion calculation. This input is then used to construct the non-interacting dual Green's function (equation (6.7)), this is then used in order to obtain the dual vertex functions through the Bethe-Salpeter equations (equation (6.19)). The dual vertex functions are then used in the Schwinger-Dyson equation in order to obtain the dual self-energy (equation (6.23)) from which the interacting dual Green's function can be obtained using the usual Dyson equation. The inner loop then proceeds by evaluating the Bethe-Salpeter equations (equation (6.19)) again with the dual Green's function, obtaining new dual vertex functions, and therefore a new dual self-energy and interacting dual Green's function. This process is iterated until the dual Green's function converges and the inner loop reaches self-consistency. An update to the impurity hybridisation function is then computed (equation (6.15)) which defines a new impurity model, different from the DMFT solution. This is then solved to provide a new input impurity Green's function and vertices. These are then used as input to the inner loop which provides a new

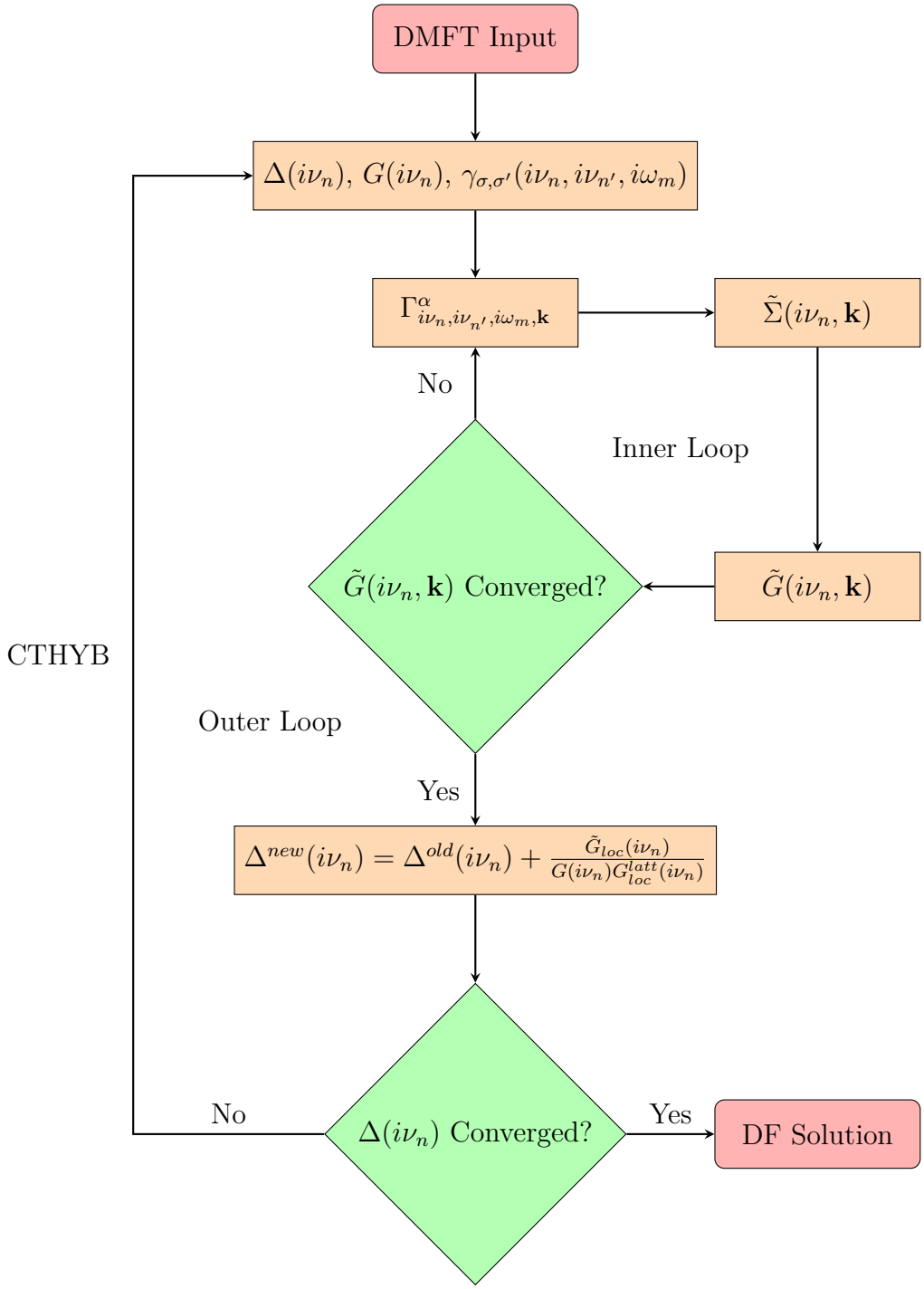

Figure 6.1: Flowchart of a dual fermion calculation showing outer and inner self-consistency loops.

hybridisation function that is then solved again until the hybridisation function and thereby the lattice self-energy converged.

The inner self-consistency loop described above has been implemented in the openDF code by Antipov et. al. [50], while the impurity model at each cycle of the outer loop is solved using the same CTHYB code modified in chapter 3. The openDF code was modified in order to be able to accept input from the CTHYB code. It was also modified in order to be able to treat problems defined on the fcc lattice as well as treat more than just nearest-neighbour hopping. In order to speed up the calculations, while solving the Bethe-Salpeter equations for each Bosonic frequency and k-point, simple parallelism was exploited making use of MPI through the Boost library [104]. The openDF code is provided with very minimal documentation and therefore significant time was spent on understanding the parameters and command-line options of the code. We also spent significant time determining the required accuracy of the input Green's functions and vertices, also how many Matsubara frequencies the input functions needed to be calculated on.

Before we go on to discuss the results and testing of the code it is worth mentioning some of the approximations made in the above approach. The first of which is that the dual interaction is truncated at the two-particle vertex (formally it consists of contributions from all n-particle vertices of the impurity model [23]). It is common practice to neglect the contributions from the higher order vertices and only a few studies have been performed where contributions from higher order vertices have been taken into account. One such study is that by Ribic et. al. where they considered the contribution of the three-particle vertex on the 2D Hubbard model [118]. They found that when the contributions from the two-particle vertex are small so are that of the three-particle vertex. However, in certain parameter regimes the contributions are not negligible and even become of the same order as that of the two-particle vertex. They find that at higher temperatures, and when doped away from half-filling, the contributions from the three-particle vertex are much smaller than those of the two-particle vertex. However, at low temperature and half-filling the contributions from the two and three-particle vertices become of

the same order. Thus, for the dual fermion calculations performed here away from half-filling around the ferromagnetic region found at the DMFT level this truncation is justified. However, it is possible that there are significant contributions from higher order vertices for the calculations performed around half-filling.

It should be noted that the calculations performed by Ribic et. al. were only performed as one-shot dual fermion calculations and were not run to self-consistency of the outer loop. This is largely due to the huge computational effort and storage requirements for the calculation of the three-particle vertex. The requirements essentially render self-consistent dual-fermion calculations taking the three-particle contribution into account currently inaccessible [119]. Even when only the two-particle vertex is taken into account the calculation of the vertex at each iteration of the outer loop is already a compute heavy task and is the bottleneck of any dual fermion calculation. When performing the calculations within this thesis the vertex calculations take on the order of days to complete, while the dual fermion calculations take on the order of hours.

The second approximation made in the above dual fermion approach is introduced by the construction of the perturbation theory of the dual self-energy. In this work we make use of the ladder approximation as implemented in the OpenDF code [50]. This approximation and has been used previously to study the anti-ferromagnetic phase transitions within the 2D and 3D Hubbard models where diagrams of this type are thought to be dominant [29, 32, 120]. The ladder dual fermion approach has also been shown to provide good results when compared with determinant Monte Carlo calculations, as well as results obtained using a diagrammatic Monte Carlo method allowing for dual diagrams to be sampled from all orders [121]. It is also thought to provide a good description of the magnons within a ferromagnetic state [23]. Thus, we believe the ladder dual fermion method to be a good choice for the construction of the dual self-energy to study the magnetic phases found in the fcc Hubbard model.

In the following sections we will cover some test calculations that were performed using the modified CTHYB solver and modified OpenDF code. These tests involve comparing the output of the new and modified codes to results obtained by

Gukelberger et. al. [121]. Following this we will go on to present the dual fermion results obtained building upon the DMFT calculations of the previous chapter.

6.2 Testing

Before performing any dual fermion calculations on the DMFT data from the fcc lattice, we needed to find out how many frequencies the input vertex functions have to be calculated on in order to obtain accurate results. To test this we first looked at the convergence of the lattice self-energy of a given dual fermion calculation with respect to the bosonic and fermionic frequency grids used. Secondly, we reproduced some results for the lattice self-energy of the Hubbard model on the square lattice from the literature. The following two subsections cover the results of these tests, starting with the choice of frequency grid.

6.2.1 Convergence of the Lattice Self-Energy

In order to test the convergence of a given dual fermion calculation with respect to the number of fermionic and bosonic frequencies used, we did some calculations in the atomic limit. This allows the input Green's functions and vertex functions to be calculated from known analytic results, removing the effect of any errors in the input from the calculation. The atomic limit single-particle Green's function is given by equation (2.38), while the hybridisation function and the vertex functions are given by:

$$\Delta(i\nu_n) = 4G(i\nu_n) \tag{6.25}$$

$$\gamma_{\uparrow,\uparrow}(i\nu_n, i\nu_{n'}, i\omega_m) = \frac{\beta U^2}{4}(\delta_{\omega_1,\omega_2} - \delta_{\omega_1,\omega_4})\Lambda_{\nu_n}\Lambda_{\nu_{n'}+\omega_m} \tag{6.26}$$

$$\begin{aligned}\gamma_{\uparrow,\downarrow}(i\nu_n, i\nu_{n'}, i\omega_m) = &-U + \frac{U^3(\omega_1^2+\omega_2^2+\omega_3^2+\omega_4^2)}{8(\omega_1\omega_2\omega_3\omega_4)^2} + \frac{3U^5}{16\omega_1\omega_2\omega_3\omega_4} \\ &+ \frac{\beta U^2}{4(1+e^{\frac{\beta U}{2}})}(2\delta_{\omega_2,-\omega_3} + \delta_{\omega_1,\omega_2})\Lambda_{\omega_2}\Lambda_{\omega_3} \\ &- \frac{\beta U^2}{4(1+e^{\frac{-\beta U}{2}})}(2\delta_{\omega_1,\omega_4} + \delta_{\omega_1,\omega_2})\Lambda_{\omega_1}\Lambda_{\omega_3}\end{aligned} \tag{6.27}$$

where $\omega_1 = \nu_n$, $\omega_2 = \nu_n + \omega_m$, $\omega_3 = \nu_{n'}$, $\omega_4 = \nu_{n'} + \omega_m$ and $\Lambda_\omega = 1 + \frac{U^2}{4\omega^2}$ as given in the following paper [50].

The input Green's functions were calculated for all combinations of $n = n' \in [4, 160]$ and $m \in [1, 16]$ for $\beta = 1.0$ using $N_k = 16$ k-points in each dimension. Note that here we are quoting the number of positive frequencies used, so the total number of frequencies in the grids are $2n$ and $2n - 1$ respectively for fermionic and bosonic grids. A calculation performing the inner self-consistency loop was then performed for each of the inputs, all of the calculations were found to converge in a small number of loops.

When judging the convergence of the calculation with respect to the frequency grids, we used the lattice self-energy plotted along the high symmetry path of the 1Bz. For the square lattice the path covers three high symmetry points and takes the following form.

$$\Gamma = (0, 0) \rightarrow X = (\pi, 0) \rightarrow W = (\pi, \pi) \rightarrow \Gamma$$

Momentum dependent functions are then plotted along this path as a function of the distance along the path. It is also worth noting that the momentum dependence of the lattice self-energy rapidly decays as a function of frequency back on the DMFT result. This is because the high-frequency momentum independent behaviour of the self-energy has to be reproduced and is already present in the DMFT result [121]. This behaviour of the lattice and DMFT self-energy is shown later in the following section. Thus, when judging the convergence of the calculations we look for convergence of the lowest Matsubara frequency of the lattice self-energy, where the momentum dependence is expected to be largest.

Figures 6.2a and 6.2b show the real and imaginary parts of the lattice self-energy plotted along the high symmetry path. These were calculated using different numbers of fermionic frequencies, however, the number of bosonic frequencies was fixed to 16. We find that there is very little dependence of the real part of the lattice self-energy on the number of fermionic frequencies used. The results are essentially indistinguishable on this scale once 16 fermionic frequencies are used.

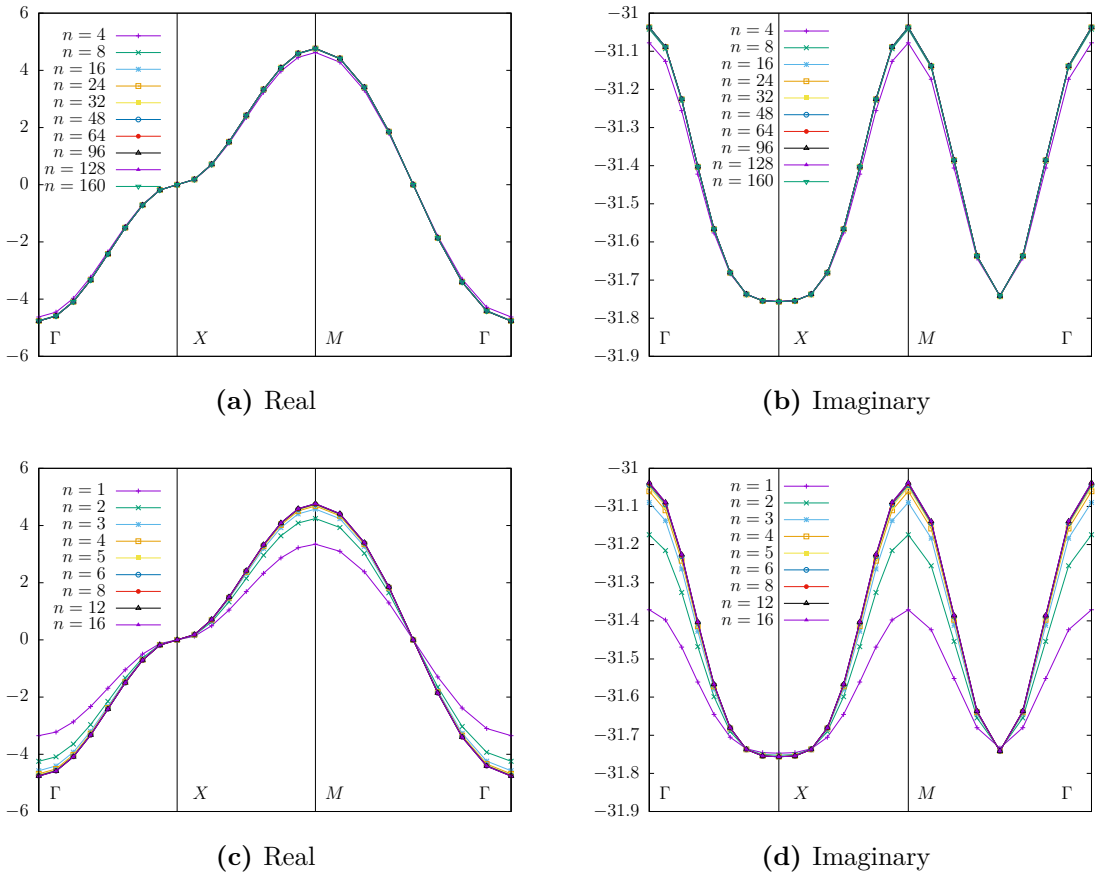

(a) Real **(b)** Imaginary

(c) Real **(d)** Imaginary

Figure 6.2: Plots of the real and imaginary parts of $\Sigma(\mathbf{k}, i\nu_0)$ plotted along the high symmetry path of the 1Bz for atomic limit input Green's functions. Top: fixed number of bosonic frequencies (16) and varying numbers of fermionic frequencies. Bottom: fixed number of fermionic frequencies (160) and varying numbers of bosonic frequencies.

This is in line with what was found in the performance analysis of Antipov where the normalised difference in the lattice self-energy at the center of the 1Bz was found to be on the order of $\sim 10^{-5}$ for $n \sim 10$ fermionic frequencies and above [50].

This behaviour can be somewhat understood by considering that the input impurity vertexes are only used in conjunction with the dual Green's function which decays rapidly as a function of frequency [5]. Thus, we would expect the high-frequency parts of the input vertex functions to be highly suppressed and not provide much of a contribution to the dual fermion result. Hence, we observe rapid convergence of the lattice self-energy with respect to frequency grid.

Figures 6.2c and 6.2d show the real and imaginary parts of the lattice self-energy plotted along the high symmetry path calculated using different numbers

of bosonic frequencies with the number of fermionic frequencies fixed to 160. We find a much stronger dependence on the number of bosonic frequencies used in both the real and imaginary parts of the lattice self-energy. However, again we find rapid frequency convergence, with the results being essentially indistinguishable on this scale once 6 bosonic frequencies are used.

From the above we are able to tell that in order to obtain accurate results we only require relatively small numbers of frequencies. However, these calculations were performed only at one temperature and the frequencies are temperature dependent. Thus, at lower temperatures where the spacing between the frequencies gets smaller we will require larger numbers of frequencies. In the following work it was chosen that for all calculations the largest fermionic frequency must have an absolute value larger than 100. This ensures that the vertices and Green's functions have decayed enough and all relevant information is captured.

We now turn our attention to using the above information in order to replicate results from the literature in order to test if the modified CTHYB and OpenDF codes are able to produce accurate results away from the atomic limit.

6.2.2 Reproducing Results From The Literature

Gukelberger et. al. studied the Hubbard model on the square lattice using the dual fermion method in a paper where they introduce a diagrammatic Monte Carlo method for sampling dual fermion diagrams [121]. Within this paper they also present results for dual fermion calculations using the ladder approximation, as well as the self-consistent ladder approximation used within this project. Gukelberger et. al. found that the self-consistent ladder approximation was able to accurately reproduce results for the lattice self-energy for a wide range of parameters when compared with numerically exact determinant Monte Carlo calculations. Thus, being able to reproduce the above results serves as a good test that the code produced and modified for this project is able to perform dual fermion calculations accurately.

In order to reproduce the results DMFT calculations were performed for $\beta = 2.0$ ($T = 0.5$) at half filling ($\mu = \frac{U}{2}$) with Coulomb interactions of $U = 4.0$ and 8.0.

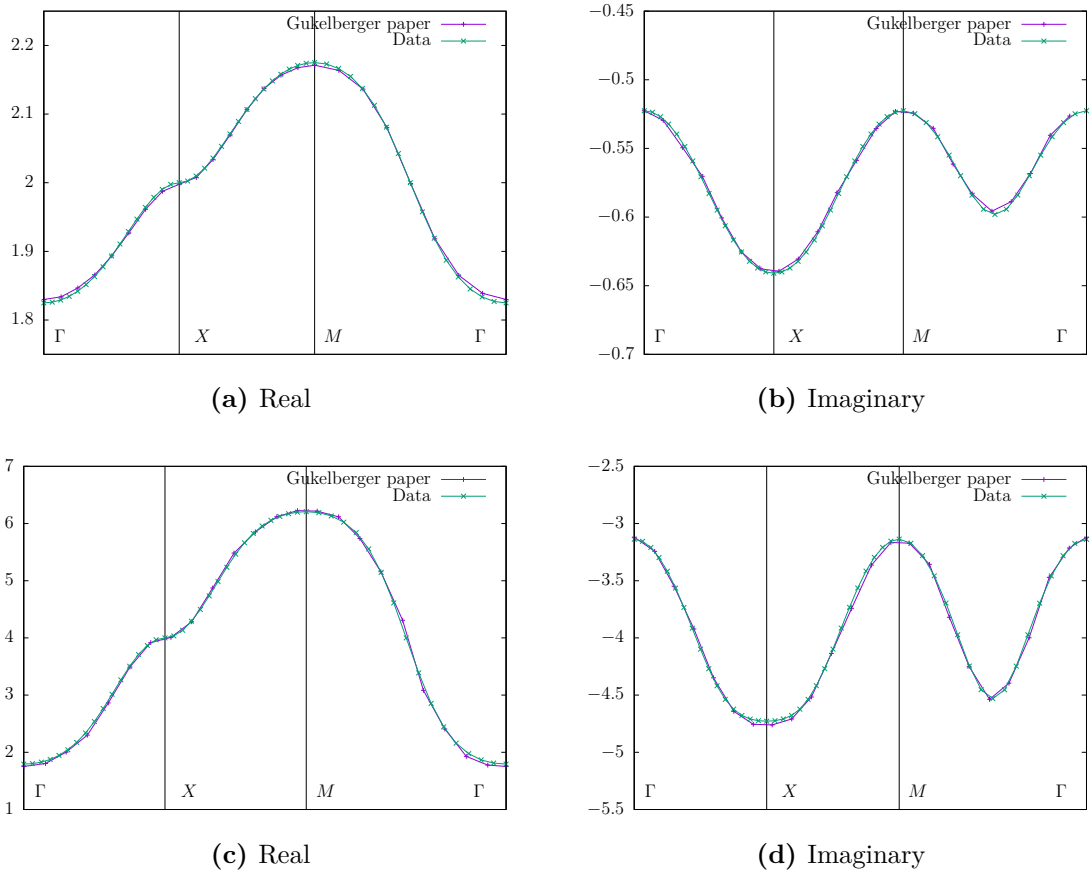

(a) Real **(b)** Imaginary

(c) Real **(d)** Imaginary

Figure 6.3: Plots of $\Sigma(\mathbf{k}, i\nu_0)$ along the high symmetry path of the 1Bz. Results are calculated at $\beta = 2.0$ for $U = 4.0$ (Top) and $U = 8.0$ (bottom). Reference data is reproduced from figures 5 and 6 of this paper by Gukelberger et. al. [121].

The two-particle Green's functions and corresponding vertex functions were then calculated and the ladder dual fermion self-consistency procedure was performed. The vertex functions were calculated on a frequency grid consisting of 15 positive fermionic frequencies and 3 positive bosonic frequencies. It was found that for both values of the Coulomb interaction the calculation converged relatively quickly, the results essentially converged after just three outer self-consistency loops. However, this was to be expected for these cases due to the the self-consistent result laying very close to that of the single loop calculation, as shown in the paper.

In figure 6.3 we plot the lowest positive Matsubara frequency of the self-energy along the same high symmetry path of the 1Bz described in the section above, this reproduces figures 5 and 6 from the paper. We find that we are able to reproduce

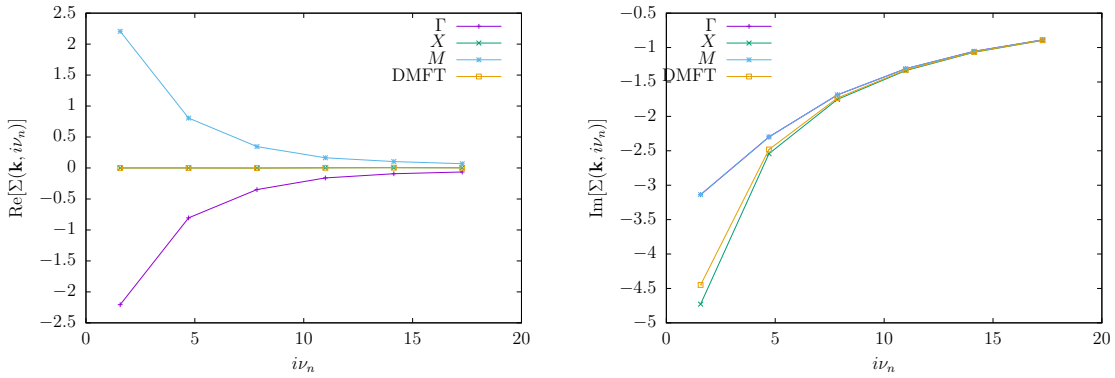

(a) Real **(b)** Imaginary

Figure 6.4: Plots of the low-frequency part of $\Sigma(\mathbf{k}, i\nu_n)$ at the high symmetry points of the 1Bz plotted alongside the DMFT Self-energy. Results are calculated at $\beta = 2$ for $U = 8$ at half-filling.

the momentum dependence of the lattice self-energy remarkably well for both values of the Coulomb interaction. (There are some very small deviations between our data and that of the paper, however, this could be due to the process used to extract the data from the paper.) The data from the paper have also been found to agree very well with numerically exact results from determinant Monte Carlo calculations. This shows that the self-consistent ladder dual fermion method can produce remarkably accurate results, and somewhat justifies the approximations made in this dual fermion approach [121]. Also, this displays the ability of the dual fermion method to produce accurate results even when the input Green's functions are calculated on relatively small frequency grids. From the above we can determine that we are able to perform accurate dual fermion calculations using the CTHYB and dual fermion codes modified as part of this thesis.

Earlier it was mentioned that the momentum dependence of the lattice self-energy decays rapidly as a function of frequency back onto the momentum independent DMFT result. This behaviour is displayed in figure 6.4 where we have plotted the DMFT result alongside the value of the lattice self-energy at the high symmetry points as a function of frequency. We find that, for the parameters shown here, essentially all momentum dependence for both the real and imaginary parts has decayed, even by the fifth Matsubara frequency. Thus, all the momentum

dependent corrections to the self-energy provided by this dual fermion approach have been captured.

Now that we have shown that the code is able to accurately reproduce results from the literature, we are in a position to start performing dual fermion calculations on the DMFT results of the previous chapter. The results of which form the basis of the rest of this chapter.

6.3 Ferromagnetic Instability

In this section we present results of dual fermion calculations obtained as part of this thesis covering the range of fillings over which a ferromagnetic instability was found using the DMFT method (see section 5.4). We will show plots of the lattice self-energy as well as the updated hybridisation functions, then present results for the magnetic susceptibility throughout the 1Bz. Following this we will show the predicted phase boundary of the dual fermion results, and compare this with the DMFT phase boundary.

6.3.1 Lattice Self-Energy and Hybridisation Functions

Calculations were performed for fillings in the range $n \in [1.1, 1.9]$ at temperatures of $T \in [0.6, 0.2]$ ($\beta \in [1.66, 5.0]$), starting from the DMFT results obtained in section 5.4. All the calculations converged well and fairly rapidly in 3-6 outer self-consistency loops. This is demonstrated in figures 6.5 and 6.6 where the lattice self-energy and the updated hybridisation function are plotted as a function of loop number. The data are shown for a filling of $n = 1.3$ at three temperatures covering the full range.

Figure 6.5 shows the real and imaginary parts of the lattice self-energy. We find that, in all cases, by loop two the result has essentially converged with subsequent loops making much smaller corrections. The result of the first loop is the dual fermion result from the DMFT hybridisation function. The second loop is the first time an update to the hybridisation has been taken into account and the impurity model is modified. Both the real and imaginary parts of the lattice self-energy take values in a larger range as the temperature decreases. This indicates the

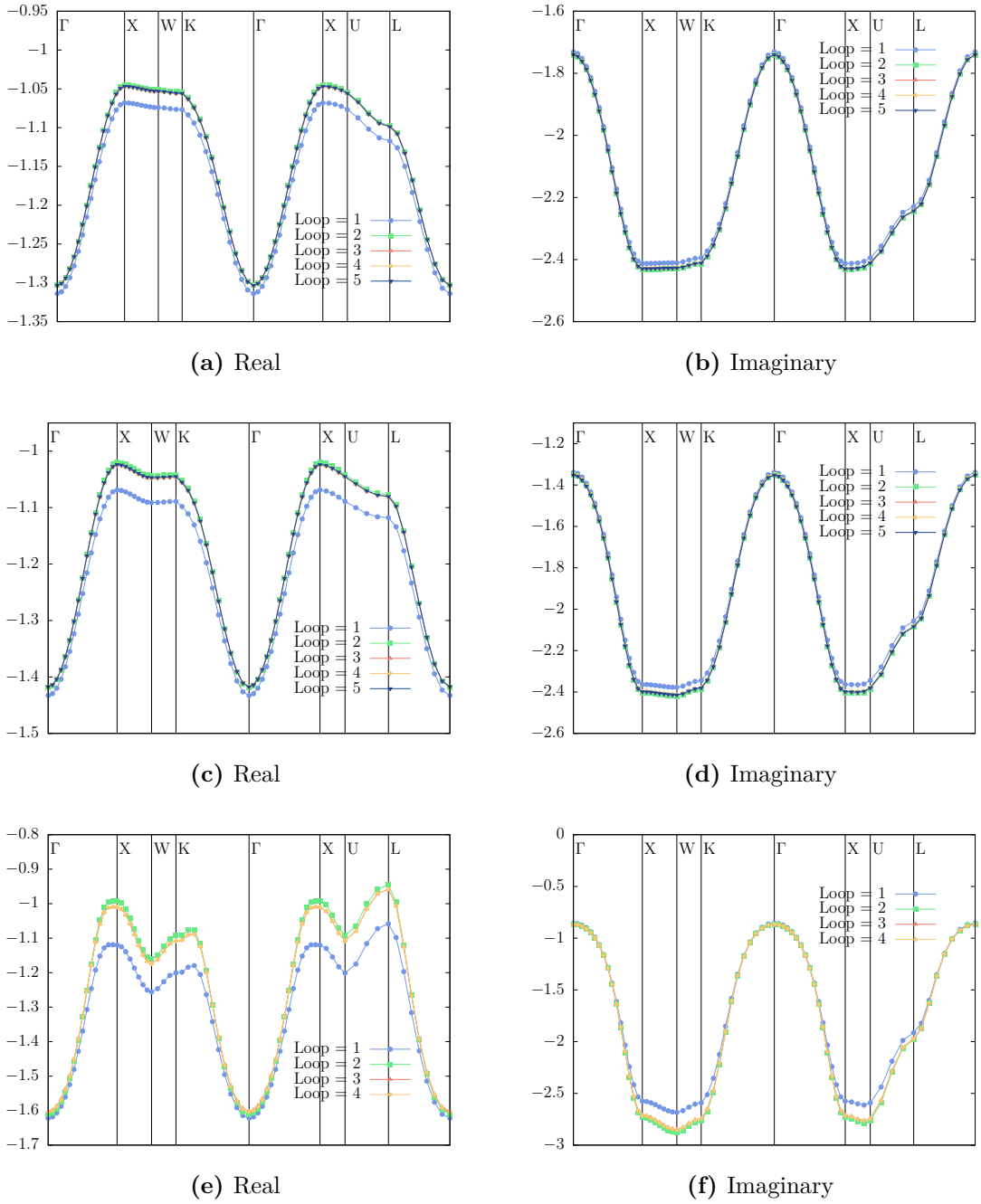

(a) Real **(b)** Imaginary

(c) Real **(d)** Imaginary

(e) Real **(f)** Imaginary

Figure 6.5: Plots of $\Sigma(\mathbf{k}, i\nu_0)$ along the high symmetry path of the 1Bz for a filling of $n = 1.3$ showing convergence of the outer self-consistency loop. Top: $\beta = 1.66$ ($T = 0.6$), middle: $\beta = 2.5$ ($T = 0.4$) and bottom: $\beta = 4.0$ ($T = 0.25$).

momentum dependence is becoming stronger at lower temperatures, i.e. the non-local corrections provided by the dual fermion calculations are most relevant at lower temperatures and closer to the transition. As the temperature is lowered we find that all of the features present at higher temperatures remain, and do not change dramatically. Interestingly at the lowest temperature shown here, just above the transition, we find the formation of a peak around the L point in the real part, as well as peak between the K and Γ point. While this is an interesting result we are not sure if it holds any physical significance.

Figure 6.6 shows the updated hybridisation functions alongside the DMFT result for the same calculations as in figure 6.5. We find that the biggest correction to the DMFT hybridisation function results from the first dual fermion loop, with subsequent loops making smaller and smaller corrections. This is also what was found by Gukelberger et. al. [121]. They found that the dual fermion ladder result was relatively close to the self-consistent ladder result. The self-consistency provides a smaller correction over the first loop result bringing the results more in line with the essentially exact DDMC results. We find that all of the updates to the hybridisation are very focused within the low-frequency region, and the DMFT result is unchanged at higher frequencies. However, corrections do occur at increasingly larger frequencies as the temperature is lowered. This behaviour is the same as what was shown for the lattice self-energy in section 6.2.2 where the DMFT results were unchanged due to the Green's functions taking the form of the high-frequency tails.

Figure 6.7 shows the converged lattice self-energy for three fillings at all temperatures calculations were performed at. Here we can see that the momentum dependence increases as the temperature is lowered and is largest in the imaginary part. We also find that as the temperature is lowered the values are shifted, while the momentum dependence takes on the same form. This is largely due to the change in the value of the DMFT result at the lowest frequency, as well as the change in the value of the lowest frequency itself. We also find that the momentum dependence decays as we increase the filling until, for very large fillings, the momentum dependence has all but disappeared and we essentially obtain the

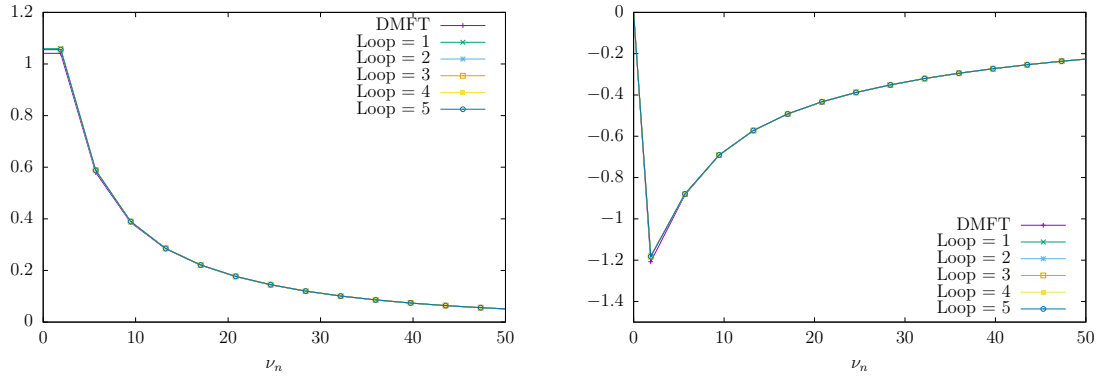

(a) Real **(b)** Imaginary

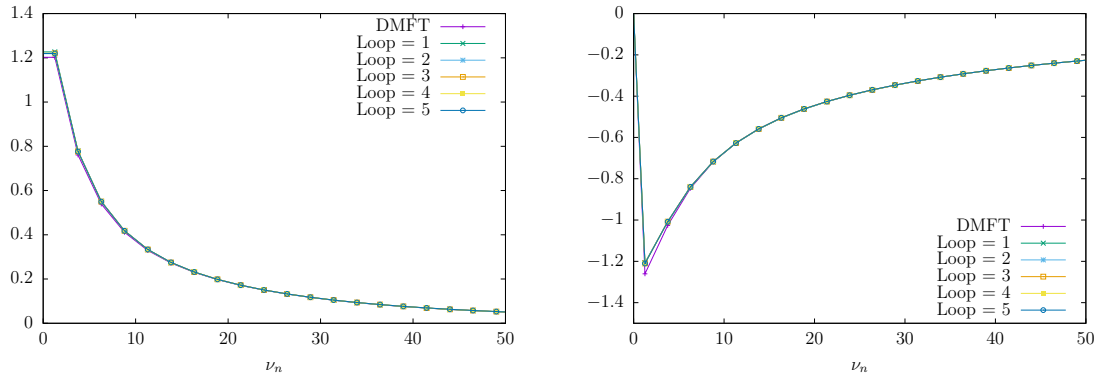

(c) Real **(d)** Imaginary

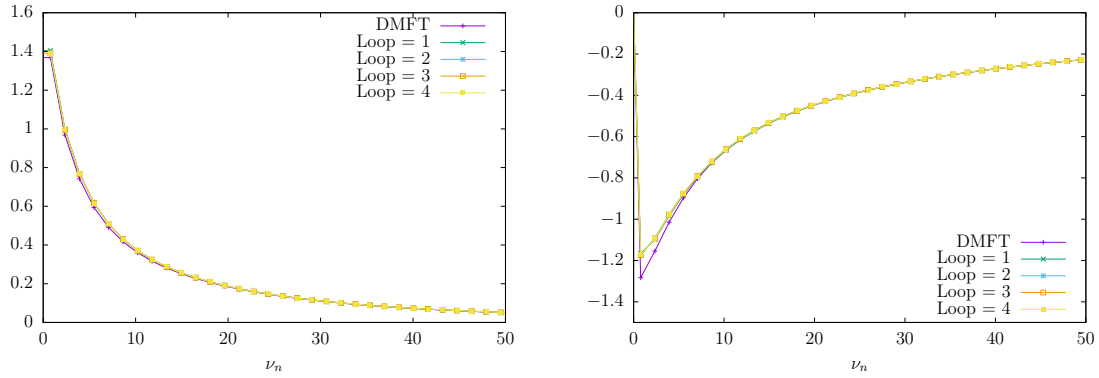

(e) Real **(f)** Imaginary

Figure 6.6: Plots of the hybridisation $\Delta(i\nu_n)$ for a filling of $n = 1.3$ showing convergence of the outer self-consistency loop. Top: $\beta = 1.66$ ($T = 0.6$), middle: $\beta = 2.5$ ($T = 0.4$) and bottom: $\beta = 4.0$ ($T = 0.25$).

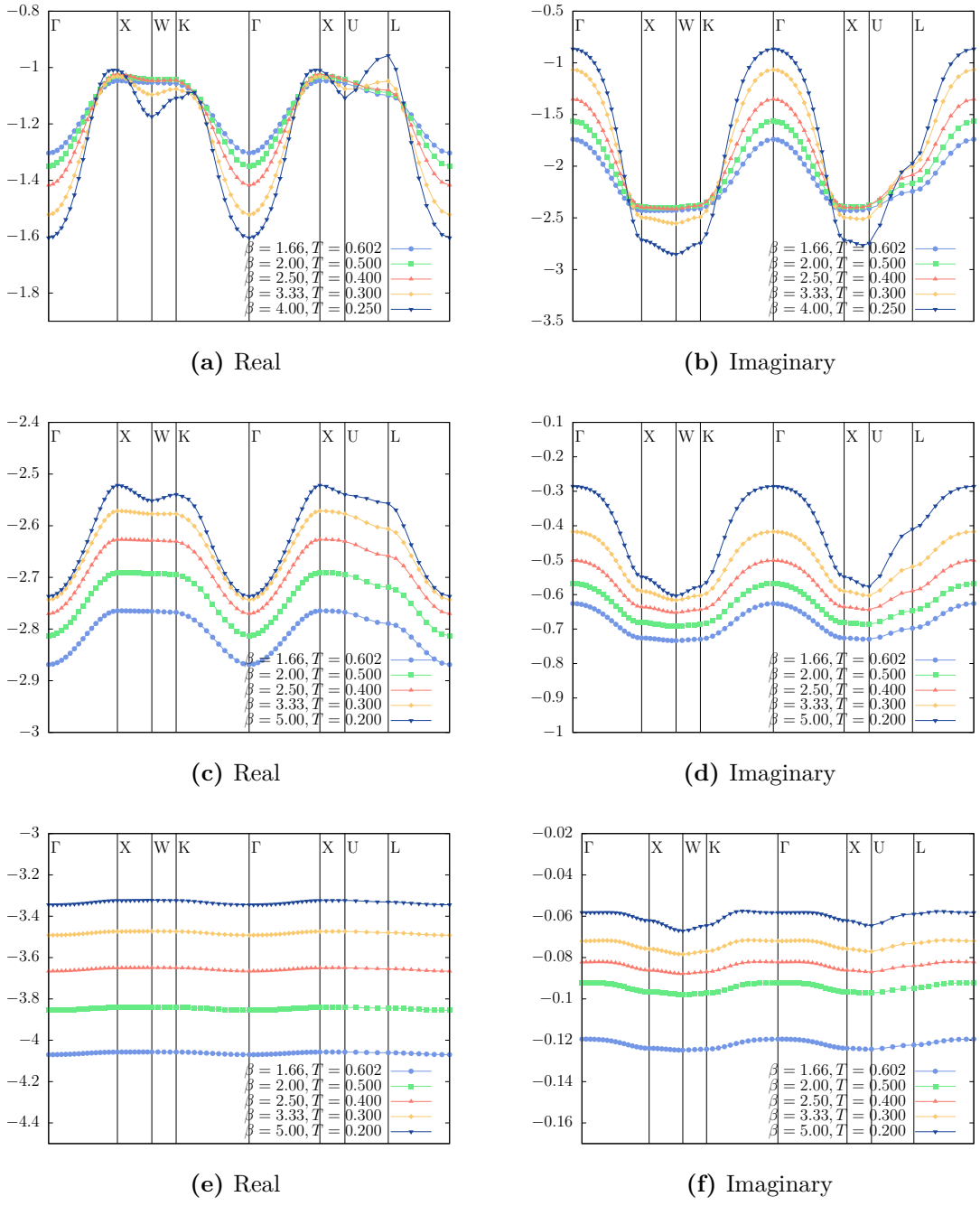

(a) Real **(b)** Imaginary

(c) Real **(d)** Imaginary

(e) Real **(f)** Imaginary

Figure 6.7: Plots of the converged lattice self-energy $\Sigma(\mathbf{k}, i\nu_0)$ along the high symmetry path of the 1Bz for three fillings at differing temperatures. Top : $n = 1.3$, middle $n = 1.6$ and bottom : $n = 1.9$.

DMFT result. The lack of momentum dependence for these higher fillings suggests that approximation that the self-energy is purely local is partially valid in this parameter region. This indicates that we would expect DMFT to perform well in this region, and any corrections to the DMFT phase boundary at higher fillings to be small. This is what we would expect for large fillings due to the low mobility of electrons near full occupation. Also, as shown in section 5.4.3, we find that the DMFT spectrum tends to that of the non-interacting case, indicating that non-local corrections should be negligible.

Once the dual fermion calculations have converged, an additional dual fermion calculation is performed in order to calculate the magnetic susceptibility [120]. The results of these calculations and the subsequently determined phase boundary are the topics of the following section.

6.3.2 Magnetic Susceptibility

Figure 6.8 shows the magnetic susceptibility along the high symmetry path of the 1Bz for three fillings where a ferromagnetic instability was found. We find that the profile of the susceptibility remains largely similar to that of the DMFT results and an instability towards a ferromagnetic state is the only divergence present. From the results shown here it is clear that the divergence at the Γ point is largest around a filling of 1.3 and decays rapidly as the filling is increased. This is again very similar to the DMFT results and suggests that any changes to the DMFT phase diagram in this region will be quantitative only.

While performing the dual fermion calculations it was found that, at lower temperatures, close to the phase boundary, the filling of the converged solution was no longer fixed at the DMFT value and had drifted slightly. This is to be expected given the outer self-consistency loop makes modifications to the hybridisation function and therefore the non-interacting Green's function supplied to the impurity solver. This has also been observed by Ribic et. al. when performing self-consistent dual fermion calculations on the 2D Hubbard model away from half-filling [119]. This is due to the self-consistent solution no longer reproducing the static part of

the self-energy ($\frac{U}{2}n$) [122]. This deviation in the filling becomes largest when we get closest to the phase boundary where the non-local corrections of the dual fermion calculations, and therefore modifications to the DMFT hybridisation function, are largest. However, the changes to the filling are still relatively small, with the largest deviation being on the order of 0.02.

Figure 6.9 shows the surface created by plotting the magnetic susceptibility at the Γ point (solid circles) Vs. n and T. As can be seen this is a smoothly varying surface showing no evidence of discontinuities or rapid changes in value. Thus, in order to account for the changes in the filling, we are able to fit a surface to the susceptibility data. This allows us to interpolate from the magnetic susceptibility data and generate datasets at fixed filling. The resulting fitted surface is shown in figure 6.9 (red wireframe). From this surface we are able to make accurate predictions of the susceptibility close to the data points. The interpolated values are shown in the plot (green crosses): they lie close to the data points from the calculations. A linear fit to this data is also shown (green lines) displaying the linear behaviour of the susceptibility. We are then able to perform the same analysis on the susceptibility data as was performed for the DMFT calculations, allowing us to extract estimates of the critical temperatures. The estimates of the critical temperatures are shown plotted on the base of the plot (filled black squares). A more detailed plot of the phase boundary can be found in figure 6.11 alongside the corresponding DMFT phase boundary found in the previous chapter.

Figure 6.10 shows the magnetic susceptibility at the Γ point for a fixed filling obtained from the above procedure, along with fits to the data. The susceptibility still diverges linearly despite the inclusion of non-local correlation, and remarkable agreement with a linear model is achieved. It is possible that the susceptibility diverges more rapidly very close to the transition. For fillings in the range, $n \in [1.3, 1.5]$, the lowest temperature shown here is already rather close to the predicted transition temperature, however, there are no signs of deviation from the linear behaviour seen at higher temperatures.

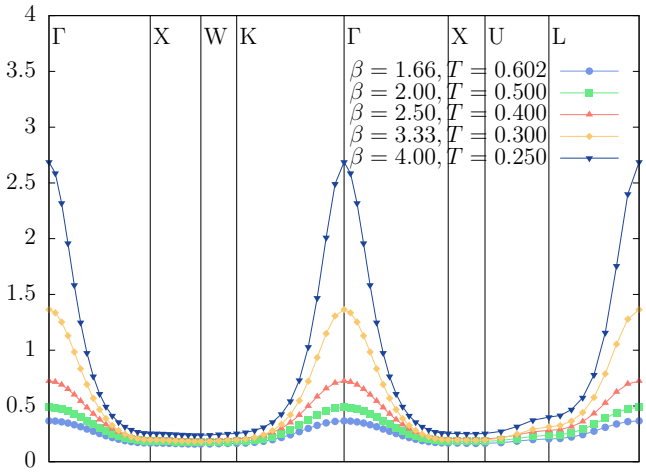

(a) $n = 1.3$

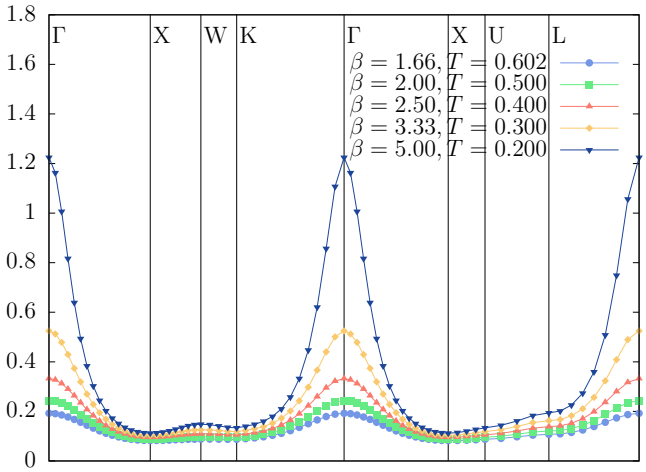

(b) $n = 1.6$

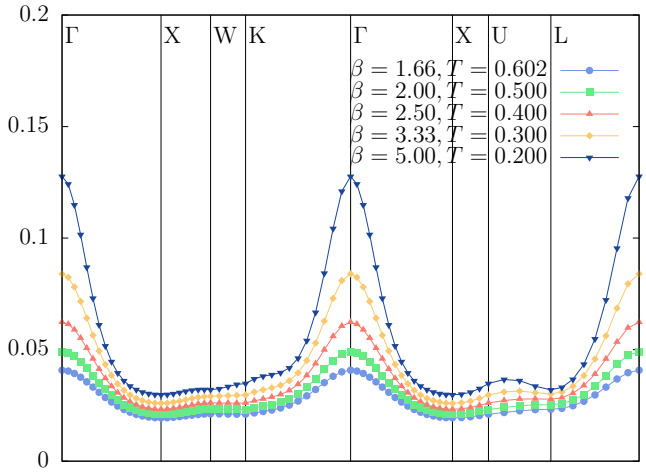

(c) $n = 1.9$

Figure 6.8: Plots of the magnetic susceptibility along the high symmetry path of the 1Bz for converged dual fermion calculations performed at three fillings.

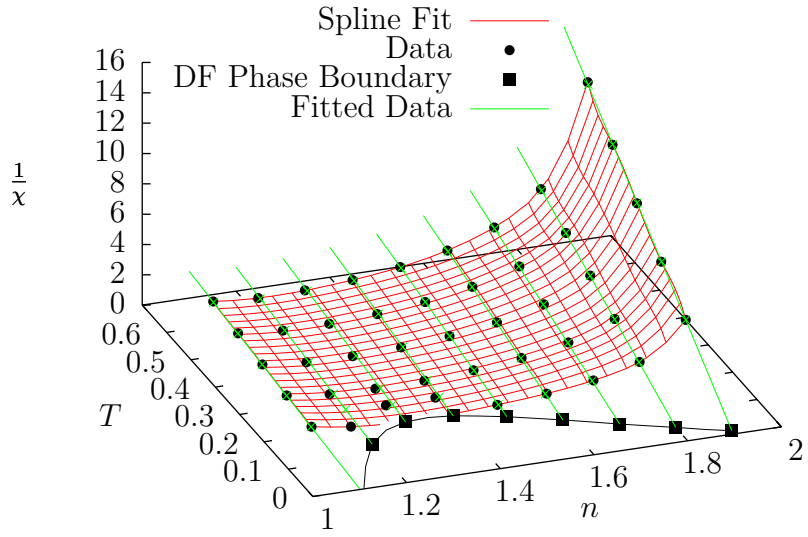

Figure 6.9: Surface plot of $(\frac{1}{\chi^m(\Gamma,0)}, T, n)$ showing one over the magnetic susceptibility at the Γ point, the fitted surface, the corresponding susceptibility data at constant filling and the linear fits to the susceptibility predicting the ferromagnetic phase boundary.

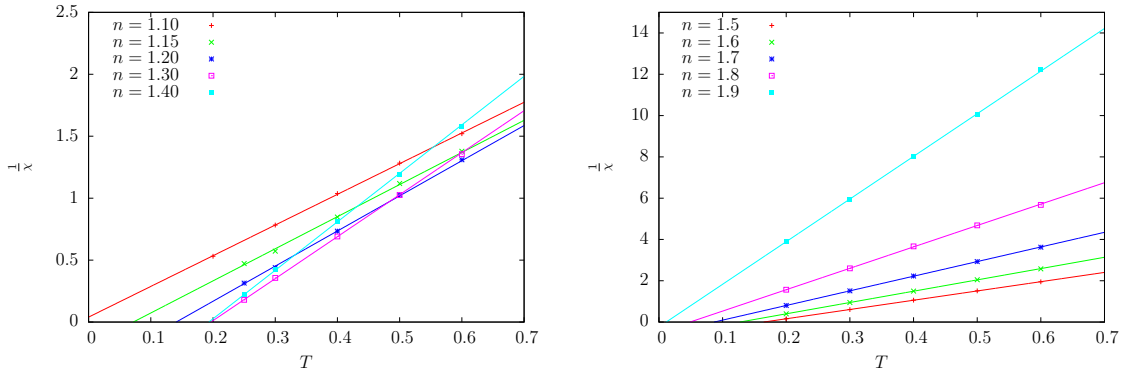

(a) $n \leq 1.4$ **(b)** $n > 1.4$

Figure 6.10: Plots showing the magnetic susceptibility data at constant filling determined from the spline surface of Figure 6.9 along with linear fits to the data.

Taking the predicted T_c values from the fits shown in figure 6.10 and plotting them in the (n, T) plane we can compare the DMFT and dual fermion phase boundaries. The errors shown on the dual fermion phase boundary are estimated in the same way as the DMFT phase boundary and represent the error from the fitting procedure and therefore estimation of T_c. We find that the errors in the dual fermion phase boundary are generally larger than that of the DMFT phase boundary. This is partially due to the critical temperatures involved being smaller and therefore further away from the susceptibility data, but also partially due to the surface fitting procedure described above.

We would expect there to be a reduction in the critical temperatures given that a mean field treatment generally overestimates critical temperatures. For example, Wahle et. al. used Hartree-Fock and DMFT to study the stability of itinerant ferromagnetism in the Hubbard model on a modified version of the Bethe lattice where the asymmetry of the density of states was able to be tuned [54]. They found that Hartree-Fock grossly overestimates the critical temperature for the ferromagnetic phase by over an order of magnitude compared to DMFT. They also note, given that the inclusion of local correlation by DMFT results in a reduction of the critical temperature it is not unreasonable to expect that the inclusion of non-local correlations missed by DMFT would reduce the critical temperatures further [54].

We find that the overall shape of the phase boundary is largely unchanged by the inclusion of non-local correlation and the corrections provided by the dual fermion calculation are quantitative. In general there is a reduction in the critical temperature across the full region, with the largest corrections occurring for the highest critical temperatures. From our calculations it appears that the lower and upper fillings above and below which we find the ferromagnetic region appear are unchanged. To within errors in the fitting procedure the dual fermion and DMFT phase boundaries tend back towards each other around the endpoints of the region. This is somewhat expected at the upper critical filling where we find the model becomes largely non-interacting in character, thus, we would already

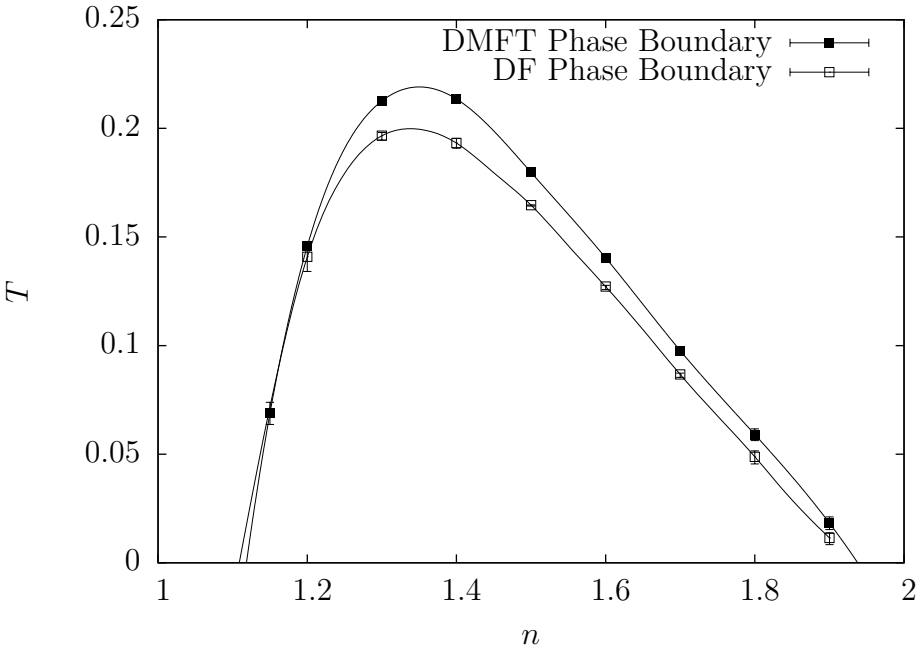

Figure 6.11: A Plot of the predicted dual fermion ferromagnetic phase boundary with errors alongside the corresponding DMFT phase boundary.

expect a DMFT treatment to work relatively well. As seen in figure 6.7 above, the dual fermion treatment of the model results in very little momentum dependence of the self-energy, indicating that the non-local corrections are small, thus, we obtain essentially the same result as DMFT.

6.4 Anti-Ferromagnetic Instability

In this section we will cover the dual fermion calculations performed for fillings covering the AFM region found using the DMFT method in section 5.5. We begin by presenting the updated hybridisation functions and the converged lattice self-energies, as well as discussing some problems encountered when performing the calculations. We then present the magnetic susceptibility data and the phase boundary predicted from the dual fermion results.

Calculations were performed for fillings in the range $n \in [0.85, 1.05]$ across the following temperature range $T \in [0.2, 0.6]$. In contrast to the calculations performed around the ferromagnetic instability we were unable to converge some calculations at lower temperatures. We found that for fillings at and close to

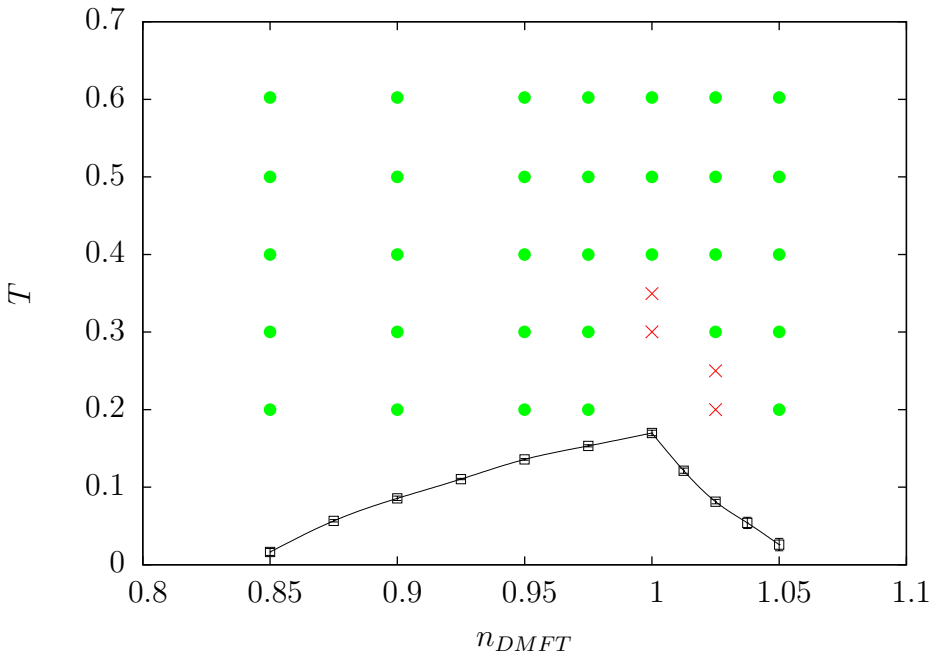

Figure 6.12: A plot showing the values of the filling and temperature for which dual fermion calculations were able to be converged (green circles) as well those for which it was not (red crosses). Shown for reference is the DMFT phase boundary.

half-filling the dual fermion code was unable to solve the Bethe-Salpeter equation using matrix inversion. This was due to the determinant of the associated matrix becoming complex or negative, indicating that the solution is out of the region of convergence for the ladder approximation [50]. The OpenDF code does allow one to solve the Bethe-Salpeter equations iteratively instead in the hope that in the subsequent loop the equation is solvable through inversion. However, we found that the problem persisted and often led to lattice self-energies exhibiting discontinuities or non-analytic behaviour. Thus, we were unable to obtain converged solutions for some fillings at lower temperatures. The fillings and temperatures for which the calculation was able to converge (green circles) and was not able to converge (red crosses) are summarised in figure 6.12.

The region where this problem was found to be worst was at half-filling below a temperature of 0.4 ($\beta = 2.5$): this is where we would expect anti-ferromagnetic fluctuations to be the largest. It has been noted before by Otsuki et. al., when performing dual fermion calculations on the 2D Hubbard model at half-filling, that

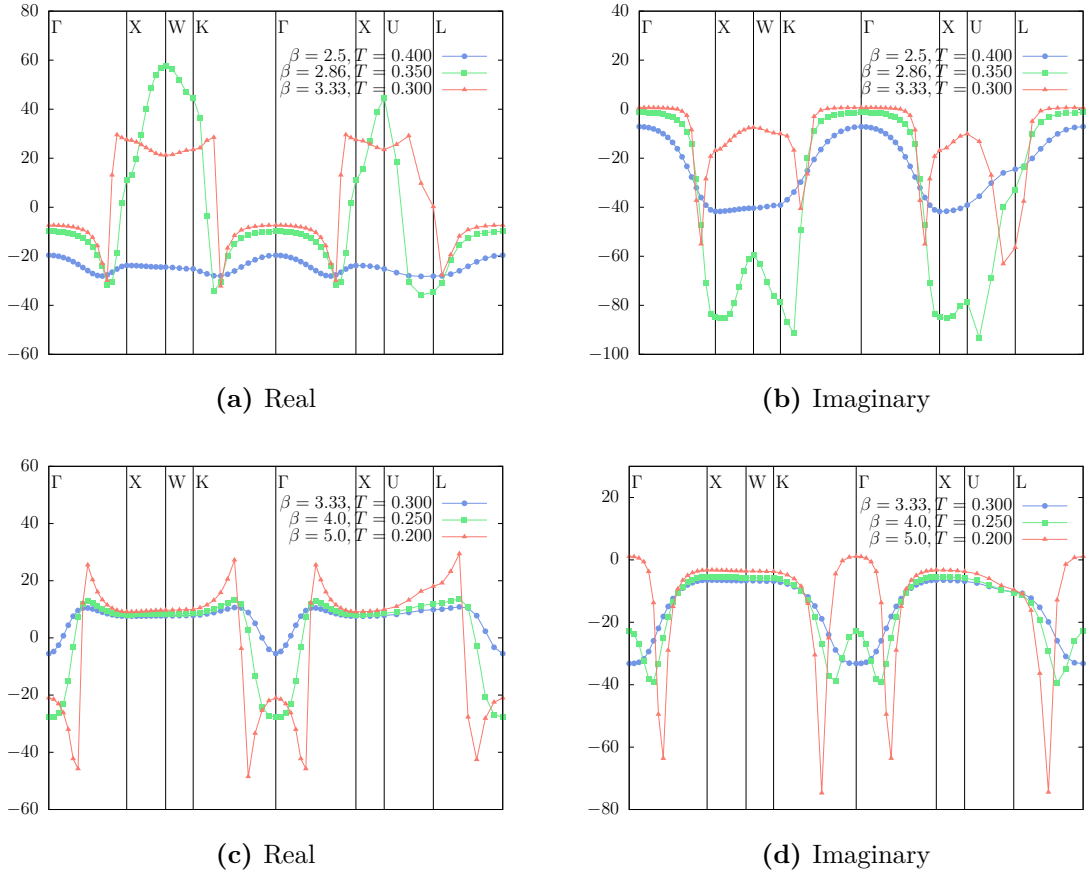

(a) Real **(b)** Imaginary

(c) Real **(d)** Imaginary

Figure 6.13: Plots of loop one lattice self-energy where the Bethe-Salpeter equation was solved using the iterative method and non-analytic results were obtained. Top : $n = 1.0$, bottom : $n = 1.025$. Note: the highest temperature on each graph shows the corresponding loop one result from a calculation that was able to be solved through matrix inversion for reference.

close to the critical temperature the convergence of the self-energy can become troublesome [5]. Within the paper the authors suggest using a method used to treat a similar problem that arises when using the FLEX method. They manipulate the eigenvalues at each iteration such that calculation does converge. After convergence is achieved they check that the solution obtained does lie within the region of convergence of the ladder approximation. If it does they conclude that the problems were caused by instability and that the converged solution is the true solution. However, we have not tried this method and instead used the iterative method described above and in the paper accompanying the OpenDF code [50].

Figure 6.13 shows plots of lattice self-energy for calculations where the Bethe-

Salpeter equation was unable to be solved through inversion. Note that the highest temperature shown on each of the graphs shows the loop one results for a temperature at which the solutions were able to be obtained using inversion and the self-energy showed no non-analytic behaviour. Figures 6.13a and 6.13b show the results for half-filling. It is clear that the two solutions obtained using the iterative method show non-analytic behaviour with both the real and imaginary parts cutting back on themselves. This behaviour is also evident in the results for $n = 1.025$, non-analytic behaviour is also observed in the imaginary part for $\beta = 5.0$ where the self-energy takes a value above zero around the Γ point.

The calculations that were able to converge did so within 3 - 7 outer loops. Calculations closer to half-filling, and at lower temperatures, required more loops to converge. Again the largest corrections were found to occur on the first loop, with subsequent loops providing smaller corrections. The following section covers the lattice self-energies and updated hybridisation functions obtained from the converged solutions.

6.4.1 Lattice Self-Energy and Hybridisation Functions

Figure 6.14 shows the converged updated hybridisation functions for three fillings at and around half-filling. We again find that most of the modifications to the hybridisation are focused around the low-frequency region with the high-frequency behaviour varying very little with temperature. Largely all of the converged solutions take the same functional form, however, sampled at the relevant Matsubara frequencies for the temperature. This is the same behaviour that is seen in the DMFT hybridisation functions. This behaviour is especially evident for a filling of $n = 0.975$ where there are only small changes to the low-frequency region of the imaginary part as the temperature is lowered. However, at half-filling and $n = 1.025$, we find that the behaviour at low-frequency changes much more with temperature. This is especially evident in the real part at half-filling and the imaginary part for $n = 1.025$. The largest modifications to the hybridisation function appear at half-filling where

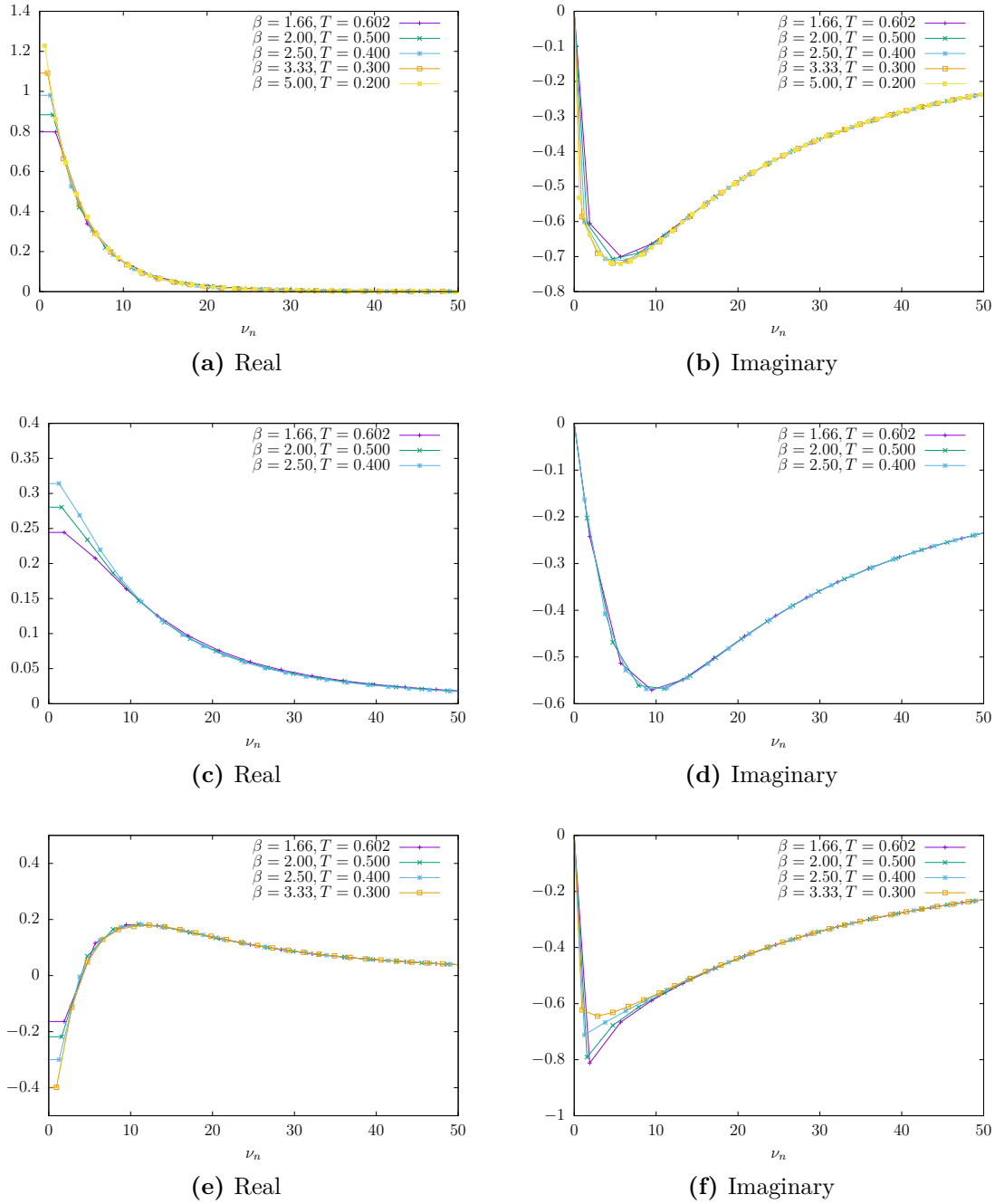

(a) Real **(b)** Imaginary

(c) Real **(d)** Imaginary

(e) Real **(f)** Imaginary

Figure 6.14: Plots of converged hybridisation functions $\Delta(i\nu_n)$ for three fillings. Top : $n = 0.975$, middle : $n = 1.0$ and bottom : $n = 1.025$.

we would expect the non-local corrections to be largest. As a result we find this is where the largest momentum dependence of the lattice self-energy is found.

Figure 6.15 shows the real and imaginary parts of the lattice self-energy for the converged solutions at the same three fillings. We find that the momentum dependence shown in both the imaginary and real parts is much larger than what was observed at higher fillings around the ferromagnetic instability. This demonstrates that in this region of the phase diagram the non-local corrections to DMFT are large and important as the self-energy is shown here to strongly depend on momentum. The momentum dependence at half-filling is over an order of magnitude larger than what was observed for any filling when studying the ferromagnetic instability. It is even significantly larger than the values obtained for the close by filling of $n = 0.975$. From the plots of the lattice self-energy we would expect the largest corrections to the phase diagram to occur at half-filling, with the corrections becoming smaller as we move away from half-filling, and less momentum dependence is observed.

It is interesting that the functional form of the real part changes as the temperature is lowered, this was not observed around the ferromagnetic instability. For $n = 1.025$ we find that a drop appears in the real part around the Γ point as the temperature is lowered. It is also interesting that at lower fillings we find the imaginary part of the lattice self-energy shifting and the momentum dependence increasing slightly when the temperature is lowered. However, at half-filling and just above we find only an increase in the momentum dependence with little to no shift present,despite the change in the value of the Matsubara frequency with temperature.

6.4.2 Magnetic Susceptibility

Before we present the results of the calculation of the magnetic susceptibility from the above dual fermion calculations, we will quickly discuss some results from the literature for the 2D and 3D Hubbard models, where anti-ferromagnetic phase transitions have previously been studied.

A paramagnetic to anti-ferromagnetic transition has previously been studied in the 2D Hubbard model using the second-order approximation dual fermion method

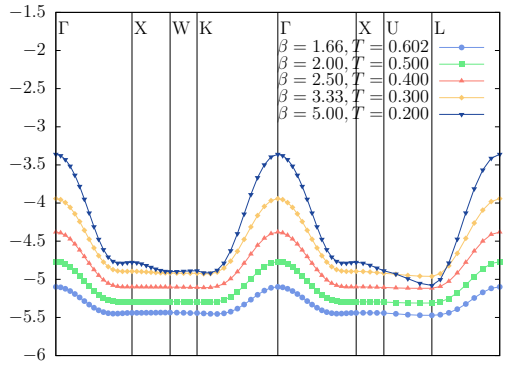

(a) Real

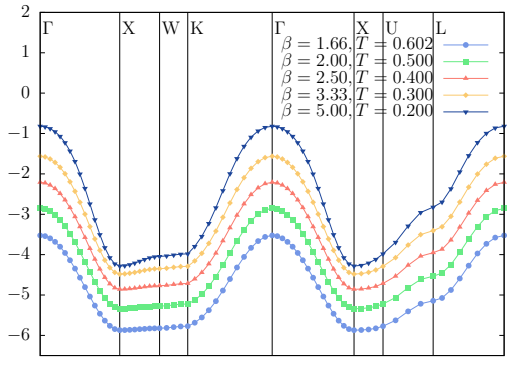

(b) Imaginary

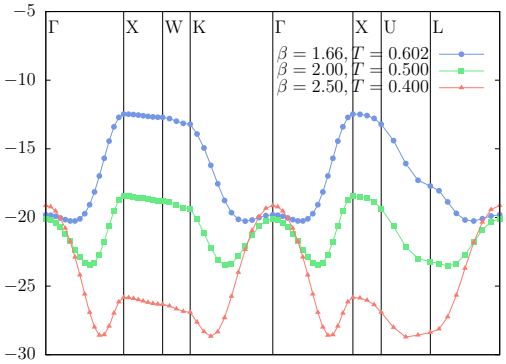

(c) Real

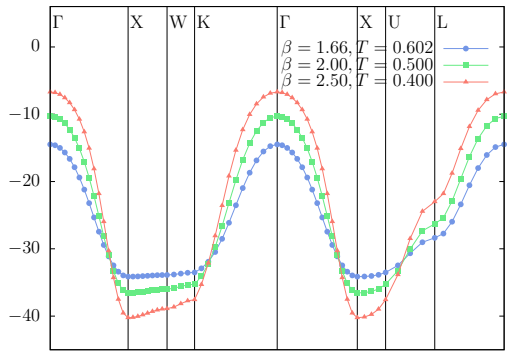

(d) Imaginary

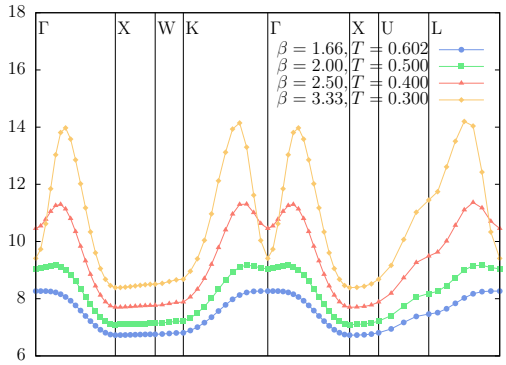

(e) Real

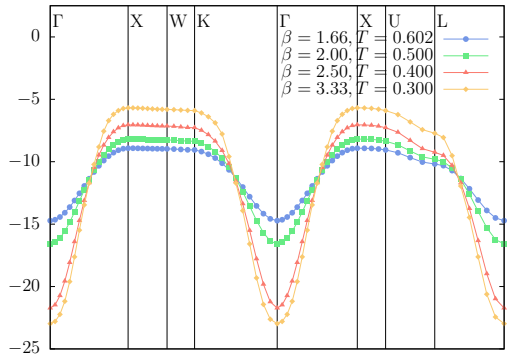

(f) Imaginary

Figure 6.15: Plots of the converged lattice self-energy $\Sigma(\mathbf{k}, i\nu_0)$ along the high symmetry path of the 1Bz for three fillings at differing temperatures. Top : $n = 0.975$, middle $n = 1.0$ and bottom : $n = 1.025$.

by Rubtsov et. al. [26]. The papers found that when a second order approximation to the dual self-energy is employed the critical temperature is decreased from the DMFT value. The ladder approach employed by Hafermann et. al. further improved upon the results bringing them in line with quantum Monte Carlo calculations [6]. However, the finite temperature transition at half-filling is known to be an artefact of the DMFT method and it is forbidden by the Mermin-Wagner theorem, the AFM state is only found at $T = 0$ [21]. A subsequent study, by Otsuki et. al., using a ladder dual fermion approach, found that the Nèel temperature at half-filling was zero as predicted by the Mermin-Wagner theorem, correcting the $T_N \neq 0$ result obtained from DMFT [5].

A dual fermion study of the paramagnetic to anti-ferromagnetic phase transition of the half-filled 3D Hubbard model on the cubic lattice has been performed by Hirschmeier et. al. [32]. They found that for small values of the Coulomb interaction the DMFT and dual fermion results coincide. For intermediate values of the interaction the dual fermion results deviate from the DMFT results, however, they provide good agreement with the estimates from quantum Monte Carlo calculations. However, for large values of the Coulomb interaction, the dual fermion result is found to deviate from the quantum Monte Carlo and large-U asymptotics, overestimating the value of the critical temperature. The authors put this down to the dual fermion calculation only including ladder diagrams in the particle-hole channel and therefore other diagrams must also contribute to the physics in this parameter regime. The authors were also able to determine the critical behaviour of the magnetic susceptibility and correlation length in the vicinity of the transition. At high temperature they found linear behaviour of the susceptibility consistent with the mean field behaviour found at the DMFT level. They also found that for large values of the Coulomb interaction, such as the one studied in this project, non-linear behaviour of the susceptibility was observed very, close to the transition. They were able to determine the critical exponents and found them to be consistent with those of the Heisenberg model.

From the above studies of the 2D and 3D Hubbard models, we would also expect a reduction in the critical temperature for the anti-ferromagnetic region Vs. the DMFT value for the model studied here. It would also be reasonable to expect that the critical exponents of the anti-ferromagnetic phase transition would also coincide with that of the Heisenberg model. We now turn to the discussion of the magnetic susceptibility obtained from the dual fermion calculations performed in this thesis.

Figure 6.16 shows the magnetic susceptibility plotted along the high symmetry path of the 1Bz for three fillings. We find that the susceptibility takes on the same profile as that of the DMFT results, with no new instabilities appearing. The susceptibility is still predominantly divergent at the X and W points with a smaller instability at the K point and some instability towards the L point. However, it remains to be seen how the critical temperatures and the interplay between the X and W phases around half-filling found at the DMFT level are affected by the inclusion of non-local correlation.

As was found to be the case around the ferromagnetic instability the fillings of the converged solutions at lower temperatures were found to change significantly from their DMFT values. This was observed for all fillings studied here. The changes in the fillings were found to be larger than in the ferromagnetic region, indicating that the non-local corrections are larger around half-filling. Interestingly the fillings were found to always change towards $n = 1.0$ and could be an indication that the inclusion of the non-local correlation is causing the onset of an insulating state by a gap starting to form around the Fermi-level.

In order to take into account the drifting of the fillings and obtain magnetic susceptibility datasets at fixed filling we use the same method for fitting a surface as was used for the ferromagnetic instability above. Figures 6.17 and 6.18 show plots of $(\frac{1}{\chi^m(\mathbf{q},0)}, n, T)$ for the X and W points respectively. We find that both the X and W point data are smoothly varying with no sudden changes or discontinuities present. The fitted surface fits the data very well in both cases and is shown as the red wireframe. The green crosses show the interpolated data points at fixed filling, while

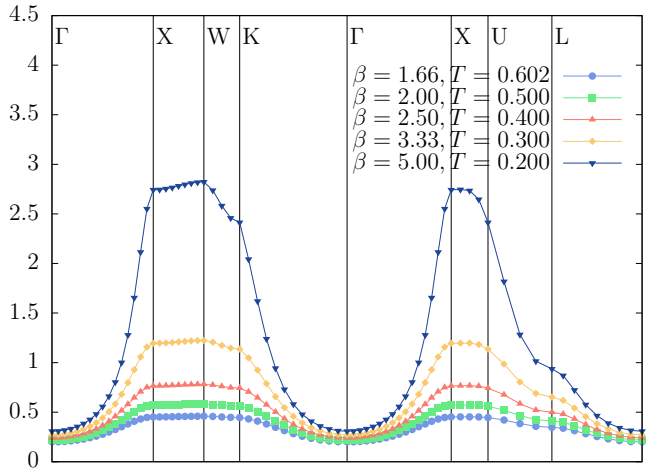

(a) $n = 0.975$

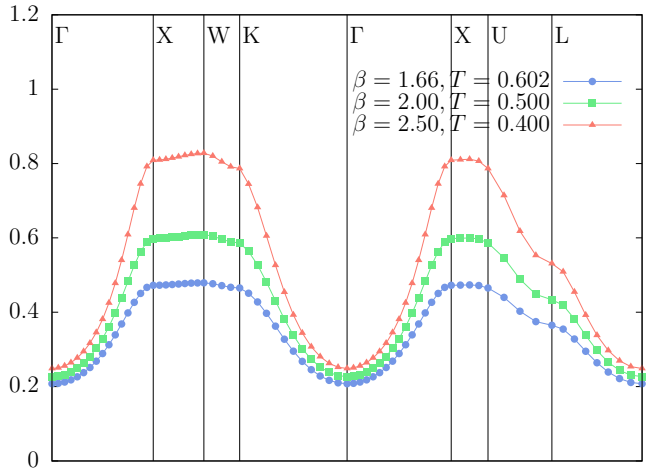

(b) $n = 1.0$

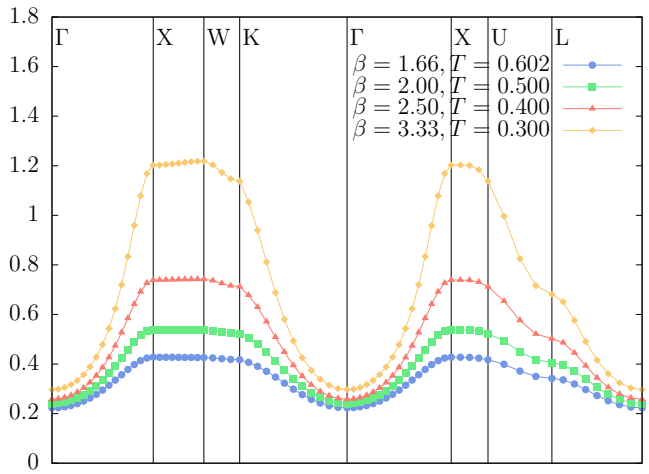

(c) $n = 1.025$

Figure 6.16: Plots the magnetic susceptibility along the high symmetry path of the 1Bz for converged dual fermion solutions for three fillings in within the AFM region.

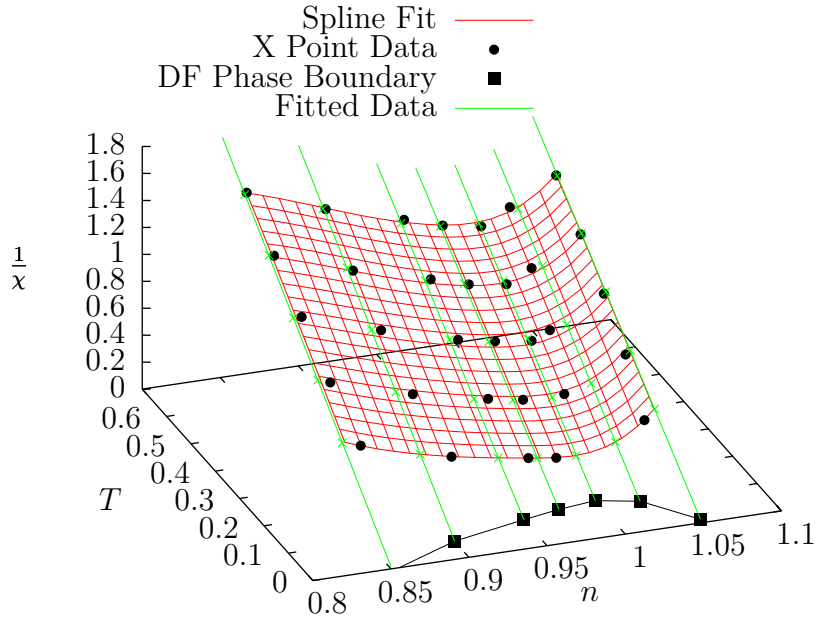

Figure 6.17: Surface plot of $(\frac{1}{\chi^m(X,0)}, T, n)$ showing one over the magnetic susceptibility at the X point, the fitted surface, the corresponding susceptibility data at constant filling and the linear fits to the susceptibility predicting the phase boundary.

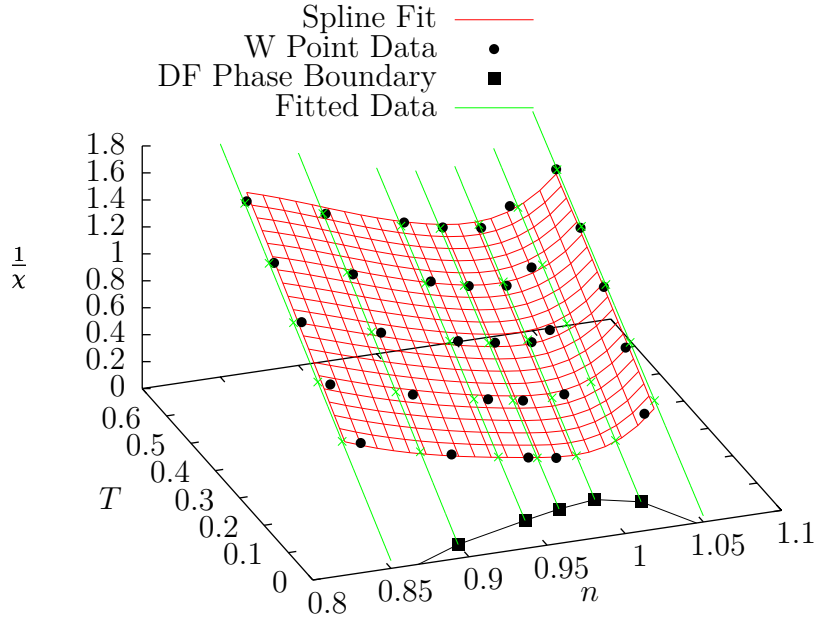

Figure 6.18: Surface plot of $(\frac{1}{\chi^m(W,0)}, T, n)$ showing one over the magnetic susceptibility at the W point, the fitted surface, the corresponding susceptibility data at constant filling and the linear fits to the susceptibility predicting the phase boundary.

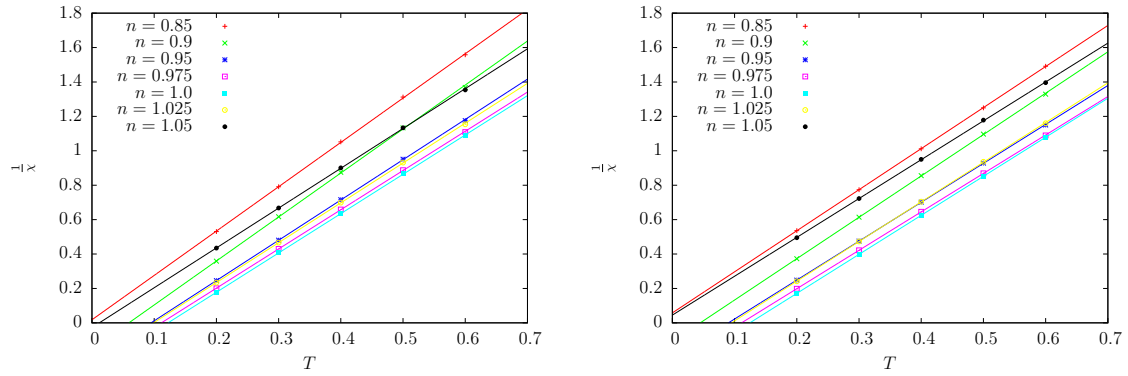

(a) X **(b)** W

Figure 6.19: Plots showing the magnetic susceptibility data at constant filling determined from the surfaces of figures 6.17 and 6.18, along with linear fits to the data. Left: X point, Right: W point.

the green lines show the fits to the interpolated data. The resulting estimates of the critical temperature are plotted on the base of the graphs as black filled squares.

We find that the data shows no evidence of deviation away from linear behaviour across the temperature range studied here. It is possible that very close to the transition the behaviour is not linear, as was found to be the case in the study of the 3D Hubbard model by Hirschmeier et. al. [32]. However, we were unable to get close enough to the transition such that we would be able to observe any non-linear behaviour. We would expect any non-linear behaviour to provide only a small reduction to the values of the critical temperatures. This is due to the non-linear behaviour occurring over such a small range of temperatures.

The linear behaviour is even more evident in figures 6.19a and 6.19b which show the fits to the susceptibility data at fixed filling for the X and W points respectively. The same error analysis as was performed in the DMFT study was performed on the fits for both the X and W point data. The 95% confidence intervals for the fits are found to be very small and produce small errors in the estimated critical temperatures, comparable to the size of those found in the DMFT study.

Figure 6.20 shows the estimates of the X and W point phase boundaries. Interestingly, the region around half-filling where it was previously found that the W point is dominant over the X point, appears to be smaller than in the DMFT

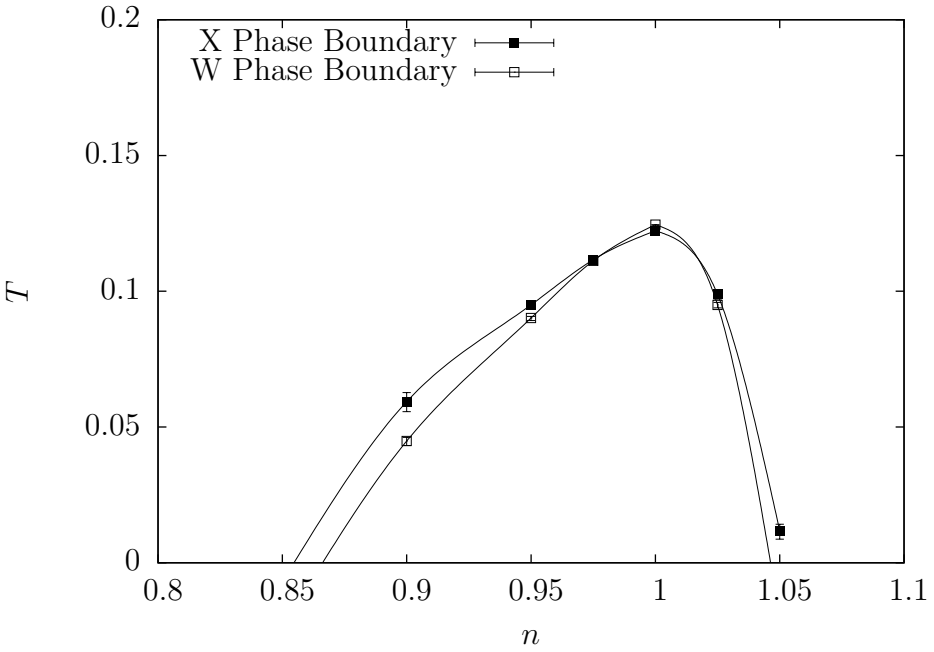

Figure 6.20: Plots of the predicted dual fermion anti-ferromagnetic phase boundary for the X and W points.

case. At half-filling, where the estimate of the W point critical temperature does take a higher value than that of the X, we find that it is within the error of the fitting procedure, thus, we can not determine if the phase is of X or W character. This is also true at $n = 0.975$ and 1.025 where the two instabilities produce very similar critical temperatures. However, further away from half-filling it is clear that the X phase is dominant, as was found in the DMFT study. For the lowest filling studied here we find that both the X and W point critical temperatures are negative, indicating that the AFM phase that was present at the DMFT level does not persist when non-local correlation is taken into account. We find a similar case at the other end of the region where the W point critical temperature is found to be negative, however, for the X point it is small but positive.

Combining the X and W point phase boundaries, taking the larger of the two estimates of the critical temperature for each filling, we can compare the dual fermion phase boundary with that of the DMFT result. This is plotted in figure 6.21. We find that the dual fermion and DMFT phase boundaries are qualitatively the same with no new features arising. For half-filling and below we find that the inclusion of

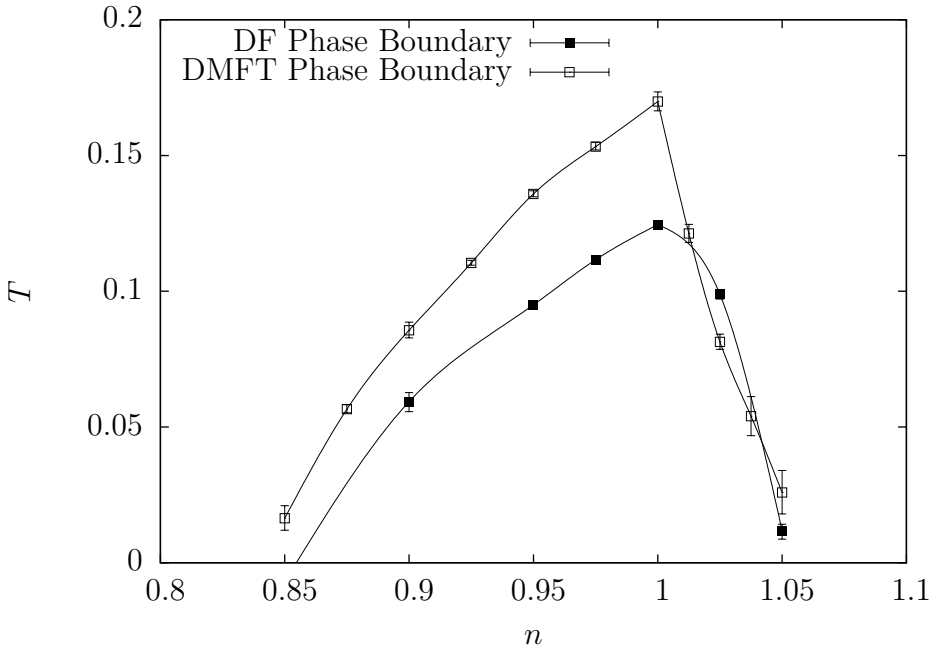

Figure 6.21: Plots of the predicted dual fermion anti-ferromagnetic phase boundary with errors alongside the corresponding DMFT phase boundary.

non-local correlation results in significantly lowered critical temperatures. This is in line with the reduction of the critical temperature found in studies of the 2D and 3D Hubbard models on the square and cubic lattices [5, 6, 32] The largest reduction is found at half-filling with successively smaller reductions from the DMFT result being found as the filling is decreased. This was somewhat predicted by the momentum dependent behaviour of the lattice self-energy discussed above. Overall this results in an increase in the lowest filling at which an anti-ferromagnetic phase can be found. This is in contrast to the ferromagnetic region where it was found that the dual fermion and DMFT phase boundaries appear to terminate at the same fillings.

Above half-filling we find that the dual fermion phase boundary predicts that the highest filling above which an anti-ferromagnetic state can be found is reduced when compared to the DMFT results. It is also interesting that for $n = 1.025$ the dual fermion phase boundary predicts an increase in the critical temperature. However, the data used to make this prediction comes from a region of the surface where there is the least data available due to the calculations not being able to

converge. Thus, we would expect the predictions made in this region of the phase diagram to be the least accurate.

7
Summary and Conclusion

In summary of the work completed as part of this thesis, the CTHYB code was heavily modified in order to adopt the segment picture [49]. This allowed for much more efficient calculations to be performed for the types of impurity problems encountered in this thesis. Alongside this, two different methods of measuring the two-particle Green's function were implemented, measurement directly in terms of Matsubara frequencies and measurements in a mixed Legendre-Fourier basis [47]. The efficient estimators methods described by Hafermann et. al. were also implemented [48]. The implementation of the measurements above allowed for the accurate calculation of the magnetic susceptibility making use of the Legendre representation of the two-particle Green's function [47]. The segment picture code and the new measurements were then extensively tested and results from the literature were replicated for a two-site model. We obtained very good agreement between both single and two-particle Green's functions when compared against results from the literature and exact diagonalisation calculations as shown in chapter 3. Building upon the above, a DMFT code was produced that is able to treat both the paramagnetic and symmetry broken phases. The DMFT code was then tested by replicating results from the literature showing the Mott transition in the 2D Hubbard model at half-filling, as shown in chapter 4. We obtained good agreement

with the results obtained by Park et. al. demonstrating the code produced and modified as part of this thesis is capable of producing correct and accurate results [2].

Once the code was written and tested it was used in order to carry out a DMFT study of the magnetic phase diagram of the Hubbard model on the fcc lattice. In order to achieve this the non-interacting density of states of the fcc lattice had to be calculated as it is not available analytically in $d = 3$. This was achieved by developing a code that implements a Monte Carlo method making use of GPUs in order to fully exploit the parallelism [91].

DMFT calculations were then performed and the magnetic susceptibility was calculated for a range of temperatures and fillings. These results showed a substantial ferromagnetic region above half-filling, as found by Ulmke using older and less accurate methods [9]. Our approach provides a significantly more precise, quantitative determination of the phase boundary. The magnetisation as a function of temperature was also calculated, allowing for a second estimate of the critical temperature to be obtained. Very good agreement between the critical temperatures determined from the susceptibility and the critical temperatures determined from the magnetisation was obtained. This further verifies the obtained ferromagnetic phase boundary and validates our approach. Anti-ferromagnetic instabilities were found at and around half-filling giving rise to a large anti-ferromagnetic phase extending below half-filling. The calculated susceptibility indicates an instability towards the X and W points in agreement with previous approximate slave boson studies [35, 36].

Single-particle spectra were also calculated using the ΩMaxEnt code for a range of fillings and temperatures above the ferromagnetic and anti-ferromagnetic regions [75]. This allowed for a demonstration of how the single-particle spectra vary with respect to changes in the filling and temperature. Further to this we show the redistribution of spectral weight between the up and down spin spectra as the paramagnetic to ferromagnetic phase boundary is crossed. Again, we obtain significantly more accurate results than those obtained previously by Ulmke for the $d = \infty$ generalisation of the fcc lattice using an older maximum

entropy approach. We also obtain the single-particle spectrum over a much wider range of the parameter space.

Following this, dual fermion calculations were performed extending the above DMFT results to investigate the effects of non-local correlation. This has not been examined previously for the fcc Hubbard model. To achieve this the OpenDF code was modified to be able to treat problems on the fcc lattice as well as take into account hopping past just nearest neighbour [50]. The code was also parallelised using Boost MPI in order to speed up the runtime. The DMFT and modified CTHYB code were further tested for use in dual fermion calculations by reproducing results for the lattice self-energy of the 2D Hubbard model from the literature [121].

All of the above code was then used to perform dual fermion calculations covering the range of fillings where the ferromagnetic and anti-ferromagnetic regions had been found at the DMFT level. This allowed for new estimates of the ferromagnetic and anti-ferromagnetic phase boundaries to be obtained with non-local correlation taken into account. The susceptibility calculated from the dual fermion results showed that no new instabilities in the susceptibility arise, and those present at the DMFT level persist, however, they are suppressed. The new critical temperatures obtained are reduced when compared to the DMFT results. The reduction in the critical temperature was found to be relatively small for the ferromagnetic region. This strongly suggests that DMFT captures almost quantitatively the exact physics of the model. Although, the dual fermion approach neglects higher-order non-local corrections beyond DMFT, however, these are likely to be even smaller in this region [118]. It is also possible that contributions from diagrams not considered in the perturbation theory for the self-energy used here could provide further corrections. The reductions in critical temperature were found to be larger for the anti-ferromagnetic region, indicating that contributions from non-local correlation are more important in this region of the phase diagram.

In the future the work presented in this thesis could be built upon in multiple ways. The first of which is the codebase modified and developed within this project can be used in order to study the Hubbard model over a much wider region of

parameter space. The code gives access to quantitative DMFT and dual fermion phase boundaries and one could study the model for varying interaction strengths across the full range of fillings. The Monte Carlo GPU code for calculating the non-interacting density of states from the dispersion relation also allows one to study the model with different values of the nearest and next-nearest neighbour hopping parameters. This allows one to study how the ferromagnetic phase is affected by the frustration of the anti-ferromagnetic phase provided by the next-nearest neighbour hopping. Preliminary results, not presented here, indicate that the ferromagnetic phase does persist in the absence of next-nearest neighbour hopping and the code developed in this project allows one to accurately determine the smaller critical temperatures, not possible in Ulmke's previous study [9]. It would also be possible to study how the ferromagnetic phase is affected by the value of the interaction, answering questions such as, how large of an interaction is required in order to observe a ferromagnetic phase.

Another interesting avenue would be to extend the modified OpenDF code further such that it is capable of treating symmetry broken phases. This would allow us to study the ferromagnetic state of the model with non-local correlation taken into account as well as study the transition from below providing further insight on the nature of the transition. It would also be interesting to further verify the obtained phase boundary by studying the leading eigenvalue of the Bethe-Salpeter equations. At a magnetic phase transition the leading eigenvalue of the Bethe-Salpeter equation in the magnetic channel will be equal to unity [5]. This allows for another method of determining the magnetic phase boundary. The instability of the dual fermion solution around half-filling also requires further investigation. It could be helpful to try and work the converged solutions at higher temperatures down towards the transition. This can be achieved by interpolating the converged solutions from higher temperatures onto a new set of Matsubara frequencies at a slightly lower temperature. This provides a good starting point for the calculation at the lower temperature as the converged solution should not lie too far from this initial guess. This process can be repeated and could allow for

solutions to be obtained closer to the phase boundary. This method has previously been used by Hirschmeier et. al. when they encountered problems with convergence close to the anti-ferromagnetic phase transition of the 3D Hubbard model [32]. This method could also allow for the dual fermion phase boundaries obtained as part of this thesis to be determined more accurately. It could also allow for any non-linear behaviour of the susceptibility very close to the transition to be determined.

References

[1] Masatoshi Imada, Atsushi Fujimori, and Yoshinori Tokura. "Metal-insulator transitions". In: *Reviews of Modern Physics* 70.4 (1998), pp. 1039–1263. URL: https://link.aps.org/doi/10.1103/RevModPhys.70.1039.

[2] H. Park, K. Haule, and G. Kotliar. "Cluster dynamical mean field theory of the mott transition". In: *Physical Review Letters* 101.18 (2008), p. 186403. URL: https://link.aps.org/doi/10.1103/PhysRevLett.101.186403.

[3] Philipp Werner and Andrew J Millis. "Doping-driven Mott transition in the one-band Hubbard model". In: *Physical Review B - Condensed Matter and Materials Physics* 75.8 (2007), p. 085108. URL: https://link.aps.org/doi/10.1103/PhysRevB.75.085108.

[4] P Hansmann et al. "Mott-Hubbard transition in V_2O_3 revisited". In: *physica status solidi (b)* 250.7 (2013), pp. 1251–1264. URL: http://doi.wiley.com/10.1002/pssb.201248476.

[5] Junya Otsuki, Hartmut Hafermann, and Alexander I. Lichtenstein. "Superconductivity, antiferromagnetism, and phase separation in the two-dimensional Hubbard model: A dual-fermion approach". In: *Physical Review B* 90.23 (2014), p. 235132. URL: http://link.aps.org/doi/10.1103/PhysRevB.90.235132.

[6] H. Hafermann et al. "Dual fermion approach to high-temperature superconductivity". In: *Journal of Superconductivity and Novel Magnetism* 22.1 (2009), pp. 45–49. URL: https://link.springer.com/article/10.1007/s10948-008-0361-9.

[7] B Keimer et al. "From quantum matter to high-temperature superconductivity in copper oxides". In: *Nature* 518.7538 (2015), pp. 179–186. URL: https://doi.org/10.1038/nature14165.

[8] W. Nolting and W. Borgiel. "Band magnetism in the Hubbard model". In: *Physical Review B* 39.10 (1989), pp. 6962–6978. URL: https://link.aps.org/doi/10.1103/PhysRevB.39.6962.

[9] M Ulmke. "Ferromagnetism in the Hubbard model on fcc-type lattices". In: *The European Physical Journal B - Condensed Matter and Complex Systems* 1.3 (1998), pp. 301–304. URL: https://link.springer.com/article/10.1007%2Fs100510050186.

[10] Alexander Cyril Hewson. *The Kondo Problem to Heavy Fermions*. Cambridge, UK: Cambridge University Press, 1993. URL: https://www.cambridge.org/core/product/identifier/9780511470752/type/book.

[11] J Hubbard. "Electron correlations in narrow energy bands". In: *Proceedings of the Royal Society of London. Series A, Mathematical and physical sciences* 276.1365 (1963), p. 238. URL: https://doi.org/10.1098/rspa.1963.0204.

[12] Antoine Georges et al. "Dynamical mean-field theory of strongly correlated fermion systems and the limit of infinite dimensions". In: *Reviews of Modern Physics* 68.1 (1996), pp. 13–125. URL: https://link.aps.org/doi/10.1103/RevModPhys.68.13.

[13] Michel Caffarel and Werner Krauth. "Exact diagonalization approach to correlated fermions in infinite dimensions: Mott transition and superconductivity". In: *Physical Review Letters* 72.10 (1994), pp. 1545–1548. URL: https://link.aps.org/doi/10.1103/PhysRevLett.72.1545.

[14] Ralf Bulla, Theo A. Costi, and Thomas Pruschke. "Numerical renormalization group method for quantum impurity systems". In: *Reviews of Modern Physics* 80.2 (2008), pp. 395–450. URL: https://link.aps.org/doi/10.1103/RevModPhys.80.395.

[15] J. E. Hirsch and R. M. Fye. "Monte Carlo Method for Magnetic Impurities in Metals". In: *Physical Review Letters* 56.23 (1986), pp. 2521–2524. URL: https://link.aps.org/doi/10.1103/PhysRevLett.56.2521.

[16] Philipp Werner et al. "Continuous-time solver for quantum impurity models". In: *Physical Review Letters* 97.7 (2006), p. 076405. URL: https://link.aps.org/doi/10.1103/PhysRevLett.97.076405.

[17] Emanuel Gull et al. "Continuous-time Monte Carlo methods for quantum impurity models". In: *Reviews of Modern Physics* 83.2 (2011), pp. 349–404. URL: https://journals.aps.org/rmp/abstract/10.1103/RevModPhys.83.349.

[18] G. Kotliar et al. "Electronic structure calculations with dynamical mean-field theory". In: *Reviews of Modern Physics* 78.3 (2006), pp. 865–951. URL: https://link.aps.org/doi/10.1103/RevModPhys.78.865.

[19] Arpita Paul and Turan Birol. "Applications of DFT + DMFT in Materials Science". In: *Annual Review of Materials Research* 49.1 (2019), pp. 31–52. URL: https://doi.org/10.1146/annurev-matsci-070218-121825.

[20] Jan Kuneš. "Efficient treatment of two-particle vertices in dynamical mean-field theory". In: *Physical Review B - Condensed Matter and Materials Physics* 83.8 (2011), p. 085102. URL: https://link.aps.org/doi/10.1103/PhysRevB.83.085102.

[21] N. D. Mermin and H. Wagner. "Erratum: Absence of ferromagnetism or antiferromagnetism in one- or two-dimensional isotropic heisenberg models (Physical Review Letters)". In: *Physical Review Letters* 17.26 (1966), p. 1307. URL: https://link.aps.org/doi/10.1103/PhysRevLett.17.1307.

[22] T. Schäfer et al. "Fate of the false Mott-Hubbard transition in two dimensions". In: *Physical Review B - Condensed Matter and Materials Physics* 91.12 (2015), p. 125109. URL: https://link.aps.org/doi/10.1103/PhysRevB.91.125109.

[23] G. Rohringer et al. "Diagrammatic routes to nonlocal correlations beyond dynamical mean field theory". In: *Reviews of Modern Physics* 90.2 (2018), p. 025003. URL: https://link.aps.org/doi/10.1103/RevModPhys.90.025003.

[24] Gabriel Kotliar et al. "Cellular dynamical mean field approach to strongly correlated systems". In: *Physical Review Letters* 87.18 (2001), pp. 186401–1–186401–4. URL: https://link.aps.org/doi/10.1103/PhysRevLett.87.186401.

[25] A. N. Rubtsov, M. I. Katsnelson, and A. I. Lichtenstein. "Dual fermion approach to nonlocal correlations in the Hubbard model". In: *Physical Review B* 77.3 (2008), p. 033101. URL: http://link.aps.org/doi/10.1103/PhysRevB.77.033101.

[26] A. N. Rubtsov et al. "Dual fermion approach to the two-dimensional Hubbard model: Antiferromagnetic fluctuations and Fermi arcs". In: *Physical Review B - Condensed Matter and Materials Physics* 79.4 (2009), p. 045133. URL: https://link.aps.org/doi/10.1103/PhysRevB.79.045133.

[27] Hartmut Hafermann et al. "Strong Electronic Correlations: Dynamical Mean-Field Theory and Beyond". English. In: *Modern Theories of Many-Particle Systems in Condensed Matter Physics SE - 4*. Ed. by Daniel C Cabra, Andreas Honecker, and Pierre Pujol. Vol. 843. Lecture Notes in Physics. Springer Berlin Heidelberg, 2012, pp. 145–214. URL: http://dx.doi.org/10.1007/978-3-642-10449-7_4.

[28] Hartmut Hafermann. "Introduction to Diagrammatic Approaches". In: *DMFT: From Infinite Dimensions to Real Materials*. 2018. Chap. 12. URL: https://www.cond-mat.de/events/correl18/manuscripts/hafermann.pdf.

[29] H. Hafermann et al. "Efficient perturbation theory for quantum lattice models". In: *Physical Review Letters* 102.20 (2009), p. 206401. URL: https://link.aps.org/doi/10.1103/PhysRevLett.102.206401.

[30] Hunpyo Lee, Gang Li, and Hartmut Monien. "Hubbard model on the triangular lattice using dynamical cluster approximation and dual fermion methods". In: *Physical Review B - Condensed Matter and Materials Physics* 78.20 (2008), p. 205117. URL: https://link.aps.org/doi/10.1103/PhysRevB.78.205117.

[31] Daniel Hirschmeier, Hartmut Hafermann, and Alexander I. Lichtenstein. "Multiband dual fermion approach to quantum criticality in the Hubbard honeycomb lattice". In: *Physical Review B* 97.11 (2018), p. 115150. URL: https://link.aps.org/doi/10.1103/PhysRevB.97.115150.

[32] Daniel Hirschmeier et al. "Mechanisms of finite-temperature magnetism in the three-dimensional Hubbard model". In: *Physical Review B - Condensed Matter and Materials Physics* 92.14 (2015), p. 144409. URL: https://link.aps.org/doi/10.1103/PhysRevB.92.144409.

[33] Andrey E. Antipov, Emanuel Gull, and Stefan Kirchner. "Critical exponents of strongly correlated fermion systems from diagrammatic multiscale methods". In: *Physical Review Letters* 112.22 (2014), p. 226401. URL: https://link.aps.org/doi/10.1103/PhysRevLett.112.226401.

[34] T. Herrmann and W. Nolting. "Ferromagnetism in the Hubbard model: Influence of the lattice structure". In: *Solid State Communications* 103.6 (1997), pp. 351–356. URL: https://www.sciencedirect.com/science/article/pii/S0038109897001920?via%3Dihub.

[35] P A Igoshev et al. “Spiral magnetism in the single-band Hubbard model: The Hartree-Fock and slave-boson approaches”. In: *Journal of Physics Condensed Matter* 27.44 (2015), p. 446002. URL: http://stacks.iop.org/0953-8984/27/i=44/a=446002?key=crossref.9a1c772b0e221df53eb152762d3329a3.

[36] M A Timirgazin et al. “Magnetic states, correlation effects and metal-insulator transition in FCC lattice”. In: *Journal of Physics: Condensed Matter* 28.50 (2016), p. 505601. URL: http://stacks.iop.org/0953-8984/28/i=50/a=505601?key=crossref.4647759d585243cb3f175a86c32aa537.

[37] N. Rosengaard and Börje Johansson. “Finite-temperature study of itinerant ferromagnetism in Fe, Co, and Ni”. In: *Physical Review B - Condensed Matter and Materials Physics* 55.22 (1997), pp. 14975–14986. URL: https://link.aps.org/doi/10.1103/PhysRevB.55.14975.

[38] J. F. Janak. “Itinerant ferromagnetism in fcc cobalt”. In: *Solid State Communications* 25.2 (1978), pp. 53–55. URL: https://www.sciencedirect.com/science/article/pii/003810987890354X.

[39] E. P. Wohlfarth. *Iron, cobalt and nickel*. 1980. URL: https://www.sciencedirect.com/science/article/pii/S1574930405801166.

[40] A. I. Lichtenstein, M. I. Katsnelson, and G. Kotliar. “Finite-Temperature Magnetism of Transition Metals: An ab initio Dynamical Mean-Field Theory”. In: *Physical Review Letters* 87.6 (2001), pp. 67205–1–67205–4. URL: https://link.aps.org/doi/10.1103/PhysRevLett.87.067205.

[41] J. Braun et al. “Spectral function of ferromagnetic 3d metals: A self-consistent LSDA+DMFT approach combined with the one-step model of photoemission”. In: *Physical Review Letters* 97.22 (2006), p. 227601. URL: https://link.aps.org/doi/10.1103/PhysRevLett.97.227601.

[42] J. Faber and G. H. Lander. “Neutron diffraction study of UO2: Antiferromagnetic state”. In: *Physical Review B* 14.3 (1976), pp. 1151–1164. URL: https://link.aps.org/doi/10.1103/PhysRevB.14.1151.

[43] B. C. Frazer et al. “Neutron-diffraction study of antiferromagnetism in UO2”. In: *Physical Review* 140.4A (1965), A1448–A1452. URL: https://link.aps.org/doi/10.1103/PhysRev.140.A1448.

[44] T Chatterji et al. “Magnetic excitations in frustrated fcc type-III antiferromagnet MnS 2”. In: *Journal of Physics Condensed Matter* 31.12 (2019), p. 125802. arXiv: 1812.07267. URL: https://iopscience.iop.org/article/10.1088/1361-648X/aafaeb.

[45] A Dönni et al. “F.c.c. type-III antiferromagnetism in YbN”. In: *Zeitschrift für Physik B Condensed Matter* 80.2 (1990), pp. 269–274. URL: https://doi.org/10.1007/BF01357513.

[46] A. Dönni et al. “Long-range f.c.c. antiferromagnetic ordering of type III in YbAs”. In: *Solid State Communications* 71.5 (1989), pp. 365–368. URL: https://www.sciencedirect.com/science/article/pii/0038109889907722.

[47] Lewin Boehnke et al. “Orthogonal polynomial representation of imaginary-time Green’s functions”. In: *Physical Review B* 84.7 (2011), p. 075145. URL: http://link.aps.org/doi/10.1103/PhysRevB.84.075145.

[48] Hartmut Hafermann, Kelly R. Patton, and Philipp Werner. "Improved estimators for the self-energy and vertex function in hybridization-expansion continuous-time quantum Monte Carlo simulations". In: *Physical Review B* 85.20 (2012), p. 205106. URL: https://link.aps.org/doi/10.1103/PhysRevB.85.205106.

[49] Priyanka Seth et al. "TRIQS/CTHYB: A continuous-time quantum Monte Carlo hybridisation expansion solver for quantum impurity problems". In: *Computer Physics Communications* 200 (2016), pp. 274–284. URL: https://www.sciencedirect.com/science/article/pii/S001046551500404X?via%3Dihub.

[50] Andrey E. Antipov, James P.F. LeBlanc, and Emanuel Gull. "Opendf - An Implementation of the Dual Fermion Method for Strongly Correlated Systems". In: *Physics Procedia* 68 (2015), pp. 43–51. URL: https://www.sciencedirect.com/science/article/pii/S1875389215007178.

[51] Mark Jarrell and J. E. Gubernatis. "Bayesian inference and the analytic continuation of imaginary-time quantum Monte Carlo data". In: *Physics Report* 269.3 (1996), pp. 133–195. URL: https://www.sciencedirect.com/science/article/pii/0370157395000747.

[52] Antoine Georges and Gabriel Kotliar. "Hubbard model in infinite dimensions". In: *Physical Review B* 45.12 (1992), pp. 6479–6483. URL: https://link.aps.org/doi/10.1103/PhysRevB.45.6479.

[53] J. Han and M. Jarrell. "Multiorbital Hubbard model in infinite dimensions: Quantum Monte Carlo calculation". In: *Physical Review B - Condensed Matter and Materials Physics* 58.8 (1998), R4199–R4202. URL: https://link.aps.org/doi/10.1103/PhysRevB.58.R4199.

[54] J. Wahle et al. "Microscopic conditions favoring itinerant ferromagnetism". In: *Physical Review B - Condensed Matter and Materials Physics* 58.19 (1998), pp. 12749–12757. URL: https://link.aps.org/doi/10.1103/PhysRevB.58.12749.

[55] Fabian H. L. Essler et al. *The One-Dimensional Hubbard Model*. Cambridge University Press, 2005. URL: https://www.cambridge.org/core/product/identifier/9780511534843/type/book.

[56] T. Siro and A. Harju. "Exact diagonalization of the Hubbard model on graphics processing units". In: *Computer Physics Communications* 183.9 (2012), pp. 1884–1889. URL: https://www.sciencedirect.com/science/article/pii/S0010465512001452.

[57] P. W. Anderson. "Localized magnetic states in metals". In: *Physical Review* 124.1 (1961), pp. 41–53. URL: https://link.aps.org/doi/10.1103/PhysRev.124.41.

[58] Gerald D. Mahan. *Many-Particle Physics*. 3rd ed. Physics of Solids and Liquids. Springer US, 2000, pp. XII, 785. URL: https://www.springer.com/gp/book/9780306463389.

[59] G. Rohringer, A. Valli, and A. Toschi. "Local electronic correlation at the two-particle level". In: *Physical Review B - Condensed Matter and Materials Physics* 86.12 (2012), p. 125114. URL: https://link.aps.org/doi/10.1103/PhysRevB.86.125114.

[60] Georg Rohringer. "New routes towards a theoretical treatment of nonlocal electronic correlations". In: November 2013 (2013), p. 318. URL: https://inis.iaea.org/search/search.aspx?orig_q=RN:46109653.

[61] A. N. Rubtsov, V. V. Savkin, and A. I. Lichtenstein. "Continuous-time quantum Monte Carlo method for fermions". In: *Physical Review B - Condensed Matter and Materials Physics* 72.3 (2005), p. 035122. URL: https://link.aps.org/doi/10.1103/PhysRevB.72.035122.

[62] E. Gull et al. "Continuous-time auxiliary-field Monte Carlo for quantum impurity models". In: *EPL* 82.5 (2008), p. 57003. URL: http://stacks.iop.org/0295-5075/82/i=5/a=57003?key=crossref.a04bd39c153e80d2afe29b4a20da2527.

[63] Emanuel Gull et al. "Performance analysis of continuous-time solvers for quantum impurity models". In: *Physical Review B - Condensed Matter and Materials Physics* 76.23 (2007), p. 235123. URL: https://link.aps.org/doi/10.1103/PhysRevB.76.235123.

[64] Emanuel Gull. "Continuous-time quantum Monte Carlo algorithms for fermions". In: *Thesis* (2008). URL: https://doi.org/10.3929/ethz-a-005722583.

[65] Philipp Werner. "Diagrammatic Monte Carlo simulation of quantum impurity models – weak and strong coupling approach". In: *International Summer School on Numerical Methods for Correlated Systems in Condensed Matter, Sherbrooke, Canada* (2008). URL: https://pitp.phas.ubc.ca/confs/sherbrooke/archives/pitpcifar2008_qmc_werner.pdf.

[66] Nicholas Metropolis et al. "Equation of state calculations by fast computing machines". In: *The Journal of Chemical Physics* 21.6 (1953), pp. 1087–1092. URL: http://aip.scitation.org/doi/10.1063/1.1699114.

[67] W K Hastings. "Monte Carlo Sampling Methods Using Markov Chains and Their Applications". In: *Biometrika* 57.1 (1970), pp. 97–109. URL: http://www.jstor.org/stable/2334940.

[68] R Bulla, A C Hewson, and Th Pruschke. "Numerical renormalization group calculations for the self-energy of the impurity Anderson model". In: *Journal of Physics Condensed Matter* 10.37 (1998), pp. 8365–8380. URL: http://stacks.iop.org/0953-8984/10/i=37/a=021?key=crossref.a26beff970abb950cbf9ad35e6c11e4c.

[69] Olivier Parcollet et al. "TRIQS: A toolbox for research on interacting quantum systems". In: *Computer Physics Communications* 196 (2015), pp. 398–415. URL: http://www.sciencedirect.com/science/article/pii/S0010465515001666.

[70] Andrey E. Antipov, Igor Krivenko, and Sergei Iskakov. "aeantipov/pomerol: 1.2". In: (2017). URL: https://doi.org/10.5281/zenodo.825870#.XVbOAjGTnvQ.mendeley.

[71] Xin Wang, Hung The Dang, and Andrew J. Millis. "High-frequency asymptotic behavior of self-energies in quantum impurity models". In: *Physical Review B - Condensed Matter and Materials Physics* 84.7 (2011), p. 073104. URL: https://link.aps.org/doi/10.1103/PhysRevB.84.073104.

[72] H J Vidberg and J W Serene. "Solving the Eliashberg equations by means ofN-point Padé approximants". In: *Journal of Low Temperature Physics* 29.3 (1977), pp. 179–192. URL: https://doi.org/10.1007/BF00655090.

[73] Mark Jarrell. "The Maximum Entropy Method : Analytic Continuation of QMC Data". In: *Correlated Electrons: From Models to Materials*. Vol. 2. Forschungszentrum Jülich GmbH Institute for Advanced Simulation, 2012. Chap. 13. URL: https://www.cond-mat.de/events/correl12/manuscripts/correl12.pdf.

[74] Dominic Bergeron and A.-M. S. Tremblay. "Algorithms for optimized maximum entropy and diagnostic tools for analytic continuation". In: *Physical Review E* 94.2 (2016), p. 023303. URL: https://link.aps.org/doi/10.1103/PhysRevE.94.023303.

[75] Dominic Bergeron. *ΩMaxEnt Maximum Entropy method code*. 2016. URL: https://www.physique.usherbrooke.ca/MaxEnt/index.php?title=Main_Page.

[76] Andrey S Mishchenko. "Stochastic Optimization Method for Analytic Continuation". In: *Correlated Electrons: From Models to Materials Modeling and Simulation Vol. 2* 2 (2012). URL: http://www.cond-mat.de/events/correl12/manuscripts/mishchenko.pdf.

[77] A. S. Mishchenko et al. "Diagrammatic quantum Monte Carlo study of the Fröhlich polaron". In: *Physical Review B - Condensed Matter and Materials Physics* 62.10 (2000), pp. 6317–6336. URL: https://link.aps.org/doi/10.1103/PhysRevB.62.6317.

[78] Ryan Levy, J. P. F. LeBlanc, and Emanuel Gull. "Implementation of the Maximum Entropy Method for Analytic Continuation". In: *Computer Physics Communications* 215 (2016), pp. 149–155. URL: https://www.sciencedirect.com/science/article/pii/S0010465517300309?via%3Dihub.

[79] Walter Metzner and Dieter Vollhardt. "Correlated lattice fermions in $d = \infty$ dimensions". In: *Physical Review Letters* 62.3 (1989), pp. 324–327. URL: https://link.aps.org/doi/10.1103/PhysRevLett.62.324.

[80] E Muller-Hartmann. "The Hubbard model at high dimensions: some exact results and weak coupling theory". In: *Zeitschrift für Physik B Condensed Matter* 76.2 (1989), pp. 211–217. URL: https://doi.org/10.1007/BF01312686.

[81] Dieter Vollhardt, Krzysztof Byczuk, and Marcus Kollar. "Dynamical Mean-Field Theory". In: *Strongly Correlated Systems: Theoretical Methods*. Ed. by Adolfo Avella and Ferdinando Mancini. Berlin, Heidelberg: Springer Berlin Heidelberg, 2012, pp. 203–236. URL: http://link.springer.com/10.1007/978-3-642-21831-6_7.

[82] J J Binney et al. *The Theory of Critical Phenomena: An Introduction to the Renormalization Group*. New York, NY, USA: Oxford University Press, Inc., 1992. URL: https://global.oup.com/academic/product/the-theory-of-critical-phenomena-9780198513933?cc=gb&lang=en&.

[83] Marcus Kollar. "Introduction to Dynamical Mean-Field Theory". In: *The LDA+DMFT approach to strongly correlated matter*. Vol. 1. 2011. Chap. 5. URL: https://www.cond-mat.de/events/correl11/manuscripts/kollar.pdf.

[84] Thomas Maier et al. "Quantum cluster theories". In: *Reviews of Modern Physics* 77.3 (2005), pp. 1027–1080. URL: https://link.aps.org/doi/10.1103/RevModPhys.77.1027.

[85] Thomas Schäfer, Alessandro Toschi, and Karsten Held. "Dynamical vertex approximation for the two-dimensional Hubbard model". In: *Journal of Magnetism and Magnetic Materials* 400 (2016), pp. 107–111. URL: https://www.sciencedirect.com/science/article/pii/S030488531530411X.

[86] Gabriel Kotliar and Dieter Vollhardt. *Strongly Correlated Materials: Insights From Dynamical Mean-Field Theory*. 2004. URL: http://physicstoday.scitation.org/doi/10.1063/1.1712502#.XXEjQOLVc0Y.mendeley.

[87] Rok Žitko, Janez Bonča, and Thomas Pruschke. "Van Hove singularities in the paramagnetic phase of the Hubbard model: DMFT study". In: *Physical Review B - Condensed Matter and Materials Physics* 80.24 (2009), p. 245112. URL: https://link.aps.org/doi/10.1103/PhysRevB.80.245112.

[88] Eva Pavarini. "Linear Response Functions". In: *DMFT at 25: Infinite Dimensions*. 2014. Chap. 6. URL: https://www.cond-mat.de/events/correl14/manuscripts/pavarini.pdf.

[89] V. Zlatic and B. Horvatic. "The local approximation for correlated systems on high dimensional lattices". In: *Solid State Communications* 75.3 (1990), pp. 263–267. URL: https://www.sciencedirect.com/science/article/pii/003810989090282G.

[90] M. Jarrell. "Hubbard model in infinite dimensions: A quantum Monte Carlo study". In: *Physical Review Letters* 69.1 (1992), pp. 168–171. URL: https://link.aps.org/doi/10.1103/PhysRevLett.69.168.

[91] Louis-François Arsenault, Patrick Sémon, and A.-M. S. Tremblay. "Benchmark of a modified iterated perturbation theory approach on the fcc lattice at strong coupling". In: *Physical Review B* 86.8 (2012), p. 085133. URL: https://link.aps.org/doi/10.1103/PhysRevB.86.085133.

[92] Eleftherios N. Economou. "Green's Functions for Tight-Binding Hamiltonians". In: *Green's Functions in Quantum Physics*. Berlin, Heidelberg: Springer Berlin Heidelberg, 2006, pp. 77–110. URL: http://link.springer.com/10.1007/3-540-28841-4_5.

[93] Tohru Morita. "Useful procedure for computing the lattice Green's function - Square, tetragonal, and bcc lattices". In: *Journal of Mathematical Physics* 12.8 (1971), pp. 1744–1747. URL: http://aip.scitation.org/doi/10.1063/1.1665800.

[94] D. Vollhardt et al. "Metallic Ferromagnetism — An Electronic Correlation Phenomenon". In: *Band-Ferromagnetism*. Ed. by Klaus Baberschke, Wolfgang Nolting, and Markus Donath. Berlin, Heidelberg: Springer Berlin Heidelberg, 2001, pp. 191–207. URL: http://link.springer.com/10.1007/3-540-44610-9_13.

[95] D Vollhardt et al. "Non-perturbative approaches to magnetism in strongly correlated electron systems". In: *Zeitschrift für Physik B Condensed Matter* 103.2 (1996), pp. 283–292. URL: https://doi.org/10.1007/s002570050375.

[96] D. Vollhardt et al. "Metallic ferromagnetism: Progress in our understanding of an old strong-coupling problem". In: *Advances in Solid State Physics 38*. Berlin, Heidelberg: Springer Berlin Heidelberg, 1999, pp. 383–396. URL: http://www.springerlink.com/index/10.1007/BFb0107631.

[97] W. Hofstetter and D. Vollhardt. "Frustration of antiferromagnetism in the t-t'-Hubbard model at weak coupling". In: *Annalen der Physik* 7.1 (1998), pp. 48–55. URL: http://doi.wiley.com/10.1002/andp.2060070105.

[98] Thoralf Hanisch, Götz S. Uhrig, and Erwin Müller-Hartmann. "Lattice dependence of saturated ferromagnetism in the Hubbard model". In: *Physical Review B - Condensed Matter and Materials Physics* 56.21 (1997), pp. 13960–13982. URL: https://link.aps.org/doi/10.1103/PhysRevB.56.13960.

[99] Harald Ibach and Hans Lüth. "Structure of Solid Matter". In: *Solid-State Physics: An Introduction to Principles of Materials Science*. Berlin, Heidelberg: Springer Berlin Heidelberg, 2009, pp. 21–49. URL: https://doi.org/10.1007/978-3-540-93804-0_2.

[100] S H Simon. *The Oxford Solid State Basics*. OUP Oxford, 2013. URL: https://global.oup.com/academic/product/the-oxford-solid-state-basics-9780199680771?cc=gb&lang=en&.

[101] John Nickolls et al. "Scalable parallel programming with CUDA". In: *Queue* 6.2 (2008), pp. 40–53. URL: http://portal.acm.org/citation.cfm?doid=1365490.1365500.

[102] Mutsuo Saito and Makoto Matsumoto. "Variants of Mersenne Twister suitable for Graphic Processors". In: *ACM Transactions on Mathematical Software* 39.2 (2013). URL: http://arxiv.org/abs/1005.4973.

[103] NVIDIA. *CUDA Toolkit CURAND Guide*. Santa Clara, 2012. URL: https://docs.nvidia.com/cuda/curand/index.html.

[104] *BOOST C++ Libraries*. 2016. URL: https://www.boost.org/.

[105] Yosuke Nagaoka. "Ferromagnetism in a narrow, almost half-filled s band". In: *Physical Review* 147.1 (1966), pp. 392–405. URL: https://link.aps.org/doi/10.1103/PhysRev.147.392.

[106] Martin Ulmke. "Ferromagnetism in the Hubbard Model on the Infinite Dimensional fcc Lattice". In: (1995). URL: http://arxiv.org/abs/cond-mat/9512044.

[107] S. Bei der Kellen, W. Nolting, and G. Borstel. "Magnetic phase transitions in narrow nondegenerate energy bands". In: *Physical Review B* 42.1 (1990), pp. 447–457. URL: https://link.aps.org/doi/10.1103/PhysRevB.42.447.

[108] R. Bulla, D. Vollhardt, and T. A. Costi. "Finite-temperature numerical renormalization group study of the Mott transition". In: *Physical Review B - Condensed Matter and Materials Physics* 64.4 (2001), p. 045103. URL: https://link.aps.org/doi/10.1103/PhysRevB.64.045103.

[109] Robert Peters and Thomas Pruschke. "Half-filled Hubbard model on a Bethe lattice with next-nearest-neighbor hopping". In: *Physical Review B - Condensed Matter and Materials Physics* 79.4 (2009), p. 045108. URL: https://link.aps.org/doi/10.1103/PhysRevB.79.045108.

[110] R Peters and Th Pruschke. "Magnetic phase diagram of the Hubbard model with next-nearest neighbor hopping". In: *Physica B: Condensed Matter* 404.19 (2009), pp. 3249–3252. URL: http://stacks.iop.org/1367-2630/11/i=8/a=083022?key=crossref.a1684f8de692c21b643aefaf0127d112.

[111] G. Kotliar, Sahana Murthy, and M. J. Rozenberg. "Compressibility Divergence and the Finite Temperature Mott Transition". In: *Physical Review Letters* 89.4 (2002), p. 046401. URL: https://link.aps.org/doi/10.1103/PhysRevLett.89.046401.

[112] Marcelo J. Rozenberg, R. Chitra, and Gabriel Kotliar. "Finite temperature mott transition in the hubbard model in infinite dimensions". In: *Physical Review Letters* 83.17 (1999), pp. 3498–3501. URL: https://link.aps.org/doi/10.1103/PhysRevLett.83.3498.

[113] M. Hettler et al. "Dynamical cluster approximation: Nonlocal dynamics of correlated electron systems". In: *Physical Review B - Condensed Matter and Materials Physics* 61.19 (2000), pp. 12739–12756. URL: https://link.aps.org/doi/10.1103/PhysRevB.61.12739.

[114] Michael Potthoff. "Cluster Extensions of Dynamical Mean-Field Theory". In: *DMFT: From Infinite Dimensions to Real Materials*. 2018. Chap. 5. URL: https://www.cond-mat.de/events/correl18/manuscripts/potthoff.pdf.

[115] A. Toschi, A. A. Katanin, and K. Held. "Dynamical vertex approximation: A step beyond dynamical mean-field theory". In: *Physical Review B - Condensed Matter and Materials Physics* 75.4 (2007), p. 045118. URL: https://link.aps.org/doi/10.1103/PhysRevB.75.045118.

[116] Karsten Held. "Dynamical Vertex Approximation". In: *DMFT at 25: Infinite Dimensions*. 2014. Chap. 10. URL: https://www.cond-mat.de/events/correl14/manuscripts/held.pdf.

[117] Alexander Lichtenstein. "Path Integrals and Dual Fermions". In: *The Physics of Correlated Insulators, Metals, and Superconductors*. 2017. Chap. 10. URL: https://www.cond-mat.de/events/correl17/manuscripts/lichtenstein.pdf.

[118] T. Ribic et al. "Role of three-particle vertex within dual fermion calculations". In: *Physical Review B* 96.23 (2017), p. 235127. arXiv: 1710.00648. URL: https://link.aps.org/doi/10.1103/PhysRevB.96.235127.

[119] T. Ribic, P. Gunacker, and K. Held. "Impact of self-consistency in dual fermion calculations". In: *Physical Review B* 98.12 (2018), p. 125106. arXiv: 1805.10996. URL: https://link.aps.org/doi/10.1103/PhysRevB.98.125106.

[120] S. Brener et al. "Dual fermion approach to susceptibility of correlated lattice fermions". In: *Physical Review B - Condensed Matter and Materials Physics* 77.19 (2008), p. 195105. URL: https://link.aps.org/doi/10.1103/PhysRevB.77.195105.

[121] Jan Gukelberger, Evgeny Kozik, and Hartmut Hafermann. "Diagrammatic Monte Carlo approach for diagrammatic extensions of dynamical mean-field theory: Convergence analysis of the dual fermion technique". In: *Physical Review B* 96.3 (2017), p. 035152. URL: http://link.aps.org/doi/10.1103/PhysRevB.96.035152.

[122] Erik G.C.P. Van Loon, Mikhail I. Katsnelson, and Hartmut Hafermann. "Second-order dual fermion approach to the Mott transition in the two-dimensional Hubbard model". In: *Physical Review B* 98.15 (2018), p. 155117. URL: https://link.aps.org/doi/10.1103/PhysRevB.98.155117.